

# **Astrophysical Applications of Gravitationally Lensed Quasars: from Dark Matter Halos to the Structure of Quasar Accretion Disks**

THÈSE N° 4235 (2008)

PRÉSENTÉE LE 16 DÉCEMBRE 2008  
À LA FACULTÉ SCIENCES DE BASE  
LABORATOIRE D'ASTROPHYSIQUE  
PROGRAMME DOCTORAL EN PHYSIQUE

ÉCOLE POLYTECHNIQUE FÉDÉRALE DE LAUSANNE

POUR L'OBTENTION DU GRADE DE DOCTEUR ÈS SCIENCES

PAR

**Alexander EIGENBROD**

acceptée sur proposition du jury:

Prof. G. Gremaud, président du jury  
Prof. G. Meylan, Dr F. Courbin, directeurs de thèse  
Prof. M. Chapochnikov, rapporteur  
Prof. T. Courvoisier, rapporteur  
Prof. P. Schneider, rapporteur



ÉCOLE POLYTECHNIQUE  
FÉDÉRALE DE LAUSANNE

Suisse  
2008





# Abstract

Gravitational lensing describes how light is deflected as it passes in the vicinity of a mass distribution. The amplitude of the deflection is proportional to the mass of the deflector, called “gravitational lens”, and is generally weak, even for large masses. The faintness of this phenomenon explains why gravitational lensing remained essentially unobserved until the late 1970s (only gravitational lensing by the Sun has been observed during the solar eclipse of 1919). Before that time, gravitational lensing was considered merely as a theoretical curiosity. However, the situation dramatically changed with the discovery of the first extragalactic gravitational lens in 1979. Since then, together with the technological progress of astronomical instruments, gravitational lensing has turned from a curiosity into a powerful tool to address important astrophysical and cosmological questions.

The present thesis focuses on applications related to gravitationally lensed quasars. Quasars are active galactic nuclei, where matter is heated up as it spirals down onto the central supermassive black hole. When a galaxy is located on the line of sight to a distant quasar, it acts as a gravitational lens and produces multiple images of this background source. The light of the quasar follows different paths for each of its images. Thus, variations of the intrinsic quasar luminosity are observed at different times in each image. The time delays between the images can be used to determine the Hubble constant  $H_0$ , because they are inversely proportional to  $H_0$ . This constant describes the current expansion rate of the Universe, and is one of the fundamental parameters of cosmological models. Many efforts have been spent over the years to determine  $H_0$ , but its value is still poorly constrained. Gravitational lensing has the potential to noticeably decrease the uncertainty of  $H_0$ . In practice, this requires regular and long-term monitoring of lensed quasars. We have run a series of numerical simulations to both optimize the available telescope time, and measure the time delays with an accuracy of a few percent. The results of these simulations are presented in the form of compact plots to be used to optimize the observational strategy of present and future monitoring programs.

Once the time delays are measured, one can infer estimates of  $H_0$ , provided several other observational constraints are available. A key element to accurately convert time delays into  $H_0$  is the redshift of the lensing galaxy. These redshift measurements are difficult because lensing galaxies are generally hidden in the glare of the much brighter quasar images. As a consequence, lens redshifts are often poorly constrained or even completely unknown. We have acquired spectroscopic data of sixteen lensing galaxies with the Very Large Telescope located in Chile. In combination with a powerful deconvolution algorithm, we determine the redshift of these sixteen lensing galaxies, which represents about 25% of all currently known quasar lensing galaxies. These results are useful for

both  $H_0$  determinations and statistical studies of gravitational lenses, which can be used to provide new constraints on cosmological parameters.

While the first part of this thesis focuses on the acquisition of observational constraints for the lens models, the main part consists in using the phenomenon of microlensing to determine the energy profile (or spatial structure) of quasar accretion disks. Microlensing is produced by the stars located in the lensing galaxy. These stars act as secondary lenses, and are called microlenses. Since the stars are moving in the galaxy, they induce flux and color variations in the images of the lensed quasar. These effects can be used as a natural telescope to probe the still mysterious inner structures of quasars with a spatial resolution about ten thousand times better than the capacities of current astronomical instruments, including the Very Large Telescope Interferometer. We present a three-year long spectrophotometric monitoring of the lensed quasar QSO 2237+0305, also known as the Einstein Cross, conducted at the Very Large Telescope. This monitoring reveals significant microlensing-induced variations in the spectra of the quasar images. In a subsequent analysis, we find that the source responsible for the optical and ultraviolet continuum has an energy profile well reproduced by a power-law  $R \propto \lambda^\zeta$  with  $\zeta = 1.2 \pm 0.3$ , where  $R$  is the size of the source emitting at wavelength  $\lambda$ . This agrees with the predictions of the standard thin accretion disk model and is, so far, the most accurate determination of a quasar energy profile.

As a complement to our microlensing study, we have obtained high spectral and spatial resolution observations of the lensing galaxy of QSO 2237+0305. Our spectroscopic data are acquired with the SINFONI, FLAMES, and FORS2 spectrographs of the Very Large Telescope. We describe the reduction of these data, and provide the currently best and most complete determination of the kinematics of a gravitational lens. The comparison of our data with previously published dynamical models suggests that those may have overestimated the mass of the galaxy bulge. Thus, new and more sophisticated models are required. These models, combined with gravitational lensing, will provide two independent constraints on the mass distribution. This will allow to better determine the quantity and distribution of dark matter in this lensing galaxy, and especially in its extended halo.

## Keywords

Accretion disk, astrophysics, cosmological parameters, cosmology, dark matter, deconvolution, Einstein Cross, gravitational lensing, Hubble constant, microlensing, QSO 2237+0305, quasar, redshift, spectroscopy, time delay.

# Résumé

L'effet de lentille gravitationnelle décrit la façon dont la lumière est défléchié lorsqu'elle passe à proximité d'une masse. Cette déviation est d'autant plus marquée que la masse du déflecteur, appelé lentille gravitationnelle, est grande, mais demeure faible même pour des objets massifs. La faiblesse de ce phénomène explique pourquoi pratiquement aucune lentille gravitationnelle n'a été observée avant la fin des années 1970 (seul l'effet de lentille du Soleil a été observé durant l'éclipse de Soleil en 1919), et pourquoi l'effet de lentille gravitationnelle était considéré comme une curiosité théorique. La situation a considérablement changé avec la découverte, en 1979, de la première lentille gravitationnelle extragalactique. Dès lors, porté par les progrès technologiques des instruments astronomiques, l'effet de lentille gravitationnelle est passé d'une simple curiosité à un puissant outil pouvant répondre à d'importants problèmes astrophysiques et cosmologiques.

Cette thèse porte sur des applications liées aux quasars subissant l'effet de lentille gravitationnelle. Un quasar est un noyau actif de galaxie, dans lequel la matière est chauffée alors qu'elle tombe en spiralant sur le trou noir supermassif central. Lorsqu'une galaxie est située sur la ligne de visée d'un quasar, elle joue le rôle de lentille et produit de multiples images du quasar se trouvant à l'arrière plan. La lumière du quasar suit des chemins différents pour chacune de ces images. Par conséquent, si la luminosité intrinsèque du quasar varie au cours du temps, nous observerons ces variations à des instants différents dans chacune des images. Les retards temporels entre les images peuvent être utilisés pour déterminer la constante de Hubble  $H_0$ , car ils sont inversement proportionnels à  $H_0$ . Cette constante décrit l'actuel taux d'expansion de l'Univers. Elle fait partie des paramètres fondamentaux des modèles cosmologiques. De nombreux travaux ont été entrepris afin de déterminer  $H_0$ , mais sa valeur n'est pas encore mesurée précisément. L'étude des lentilles gravitationnelles a le potentiel de considérablement diminuer l'incertitude de  $H_0$ . En pratique, ces mesures nécessitent des observations régulières s'étendant sur plusieurs années. Nous avons effectué une série de simulations numériques afin d'optimiser l'usage du temps d'observation à disposition, et d'atteindre une précision de mesure de quelques pourcents sur les retards temporels. Les résultats de ces simulations sont présentés sous forme de graphiques qui peuvent être utilisés pour optimiser la stratégie d'observation des programmes actuels et futurs de suivi de quasars subissant l'effet de lentille.

Une fois que les retards temporels sont mesurés et que plusieurs autres éléments sont connus, nous pouvons en déduire la valeur de  $H_0$ . Un des éléments clés pour la conversion des délais temporels en  $H_0$  est le décalage vers le rouge (*redshift*) de la galaxie-lentille. La mesure de ces décalages est difficile car la lentille est généralement cachée par les images nettement plus lumineuses du quasar. Par conséquent, les décalages vers le rouge

de nombreuses galaxies-lentilles sont souvent mal définis, voire complètement inconnus. Nous avons obtenu des données spectroscopiques de seize galaxies-lentilles avec le *Very Large Telescope* situé au Chili. En combinant ces données avec un puissant algorithme de déconvolution, nous avons pu déterminer le décalage vers le rouge de ces seize galaxies, ce qui représente environ 25% de tous les redshifts de lentilles de quasars connus à ce jour. Ces résultats sont utiles, d'une part, pour la détermination de  $H_0$  et, d'autre part, pour des études statistiques des lentilles gravitationnelles qui peuvent apporter de nouvelles contraintes sur les paramètres cosmologiques.

Alors que la première partie de cette thèse est focalisée sur l'acquisition d'observations pour contraindre les modèles de lentilles, la partie principale consiste à utiliser l'effet de microlentille gravitationnelle pour déterminer le profil d'énergie (ou la structure spatiale) du disque d'accrétion d'un quasar. L'effet de microlentille est produit par les étoiles de la galaxie-lentille. Ces étoiles jouent le rôle de lentilles secondaires, appelées microlentilles. Puisque ces étoiles se déplacent à l'intérieur de la galaxie, elles induisent des variations de l'intensité et de la couleur des images du quasar subissant l'effet de lentille. Ces variations peuvent être utilisées comme un télescope naturel pour sonder les structures internes, encore mal connues, des quasars, et ceci avec une résolution spatiale surpassant dix mille fois les capacités des instruments astronomiques actuels incluant le *Very Large Telescope Interferometer*. Nous présentons un suivi spectrophotométrique de plus de trois ans, effectué au *Very Large Telescope*, du quasar QSO 2237+0305 subissant l'effet de lentille gravitationnelle induit par une galaxie d'avant-plan. Ce quasar est également connu sous le nom de la Croix d'Einstein. Ce suivi révèle d'importantes variations dans les spectres des images du quasar provoquées par l'effet de microlentille. Dans une analyse subséquente, nous montrons que la source responsable de l'émission du continu optique et ultraviolet possède un profil d'énergie bien représenté par la loi de puissance  $R \propto \lambda^\zeta$  avec  $\zeta = 1.2 \pm 0.3$ , où  $R$  est la taille de la source émettant à la longueur d'onde  $\lambda$ . Ceci concorde avec les prédictions du modèle standard pour les disques d'accrétion minces et représente, à ce jour, la détermination la plus précise du profil d'énergie d'un quasar.

En complément à notre étude de l'effet de microlentille, nous avons obtenu des observations à hautes résolutions spectrale et spatiale de la galaxie-lentille dans QSO 2237+0305. Nos données spectroscopiques sont acquises avec les spectrographes SINFONI, FLAMES, et FORS2 du *Very Large Telescope*. Nous décrivons la réduction de ces données et obtenons la meilleure et plus complète détermination de la cinématique d'une lentille gravitationnelle. La comparaison de nos données avec les prédictions de précédents modèles dynamiques suggère que ces derniers ont peut-être surestimé la masse du bulbe de la galaxie. Par conséquent, de nouveaux modèles, plus sophistiqués, sont nécessaires. Ces modèles, combinés à l'effet de lentille gravitationnelle, apporteront deux contraintes indépendantes sur la distribution de matière. Ceci devraient permettre de mieux déterminer la quantité et la distribution de la matière sombre dans cette galaxie-lentille, et notamment dans son halo.

## Mots-clés

Astrophysique, constante de Hubble, cosmologie, Croix d'Einstein, décalage vers le rouge (*redshift*), déconvolution, disque d'accrétion, lentille gravitationnelle, matière sombre, microlentille, paramètres cosmologiques, QSO 2237+0305, quasar, retard temporel, spectroscopie.

# Acknowledgments

Completing this doctoral work has been a wonderful and enriching experience from both scientific and human points of view. There are many people who I want to sincerely thank for their contributions throughout these four last years.

First of all, I want to express my gratitude to Professor Georges Meylan for his trust, and for giving me the opportunity to complete this PhD thesis at the Laboratory of Astrophysics (LASTRO) of the Ecole Polytechnique Fédérale de Lausanne (EPFL). I warmly thank Frédéric Courbin for his many advices, his availability, his communicative enthusiasm, and for the great times we have shared together at the LASTRO or during travels, conferences, and observing nights at the Very Large Telescope in Chile.

I would also like to thank the members of the jury for the time they have spent examining this thesis. In particular, I thank Professor Peter Schneider who travelled from Bonn to Lausanne to attend my thesis examination.

On the foreign front, I must thank the Heidelberg group at the Astronomisches Rechen-Institut, especially Professor Joachim Wambsganss, for their hospitality and help during our microlensing study of the Einstein Cross. I must also thank Professor Eric Agol of the University of Washington for fascinating email exchanges, and for giving me an initiation to the incredible physics of accretion disks. I am deeply indebted to the staff of the European Southern Observatory (ESO) operating the Very Large Telescope for providing us with excellent data, and for being very helpful in accomplishing our monitoring of the Einstein Cross.

The LASTRO shares the buildings of the Observatory in Sauverny with the Department of Astronomy of the University of Geneva. Together these two institutes form a group of fabulous colleagues. I would like to thank all of them (astronomers, computer scientists, fellow PhD students, secretaries, ...) for the great atmosphere they create at the Observatory, and for making it such a remarkable place to work. In particular, I thank my office neighbour Christel Vuissoz for supporting me all these years, for providing delicious cookies, and for growing so nice and numerous plants in our office. I thank Dominique Sluse for his many helpful and valuable insights, but also for his friendly company during our shared travels, conferences, and workshops. I also sincerely thank our group's secretary Nicole Tharin for her kindness, her sense of humour, and her efficiency in solving our administrative problems.

There are countless others who have been there for me throughout my time as a graduate student. I can not cite them all here, but I would like to thank my friends in Switzerland for the great times, laughs, evenings, holidays, etc., we spent together. From the underwater world, many thanks to my dive buddies and diving instructors of the late

Interdiving dive center. The underwater world has always been a great place to refill my batteries and experience the extraordinary feelings of weightlessness and absolute tranquility. From the aeronautical world, I am grateful to my instructors and fellow student pilots of the flight school Aéroformation. It has been a great pleasure to be able to discover and share the passion of flying with them. Flying definitely provides some of the most amazing and exciting sensations and an incredible feeling of freedom.

I want to express my deepest gratitude to my family, to my grandmother Erika Sommer: Vielen Dank liebe Omi!, to my brother Nicolai: Merci frérot!, and particularly to my parents Angelika and Gerhard, who supported me in all my decisions. Ich danke Euch aus tiefstem Herzen für Eure Liebe und stetige Unterstützung. Ihr seid die besten Eltern, die man sich wünschen kann! I also would like to thank the Dan family, especially Emilia for her delicious Romanian specialities, and Adrian for his thorough proofreading. Mulțumesc mult! Finally, thank you Delia for your love and for your tremendous support. Thank you for being who you are, and for so much more. Te iubesc micuța mea!

# Contents

<b>Abstract</b>	<b>i</b>
<b>Résumé</b>	<b>iii</b>
<b>Acknowledgments</b>	<b>v</b>
<b>1 Introduction</b>	<b>1</b>
1.1 Outline . . . . .	3
<b>Part I. Theoretical background</b>	<b>4</b>
<b>2 Basics of modern cosmology</b>	<b>7</b>
2.1 The cosmological principle . . . . .	8
2.2 The Friedmann-Lemaître-Robertson-Walker metric . . . . .	8
2.3 The Hubble constant . . . . .	9
2.4 The cosmological redshift . . . . .	10
2.5 The Friedmann equations . . . . .	10
2.6 The energy components of the Universe . . . . .	11
2.7 The critical density . . . . .	12
2.8 The density parameters . . . . .	13
2.9 Cosmological distances . . . . .	14
2.10 Observational cosmology . . . . .	15
2.11 The concordance model . . . . .	19
2.12 New questions . . . . .	20
<b>3 Active galactic nuclei</b>	<b>23</b>
3.1 The classification scheme . . . . .	24
3.2 The unified scheme . . . . .	25
3.3 The standard thin accretion disk model . . . . .	30
3.4 Problems with the standard thin accretion disk model . . . . .	33
<b>4 Gravitational lensing</b>	<b>35</b>
4.1 Historical background . . . . .	35
4.2 The lens equation . . . . .	36

4.3	The deflection angle . . . . .	36
4.4	The deflection potential . . . . .	39
4.5	The arrival time and Fermat's principle . . . . .	40
4.6	The time delays and the Hubble constant . . . . .	40
4.7	Images and magnification of a lensed source . . . . .	41
4.8	Properties of ordinary images . . . . .	44
4.9	Critical curves and caustics . . . . .	44
4.10	The mass-sheet degeneracy . . . . .	45
4.11	Modeling gravitational lenses . . . . .	46
4.12	Microlensing . . . . .	49
<b>Part II. COSMOGRAIL</b>		<b>51</b>
<b>5</b>	<b>Measuring time delays</b>	<b>53</b>
5.1	Introduction . . . . .	53
5.1.1	Observational and theoretical challenges . . . . .	54
5.1.2	The COSMOGRAIL project . . . . .	55
5.2	Determination of the optimal sampling of observations . . . . .	55
5.2.1	Simulation of lightcurves . . . . .	57
5.2.2	Extracting the time delay . . . . .	57
5.2.3	Results . . . . .	57
5.3	Discussion . . . . .	59
5.4	Paper presenting how to sample the lightcurves of gravitationally lensed quasars to measure accurate time delays . . . . .	61
<b>6</b>	<b>The redshift of lensing galaxies</b>	<b>75</b>
6.1	Introduction . . . . .	75
6.2	Spatial deconvolution . . . . .	76
6.2.1	The MCS deconvolution algorithm . . . . .	76
6.2.2	The MCS deconvolution algorithm for spectra . . . . .	76
6.3	Spectroscopy with the Very Large Telescope . . . . .	82
6.3.1	Instrumental setup . . . . .	82
6.3.2	Data reduction . . . . .	83
6.3.3	Flux calibration . . . . .	85
6.3.4	Spatial deconvolution of the spectra . . . . .	86
6.3.5	Deconvolution without PSF stars . . . . .	86
6.3.6	Results . . . . .	89
6.4	The lensed quasar SDSS J0924+0219 . . . . .	90
6.5	Discussion . . . . .	91
6.6	Paper presenting the determination of the redshift of the lensing galaxy, the quasar spectral variability, and the Einstein rings in SDSS J0924+0219 . . . . .	95
6.7	Paper presenting the determination of the redshift of the lensing galaxy in eight gravitationally lensed quasars . . . . .	109
6.8	Paper presenting the determination of the redshift of the lensing galaxy in seven gravitationally lensed quasars . . . . .	119



---

<b>Part III. The Einstein Cross</b>	<b>127</b>
<b>7 Microlensing: a natural telescope</b>	<b>129</b>
7.1 The Einstein Cross QSO 2237+0305 . . . . .	134
7.2 Spectrophotometric monitoring of QSO 2237+0305 . . . . .	137
7.2.1 Instrumental setup . . . . .	138
7.2.2 Data reduction . . . . .	138
7.2.3 Flux calibration . . . . .	139
7.2.4 Spatial deconvolution of the spectra . . . . .	139
7.2.5 Results . . . . .	139
7.3 Energy profile of the accretion disk . . . . .	140
7.3.1 Previous studies . . . . .	141
7.3.2 Inverse ray-shooting . . . . .	145
7.3.3 Observed microlensing lightcurves . . . . .	146
7.3.4 Simulated microlensing lightcurves . . . . .	147
7.3.5 Bayesian analysis . . . . .	148
7.3.6 Results . . . . .	149
7.4 Discussion . . . . .	149
7.5 Paper presenting the spectrophotometric monitoring of QSO 2237+0305 with the Very Large Telescope . . . . .	151
7.6 Paper presenting the determination of the energy profile of the accretion disk in QSO 2237+0305 . . . . .	169
<b>8 Dynamics versus gravitational lensing</b>	<b>185</b>
8.1 Introduction . . . . .	185
8.2 Integral-field spectroscopy with FLAMES . . . . .	187
8.2.1 Observations and data reduction . . . . .	187
8.2.2 Data analysis and results . . . . .	188
8.3 Integral-field spectroscopy with SINFONI . . . . .	191
8.3.1 Observations and data reduction . . . . .	191
8.3.2 Data analysis and results . . . . .	191
8.4 Long-slit spectroscopy with FORS2 . . . . .	193
8.4.1 Observations and data reduction . . . . .	193
8.4.2 Data analysis and results . . . . .	193
8.5 Discussion . . . . .	195
<b>9 General conclusions and outlook</b>	<b>199</b>
<b>Bibliography</b>	<b>203</b>
<b>Publications</b>	<b>213</b>
<b>Curriculum Vitae</b>	<b>215</b>



*“Science is facts; just as houses are made of stones, so is science made of facts; but a pile of stones is not a house and a collection of facts is not necessarily science.”*  
*Henri Poincaré (1854 - 1912)*

# Chapter 1

## Introduction

The deflection of light passing close to a mass concentration was already mentioned in 1704, when Sir Isaac Newton wondered :

*“Do not bodies act upon light at a distance, and their action bend its rays; and is not this action strongest at the least distance?”*

Even though the phenomenon was known, it took more than two centuries before gravitational lensing could be consistently explained through Albert Einstein’s theory of General Relativity. Since the beginning of the 20<sup>th</sup> century and especially in the last thirty years, together with the technological advances of astronomical instruments, gravitational lensing has evolved from a curiosity into a powerful tool to address astrophysical and cosmological questions. Applications of gravitational lensing are numerous, and we briefly summarize some selected highlights.

Gravitational light deflection is determined by the mass distribution in the lensing object, and is equally sensitive to dark and luminous matter. Lensing is therefore an ideal tool for measuring the total mass of astronomical bodies. Several important discoveries were made using gravitational lensing, e.g., the discovery of a portion of dark matter in the form of low-mass stars in our Galaxy (e.g., Alcock et al., 1993; Aubourg et al., 1993), the detection of one of the smallest known extrasolar planets (Beaulieu et al., 2006), the detection of massive large-scale structures in our Universe (e.g., Van Waerbeke et al., 2000), and the finding of a direct empirical proof of the existence of dark matter (Clowe et al., 2006).

An interesting property of gravitational lenses is that they act as natural telescopes. Since lenses can magnify background sources, these appear brighter than they would without a lens. This magnification effect has yielded spectacular results, such as the detection of some of the most distant galaxies in the Universe (with  $z \simeq 7$  by Kneib et al., 2004). The stars in a lensing galaxy can act as numerous secondary microlenses,

and because these stars are moving in the lensing galaxy, they induce flux and color variations in the images of the lensed background source. These effects can be used as a natural telescope to resolve and probe the inner structures of lensed quasars with a spatial resolution of about one micro-arcsecond (e.g., Kayser et al., 1986). This is far beyond the reach of any presently available telescope. For instance, the MID-infrared Instrument (MIDI) of the Very Large Telescope Interferometer (VLTI) of the European Southern Observatory (ESO) reaches an angular resolution of about 10 milli-arcseconds in the infrared. This resolution corresponds to a building of ten floors on the Moon seen from the Earth. Even though these performances are exceptional, gravitational lensing can reach a resolution about ten thousand times better.

Other applications of gravitational lensing provide estimates of cosmological parameters. For example, the probability that a distant object is strongly lensed is proportional to the number of possible lensing objects along the line of sight, and because the volume element as a function of distance depends on the cosmological model, it is thus quite sensitive to dark energy. Statistical studies of gravitational lenses therefore provide constraints on the density of dark energy in the Universe (e.g., Fukugita et al., 1990; Turner, 1990). The Hubble constant  $H_0$  is another cosmological parameter that can be estimated from gravitational lensing. This constant is a fundamental parameter of current cosmological models because it describes the actual expansion rate of the Universe, and because it sets the scale of extragalactic distances. Despite the observational efforts spent over the years, and the numerous different techniques developed to measure  $H_0$ , its value is still poorly constrained, and its uncertainty reaches 10% (Freedman et al., 2001). Gravitational lensing has the potential to noticeably decrease this uncertainty through the so-called time-delay method (Refsdal, 1964a). This method is based on the property that a galaxy situated on the line of sight of a distant background source produces multiple and magnified images of the source. The light of these images follows different paths, and hence intrinsic variations of the source are observed at different times in each image. The time delays between the images are proportional to  $H_0^{-1}$ , and hence can be used to determine its value.

The present thesis focuses on applications related to a particular kind of gravitational lenses: gravitationally lensed quasars. Quasars are active galactic nuclei and are the brightest objects known in the Universe. Presently, there are approximately one hundred identified lensed quasars<sup>1</sup>, and hence only one in five hundred quasars is lensed. The theory of gravitational lensing is now well understood, and one of the main difficulties encountered by quasar lensing applications is the acquisition of the data. Observations of gravitational lenses are challenging, because the deflection of light is a weak phenomenon, and the typical angular separation between the multiple images of a lensed quasar is about one arcsecond. Observations of lensed quasars are hence only possible with sub-arcsecond spatial resolutions. Such resolutions are reached by space-based telescopes, or large ground-based telescopes, but are much more difficult to reach with more common 1m-class ground-based telescopes.

---

<sup>1</sup>See <http://cfa-www.harvard.edu/castles> .

---

## 1.1 Outline

In the first part of this thesis, we give a theoretical introduction. In particular, we remind in Chapter 2 some basics of modern cosmology and present the current state of observational cosmology. In Chapter 3, we give some insights on active galactic nuclei with a specific focus on quasars. We present the basics of gravitational lensing in Chapter 4.

The second part of this thesis presents the COSMOGRAIL project. This project aims at measuring the Hubble constant  $H_0$  with unprecedented accuracy using the time-delay method mentioned earlier. In practice, this requires regular and long-term (over several years) monitoring of several lensed quasars. COSMOGRAIL has the unique opportunity to use partly dedicated 1m-class telescopes and hence large amounts of observing time are available. In order to use the available time in the most efficient manner, we present in Chapter 5 numerical simulations that define the optimal observing strategy to adopt for the determination of the time delays of a given lensed quasar.

Once the time delays are measured, one can infer estimates of  $H_0$  from the time-delay method if several additional elements are provided. These elements are : (i) the astrometry of the lens and of the lensed images, (ii) the distances to the source and to the lens, and (iii) the model of the mass distribution of the lens. Measures of the astrometry are straightforward, and recent observations with the Hubble Space Telescope (HST) reach precisions of about 5 milli-arcseconds. The correct evaluation of the distances of the background source and especially of the lens are much more difficult. Whereas the distance of the source is well determined for the majority of all known gravitationally lensed quasars, the distance of the much fainter lensing galaxies are often poorly constrained and sometimes even completely unknown. In Chapter 6, we describe how to determine the distance of lensing galaxies by using deep spectroscopic data in combination with a powerful deconvolution algorithm.

In the third and last part, we focus on one particular lensed quasar, namely the Einstein Cross QSO 2237+0305. This object is famous because of the unusual proximity of its lensing galaxy, which provides a privileged laboratory for lensing experiments. In Chapter 7, we present our spectrophotometric monitoring of the Einstein Cross conducted at the Very Large Telescope. Microlensing by stars located in the lensing galaxy induces chromatic flux variations in the spectra of the quasar images. We use these variations to infer the spatial structure (or energy profile) of the accretion disk surrounding the central supermassive blackhole of the lensed quasar. In Chapter 8, we take advantage of the proximity of the lens in QSO 2237+0305 to conduct a detailed study of its stellar kinematics using long-slit and integral-field spectroscopy. The kinematics can be used to trace the mass distribution in the lensing galaxy, which we compare to the mass distribution inferred from gravitational lensing. The combination of these two independent methods offer a promising way of determining the mass distribution in the extended dark matter halo. Finally, we present the conclusion of this thesis and give perspectives for the future.



# Part I

## Theoretical background





*“The most incomprehensible thing about the world is that it is at all comprehensible.”*  
*Albert Einstein (1879 - 1955)*

## Chapter 2

# Basics of modern cosmology

Cosmology is the study of the Universe in its totality, and has fascinated mankind for thousands of years from various points of view including science, philosophy, and religion. In recent times, science has come to play a more central role in our understanding of the Universe through theoretical and technological developments. Since the last decade, we are witnessing an epoch of tremendous discoveries in cosmology.

The general picture that science has led to is known as the concordance model and a cartoon of the evolution of the Universe is depicted in Fig. 2.1. Following this model, the history of the Universe began some 13.7 billions of years ago with the Big Bang, an extremely hot and dense state. From this moment on, the Universe started to expand and cool down. At the very beginning, the Universe is thought to have undergone a phase of exponential expansion called inflation. The physical details of the inflationary scenario are still not well understood, and it is not yet clear what put an end to the inflation, after which the normal Friedmann evolution of the Universe began.

A few minutes after the Big Bang, protons and neutrons began to combine in the process of nuclear fusion and formed the first atomic nuclei, predominantly helium, as well as very small quantities of other simple nuclei. This primordial nucleosynthesis only lasted for about twenty minutes, after which the temperature and density of the Universe fell to the point where nuclear fusion can not continue. As the Universe was continuing to cool down, electrons began to be captured by the ions, forming first atoms. This process is known as recombination and occurred approximately 400,000 years after the Big Bang. As most of these atoms were neutral, the Universe became transparent to photons for the first time. Photons emitted at that time, are those that we see today in the Cosmic Microwave Background (CMB) radiation. This thermal radiation is a visible relic of the Big Bang and follows a blackbody spectrum with a temperature of 2.725 K.

About 400 millions years later, the matter in the Universe slowly assembled driven by gravitation. First stars and active galactic nuclei (AGNs) were created and started to radiate so intensely that they reionized the whole Universe. Galaxies assembled in groups and clusters, creating always larger structures.

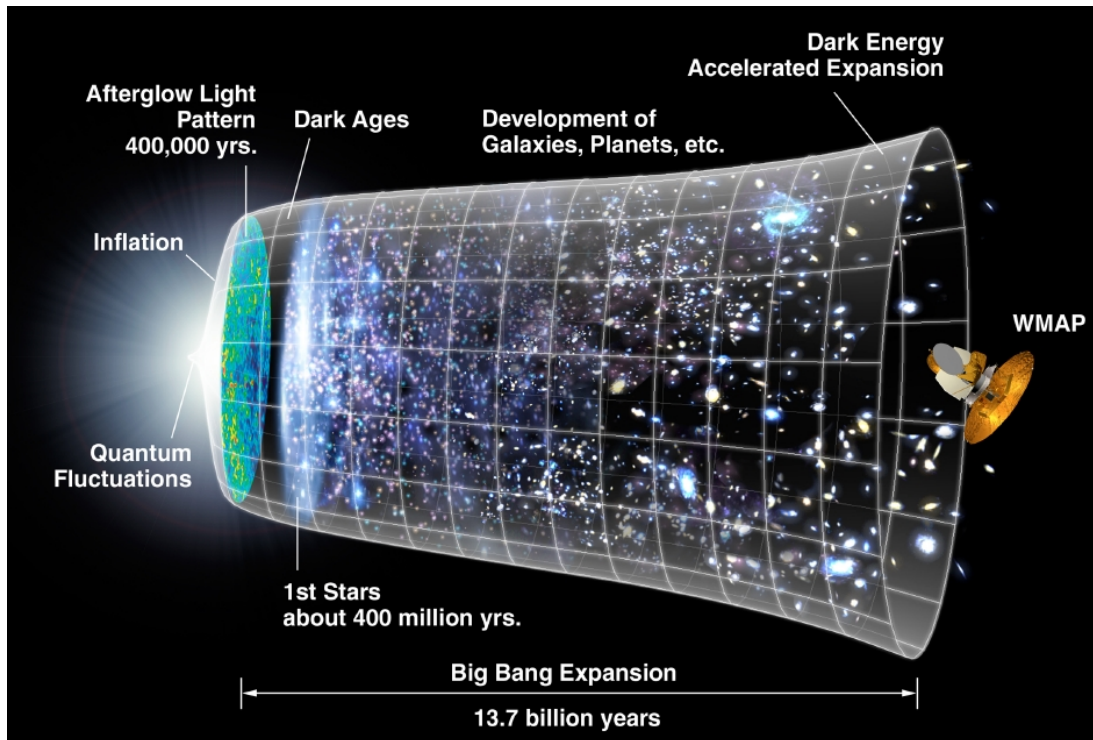


Figure 2.1: The history of the Universe illustrated by the NASA/WMAP Science Team.

Given this general picture, we will briefly review some theoretical concepts on which the current cosmological model is based, and which are necessary for the description of the phenomenon of gravitational lensing in Chapter 4.

## 2.1 The cosmological principle

The cosmological principle is not formally a principle, but rather an assumption or mathematically speaking an axiom, that is based on observed properties of the Universe, and states that

*“On large spatial scales, the Universe is homogeneous and isotropic.”*

Isotropy implies that the Universe has the same characteristics in all directions, and homogeneity means that the Universe is identical everywhere in space. Maybe the most important implication of this principle is that there is no preferred place in the Universe.

## 2.2 The Friedmann-Lemaître-Robertson-Walker metric

When applied, the cosmological principle severely restricts the large variety of possible cosmological theories. An exact solution of the Einstein field equations of General Relativity describing a homogeneous and isotropic Universe was first found by Alexander Friedmann (1922). Later, Georges Lemaître (1927) arrived independently at similar results as Friedmann. Howard Percy Robertson and Arthur Geoffrey Walker explored the

problem further during the 1930s, and proved the uniqueness of the Friedmann-Lemaître-Robertson-Walker (FLRW) metric (i.e. the FLRW metric is the only one on a Lorentzian manifold that is both homogeneous and isotropic). Walker (1935) considered the metric

$$c^2 d\tau^2 = c^2 dt^2 - R^2(t) \left( \frac{dr^2}{1 - kr^2} + r^2 (d\theta^2 + \sin^2 \theta d\phi^2) \right) = g_{\mu\nu} dx^\mu dx^\nu$$

where  $k$  describes the curvature and is time-independent, and  $R(t)$  is the scale factor and is explicitly time dependent. This metric leaves some choice of normalization, commonly  $k$  is specified to be equal to  $\pm 1$  or  $0$  by using an appropriate normalization of the coordinates. Robertson (1935) considered the following solution of the Einstein field equations

$$c^2 d\tau^2 = c^2 dt^2 - R^2(t) (d\chi^2 + S_k^2(\chi) (d\theta^2 + \sin^2 \theta d\phi^2)) = g_{\mu\nu} dx^\mu dx^\nu .$$

One can verify that these two metrics are equivalent by defining

$$r(\chi) = S_k(\chi) = \begin{cases} \sin(\chi) & \text{if } k = 1 \\ \chi & \text{if } k = 0 \\ \sinh(\chi) & \text{if } k = -1 . \end{cases}$$

Frequently the scale factor  $R(t)$  is normalized to its actual value  $R_0$ , and is then written

$$a(t) \doteq \frac{R(t)}{R_0} .$$

The FLRW metric nicely incorporates the idea of a uniformly expanding cosmological model with no center.

## 2.3 The Hubble constant

The Hubble parameter  $H(t)$ , also called the expansion rate of the Universe, is defined by

$$H(t) \doteq \frac{\dot{R}(t)}{R(t)} = \frac{\dot{a}(t)}{a(t)} = \frac{d}{dt} \ln(a(t))$$

where  $\dot{R} = dR/dt$  and  $\dot{a} = da/dt$ . The value of  $H(t)$  measured today is written  $H_0$  and is called the Hubble constant. The relation between the distances and the observed radial velocities of nearby galaxies can be obtained from the proper distance  $D_P = R(t) \chi$  of the source. Even if the source remains at the same comoving coordinates (i.e.  $\chi$ ,  $\theta$  and  $\phi$  are constant), the proper distance of the source changes with time because of the time-dependence of the scale factor  $R(t)$ . Due to this, the source has an apparent radial velocity  $v_r$  with respect to the observer given by

$$v_r = \frac{dD_P}{dt} = \dot{R} \chi = \frac{\dot{R}}{R} D_P = H(t) D_P .$$

This relation was first predicted theoretically by Lemaître (1927), and was observed for the first time in 1929 by Edwin Hubble, and is now known as Hubble's law. Hubble (1929) measured the distances of nearby galaxies by observing Cepheid variable stars. He proved that the galaxies are receding in every direction at speeds directly proportional to their distance. This provided the first observational evidence for the expansion of the Universe.

## 2.4 The cosmological redshift

Photons emitted by a distant source located at the comoving radial coordinate  $r = r_e$  will travel through the Universe until they reach us at  $r = 0$ . If they follow a radial geodesic (i.e.  $d\theta = d\phi = 0$ ), we know from the FLRW metric that

$$0 = g_{\mu\nu} dx^\mu dx^\nu = c^2 dt^2 - R^2(t) \frac{dr^2}{1 - kr^2} \Rightarrow c \frac{dt}{R(t)} = - \frac{dr}{\sqrt{1 - kr^2}} .$$

If a photon is emitted at a comoving time coordinate  $t_e$ , it will reach us at a time  $t_o$ . In the same manner, a photon emitted at  $t_e + \delta t_e$  will reach us at  $t_o + \delta t_o$ , and thus

$$c \int_{t_e}^{t_o} \frac{dt}{R(t)} = - \int_{r_e}^0 \frac{dr}{\sqrt{1 - kr^2}} = c \int_{t_e + \delta t_e}^{t_o + \delta t_o} \frac{dt}{R(t)} .$$

We can rewrite this

$$\int_{t_e}^{t_o} \frac{dt}{R(t)} = \int_{t_e}^{t_e + \delta t_e} \frac{dt}{R(t)} + \int_{t_e + \delta t_e}^{t_o} \frac{dt}{R(t)} = \int_{t_e + \delta t_e}^{t_o} \frac{dt}{R(t)} + \int_{t_o}^{t_o + \delta t_o} \frac{dt}{R(t)} = \int_{t_e + \delta t_e}^{t_o + \delta t_o} \frac{dt}{R(t)} .$$

And hence, for sufficiently small  $\delta t_e$  and  $\delta t_o$ , we can consider  $R(t)$  to remain approximately constant over the time intervals  $[t_e; t_e + \delta t_e]$  and  $[t_o; t_o + \delta t_o]$ , leading to

$$\int_{t_e}^{t_e + \delta t_e} \frac{dt}{R(t)} = \int_{t_o}^{t_o + \delta t_o} \frac{dt}{R(t)} \Rightarrow \frac{\delta t_e}{R(t_e)} = \frac{\delta t_o}{R(t_o)} \Rightarrow \frac{\delta t_o}{\delta t_e} = \frac{\nu_e}{\nu_o} = \frac{\lambda_o}{\lambda_e} = \frac{R(t_o)}{R(t_e)}$$

where  $\lambda$  and  $\nu = c/\lambda$  are the wavelength and frequency of the photon, respectively. As a consequence, the observed wavelength  $\lambda_o$  is shifted relative to the emitted wavelength  $\lambda_e$ . This shift  $z$  is defined by

$$z \doteq \frac{\lambda_o - \lambda_e}{\lambda_e} = \frac{R(t_o)}{R(t_e)} - 1 = \frac{a(t_o)}{a(t_e)} - 1 .$$

Since Hubble (1929) discovered his famous law, our Universe is known to be expanding. This implies for the scale factor that  $R(t_o) > R(t_e) \Rightarrow \lambda_o > \lambda_e$ . Hence, due to the expansion of the Universe, the observed wavelengths of distant objects are *redshifted* relative to the emitted wavelengths.

This redshift is not a Doppler redshift, in the sense that the galaxies and the observer are not moving away from each other, but instead it is the space between them that expands. Hence, the cosmological redshift is by itself a property of the expanding spacetime.

## 2.5 The Friedmann equations

Considering the FLRW metric describing an isotropic and homogeneous Universe, one can compute the Ricci tensor defined by

$$R_{\alpha\beta} = R^\gamma_{\alpha\gamma\beta} = \partial_\gamma \Gamma^\gamma_{\alpha\beta} - \partial_\beta \Gamma^\gamma_{\alpha\gamma} + \Gamma^\sigma_{\alpha\beta} \Gamma^\gamma_{\sigma\gamma} - \Gamma^\sigma_{\alpha\gamma} \Gamma^\gamma_{\sigma\beta}$$

where the  $\Gamma$ s are the Christoffel symbols

$$\Gamma^\gamma_{\alpha\beta} = \frac{1}{2} g^{\gamma\delta} [\partial_\beta g_{\delta\alpha} + \partial_\alpha g_{\delta\beta} - \partial_\delta g_{\alpha\beta}] .$$

After some algebra, we get

$$R_{00} = -\frac{3}{c^2} \frac{\ddot{a}}{a} \quad R_{0i} = 0 \quad R_{ij} = -\frac{1}{a^2 c^2} \left( a\ddot{a} + 2\dot{a}^2 + \frac{2k c^2}{R_0^2} \right) g_{ij} .$$

The cosmological principle states that the Universe looks the same in all directions and from any observing point. We can take this a stage further and assert that all the laws of physics take the same form independently of the reference frame. Mathematically speaking, this states that any law of physics has to be covariantly conserved, i.e. a coordinate transformation does not affect physical observables. Following this idea, Albert Einstein found the Einstein tensor  $G_{\mu\nu}$ , which is covariantly conserved, and established his famous field equations

$$G_{\mu\nu} = R_{\mu\nu} - \frac{1}{2} g_{\mu\nu} R - \Lambda g_{\mu\nu} = \frac{8\pi G}{c^4} T_{\mu\nu}$$

where  $T_{\mu\nu}$  is the energy-momentum tensor and  $\Lambda$  is the cosmological constant. These field equations link the spacetime geometry  $G_{\mu\nu}$  with its energy content  $T_{\mu\nu}$ . The most general form of  $T_{\mu\nu}$  compatible with the cosmological principle is

$$T_{\mu\nu} = \frac{1}{c^2} (\rho c^2 + p) \omega_\mu \omega_\nu - P g_{\mu\nu} \quad \text{with} \quad \omega_\mu = g_{\mu\nu} \frac{dx^\nu}{d\tau} \quad \text{and} \quad \omega^\mu \omega_\mu = c^2 .$$

This is the energy-momentum tensor of a perfect fluid, i.e. a fluid that is completely characterized by its rest frame energy density  $\rho c^2$  and isotropic pressure  $P$ . In the fluid rest-frame, we have  $\omega^\mu = (c, 0, 0, 0)$  implying  $T_{00} = \rho c^2$  and  $T_{ii} = -P g^{ii}$ . Introducing this into Einstein's field equations leads to the Friedmann equations (Friedmann, 1922)

$$\begin{cases} \left( \frac{\dot{a}}{a} \right)^2 &= \frac{8\pi G}{3} \rho - \frac{k c^2}{R_0^2 a^2} + \frac{1}{3} \Lambda c^2 \\ \frac{\ddot{a}}{a} &= -\frac{4\pi G}{3} \left( \rho + \frac{3P}{c^2} \right) + \frac{1}{3} \Lambda c^2 . \end{cases}$$

These equations can be integrated with respect to time, and give

$$\frac{d}{dt} (\rho c^2 a^3) + P \frac{d}{dt} (a^3) = 0 .$$

This equation is equivalent to the first law of thermodynamics applied to an adiabatic expansion, i.e.  $dU = -P dV$ , where  $V$  is the volume and  $U$  is the internal energy of the system. This expresses the conservation of energy in the Universe.

## 2.6 The energy components of the Universe

A powerful approximate model for the energy content of the Universe is obtained by dividing the content of the Universe in three different perfect fluids: one non-relativistic component  $\rho_m c^2$ , one relativistic component  $\rho_r c^2$ , and one (still mysterious) component related to the energy of the vacuum  $\rho_\Lambda c^2$  and sometimes referred to as dark energy. With these definitions, we can rewrite the Friedmann equations

$$\begin{cases} \left( \frac{\dot{a}}{a} \right)^2 &= \frac{8\pi G}{3} \rho - \frac{k c^2}{R_0^2 a^2} \\ \frac{\ddot{a}}{a} &= -\frac{4\pi G}{3} \left( \rho + \frac{3P}{c^2} \right) \end{cases}$$

where  $\rho = \rho_m + \rho_r + \rho_\Lambda$  and  $P = P_m + P_r + P_\Lambda$ .

### Pressure-Free Matter

The matter contained in stars, galaxies, as well as gas in the intergalactic medium, is composed of non-relativistic particles and the pressure induced by the slow motion (with respect to the speed of light) of these particles is gravitationally completely insignificant. Hence, the corresponding equation of state is well approximated by  $P_m = 0$  and from the integrated Friedmann equations, we get

$$\frac{d}{dt} (\rho_m c^2 a^3) = 0 \quad \Leftrightarrow \quad \rho_m a^3 = \text{constant}.$$

### Radiation

For particles moving with large velocities (e.g., photons), the pressure is no longer negligible and the energy density is related to the pressure by the equation of state  $P_r = \frac{1}{3}\rho_r c^2$ . The integrated Friedmann equations then give

$$\frac{d}{dt} (\rho_r a^3) + \frac{\rho_r}{3} \frac{d}{dt} (a^3) = 0 \quad \Leftrightarrow \quad \frac{d}{dt} \left[ \ln(\rho_r) + \frac{4}{3} \ln(a^3) \right] = 0 \quad \Leftrightarrow \quad \rho_r a^4 = \text{constant}.$$

### Vacuum Energy

If we assume that the geometrical term  $\Lambda g_{\mu\nu}$  that appears in the Einstein field equations is caused by an energy-momentum tensor  $T_{\Lambda\mu\nu}$  related to the vacuum, we get

$$T_{\Lambda\mu\nu} \doteq \frac{\Lambda c^4}{8\pi G} g_{\mu\nu}.$$

The Universe being homogeneous and isotropic, we can consider the vacuum as a perfect fluid, and hence

$$\rho_\Lambda c^2 = T_{\Lambda 00} = \frac{\Lambda c^4}{8\pi G} \quad \Rightarrow \quad \rho_\Lambda = \text{constant}.$$

The integrated Friedmann equations then imply

$$(\rho_\Lambda c^2 + P_\Lambda) \frac{d}{dt} (a^3) = 0 \quad \Rightarrow \quad P_\Lambda = -\rho_\Lambda c^2.$$

This means that the vacuum has a negative pressure and implies that the vacuum energy acts like a repulsive force and therefore has a tendency to accelerate the expansion of the Universe.

Over the past two decades, there has been growing evidence that the expansion rate of the Universe is indeed accelerating. The most direct evidence is provided by supernova observations (e.g., Perlmutter et al., 1999) and implies that a form of repulsive dark energy must exist. The nature of this dark energy is still unknown. Dark energy is commonly described by the equation of state  $P_{DE} = w \rho_{DE} c^2$ . In the concordance model, dark energy is identified with the vacuum energy and hence  $w = -1$ .

## 2.7 The critical density

The first Friedmann equation reveals that there is a direct connection between the density of the Universe and its global geometry

$$H^2(t) = \frac{8\pi G}{3} \rho - \frac{k c^2}{R_0^2 a^2(t)}.$$

For a given rate of expansion  $H(t)$ , there is a critical density  $\rho_c(t)$  that will yield  $k = 0$ , making the comoving part of the metric look Euclidean.

$$\rho_c(t) \doteq \frac{3 H^2(t)}{8\pi G} .$$

We can consider three different geometries for the Universe:

- if  $k = 0 \Leftrightarrow \rho(t) = \rho_c(t)$ , the three-dimensional space for any fixed time  $t$  is Euclidean, i.e. flat.
- if  $k = 1 \Leftrightarrow \rho(t) > \rho_c(t)$ , the space is closed, i.e. it has a finite volume, but has no boundaries (e.g., the surface of a sphere is a closed two-dimensional space), and has a spherical symmetry.
- if  $k = -1 \Leftrightarrow \rho(t) < \rho_c(t)$ , the space is called hyperbolic and is open, i.e. it is unbound and infinite.

## 2.8 The density parameters

In order to simplify the Friedmann equations, the energy density is commonly normalized with the critical density  $\rho_c$ . This defines the density parameters

$$\Omega_i(t) \doteq \frac{\rho_i(t) c^2}{\rho_c(t) c^2} = \frac{8\pi G}{3 H^2(t)} \rho_i(t) \quad \text{where} \quad i = m, r, \text{ or } \Lambda .$$

For instance, the density parameter of the vacuum is

$$\Omega_\Lambda(t) \doteq \frac{\rho_\Lambda c^2}{\rho_c(t) c^2} = \frac{\Lambda c^4}{8\pi G} \frac{8\pi G}{3 c^2 H^2(t)} = \frac{\Lambda c^2}{3 H^2(t)} .$$

In a similar way, we can define an energy density  $\rho_k$  for the curvature and its corresponding density parameter  $\Omega_k$

$$\frac{8\pi G}{3} \rho_k = -\frac{k c^2}{R_0^2} \quad \Leftrightarrow \quad \Omega_k(t) \doteq \frac{\rho_k c^2}{\rho_c(t) c^2} = -\frac{k c^2}{H^2(t) R_0^2} .$$

We can rewrite the first Friedmann equation using these definitions

$$1 = \Omega_m + \Omega_r + \Omega_\Lambda + \Omega_k \quad \Leftrightarrow \quad \Omega_k = 1 - \Omega_m - \Omega_r - \Omega_\Lambda .$$

We can also write

$$\left(\frac{\dot{a}}{a}\right)^2 = H_0^2 \frac{a_0^2}{a^2} \left(1 - \frac{8\pi G}{3 H_0^2} \left(\rho_m(t_0) + \rho_r(t_0) + \rho_\Lambda(t_0) - (\rho_m + \rho_r + \rho_\Lambda) \frac{a^2}{a_0^2}\right)\right) .$$

We have already mentioned that

$$\rho_m a^3 = \rho_m(t_0) a_0^3 \quad ; \quad \rho_r a^4 = \rho_r(t_0) a_0^4 \quad ; \quad \rho_\Lambda = \rho_\Lambda(t_0) .$$

Hence, written in terms of the density parameters  $\Omega_{i0} = \Omega_i(t_0)$  at the time  $t = t_0$ , this gives

$$\left(\frac{\dot{a}}{a}\right)^2 = H_0^2 \left( (1 - \Omega_{m0} - \Omega_{r0} - \Omega_{\Lambda0}) \left[\frac{a}{a_0}\right]^{-2} + \Omega_{m0} \left[\frac{a}{a_0}\right]^{-3} + \Omega_{r0} \left[\frac{a}{a_0}\right]^{-4} + \Omega_{\Lambda0} \right) .$$

## 2.9 Cosmological distances

The comoving coordinate system  $(ct, \chi, \theta, \phi)$ , or equivalently  $(ct, r, \theta, \phi)$ , relates to proper distances (i.e. distances measured in a hypersurface of constant proper time  $t$ ) in a space-time described by the FLRW metric. The proper distance  $D_P$  of a point  $P_1$  from another point  $P_2$  is the distance measured by a chain of rulers held by observers which connect  $P_1$  to  $P_2$  at a given time  $t$

$$D_P(t) \doteq R(t) \chi_{12} \quad \text{with} \quad \chi_{12} = (\chi_2 - \chi_1) = \int_{r_1}^{r_2} \frac{dr}{\sqrt{1 - kr^2}} .$$

To express  $\chi_{12}$  in terms of measurable quantities, we consider a photon ( $c^2 d\tau^2 = 0$ ) traveling along a radial geodesic ( $d\theta = d\phi = 0$ ). This yields

$$\begin{aligned} \chi_{12} &= - \int_{t_2}^{t_1} \frac{c dt}{R(t)} = \frac{1}{R_0} \int_{a_1}^{a_2} \frac{c}{a^2 (\dot{a}/a)} da \\ &= \frac{c}{H_0 R_0 a_0} \int_{a_1}^{a_2} \frac{1}{\sqrt{(1 - \Omega_{m0} - \Omega_{r0} - \Omega_{\Lambda 0}) \left[\frac{a}{a_0}\right]^{-2} + \Omega_{m0} \left[\frac{a}{a_0}\right]^{-3} + \Omega_{r0} \left[\frac{a}{a_0}\right]^{-4} + \Omega_{\Lambda 0}}} \frac{a_0}{a^2} da . \end{aligned}$$

From the definition of the redshift we have  $a = a_0/(1 + z)$  and thus

$$\chi_{12} = \frac{c}{H_0 R_0} \int_{z_1}^{z_2} \frac{dz}{\sqrt{(1 - \Omega_{m0} - \Omega_{r0} - \Omega_{\Lambda 0}) (1 + z)^2 + \Omega_{m0} (1 + z)^3 + \Omega_{r0} (1 + z)^4 + \Omega_{\Lambda 0}}} .$$

We can not measure proper distances to astronomical objects in any direct way. Distant objects are observed only through the light they emit. Light takes a finite time to travel to us, and, in this elapsed time, the scale factor  $R(t)$  may have changed. Therefore, we can not physically make any distance measurements along a hypersurface of constant proper time, but only along the set of light paths traveling to us from the past. However, one can define operationally other kinds of distance which are, at least in principle, directly measurable.

One such distance is the angular-diameter distance which is constructed to preserve a geometrical property of the Euclidean space, namely the variation of the angular size of an object with its distance to an observer. Let  $d_P(t_2)$  be the proper diameter of the source placed at  $P_2$  at time  $t_2$ . If the angle subtended by  $d_P(t_2)$  is denoted  $\Delta\theta$ , the Robertson-Walker metric implies then

$$d_P(t_2) = R(t_2) S_k(\chi_{12}) \Delta\theta .$$

We define the angular-diameter distance  $D_A(P_1, P_2)$  from the source to the observer to be

$$D_A(P_1, P_2) \doteq \frac{d(t_2)}{\Delta\theta} = R(t_2) S_k(\chi_{12}) = \frac{R_0}{1 + z_2} S_k(\chi_{12}) .$$

We have already mentioned that  $\sqrt{-\Omega_{k0}/k} = c/(H_0 R_0)$ , if  $k \neq 0$ . Moreover the first Friedmann equation gives  $\Omega_k = 1 - \Omega_m - \Omega_r - \Omega_\Lambda$ , thus

$$R_0 = \frac{c}{H_0} \frac{1}{\sqrt{|\Omega_{k0}|}} = \frac{c}{H_0} |1 - \Omega_{m0} - \Omega_{r0} - \Omega_{\Lambda 0}|^{-1/2} \quad \text{if } k \neq 0 .$$



From this, we get the angular-diameter distance of the source at redshift  $z_2$ , as measured by an observer located at a redshift  $z_1 < z_2$

$$D_A(z_1, z_2) = \begin{cases} \frac{1}{(1+z_2)} \frac{c}{H_0} \frac{1}{\sqrt{|\Omega_{k0}|}} \sin\left(\sqrt{|\Omega_{k0}|} \frac{H_0}{c} D_C\right) & \text{if } \Omega_{k0} < 0 \Leftrightarrow k > 0 \\ \frac{1}{(1+z_2)} D_C & \text{if } \Omega_{k0} = 0 \Leftrightarrow k = 0 \\ \frac{1}{(1+z_2)} \frac{c}{H_0} \frac{1}{\sqrt{\Omega_{k0}}} \sinh\left(\sqrt{\Omega_{k0}} \frac{H_0}{c} D_C\right) & \text{if } \Omega_{k0} > 0 \Leftrightarrow k < 0 \end{cases}$$

where  $D_C \doteq D_P(t_0) = R_0 \chi_{12}$  is the comoving distance, and

$$D_C = \frac{c}{H_0} \int_{z_1}^{z_2} \frac{dz}{\sqrt{(1 - \Omega_{m0} - \Omega_{r0} - \Omega_{\Lambda 0})(1+z)^2 + \Omega_{m0}(1+z)^3 + \Omega_{r0}(1+z)^4 + \Omega_{\Lambda 0}}}.$$

Note that in general,  $D_A(z_1, z_2) \neq D_A(0, z_2) - D_A(0, z_1)$ .

## 2.10 Observational cosmology

Extensive observational studies over the past decades have led to four main cosmological observations which all validate the Big-Bang theory: (i) the expansion of the Universe, (ii) the black-body spectrum of the cosmological microwave background (CMB), (iii) the density fluctuations seen in the CMB and in the distribution of galaxies, and (iv) the abundances of primordial elements. Together, they provide extremely strong constraints on cosmological models and show that the Universe began some 13.7 billion years in a very hot and dense state, that it expanded and cooled down since then, and that the expansion is currently accelerating.

### The expansion of the Universe and the Hubble constant

The expansion of the Universe was first observed by Hubble (1929), who established the recession of nearby galaxies described by his famous law  $v_r = H_0 D_P$ . The Hubble constant  $H_0$  is a particularly important parameter because any extragalactic distance determination is directly related to it. A lot of different methods have been developed to measure  $H_0$  and most of these methods are based on so-called distance indicators. Common distance indicators are stellar objects that can be used as standard candles, e.g., Cepheids or type Ia supernovae (SNIa). Cepheids are relatively young bright pulsating stars and are known for their period-luminosity relation. The measurement of the pulsation period determines the absolute magnitude of the star, which compared to its apparent magnitude, yields the distance. These stars are used as primary distance indicators, but their use is currently limited to approximately 30 Mpc. Determination of greater distances require brighter distance indicators such as SNIa.

When a white dwarf accretes matter from a companion star, it increases the temperature and density inside its core. When the white dwarf reaches the Chandrasekhar limit of  $1.38 M_\odot$ , the temperature and density of its core are high enough to ignite carbon fusion and the white dwarf is destroyed in a SNIa explosion. Because of this limit in mass, SNIa all have basically the same initial energy, resulting in explosions with similar lightcurves. The properties of these lightcurves can be used to determine the luminosity distance of the SNIa. Measuring the redshift of the host galaxy then determines the

luminosity distance-redshift relation, which provides important observational constraints on cosmological parameters. Recent systematic searches for distant SNIa have been able to determine this distance-redshift relation up to a redshift of  $z \simeq 2$  (e.g., Astier et al., 2006; Wood-Vasey et al., 2007; Riess et al., 2007). These studies have led to the important result that the expansion of the Universe is currently accelerating.

Other distance indicators are based on observed properties of galaxies. The Tully-Fisher (Tully & Fisher, 1977) relation is an empirical relationship between the intrinsic luminosity of spiral galaxies and their maximum rotational velocity. A similar relationship, known as the Faber-Jackson (Faber & Jackson, 1976) relation exists for elliptical galaxies between their intrinsic luminosity and their velocity dispersion. This relation has been improved by (Djorgovski & Davis, 1987), and is known as the fundamental plane. This plane defines the relation between the effective radius, average surface brightness and central velocity dispersion of elliptical galaxies. One further method, called the surface brightness fluctuation method (Tonry & Schneider, 1988), is based on the fact that galaxies are made of a finite number of stars and on the hypothesis that the number  $N$  of stars per unit area follows a Poissonian distribution with standard deviation  $\sqrt{N}$ . The relative fluctuations of the number of stars per unit area hence scales as  $1/\sqrt{N}$ . For a given solid angle  $d\omega$ , the corresponding area  $dS$  depends on the angular-diameter distance  $D_A$  of the galaxy with  $dS = D_A^2 d\omega$ . The larger the distance, the larger the number of stars contained in the solid angle  $d\omega$  and the smaller the relative fluctuations. Once calibrated with primary distance indicators, these surface brightness fluctuations give an estimate of the distance.

The problem with these methods, except for the Cepheids, is that there are secondary distance indicators, i.e. there are calibrated using primary distance indicators. Errors in the distances estimated from the primary distance indicators will therefore directly affect the secondary distance indicators, increasing the systematic errors. To minimize this effect, it is crucial to obtain accurate and reliable primary distance indicators. This was the aim of the Hubble Space Telescope (HST) Key Project (Freedman et al., 2001), which established an accurate local distance scale using Cepheids. The project then used this distance scale for secondary distance indicators, and obtained  $H_0 = 72 \pm 8 \text{ km s}^{-1} \text{ Mpc}^{-1}$ .

Alternative methods to determine  $H_0$  are independent of any distance indicators and can directly be applied to very large distances. One of these methods is based on the Sunyaev-Zeldovich effect (Sunyaev & Zeldovich, 1970). This effect is the result of high energy electrons in the hot gas of galaxy clusters distorting the CMB radiation through inverse Compton scattering, in which some of the energy of the electrons is transferred to the low energy CMB photons. The observed distortions  $\Delta I_{CMB}$  in the CMB intensity  $I_{CMB}$  depend on the gas temperature  $T$  and electron density  $n_e$

$$\frac{|\Delta I_{CMB}|}{I_{CMB}} \propto n_e R T$$

with  $R$  being the physical extent of the cluster along the line of sight. The surface brightness of the gas X-ray radiation behaves as  $I_X \propto R n_e^2$ . The temperature  $T$  of the gas is determined from the X-ray spectrum and thus, the length  $R$  can be determined

$$R \propto \frac{1}{I_X} \left( \frac{1}{T} \frac{|\Delta I_{CMB}|}{I_{CMB}} \right)^2.$$

Assuming the cluster has a spherical symmetry the observed angular extent is  $\Delta\theta = R/D_A$ , where  $D_A$  is the angular-diameter distance. This distance can be used together with the

redshift of the cluster to determine  $H_0$ . The systematic errors affecting  $H_0$  estimates using the Sunyaev-Zeldovich effect are still large, of the order  $20 \text{ km s}^{-1} \text{ Mpc}^{-1}$  (e.g., Udomprasert et al., 2004; Jones et al., 2005; Bonamente et al., 2006). However, there is hope in the future to decrease these errors as more clusters are being observed.

Finally, we mention one further method to measure  $H_0$  without using distance indicators. This method is based on the gravitational lensing of quasars and was proposed by Sjur Refsdal (1964a). The intrinsic flux variations of a lensed quasar are seen at different times in its lensed images, because the light seen in each image follows different deflected paths from the source to the observer. The observed time delays between the images are directly related to  $H_0$  and hence can be used to measure it. More details about the application of this method are given in Section 4.6.

## The Cosmic Microwave Background (CMB)

The CMB was discovered by Penzias & Wilson (1965) and gives a snapshot of the Universe at the epoch of the recombination, when the Universe was about 400,000 years old and became transparent to photons. Two great successes of modern cosmology are the prediction of the almost perfect black-body spectrum of the CMB (nearly isotropic at a temperature of 2.725 K) and the detailed prediction of the power spectrum of its anisotropies (reaching an amplitude  $\Delta T/T \simeq 10^{-5}$ ). These inhomogeneities were accurately measured by the Wilkinson Microwave Anisotropy Probe (WMAP) (Hinshaw et al., 2008, see Fig. 2.2).

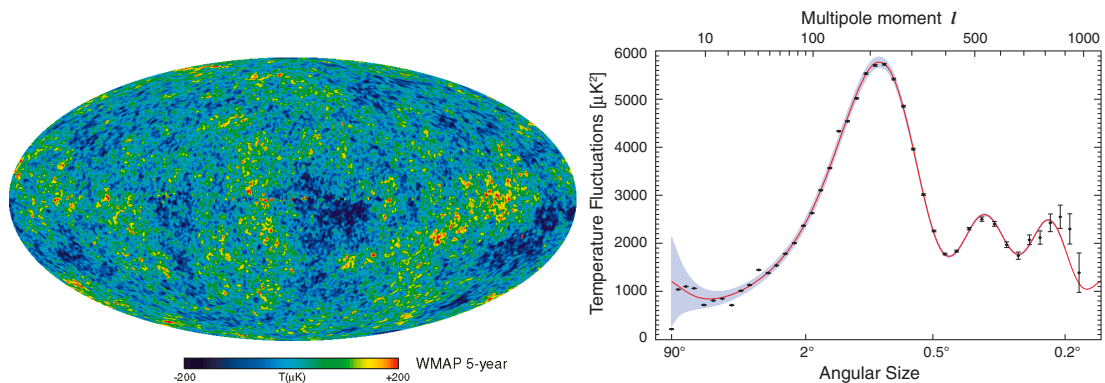


Figure 2.2: *Left:* The CMB temperature fluctuations from the 5-year WMAP data seen over the full sky (Hinshaw et al., 2008). *Right:* Power spectrum of the temperature anisotropies measured by Hinshaw et al. (2008). This plot shows the temperature fluctuations as a function of angular sizes.

The structure of the CMB anisotropies is principally determined by the Baryon<sup>1</sup> Acoustic Oscillations (BAO) that arise from a competition in the photon-baryon plasma in the early Universe. The pressure of the photons tends to erase anisotropies, whereas the gravitational attraction of the baryons makes them tend to collapse. These two effects compete and create acoustic oscillations which give the CMB its characteristic peak structure. The angular scales of these peaks depend on several cosmological parameters, and are particularly efficient in constraining them. For instance, the angular scale of the first peak determines the curvature  $\Omega_{k0}$  of the Universe. The second peak (truly the ratio of the

<sup>1</sup>Baryons are particles made of three quarks. The most common baryons are the proton and the neutron.

odd peaks to the even peaks) determines the baryon density  $\Omega_{b0}$ . The third peak gives information about both the baryons and dark matter densities and leads to the conclusion that an important part of the matter in the Universe is dark and mostly non-baryonic.

### Primordial nucleosynthesis

Only a few minutes after the Big Bang, protons and neutrons began to combine and produce the first light atomic nuclei: deuterium, helium, lithium, and some traces of other nuclei. The abundances of these primordial elements are determined

by observing astronomical objects in which very little stellar nucleosynthesis has taken place (such as certain dwarf galaxies) or by observing objects that are very far away, and thus can be seen in a very early stage of their evolution (such as distant quasars). The derived abundances and their comparison with detailed models of nucleosynthesis in the early Universe (e.g., Tytler et al., 2000) imply that the baryonic energy density is  $\Omega_{b0} \approx 0.04$ . But since  $\Omega_{m0}$  is much larger, this result implies that most of the matter in the Universe is dark, and that only a small fraction of it is baryonic.

### Large-scale structures

The CMB anisotropies indicate very small inhomogeneities at the time of recombination. Whereas, the inhomogeneities observed today in the form of large-scale structures, like galaxy clusters or filaments, are massive perturbations with a mean density more than hundred times larger than the mean density of the Universe. It is believed that the density fluctuations that we see today have evolved from much smaller fluctuations in the early Universe. The evolution of these inhomogeneities is driven by gravitation and depends on the expansion rate of the Universe, which further increases the density contrast. As a consequence, the scale length of the fluctuations decreases with time (i.e. at smaller redshift), while their amplitude increases. The relation between the amplitude and the scale length defines the power spectrum and can be used to derive constraints on cosmological parameters. Large-scale fluctuations are observed in the CMB anisotropies, while smaller scales are probed by the distribution of galaxies, which can be determined from large surveys such as the 2 degree Field Galaxy Redshift Survey (Colless et al., 2001, see Fig. 2.3) or the Sloan Digital Sky Survey (Stoughton et al., 2002). These surveys detect the density fluctuations in the clustering of galaxies and use them to constrain cosmological parameters (e.g., Eisenstein et al., 2005; Percival et al., 2007).

Other means to derive the spatial distribution of matter are based on measurements of weak gravitational lensing. The massive structures situated along the line of sight deflect the light emitted by background galaxies and induce distortions in the galaxy images. The observed distortions can therefore be used to determine the intervening mass distributions. Lensing surveys are complementary to both galaxy surveys and CMB observations as they probe the density power spectrum at modest redshifts, i.e. at smaller scales. Over the past few years, there has been dramatic progress in using weak lensing data as a probe of mass fluctuations in the nearby Universe (for a recent review, see Munshi et al., 2008).

The comparison of the observed galaxy distribution with numerical simulations (e.g., the Millenium simulation by Springel et al., 2005) implies that most of the matter must be composed of non-relativistic Cold Dark Matter (CDM) and indicates that structures grow hierarchically (bottom-up) with small objects collapsing first and merging in a continuous hierarchy of more and more massive objects up to the scale of superclusters and filaments.

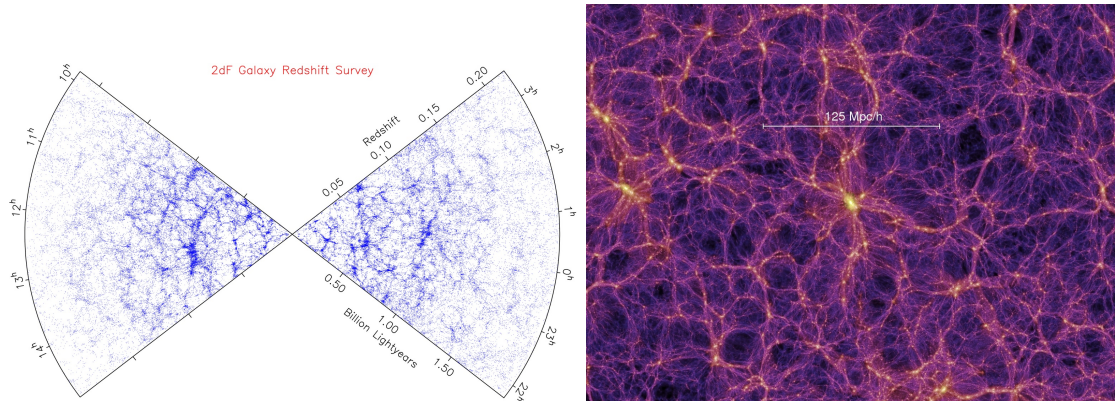


Figure 2.3: *Left*: The spatial distribution of galaxies observed by the 2 degree Field Galaxy Redshift Survey (Colless et al., 2001). *Right*: Large-scale structures obtained from the Millenium simulation (Springel et al., 2005).

## 2.11 The concordance model

All the observations mentioned in the previous section give a variety of different constraints on the cosmological parameters. Komatsu et al. (2008) have combined the WMAP data with measurements of the Hubble constant, supernova data, and large-scale structure observations. They obtained estimates of the cosmological parameters with an unprecedented accuracy (see Table 6 of Hinshaw et al., 2008). The combination of all these observations is so constraining (see Fig. 2.4) that there is little room for significant modifications of the concordance model, or  $\Lambda$ CDM model.

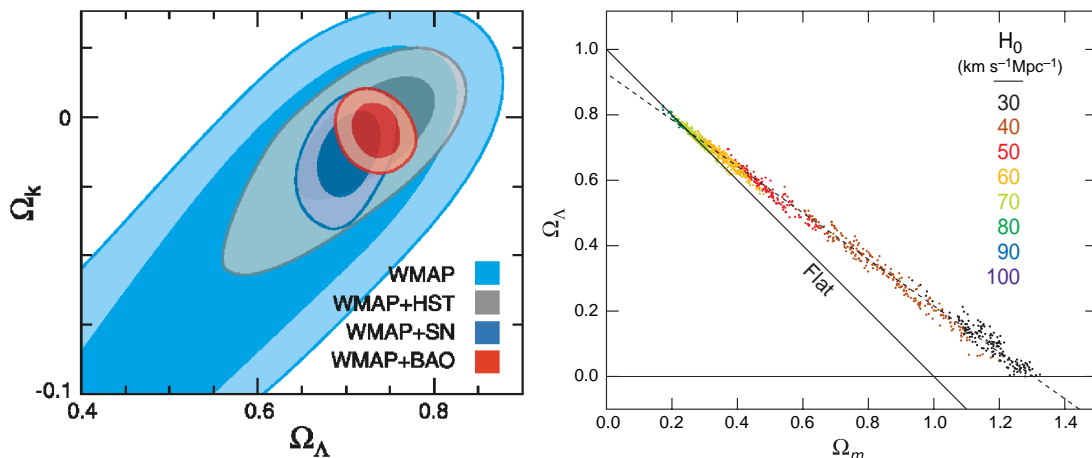


Figure 2.4: *Left*: Constraints on the present-day spatial curvature parameter  $\Omega_{k0}$  and dark energy density  $\Omega_{\Lambda0}$  obtained from a combination of the WMAP data with measurements of the Hubble constant (HST), supernova data (SN), and large-scale structure observations (BAO) as computed by Komatsu et al. (2008). *Right*: Range of cosmological models consistent with the WMAP data only (Spergel et al., 2007). The WMAP on its own provides only highly degenerate constraints on  $H_0$ .

In this cosmological model the Universe is flat (i.e.  $\Omega_{k0} = 0$ ), the dark energy has an equation of state of a cosmological constant (i.e.  $w = -1$ ), a dark matter density  $\Omega_{c0} = 0.233 \pm 0.013$ , a baryon density  $\Omega_{b0} = 0.0462 \pm 0.0015$ , and a dark energy density  $\Omega_{\Lambda 0} = 0.721 \pm 0.015$ . The total mass density is  $\Omega_{m0} = 0.279 \pm 0.015$  and the Hubble constant is  $H_0 = 70.1 \pm 1.3 \text{ km s}^{-1} \text{ Mpc}^{-1}$ .

However, it should be noted that this value of  $H_0$  is obtained only in the case of the  $\Lambda$ CDM model, where  $\Omega_{k0} = 0$  and  $w = -1$  are imposed. Without these assumptions, the analysis of the WMAP data on its own provides only highly degenerate constraints on  $H_0$  (Spergel et al., 2007, see Fig 2.4) and the uncertainties on  $H_0$  are still of the order of 10%. The currently favored value is  $H_0 = 72 \pm 8 \text{ km s}^{-1} \text{ Mpc}^{-1}$  from the HST Key Project (Freedman et al., 2001). We will see in Chapter 4 how gravitational lensing can possibly decrease this uncertainty by a factor of ten.

## 2.12 New questions

The concordance model is a remarkable achievement. Especially if one considers the huge variety of methods and processes that have entered the determination of its parameters and how well they all fit together. This cosmological model gives us now a more precise picture of the past evolution of the Universe, but it has also raised a new set of questions: What is dark matter if less than 20% of the matter is baryonic? What is the nature of dark energy, which accounts for more than 70% of the total energy in the Universe?

### Dark matter

Dark matter is by definition not directly observable, but its presence can be detected through gravitational interactions. The existence of dark matter was already pointed out by Zwicky (1937b) who studied the dynamics of galaxies and galaxy clusters. He showed that the amount of visible matter is too small by several order of magnitudes to explain the observed dynamics in these objects. These findings are confirmed by cosmological observations such as primordial element abundances, which imply that a large fraction of the matter in the Universe must be dark and that less than 20% is baryonic.

Gravitational lensing offers another efficient tool to detect and study dark matter (see Chapter 4). A very impressive result was found by Clowe et al. (2006), who provided one of the best evidence for the existence of dark matter in the Bullet Cluster 1E0657–558 (see Fig. 2.5). This object is the result of the collision of two galaxy clusters, where the collisionless stellar component and the X-ray emitting hot gas are spatially segregated. What is striking in this object is that the mass distribution, determined through gravitational lensing, does not trace the gas distribution as expected (the intergalactic gas is considered to be the dominant baryonic mass component), but rather approximately traces the distribution of galaxies. This particularity can not be explained through a modification of the gravitational force law and thus, proves that the majority of the matter in the system has to be dark and weakly interacting.

Even though we can detect dark matter, its exact physical properties are still uncertain. We know from large-scale structure observations that it is cold (i.e. moving slowly in comparison with the speed of light) and weakly interacting. Likely dark matter candidates are exotic elementary particles. Many experiments, especially in particle physics, are currently searching for these dark matter particles, but no conclusive evidence has been found yet. The next generation of particle accelerators, such as the Large Hadron Collider

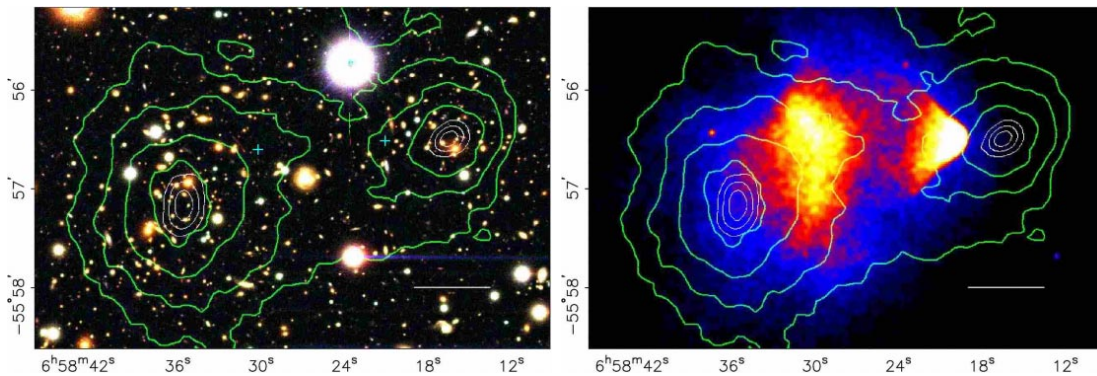


Figure 2.5: *Left:* Color image of the Bullet Cluster (Clowe et al., 2006). The white bar represents 200 kpc at the distance of the cluster. *Right:* X-ray image of the cluster tracing the hot plasma. The green contours are the gravitational lensing reconstruction of the surface mass density. Clearly, the mass distribution does not trace the gas distribution, but rather traces the distribution of galaxies, indicating that most of the matter in this system has to be dark and weakly interacting.

(LHC), may reach sufficiently high energy to discover new particles and new physics, as these new particles may lie outside the standard model of particle physics, e.g., the axion or supersymmetric particles like the neutralino.

## Dark energy

Even more surprising than the existence of dark matter is the discovery that more than 70% of the Universe consists of a mysterious dark energy. At the present time, there are no precise ideas of what this dark energy can be and simple estimates of the density of vacuum energy  $\rho_\Lambda$  from quantum field theory are 120 orders of magnitudes off. The concordance model assumes that the equation of state of the dark energy is  $P_{DE} = w \rho_{DE} c^2$  with  $w = -1$ , but other equations of state with different  $w$  values or even time-dependent values can not be ruled out completely.

Probing the nature of dark energy is one of the main priorities of observational cosmology. In the near future, new satellites such as the ESA Planck mission will measure the CMB anisotropies with even a better precision than WMAP. Several weak lensing surveys such as the Canada-France-Hawaii Telescope Legacy Survey (CFHTLS), VLT Survey Telescope Kilo-Degree Survey (VST-KIDS), Panoramic Survey Telescope & Rapid Response System (Pan-Starrs), and the Dark Energy Survey will provide the first weak lensing surveys covering very large sky areas and depth. In the long run, even more ambitious programmes such as the ESA satellite EUCLID, the NASA satellite SuperNova Acceleration Probe (SNAP), and Large-aperture Synoptic Survey Telescope (LSST) are planned.

As it stands now from the theoretical point of view, the investigation of the nature of dark matter and dark energy provides one of the biggest challenges to both cosmology and particle physics. Despite the impressive recent results in the field of observational cosmology, tighter observational constraints are required in order to test new theoretical



developments. In this respect, gravitational lensing has become a very efficient tool in the past few years and it plays now an increasingly important role for providing new observational constraints.



*“The irrationality of a thing is no argument against its existence, rather a condition of it.”  
Friedrich Nietzsche (1844 - 1900)*

## Chapter 3

# Active galactic nuclei

Active galaxies are among the most exciting and challenging phenomena in modern astrophysics. They are the most powerful and luminous objects in the Universe. They possess in their nucleus an amazing power source, pouring out the same energy as that emitted by a thousand galaxies like the Milky Way (up to  $10^{48}$  erg  $s^{-1}$ ). It is even more amazing that this source occupies a volume of space only the size of the Solar system (i.e.  $\sim 10^{15}$  cm). Many competing theories endeavoured to explain this intriguing phenomenon. It is now commonly admitted that active galactic nuclei (AGNs) are powered by supermassive black holes and that accretion of gas into this central black hole is at the origin of the incredible luminosity of AGNs (e.g., Rees, 1984). The accretion flow is thought to be the source of the X-ray, ultraviolet, and optical continuum emission. This emission ionizes the gas located in both the broad and narrow-line regions and may also be the source of winds and jets.

Despite the fact that much of the large-scale structure of AGNs has now been observationally verified, we still do not understand the central engine itself. The main difficulty in achieving this goal is that the central accretion flow occurs in a region too small to be resolved even at the distances of the nearest AGNs. However, there are some interesting exceptions. Indeed, gravitational lensing acts like a natural magnifying glass and can be used to resolve the most inner parts of a gravitationally lensed AGN (see Chapter 7).

Since their discovery, active galaxies have been observed through the entire electromagnetic spectrum and astronomers have reported numerous interesting properties of their spectra, variability, and geometry. Although there were many similarities (a bright compact nucleus, a wide spectral continuum, and time variability), there were also many differences (the presence or absence of broad emission lines, the strength of radio and X-ray emission, etc). These observational differences conducted to a complex classification of these objects. The original classification scheme is simply based on observational properties rather than something truly fundamental or unique about the class thereafter named, and the boundary between two classes is often arbitrary. The ultimate goal is thus to reorganize this classification scheme and replace it by a picture of specific physical

processes that are believed to occur in various galaxies. This is the goal of the unified scheme of AGNs, that must be able to explain why these processes produce the particular classes of active galaxies that we observe.

### 3.1 The classification scheme

With the discovery of active galaxies, which started with the findings of Carl Seyfert during the 1940s, astronomers also discovered how broad the diversity among these objects is. In order to be able to better understand these objects, astronomers followed a common method used in science: they built a classification scheme. The classification went hand in hand with new discoveries, but unfortunately the naming of the new types was neither systematic nor unique. Hence, the classification took many forms: after the name of the discoverer, from the identification of unusual spectral properties, or from unusual morphological characteristics. This conducted to a classification that seems a bit confusing at first sight, but that permits a better understanding that may eventually lead to a re-ordering or unification. Before discussing the unification scheme that has emerged in the 1980s, we briefly review some of the main classes of AGNs.

#### Seyfert galaxies

These objects were discovered by Carl Seyfert (1941). They have similar morphologies to normal spiral galaxies, but reveal significant emission lines and continuum in their spectra. Seyferts are subdivided into two categories: Seyfert 1 and 2. In Seyfert 1 galaxies, the permitted lines, originating mainly from hydrogen but also He I, He II and Fe II, are broad with full widths at half maxima corresponding to velocities up to 10000 km/s. The forbidden lines such as [O III] lack the very broad wings. Whereas in Seyfert 2 galaxies, both permitted and forbidden lines are narrow (with velocity widths ranging up to 1000 km/s). This conducted to the inevitable conclusion that Seyfert 2 galaxies do not possess a broad-line region. However, new observational techniques (i.e. spectropolarimetry, see e.g., Antonucci & Miller, 1985) have revealed that at least some of them have broad emission lines in polarized light. The mechanism is explained by a thick molecular torus that hides the central engine, but acts like a mirror reflecting and polarizing the light from the broad-line region. This was one of the most crucial observational discoveries in AGN research, paving the way for the unified model of AGN activity.

#### Quasars or QSOs

Quasars are giants in the AGN classes. Their active nucleus is many times brighter than their host galaxy. These mysterious objects were first discovered in the radio domain, but were identified later, in the early 1960s, by optical astronomers who provided the observations that would eventually reveal their true nature. On the first optical photographs these objects appeared like punctual sources, and were therefore called quasi-stellar radio sources (abbreviated to QSRs, which became quasars). One of the most striking observational features of this new class of objects was the presence of very broad optical emission lines with widths of up to 10000 km/s. An intriguing question arises in attempting to decide at what point a quasar ceases to be a quasar and becomes a Seyfert 1. A convention has arisen whereby if a broad-emission line object is brighter than  $M_B = -23$  mag, then

it is referred to as a quasar. However, there is nothing physical in this boundary and it highlights the lack of clarification in the differentiation between the classes of AGNs.

We now know that the overwhelming majority ( $\sim 90\%$ ) of quasars have weak radio emission compared to the optical emission and these are often referred to as radio-quiet quasars. Strictly speaking the name quasar was given to the radio-loud sources, while the radio-quiet variety tended to be called quasi-stellar objects (QSOs), but it is now more common to speak of radio-loud and radio-quiet quasars.

### Radio galaxies

Observations with powerful radio arrays such as the Very Large Array have distinguished two categories of radio loud galaxies: lobe-dominated and core-dominated sources. In core-dominated sources the strong radio emission emanates from a compact core on a scale of an arcsecond or less. For lobe-dominated sources the radio emission can extend over several tens of kpc. The astronomers Fanaroff & Riley (1974) considered two sub-classes of lobe-dominated radio galaxies: FRI and FRII. The FRI sources have lower luminosities and exhibit very extended twin lobe structures. The FRII objects are more powerful and their lobes are usually single-sided or, when double, one side is many times brighter than the other. The jets have a smaller opening angle and are frequently dominated by bright knots rather than having a smooth appearance.

### Blazars

This class includes BL Lacertae objects (BL Lac) and optically violent variables (OVV). To a first approximation these objects have strong similarities with a radio-loud flat spectrum and strong and rapid variability. BL Lac objects were named after the first member of the class discovered, which was previously catalogued as a variable star under the name BL Lacertae. Further investigations revealed that the so-called star was in fact an AGN. A simple interpretation of a blazar is that it is an object that possesses beamed emission from a relativistic jet which is aligned roughly toward the line of sight to the observer. This powerful jet produces the observed radio spectrum through synchrotron emission (i.e. relativistic electrons in a magnetic field). What immediately differentiates BL Lac objects from OVVs is that BL Lac objects have a featureless continuum spectrum, while OVVs have very broad and strong optical emission lines.

## 3.2 The unified scheme

Based on decades of detailed investigations of active galaxies, a unification paradigm has emerged in which AGNs share certain fundamental ingredients illustrated in Fig. 3.1 and which are

1. a central supermassive black hole,
2. an accretion disk,
3. high velocity gas, usually referred to as the broad-line region,
4. lower velocity gas in the narrow line region,
5. an obscuring torus of gas and dust, hiding the broad-line region from some directions,

6. a relativistic jet, typically formed within 100 AU of the black hole and extending outward for tens of kpc and, in some cases, as much as one Mpc.

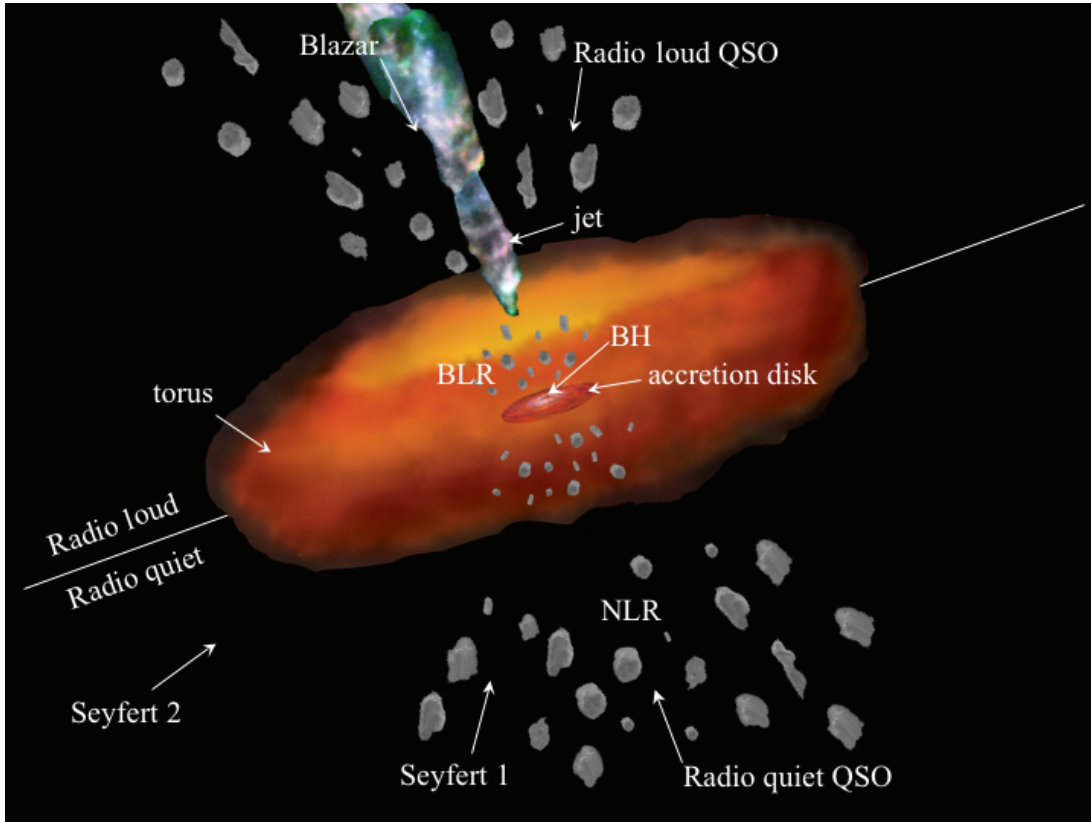


Figure 3.1: The unified scheme of active galactic nuclei (not to scale). The central black hole and the accretion disk are surrounded by a thick torus of dust and gas. The broad line region is located within this torus and is composed of small clouds of gas orbiting the central region and producing the broad emission lines. Farther out is the narrow line region, characterized by slower orbiting clouds producing the narrow emission lines. The orientation of the observer relative to the torus axis determines the classification of the source. The presence or absence of radio jets determines whether the source is radio loud or radio quiet.

The unified scheme holds that all AGNs have the same ingredients, though certainly with intrinsic variations in black hole mass, ionization parameter, size, density, luminosity, etc. According to unification, many of the principal observational characteristics of AGNs such as overall spectral energy distribution and emission line type (broad or narrow) simply stem from orientation rather than from some fundamental intrinsic difference. In this scenario, broad line (type 1) objects are those whose core can be viewed directly, whereas objects showing narrow lines (type 2) possess a broad-line region hidden by the obscuring nature of the torus due to its orientation with respect to the observer.

Nevertheless, and despite its success, the unification scheme does not explain all observed properties of AGNs. For instance, the unification of radio-loud and radio-quiet objects remains problematic, particularly in explaining the vast range in radio power and

jet extents. The presence of relativistic jets (present in radio-loud, but absent in radio-quiet AGNs) is probably linked to the properties of the central black hole, such as accretion rate, black hole mass and spin, and its orientation. The formation of relativistic jets indeed requires that a sufficient amount of particles are accreted and that the electromagnetic forces are strong enough to form and collimate the jets.

### The supermassive black hole

The principal energy provider for the AGN luminosity is gravitational energy, and the mediator of this is a supermassive (i.e.  $10^6 - 10^9 M_{\odot}$ ) black hole located at the very centre of the host galaxy. The black hole works like an enormous engine, converting potential energy of infalling material into kinetic and electromagnetic energy. This central engine is a complex mixture of intense photon field, energetic charged particles and, potentially, pair production. These numerous high-energy processes combine and generate the observed hard X-ray (in the 2 – 20 keV range) power-law emission.

### The accretion disk

Matter is inexorably attracted towards the central black hole and since this infalling material has non-zero angular momentum, it forms an accretion disk spinning around the central black hole. The diameter of the disk is typically  $\sim 100 \text{ AU} \sim 10^{-3} \text{ pc} \sim 10^{15} \text{ cm}$ . Interactions between the infalling material are thought to generate viscosity within the disk and to result in an outward transfer of angular momentum, thereby allowing the material to spiral gradually inward (Shakura & Sunyaev, 1973; Novikov & Thorne, 1973). The nature of this viscosity is still not well understood, but it is thought to be caused by dissipative processes that convert a significant fraction of the gravitational energy into heat, magnetic fields, and outflowing kinetic energy in the form of winds. The heating of the disk results in a temperature gradient, the disk being hotter towards the center. The innermost part of the accretion disk, i.e. at a distance of  $\sim 1 \text{ AU} \sim 10^{-5} \text{ pc} \sim 10^{13} \text{ cm}$  from the black hole, becomes an extremely hot ( $> 10^5 \text{ K}$ ) and intense source of thermal emission. The temperature is such that the material emits over a wide range of wavelength reaching up to the X-ray domain (Shields, 1978). Most of the emission of the disk is observed as a continuum extending from the near infrared at  $1 \mu\text{m}$  to past  $1000 \text{ \AA}$  in the ultraviolet. It is called the big blue bump. In order to produce this continuum, the central engine has to be fueled with an accretion rate of about  $1 - 100 M_{\odot}/\text{yr}$ .

### The broad-line region (BLR)

The gas of the BLR is photoionized by the ultraviolet and X-ray emission of the central engine and reaches temperatures in the range 15000 to 20000 K. This highly ionized gas produces the broad emission lines, see Fig. 3.2. In order to broaden these lines to the observed extent, the gas must have large velocities, typically reaching 5000 km/s and in some extreme cases 15000 km/s. In addition of the broad emission lines, there are other important spectral features produced within the BLR. For instance, the central continuum sources ionizes singly ionized iron (Fe II) producing a blend of emission lines, which forms a continuum-like feature predominantly in the 2000 and 3000 Å region. Along with the Balmer continuum radiation, this forms a pronounced humping in the spectrum, sometimes referred to as the small blue bump.

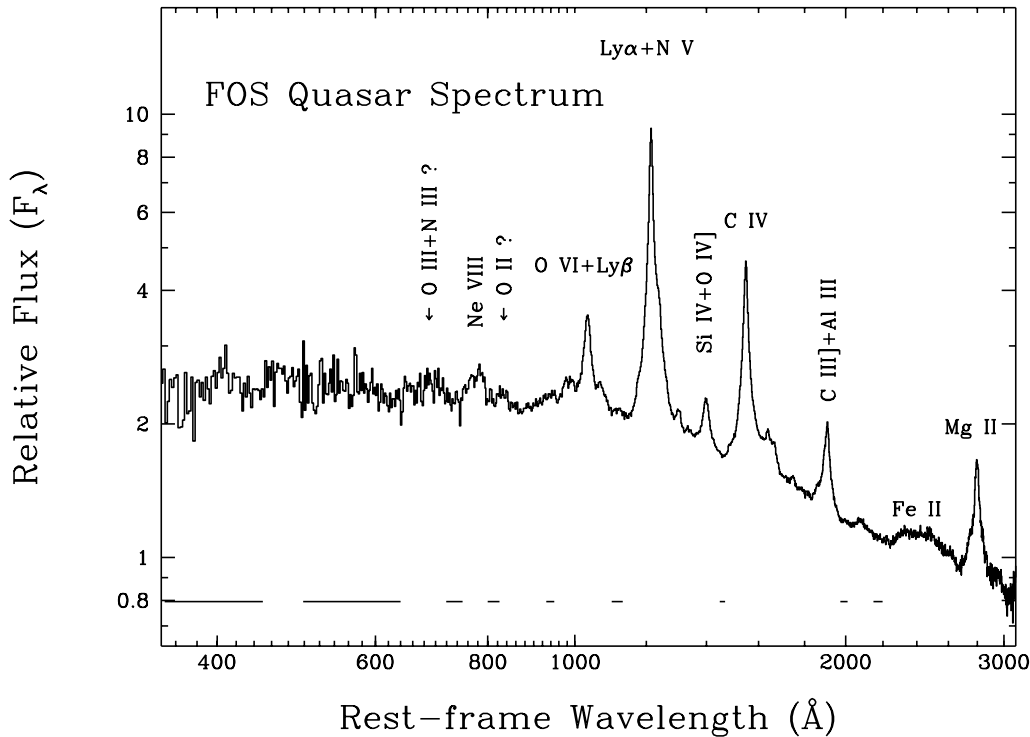


Figure 3.2: Composite quasar spectrum obtained by Zheng et al. (1997) with the Hubble Space Telescope (HST) Faint Object Spectrograph (FOS). Prominent emission lines are labeled.

These spectral features give important informations on the structure of the BLR, e.g., the presence and/or absence of given semi-forbidden and forbidden lines are dependent on the electron density of the BLR. This constrains the density to approximately  $10^{10} \text{ cm}^{-3}$ . This number can then be used as an input in photoionization models that predict the strengths of the emission lines relative to the continuum. The observed ratios are found to be much less than expected and, as a consequence, some of the continuum radiation must be escaping directly into space without interacting with the gas. Therefore, the gas in the BLR cannot be uniformly distributed, but is clumpy, i.e. probably distributed in numerous small discrete clouds.

Because the BLR is too small to be resolved with optical and radio telescopes, our knowledge of this region is indirect and still very sparse. One popular method used to investigate the BLR structure is reverberation mapping. The method consists in measuring the response of line emission to a change in the continuum as well as the changes in the line profiles. The delay observed between a given variation in the continuum and the subsequent variation in the line is called the time lag. Time lags are directly related to the size of the emission region: smaller time lags corresponding to less extended regions. Observational evidences from this technique indicate that the BLR has a size between  $10^{-4}$  and  $10^{-1}$  pc and that it is stratified (e.g., Kaspi et al., 2005). The stratification is such that the high-ionization lines, e.g.,  $\text{Ly } \alpha$ ,  $\text{C III]}$ ,  $\text{C IV}$ ,  $\text{He I}$ ,  $\text{He II}$ , and  $\text{N V}$  are apparently located closer to the central engine than lower-ionization lines such as the Balmer series of hydrogen,  $\text{Mg II}$ ,  $\text{Ca II}$ , and  $\text{Fe II}$ . Although great advances have been made during the last years, there is still no consensus about the structure of the BLR and it is worth to

use alternative methods to investigate the BLR size, structure, and kinematics, e.g., with microlensing studies as described in Chapter 7.

### The narrow-line region (NLR)

All AGNs show a NLR, providing evidence for activity from a region much farther from the central source than the BLR. The emission lines show significantly lower levels of photoionization than the high-ionization lines of the BLR and they also have much lower linewidths with typically a few hundred kilometers per second. This implies that the NLR is lying at 10 – 100 pc from the central engine and is sufficiently extended that it can be resolved spatially in the nearest active galaxies. Imaging of the NLR shows that it is breaking up into clumps and filaments forming a bi-conical ionization structure around the central source.

### The molecular torus

The idea of a dense and compact molecular torus surrounding the central engine provides an elegant source of orientation-dependant obscuration and is the main element of the unification model for AGNs. The torus lies just outside the BLR but inside the NLR. Depending on the orientation of the torus, this nicely explains why the observer might not be able to see the BLR (as is the case for type 2 AGNs).

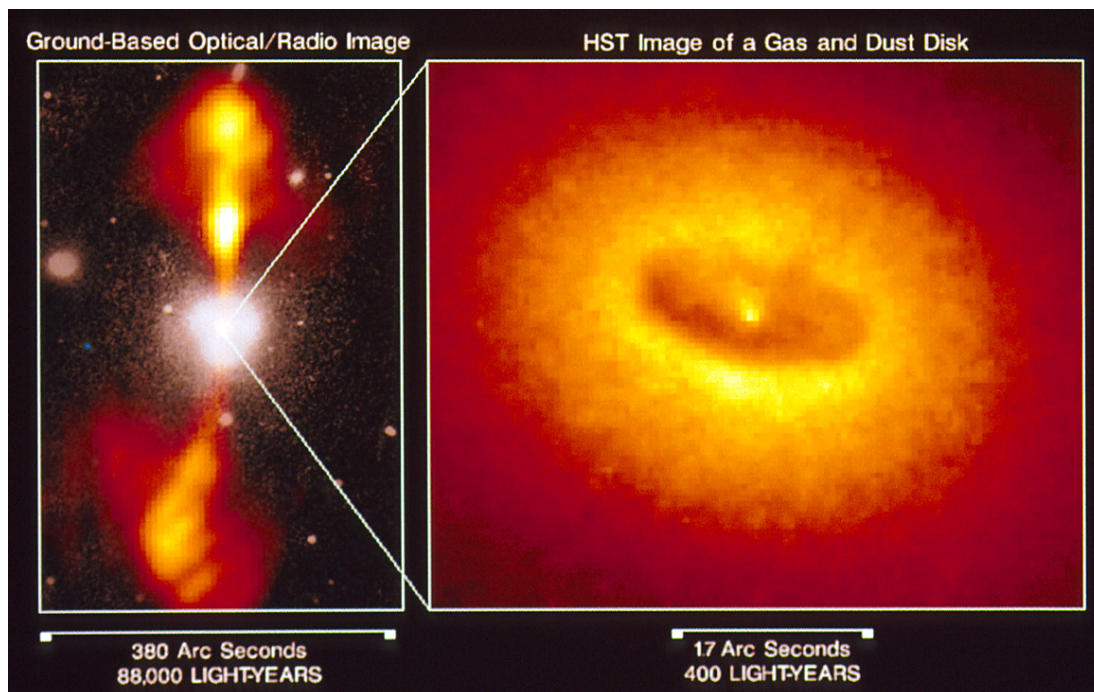


Figure 3.3: The core of the active galaxy NGC 4261 observed by Jaffe et al. (1996) with the Hubble Space Telescope suggesting a torus of gas and dust lying perpendicular to the axis of the radio emission, which is shown in the expanded view on the left by the jets.

Dust and molecular gas must be a key ingredient of this torus in order to provide enough extinction to hide the central engine and the BLR. The torus must lie at a sufficient

distance from the central source to prevent evaporation of the dust grains. This gives an inner radius of the order of a parsec. The torus is likely formed of a number of high-density clouds in order to explain the existence of dust which would otherwise be destroyed by too much frictional heating due to the orbital motions.

In nearby low luminosity AGNs, where high spatial resolution is possible, flattened dusty regions can be recognized by direct imaging. Jaffe et al. (1996) have taken spectacular images of the active galaxy NGC 4261 with the Hubble Space Telescope (see Fig. 3.3). These images suggest the existence of a molecular torus of a few hundred parsecs in radius surrounding the central engine.

### 3.3 The standard thin accretion disk model

Accretion is defined as the capture of matter by an object's gravitational field, where it is presumed that the captured material becomes coalescent with the accreting object. In contrast to other accretion flow geometries, the accretion disk paradigm has been popular for AGNs largely because it is difficult to imagine how matter could reach the central black hole with so little angular momentum that it would not be rotationally supported. Hence, the formation of an accretion disk seemed very natural (Lynden-Bell, 1969) and these disks were first thought to be geometrically thin (Pringle & Rees, 1972). First theoretical developments by Shakura & Sunyaev (1973) and Novikov & Thorne (1973) led to what is now considered as the standard thin accretion disk model. In this section, we present this standard model, which is based on the assumptions that accretion disks are stationary (i.e. independent of time), optically thick, and geometrically thin. A detailed introduction to accretion disks is given by Frank et al. (2002).

For the description of the disk, we will use the cylindrical polar coordinates  $(R, \phi, z)$ . In a geometrically thin disk, the matter lies very close to the plane  $z = 0$  and is assumed to follow circular orbits around the central black hole, which has a mass  $M_{BH}$ . The angular velocity is  $\Omega(R)$  and the corresponding azimuthal velocity is  $v_\phi = R\Omega(R)$ . In addition to  $v_\phi$ , the orbiting matter is assumed to possess a small radial velocity  $v_R \ll v_\phi$ , which is negative near the black hole, so that matter is being accreted. The disk is characterized by its surface mass density  $\Sigma(R, t)$ . Following these assumptions, we can write the conservation equations of mass and angular momentum transfer in the disk due to the radial motions. An annulus of the disk material lying at  $R$  and having a width  $\Delta R$  has a total mass  $M_R = 2\pi R \Delta R \Sigma$  and a total angular momentum  $L_R = 2\pi R \Delta R \Sigma R^2 \Omega$ . For the mass conservation of the annulus, we have

$$0 = \frac{dM_R}{dt} = \frac{\partial M_R}{\partial R} v_R + \frac{\partial M_R}{\partial t} = 2\pi \frac{\partial}{\partial R} (R\Sigma) v_R \Delta R + \frac{\partial}{\partial t} (2\pi R \Delta R \Sigma)$$

where  $v_R \doteq dR/dt$ . In the limit  $\Delta R \rightarrow 0$  we get the mass conservation equation

$$R \frac{\partial \Sigma}{\partial t} + \frac{\partial}{\partial R} (R\Sigma v_R) = 0. \quad (3.1)$$

Accretion disks probably have a differential rotation law  $\Omega(R)$  (i.e. no solid rotation) and material at neighbouring annuli moves with different angular velocity  $\Omega$ . This results in a shear between adjacent annuli of the disk, which causes dissipative processes leading to a transfer of angular momentum outwards, which allows the orbiting material to gradually fall inwards. The exact nature of these processes is still not well understood and is usually



referred to as viscosity. We suppose that this viscosity causes random motions of the particles in the disk with a mean velocity  $\bar{v}$  and a mean free path  $\lambda$  (much smaller than the size of the disk), such that the viscosity  $\nu = \lambda\bar{v}$ . Because the motions induced by the viscosity are supposed to be random, there is no net mass transfer due to the viscosity, hence

$$\dot{M}_R \left( R + \frac{\lambda}{2} \right) = \dot{M}_R \left( R - \frac{\lambda}{2} \right) = \dot{M}_R = 2\pi R \Sigma \bar{v} .$$

However, the mass from the outer disk crossing the radius  $R$  inwards has a lower angular momentum than the mass located at  $R$ . Inversely, matter crossing the radius  $R$  outwards has a higher angular momentum. Hence the random motions induced by the viscosity transfer angular momentum outwards. We can write the change  $G(R, t)$  in angular momentum  $L_R$  induced by the viscosity per unit time (see Fig. 3.4)

$$G(R, t) = \dot{M}_R \left( R + \frac{\lambda}{2} \right) \cdot \left( R - \frac{\lambda}{2} \right) \cdot v_\phi \left( R + \frac{\lambda}{2} \right) - \dot{M}_R \left( R - \frac{\lambda}{2} \right) \cdot \left( R + \frac{\lambda}{2} \right) \cdot v_\phi \left( R - \frac{\lambda}{2} \right) .$$

The first term on the right-hand side is the transfer of angular momentum from  $R + \lambda/2$  to  $R - \lambda/2$ , while the second term is the transfer from  $R - \lambda/2$  to  $R + \lambda/2$ . Because  $\lambda \ll R$ , we can neglect the terms in  $\lambda^2$  and get

$$G(R, t) = \dot{M}_R R^2 \left[ \Omega \left( R + \frac{\lambda}{2} \right) - \Omega \left( R - \frac{\lambda}{2} \right) \right] \simeq \dot{M}_R R^2 \frac{d\Omega}{dR} \lambda = 2\pi R \nu \Sigma R^2 \frac{d\Omega}{dR} .$$

This gives the change of angular momentum  $L_R$  per unit time induced by the disk viscosity. For a rotation law in which  $\Omega(R)$  decreases outwards,  $G(R)$  is negative. Hence, inner annuli lose angular momentum to the outer annuli and the matter of the disk spirals in, as expected.

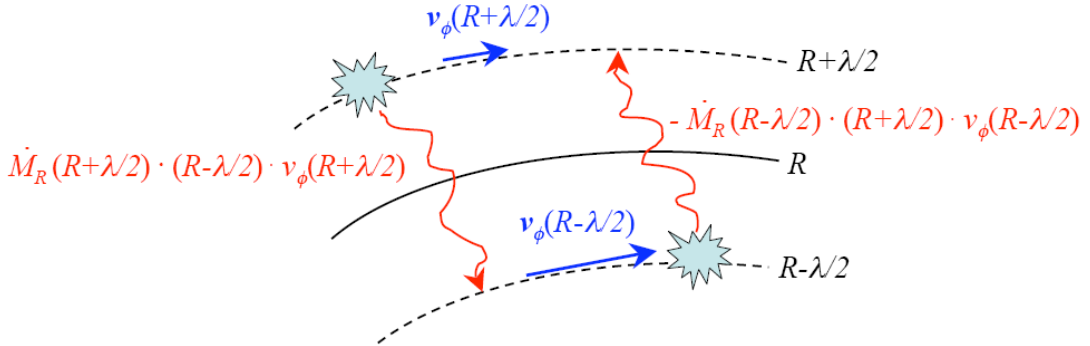


Figure 3.4: Illustration of the change  $G(R, t)$  in angular momentum  $L_R$  induced by the random motions caused by the viscosity.

Let us consider the net torque on an annulus of radius  $R$  and width  $\Delta R$ . As the annulus has both an inner and an outer edge, it is subject to competing torques. The net torque is the difference between the two and equals  $\frac{\partial G}{\partial R} \Delta R$ . We can imagine this as a force  $\frac{\partial G}{\partial R}$  acting perpendicularly to the radial direction and parallel to the azimuthal velocity  $v_\phi$  with a lever of length  $\Delta R$ . This force acts on the material of the disk and produces a mechanical power given by the product of the angular velocity  $\Omega$  and the net torque  $\frac{\partial G}{\partial R} \Delta R$

$$\Omega \frac{\partial G}{\partial R} \Delta R = \left[ \frac{\partial}{\partial R} (G\Omega) - G \frac{d\Omega}{dR} \right] \Delta R .$$

The first term on the right-hand side is the rate of transport of rotational energy through the disk material by the torque, while the second one is the local dissipation rate. Dissipation is typically due to the action of friction or turbulence and transforms mechanical energy into internal (heat) energy. Ultimately, this energy is radiated over the upper and lower faces of the disk. Remembering that the considered annulus has two plane faces, each with a surface  $2\pi R\Delta R$ , we define the energy dissipation rate  $D(r)$  per unit plane surface area as

$$D(R) \doteq \frac{1}{4\pi R} G \frac{d\Omega}{dR}. \quad (3.2)$$

The conservation equation for angular momentum is similar to that of the mass conservation, except that we must include the net torque

$$\frac{\partial G}{\partial R} \Delta R = \frac{dL_R}{dt} = \frac{\partial L_R}{\partial R} v_R + \frac{\partial L_R}{\partial t} = \frac{\partial}{\partial R} (2\pi R \Delta R \Sigma R^2 \Omega) v_R + 2\pi \frac{\partial}{\partial t} (R \Delta R \Sigma R^2 \Omega) v_R$$

and again proceeding to the limit  $\Delta R \rightarrow 0$ , we get

$$R \frac{\partial}{\partial t} (\Sigma R^2 \Omega) + \frac{\partial}{\partial R} (R \Sigma v_R R^2 \Omega) = \frac{1}{2\pi} \frac{\partial G}{\partial R}. \quad (3.3)$$

This equation shows that angular momentum of an annulus is modified by the torque induced by the disk viscosity and by the transfer of momentum of the general flow of matter towards the central black hole.

We will now assume that the disk is in a steady state, i.e. that the time derivatives are null. We get from equation (3.1) that  $R\Sigma v_R = \text{constant}$ . This represents a constant inflow of mass and since  $v_R < 0$ , we can define the accretion rate  $\dot{M} \doteq -2\pi R\Sigma v_R$ . If we further use the steady-state assumption, we get from equation (3.3)

$$R\Sigma v_R R^2 \Omega = \frac{G}{2\pi} + \frac{C}{2\pi}$$

where  $C$  is a constant related to the rate at which angular momentum flows into the black hole. We know from general relativity that there exists a minimum radius for stable orbits around a black hole. The last stable circular orbits for a maximally spinning Kerr black hole and a non-rotating Schwarzschild black hole have a radius of  $6r_g$  and  $2r_g$ , respectively, with  $r_g$  being the gravitational radius. For a black hole of mass  $M_{BH}$ , the gravitational radius is

$$r_g = \frac{GM_{BH}}{c^2} = 1.5 \times 10^{14} \left( \frac{M_{BH}}{10^9 M_\odot} \right) \text{ cm.}$$

As a consequence, accretion disks have an inner edge  $R_{in}$  in the range  $2r_g < R_{in} < 6r_g$ . Hence, the angular velocity  $\Omega(R)$  increases inwards and, at a certain radius  $R = R_*$ , it has to decrease. This implies  $\frac{d\Omega}{dR}|_{R=R_*} = 0$  and  $C = -\dot{M}\Omega R^2$ . The radius  $R_*$  is often approximated by the inner edge  $R_{in}$  of the disk (i.e.  $R_* \simeq R_{in}$ ).

A particular case, which is often considered, is where the matter follows Keplerian orbits around the central black hole. The angular velocity is then

$$\Omega(R) = \left( \frac{GM_{BH}}{R^3} \right)^{1/2}$$

and from equations (3.1), (3.2), and (3.3) we get the energy dissipated by the disk viscosity per unit area and per unit time

$$D(R) = \frac{3GM_{BH}\dot{M}}{8\pi R^3} \left[ 1 - \left( \frac{R_*}{R} \right)^{1/2} \right].$$

The dissipation increases the internal energy of the disk material. In order to remain in a steady state, the disk releases this gained energy in the form of radiation. If the disk is optically thick in the  $z$ -direction, then each annulus of the disk radiates roughly as a blackbody with a temperature  $T(R)$ . The amount  $I_\lambda$  of energy per unit surface area per unit time per unit solid angle emitted in the wavelength range between  $\lambda$  and  $\lambda + d\lambda$  by a blackbody at temperature  $T$  is given by Planck's law

$$I_\lambda(T) d\lambda = \frac{2hc^2}{\lambda^5} \frac{1}{\exp\left(\frac{hc}{\lambda kT}\right) - 1} d\lambda$$

where  $h$  is Planck's constant and  $k$  Boltzmann's constant. Integration of the specific intensity  $I_\lambda$  over all wavelengths and solid angles gives the flux  $F = \sigma T^4$  (i.e. the energy emitted per unit area and per unit time), where  $\sigma$  is the Stefan-Boltzmann constant. If each annulus is emitting like a blackbody, we have  $\sigma T^4(R) = D(R)$  and thus,

$$T(R) = \left( \frac{3GM_{BH}\dot{M}}{8\pi R^3\sigma} \left[ 1 - \left( \frac{R_*}{R} \right)^{1/2} \right] \right)^{1/4}.$$

For  $R \gg R_*$ , we have simply  $T \propto R^{-3/4}$ . Moreover, from Wien's displacement law we know that  $\lambda_{max}T = \text{constant}$  and thus, the wavelength  $\lambda_{max}$  of the peak of the blackbody spectrum is proportional to  $T^{-1}$ . Therefore, we expect the energy profile of the accretion disk at  $R \gg R_*$  to follow the power-law

$$R \propto \lambda^{4/3}.$$

To get the integrated spectrum from the disk one adds up all the Planck laws from each radius. It can be shown that if  $T \propto R^p$  then  $F_\nu \propto \nu^{3-2/p}$  (Shakura & Sunyaev, 1973). Here  $p = 3/4$  and we get the spectrum  $F_\nu \propto \nu^{1/3}$ , where  $F_\nu$  is the flux per frequency.

### 3.4 Problems with the standard thin accretion disk model

The standard model is probably the most extensively studied accretion disk model. However, given the numerous simplifying assumptions made, it is questionable if this model accurately describes real accretion disks. A big success of the standard model is that it predicts correctly the peak of radiation in the ultraviolet wavelengths ( $\sim 100 - 4000\text{\AA}$ ) observed in the spectra of most AGNs. Nevertheless, there are several other observational facts, that are not so well described by the standard model, for a review see, e.g., Koratkar & Blaes (1999).

In particular, the standard model predicts a spectral shape  $F_\nu \propto \nu^{1/3}$  from the visible ( $4000 - 8000\text{\AA}$ ) to the near-infrared ( $\sim 1 - 2\text{ }\mu\text{m}$ ). The problem is that many studies have shown that the general AGN spectral shape observed at optical and ultraviolet wavelengths is much redder, with a spectral slope  $\alpha_\nu$  (where  $F_\nu \propto \nu^{\alpha_\nu}$ ) between  $-0.2$  and  $-1$  and is

never as blue as  $\alpha_\nu = 1/3$  (e.g., Zheng et al., 1997; Vanden Berk et al., 2001). Efforts have been spent on the theoretical side to account for the observed red spectral slopes. Some improvements have been made using sophisticated disk atmosphere models (e.g., Hubeny et al., 2000) for which the spectrum generally becomes slightly redder at optical wavelengths, owing to various opacity effects and deviation from local thermodynamic equilibrium, but discrepancies between the model and observed spectra still remain (e.g., Davis et al., 2007).

On the observational side, several interesting results were obtained from polarized light studies. Optical continua of many directly visible (i.e. type 1) AGNs are known to be linearly polarized at a level of about 1% with the polarization mostly parallel to the rotation axis of the accretion disk determined from the orientation of the jet-like structure of radio emission (e.g., Antonucci, 1983; Smith et al., 2004). This polarization in Type 1 AGNs is interpreted as an indication of an equatorial scattering region that is optically thin and that surrounds the accretion disk. Polarized light therefore produces a copy of the spectrum originating in the central region before it interacts with the broad-line region and the molecular torus. A crucial difficulty is that, towards the infrared, the disk spectrum starts to be hidden under strong, hot dust emission of the molecular torus. Recently, Kishimoto et al. (2008) acquired observations of polarized light and were able to uncover the near-infrared disk spectrum from the dust emission in several quasars. They showed that the near-infrared disk spectrum is indeed as blue as predicted, (i.e.  $\alpha_\nu = 1/3$ ). This suggests that, at least for the outer near-infrared-emitting radii, the standard picture of the locally heated disk is approximately correct.

An important assumption of the standard model is that accretion disks are geometrically thin. However, more detailed consideration of the processes going on in disks (e.g., Blandford & Begelman, 2004) shows that convection and mass loss due to winds cause a substantial thickening of the disk. This is indeed seen in detailed simulations of accretion (e.g., Stone et al., 1999; Hawley & Krolik, 2001), but even though the resulting outflows are well established observationally (Crenshaw et al., 2002), the claim for geometrically thick accretion disks in AGNs still requires further observational confirmation.

Despite the observational and theoretical progress, a predictive accretion disk model which explains all the observations simultaneously does not exist yet, and the standard thin accretion disk model still remains an important reference for AGN accretion theories. Observations of the most inner parts of AGNs are still sparse, because of the difficulty in spatially resolving these distant objects. However, some progress has been made in the last years by using gravitational lensing as a natural magnifying glass to resolve the inner regions of gravitationally lensed AGNs (see Chapter 7 for more details). For instance, Morgan et al. (2008) analyzed the lightcurves of the lensed quasar PG 1115+080, and found that the effective radius of the X-ray emission is  $1.3_{-0.5}^{+1.1}$  dex smaller than that of the optical emission, with the X-ray emission generated near the inner edge of the accretion disk while the optical emission comes from scales slightly larger than those expected for a standard thin accretion disk. Another example is given by Chartas et al. (2008) who combined X-ray and optical data of HE 1104–1805, and reveal that the X-ray emitting region is compact with a half-light radius smaller than six gravitational radius, i.e. smaller than  $2 \times 10^{15}$  cm, thus placing significant constraints on AGN models.

*“Reality is merely an illusion,  
albeit a very persistent one.”  
Albert Einstein (1879 - 1955)*

## Chapter 4

# Gravitational lensing

## 4.1 Historical background

The deflection of light passing close to a mass distribution was already mentioned by Isaac Newton in the 18<sup>th</sup> century. However it was only after the formulation of General Relativity by Albert Einstein that the behavior of light in a gravitational field could be studied on a firmer theoretical ground. The first calculations related to gravitational lensing were found in some unpublished notes from 1912, where Albert Einstein considered a star perfectly aligned with a foreground mass, concluding that the source should be imaged as a ring (now called the Einstein ring) around the deflecting mass. If the alignment is not perfect, two images of the background star would be visible on either side of the lens. Einstein (1936) computed the separation of these images and concluded that the separation would be so small (a few milli-arcseconds) that *“there is no great chance of observing this phenomenon”*.

Instead of studying stars in our Galaxy, Fritz Zwicky considered whole galaxies acting as gravitational lenses. In two visionary papers, Zwicky (1937a,c) estimated the image separation of a lensed background source to be of order  $10''$ . He also computed the probability of distant galaxies to be gravitationally lensed. He found this probability to be of the order to a few tenths of a percent, hence making the discovery of extragalactic lenses *“practically a certainty”*.

Despite the encouraging predictions of Fritz Zwicky, the field of gravitational lensing rested until the beginning of the 1960's, when the subject was reopened by Sjur Refsdal in 1962 with his Master degree thesis, followed by two pioneering papers (Refsdal, 1964a,b). Although the theory was undoubted, the subject was considered by many as unrealistic since observing the phenomenon requires unprobably bright sources located at large distances. This skepticism stopped soon after, with the discovery and identification of the first quasars in 1963 and of several others later on. These discoveries provided a population of compact, luminous, and very distant sources lying behind the galaxies discovered by Fritz Zwicky. As a consequence, finding lens systems amongst them should only be

a matter of time. However, it took another 15 years and several technical developments (e.g., the first CCD detectors, the construction of large radio interferometers) until Walsh et al. (1979) found the first extragalactic gravitational lens : the quasar Q 0957+561.

Since this discovery, gravitational lensing became more popular, and today the field is booming. Several breakthroughs in astrophysics achieved in the past two decades can be attributed to gravitational lensing. Some of the most impressive examples are the discovery of a portion of dark matter in the form of low mass stars in our own Galaxy (e.g., Alcock et al., 1993; Aubourg et al., 1993), the measurement of the mass distribution in large galaxy clusters using giant luminous arcs (e.g., Kneib et al., 1996), a direct empirical proof of the existence of dark matter (Clowe et al., 2006), and the detection of massive large-scale structures in our Universe using weak-lensing techniques (e.g., Van Waerbeke et al., 2000).

In the present chapter, we review some basics of gravitational lensing, which we will use throughout this thesis. For a more complete introduction to the field see, e.g., Schneider et al. (1992) or Schneider et al. (2006).

## 4.2 The lens equation

Gravitational lensing generally affects objects located at galactic or extragalactic distances. This implies that the spatial extent (i.e. the apparent thickness) of the lens relative to the large distances involved is negligible. Hence, we will assume that the lens is "thin", i.e. that the mass distribution of the lens can be considered as located at one single distance between the source and the observer. This means that we can project the mass distribution along the line of sight and replace it by a two-dimensional mass sheet orthogonal to the line of sight, which defines the lens plane. The geometry of a gravitational lens is depicted in Fig. 4.1. Light rays from a source at distance  $D_s$  from the observer pass a mass concentration located at a distance  $D_l$  from the observer. The light rays cross the lens plane at position  $\boldsymbol{\xi}$  and the corresponding two-dimensional angular position is  $\boldsymbol{\theta} = \boldsymbol{\xi}/D_l$ . The true two-dimensional position of the source in the source plane is denoted  $\boldsymbol{\eta}$  and the corresponding angular position of the source is  $\boldsymbol{\beta} = \boldsymbol{\eta}/D_s$ . The latter defines the angular position at which we would observe the source in the absence of any deflecting mass. The distance of the source plane from the lens plane is  $D_{ls}$ . With these definitions and considering Fig. 4.1, we immediately get the lens equation

$$\boldsymbol{\eta} = \frac{D_s}{D_l} \boldsymbol{\xi} - D_{ls} \hat{\boldsymbol{\alpha}} \quad \Leftrightarrow \quad \boldsymbol{\beta} = \boldsymbol{\theta} - \frac{D_{ls}}{D_s} \hat{\boldsymbol{\alpha}}$$

where  $\hat{\boldsymbol{\alpha}}$  is the deflection angle. As the observables are angular separations (e.g., the angular position  $\boldsymbol{\theta}$  of the image), angular-diameter distances are the relevant distances, as they give the ratio of the linear diameter over the observed angular diameter.

## 4.3 The deflection angle

The deflection of light is due to the spacetime curvature induced by the mass of the lens. In other words, the metric  $g_{\mu\nu}$ , and hence the deflection angle  $\hat{\boldsymbol{\alpha}}$ , are determined by solving the Einstein field equations. However, finding such a solution has proven to be extremely difficult. The first exact solution of the Einstein field equations (besides the trivial flat space solution) was given by Karl Schwarzschild (1916). It describes the gravitational

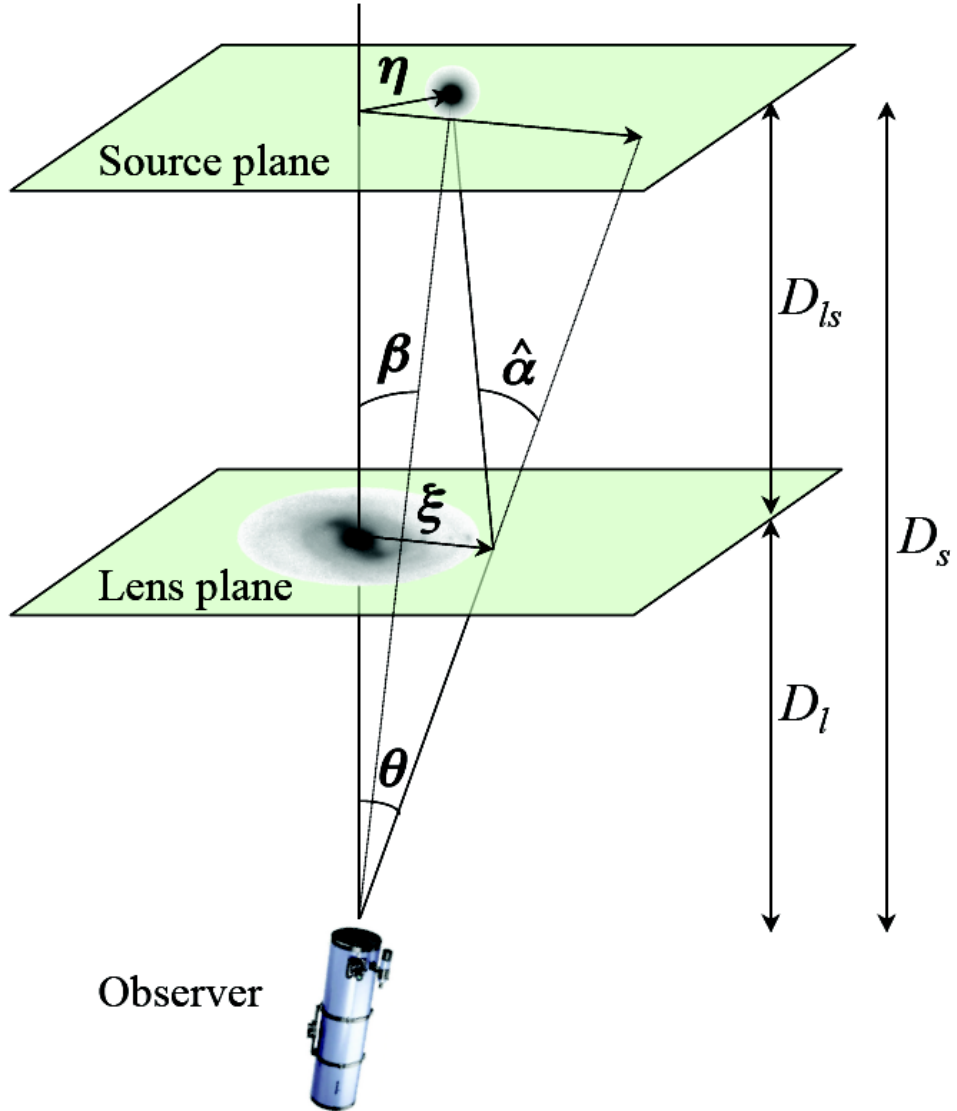


Figure 4.1: Geometry of a gravitational lens system. The lens equation is obtained from the projection of the three angles  $\beta$ ,  $\theta$ , and  $\hat{\alpha}$  on the source plane.

field outside a spherical, non-rotating mass  $M$  such as, e.g., a non-rotating star, planet, or black hole. The derivation of this solution uses spherical symmetry arguments to reduce the form of the metric to two unknown functions, which are then determined from the vacuum Einstein field equations (i.e.  $R_{\mu\nu} = 0$ ). The solution is the Schwarzschild metric

$$c^2 d\tau^2 = g_{\mu\nu} dx^\mu dx^\nu = \left(1 - \frac{r_s}{r}\right) c^2 dt^2 - \left(1 - \frac{r_s}{r}\right)^{-1} dr^2 - r^2 (d\theta^2 + \sin^2 \theta d\phi^2)$$

where  $r_s = 2GM/c^2$  is the Schwarzschild radius. This metric is also a good approximation to the gravitational field of a slowly rotating body like the Earth or Sun.

From Einstein field equations we know that a mass distribution modifies the geometry of spacetime, and that light rays passing close to this mass are deflected. To determine

how the light is deflected, we need to solve the Euler equations

$$\frac{d}{dp} \left( \frac{\partial \mathcal{L}}{\partial \dot{x}^\mu} \right) - \frac{\partial \mathcal{L}}{\partial x^\mu} = 0 \quad \text{with} \quad \dot{x}^\mu = \frac{dx^\mu}{dp}$$

where  $p$  is any parameter (e.g.,  $t$ ,  $\tau$ , etc.) describing the path of the considered particle. The Lagrangian is defined by

$$\mathcal{L} \doteq \frac{1}{2} g_{\mu\nu} \dot{x}^\mu \dot{x}^\nu .$$

Because the metric (and hence the gravitational field) has a spherical symmetry, we can choose  $\theta = \pi/2$  along the whole path  $x^\mu(p)$ , and the Euler equations lead to

$$\phi(r_2) - \phi(r_1) = \int_{r_1}^{r_2} \frac{1}{r} \left( 1 - \frac{r_s}{r} \right)^{-1/2} \left( \frac{r^2}{r_{min}^2} \frac{\left( 1 - \frac{r_s}{r_{min}} \right)}{\left( 1 - \frac{r_s}{r} \right)} - 1 \right)^{-1/2} dr$$

where  $r_{min}$  is the radial coordinate of the closest approach (not the impact parameter) of the photon relative to the deflecting mass  $M$ . The deflection angle  $\hat{\alpha}$  is defined by

$$\hat{\alpha} \doteq -\pi + 2(\phi(\infty) - \phi(r_{min})) = 2 \frac{r_s}{r_{min}} + \mathcal{O} \left[ \left( \frac{r_s}{r_{min}} \right)^2 \right] .$$

This last equation only holds for  $r_{min} \gg r_s$ , i.e. for small deflection angles (i.e.  $\hat{\alpha} \ll 1$ ), which is verified in most astrophysical cases, where typical deflection angles are of the order of  $1'' \simeq 10^{-6}$  rad. This issue may become critical in the vicinity of very compact objects (e.g., black holes), but these cases are not relevant to the present discussion. Hence, a very good approximation of the deflection angle is given by

$$\hat{\alpha} = \frac{4GM}{r_{min} c^2} .$$

If we set  $M = M_\odot$  and  $r_{min} = R_\odot$  we get the solar deflection angle  $\hat{\alpha}_\odot = 1.74''$ , which was measured during the solar eclipse of 1919. The result was twice larger than the value predicted by Isaac Newton's law of gravitation, but was in excellent agreement with the prediction of General Relativity, and made Albert Einstein world-famous.

We have already mentioned that the considered deflection angle is small in most relevant astrophysical situations. Hence the distance of closest approach  $r_{min}$  can be approximated by  $\|\boldsymbol{\xi}\|$ , which implies that the two-dimensional deflection angle satisfying the lens equation is

$$\hat{\alpha}(\boldsymbol{\xi}) = \frac{4GM}{c^2} \frac{\boldsymbol{\xi}}{\|\boldsymbol{\xi}\|^2} .$$

This is the deflection angle for a point mass. If we use this in the lens equation we get

$$\boldsymbol{\eta} = \frac{D_s}{D_l} \boldsymbol{\xi} - D_{ls} \frac{4GM}{c^2} \frac{\boldsymbol{\xi}}{\|\boldsymbol{\xi}\|^2} \quad \Leftrightarrow \quad \boldsymbol{\beta} = \boldsymbol{\theta} - \frac{4GM}{c^2} \frac{D_{ls}}{D_s D_l} \frac{\boldsymbol{\theta}}{\|\boldsymbol{\theta}\|^2} = \left( \|\boldsymbol{\theta}\| - \frac{\theta_E^2}{\|\boldsymbol{\theta}\|} \right) \frac{\boldsymbol{\theta}}{\|\boldsymbol{\theta}\|}$$

where we have defined the Einstein angle

$$\theta_E = \sqrt{\frac{4GM}{c^2} \frac{D_{ls}}{D_l D_s}} .$$



Thus, in the case of a point-mass lens, a ring-shaped image of radius  $\theta_E$  is formed when the lens, the source and the observer are aligned (i.e.  $\boldsymbol{\beta} = \mathbf{0}$ ). This ring is called an Einstein ring.

We will use the deflection angle of a point mass to compute the deflection angle for more complex mass distributions. Indeed, the smallness of the deflection angle also implies that the gravitational field is weak and that the Einstein field equations can be linearized. The deflection angle of an ensemble of point masses is then the vectorial sum of the deflection angles of the individual mass components. In the assumed thin lens approximation, we can consider the mass of the lens as a mass sheet having a surface mass density  $\Sigma(\boldsymbol{\xi})$  and being orthogonal to the line of sight. The deflection angle is then

$$\hat{\boldsymbol{\alpha}}(\boldsymbol{\xi}) = \frac{4G}{c^2} \int \frac{\Sigma(\boldsymbol{\xi}') (\boldsymbol{\xi} - \boldsymbol{\xi}')}{\|\boldsymbol{\xi} - \boldsymbol{\xi}'\|^2} d^2\xi'$$

where  $\boldsymbol{\xi} - \boldsymbol{\xi}'$  is approximately the distance of closest approach of the light ray to the deflecting mass element  $dm(\boldsymbol{\xi}') = \Sigma(\boldsymbol{\xi}') d^2\xi'$ . From the previously given definitions of the angular coordinates, we have  $\boldsymbol{\xi} = D_l \boldsymbol{\theta}$  and we define the scaled deflection angle as

$$\boldsymbol{\alpha}(\boldsymbol{\theta}) \doteq \frac{D_{ls}}{D_s} \hat{\boldsymbol{\alpha}}(D_l \boldsymbol{\theta}) = \frac{4G D_{ls} D_l}{c^2 D_s} \int \frac{\Sigma(\boldsymbol{\theta}') (\boldsymbol{\theta} - \boldsymbol{\theta}')}{\|\boldsymbol{\theta} - \boldsymbol{\theta}'\|^2} d^2\theta' = \frac{1}{\pi} \int \frac{\kappa(\boldsymbol{\theta}') (\boldsymbol{\theta} - \boldsymbol{\theta}')}{\|\boldsymbol{\theta} - \boldsymbol{\theta}'\|^2} d^2\theta'$$

where  $\kappa(\boldsymbol{\theta}) \doteq \Sigma(D_l \boldsymbol{\theta})/\Sigma_{\text{crit}}$  is the dimensionless surface mass density, also called convergence, and  $\Sigma_{\text{crit}}$  is the critical surface mass density defined by

$$\Sigma_{\text{crit}} \doteq \frac{c^2}{4\pi G} \frac{D_s}{D_{ls} D_l} .$$

It is called critical because the condition  $\Sigma \geq \Sigma_{\text{crit}}$  (i.e.  $\kappa \geq 1$ ) is sufficient to produce multiple images for some source positions. The critical surface mass density is a characteristic value between the strong and weak lensing regimes.

#### 4.4 The deflection potential

A potential can easily be found for the scaled deflection angle using the simple identity  $\nabla \ln \|\boldsymbol{\xi} - \boldsymbol{\xi}'\| = (\boldsymbol{\xi} - \boldsymbol{\xi}') / \|\boldsymbol{\xi} - \boldsymbol{\xi}'\|^2$ . The deflection potential is defined as

$$\hat{\psi}(\boldsymbol{\xi}) \doteq \frac{4G}{c^2} \int \Sigma(\boldsymbol{\xi}') \ln \|\boldsymbol{\xi} - \boldsymbol{\xi}'\| d^2\xi' \quad \text{and} \quad \hat{\boldsymbol{\alpha}} = \nabla \hat{\psi} .$$

Similarly, we can define a scaled deflection potential

$$\psi(\boldsymbol{\theta}) \doteq \frac{1}{\pi} \int \kappa(\boldsymbol{\theta}') \ln \|\boldsymbol{\theta} - \boldsymbol{\theta}'\| d^2\theta' \quad \text{and} \quad \boldsymbol{\alpha} = \nabla \psi .$$

From these definitions, the lens equation can be rewritten

$$\boldsymbol{\beta} = \boldsymbol{\theta} - \boldsymbol{\alpha}(\boldsymbol{\theta}) = \boldsymbol{\theta} - \nabla \psi(\boldsymbol{\theta}) .$$

The deflection potential is very convenient for modeling gravitational lenses and especially for computing the distortions and magnifications of the images, as we will see later on.

## 4.5 The arrival time and Fermat's principle

Another important quantity in gravitational lensing is the scaled arrival time defined as

$$\tau(\boldsymbol{\theta}) \doteq \frac{1}{2}(\boldsymbol{\theta} - \boldsymbol{\beta})^2 - \psi(\boldsymbol{\theta})$$

which has the following interesting property

$$\nabla\tau(\boldsymbol{\theta}) = \mathbf{0} \quad \Rightarrow \quad \boldsymbol{\beta} = \boldsymbol{\theta} - \nabla\psi(\boldsymbol{\theta}) = \boldsymbol{\theta} - \frac{D_{ls}}{D_s}\hat{\boldsymbol{\alpha}}(\boldsymbol{\theta}) .$$

The last equality is the lens equation. This proves that the images of a lensed source form only at stationary points of the arrival time  $\tau$ . This property is also known as Fermat's principle, which states that real light rays take paths that extremize the arrival time. The scaled arrival time, visualized as a function of the images positions, defines a three-dimensional surface and is called the arrival-time surface.

## 4.6 The time delays and the Hubble constant

Light having a finite propagation velocity, it takes a certain amount of time before the light rays emitted by a distant source can reach us. This amount of time depends on the path followed by the light rays and will differ whether the source is gravitationally lensed or not. Cooke & Kantowski (1975) derived the expression for the time difference between the lensed and unlensed cases, and showed that the light from a lensed source is delayed because of two effects. First, a light ray that is bent is longer and thus, light needs more time to propagate. This gives rise to a geometrical time delay  $\Delta t_{\text{geom}}$ . If we consider a FLRW metric and make the reasonable assumption that the scale factor  $R(t)$  does not vary significantly during  $\Delta t_{\text{geom}}$  then

$$c \Delta t_{\text{geom}} = (1 + z_l) \frac{D_l D_s}{2D_{ls}} (\boldsymbol{\theta} - \boldsymbol{\beta})^2 .$$

Second, when light rays propagate through a gravitational potential, this results in a (general relativistic) time dilation effect, which retards them. This is the well known Shapiro effect, which has been tested by radar echo delay experiments towards the inner planets of the Solar System (Shapiro et al., 1971). It is important to note that this gravitational time delay  $\Delta t_{\text{grav}}$  occurs at the redshift of the lens and then gets stretched by a factor  $(1 + z_l)$  due to cosmic expansion

$$c \Delta t_{\text{grav}} = -(1 + z_l) \hat{\psi}(\boldsymbol{\xi}) + \text{constant} .$$

Cooke & Kantowski (1975) showed that the gravitational time delay can be significant and should not be neglected. The total time delay  $\Delta t$  is hence, the sum of the two

$$c \Delta t = (1 + z_l) \frac{D_l D_s}{D_{ls}} \left( \frac{1}{2} (\boldsymbol{\theta} - \boldsymbol{\beta})^2 - \psi(\boldsymbol{\theta}) \right) + \text{constant}$$

where we have introduced the scaled deflection potential  $\psi(\boldsymbol{\theta})$ . Unfortunately, because the unlensed source is not observable, the time delay  $\Delta t$  can not be measured. However,

the difference between the time delays  $\Delta t_A$  and  $\Delta t_B$  affecting two different lensed images A and B of the background source can be determined

$$\Delta t_B - \Delta t_A = \frac{1+z_l}{c} \frac{D_l D_s}{D_{ls}} \left( \frac{1}{2}(\boldsymbol{\theta}_B - \boldsymbol{\beta})^2 - \frac{1}{2}(\boldsymbol{\theta}_A - \boldsymbol{\beta})^2 - \psi(\boldsymbol{\theta}_B) + \psi(\boldsymbol{\theta}_A) \right).$$

We immediately see that the time delay depends on angular-diameter distances, which themselves depend on the density parameters  $\Omega_{m0}$  and  $\Omega_{\Lambda 0}$ , the redshifts of the source  $z_s$  and lens  $z_l$ , and  $H_0$ . The dependence of the time delays on the energy densities  $\Omega_{\Lambda 0}$  and  $\Omega_{m0}$  are weak, but what makes them particularly interesting is that they are, as the angular-diameter distances, directly proportional to  $H_0^{-1}$ . As a consequence, gravitational lensing can provide, via the measurement of time delays, a direct estimation of the Hubble constant. This method is known as the time-delay method and was first proposed by Refsdal (1964a).

It is also interesting to note that the difference between the time delays of two images depends on the difference of the potential at the image positions. Thus, for a given deflecting mass, time delays tend to be larger for steeper mass profiles. Hence, time delays can also be used to determine the mass profiles of lensing galaxies (e.g., Kochanek, 2002).

## 4.7 Images and magnification of a lensed source

From the expression of the deflection angle, we know that a light ray passing closer to the lensing mass is more deflected than a light ray passing farther away. Hence light beams are not only deflected but are also distorted. The situation is illustrated in Fig. 4.2, where an extended source is gravitationally lensed by a mass distribution. The source has a surface  $d\eta_1 d\eta_2$  measured in the source plane. If no lens is present, the solid angle that the source subtends on the sky is simply  $d\Omega_s = d\eta_1 d\eta_2 / D_s^2$ . Because of the mass distribution, the light rays are deflected and the image of the source has an apparent surface  $d\xi_1 d\xi_2$  in the lens plane, subtending a solid angle  $d\Omega_l = d\xi_1 d\xi_2 / D_l^2$ . Since gravitational lensing is not linked to emission or absorption of radiation, the surface brightness (or specific intensity)  $I$  is preserved. Although we will not prove it here, this is a consequence of Liouville's theorem, and of the fact that the lens equation is a gradient mapping. The flux of the unlensed source is  $F_0 = I d\Omega_s$  and the flux of the lensed source image is  $F = I d\Omega_l$ . The change in flux due to the deflecting mass is called the magnification and is defined as

$$\mu \doteq \frac{F}{F_0} = \frac{d\Omega_l}{d\Omega_s} = \frac{d\xi_1 d\xi_2}{d\eta_1 d\eta_2} \left( \frac{D_s}{D_l} \right)^2.$$

The lens equation gives the expression of  $\boldsymbol{\beta}(\boldsymbol{\theta})$ . Reminding  $\boldsymbol{\beta} = \boldsymbol{\eta} / D_s$  and  $\boldsymbol{\theta} = \boldsymbol{\xi} / D_l$ , we get

$$\frac{d\eta_1 d\eta_2}{d\xi_1 d\xi_2} \left( \frac{D_l}{D_s} \right)^2 = \frac{d\beta_1 d\beta_2}{d\theta_1 d\theta_2} = \det \frac{\partial \boldsymbol{\beta}(\boldsymbol{\theta})}{\partial \boldsymbol{\theta}} \frac{d\theta_1 d\theta_2}{d\theta_1 d\theta_2} = \det \frac{\partial \boldsymbol{\beta}(\boldsymbol{\theta})}{\partial \boldsymbol{\theta}}.$$

Note that the second equality is only valid if the source is much smaller than the angular scale on which the lens properties change, i.e. if the lens mapping  $\boldsymbol{\theta} \rightarrow \boldsymbol{\beta}$  can be linearized locally. The distortions of images are then described by the Jacobian matrix

$$\mathcal{A} = \frac{\partial \boldsymbol{\beta}(\boldsymbol{\theta})}{\partial \boldsymbol{\theta}} = \left( \delta_{ij} - \frac{\partial^2 \psi(\boldsymbol{\theta})}{\partial \theta_i \partial \theta_j} \right) = \begin{pmatrix} 1 - \kappa - \gamma_1 & -\gamma_2 \\ -\gamma_2 & 1 - \kappa + \gamma_1 \end{pmatrix}$$

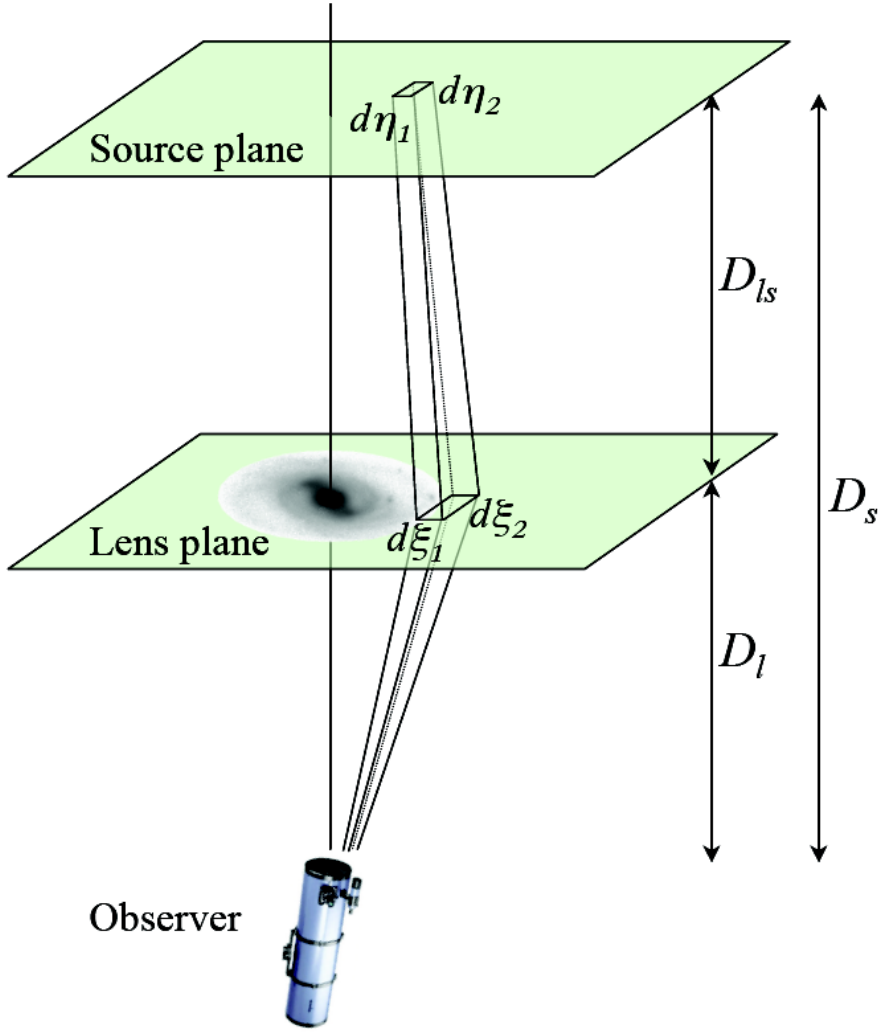


Figure 4.2: Light beams are not only deflected, but also distorted. The observed solid angle  $d\Omega_l = d\xi_1 d\xi_2/D_l^2$  subtended by the lensed image, as seen by the observer, is different from the solid angle  $d\Omega_s = d\eta_1 d\eta_2/D_s^2$  subtended by the unlensed source. As a consequence, the image of the source is modified in brightness and in shape.

where we have used the lens equation  $\boldsymbol{\beta} = \boldsymbol{\theta} - \nabla\psi(\boldsymbol{\theta})$ , and the following definitions

$$\gamma_1(\boldsymbol{\theta}) \doteq \frac{1}{2} \left( \frac{\partial^2\psi(\boldsymbol{\theta})}{\partial\theta_1^2} - \frac{\partial^2\psi(\boldsymbol{\theta})}{\partial\theta_2^2} \right) ; \quad \gamma_2(\boldsymbol{\theta}) \doteq \frac{\partial^2\psi(\boldsymbol{\theta})}{\partial\theta_1\partial\theta_2} ; \quad \kappa(\boldsymbol{\theta}) \doteq \frac{1}{2} \left( \frac{\partial^2\psi(\boldsymbol{\theta})}{\partial\theta_1^2} + \frac{\partial^2\psi(\boldsymbol{\theta})}{\partial\theta_2^2} \right) .$$

We have introduced the components of the shear  $\gamma = \sqrt{\gamma_1^2 + \gamma_2^2}$ . The Jacobian matrix  $\mathcal{A}$  has the two eigenvalues  $1 - \kappa \pm \gamma$ . Lensed images are stretched in the two eigendirections of  $\mathcal{A}$ . The images are thus distorted in shape and in size. The shape distortion is due to the shear  $\gamma$  (i.e. the tidal gravitational field), whereas the magnification (the change in size) is caused by both isotropic focusing due to the local surface mass density  $\kappa$  and anisotropic focusing due to the shear  $\gamma$ .

The magnification factor  $\mu$  is given by the inverse of the Jacobian of the lens mapping  $\boldsymbol{\theta} \rightarrow \boldsymbol{\beta}$  and hence,

$$\mu(\boldsymbol{\theta}) = \left[ \det \frac{\partial \boldsymbol{\beta}(\boldsymbol{\theta})}{\partial \boldsymbol{\theta}} \right]^{-1} = \frac{1}{(1 - \kappa)^2 - \gamma^2}.$$

Since the intrinsic luminosity of the source is generally unknown, the magnification in a lens system is not observable. However the flux ratios of different images provide a direct measurement of the corresponding magnification ratios, and thus, can be used to constrain the lens model.

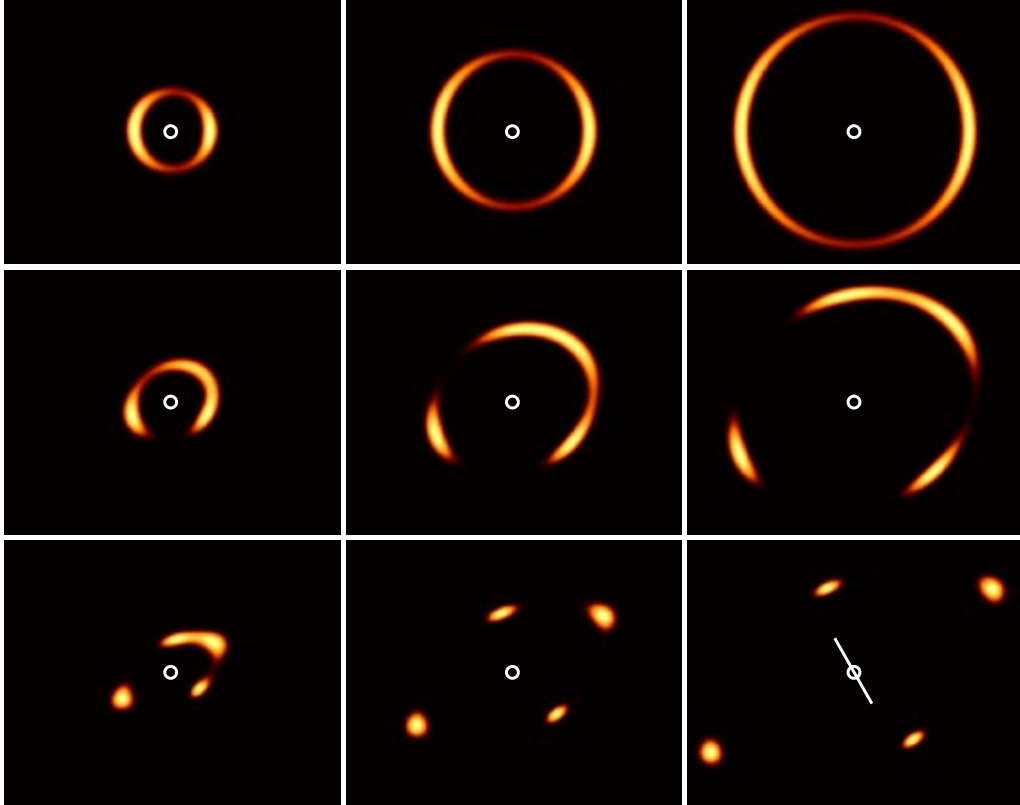


Figure 4.3: Effect of increasing surface density  $\kappa$  and shear  $\gamma$  on the images of a lensed background source. The white circles indicate the position of the lens. The surface density is increased from left to right. The external shear added to the lens model is increased from top to bottom. The white line in the last panel points in the direction of the mass concentration responsible for the external shear. The shape distortions of the images are due to the shear (internal plus external), whereas the magnification (the change in size) is caused by both isotropic focusing due to the local surface mass density  $\kappa$  and anisotropic focusing due to the shear  $\gamma$ .

So far, we have considered isolated lenses. However, several studies (e.g., Momcheva et al., 2006; Williams et al., 2006) have revealed that approximately two out of three lensing galaxies are located in galaxy groups. This additional mass distribution will disturb the gravitational potential of the lens. In most cases the disturbers are located far enough to only have very small contributions to the total surface mass density, but they will

nevertheless contribute to the tidal gravitational field, i.e. they will add shear to the lensing potential. To account for such perturbations, models of a perturbed gravitational lens have to include an external shear, cf. Section 4.11. The effect of external shear on the lensed images are illustrated in Fig. 4.3.

## 4.8 Properties of ordinary images

We have seen that images of a lensed source form at stationary points of the arrival-time surface  $\tau(\boldsymbol{\theta})$ . These stationary points can be of three types: either minima, maxima, or saddle points. When the lensed source is intrinsically variable, its flux variations will be observed first at a minimum, then at a saddle point, and finally at a maximum. If there are several stationary points of the same type, the image located the farthest away from the lens will be leading. Examples of stationary points together with contours of the arrival-time surface, called isochrones, are illustrated in Fig. 4.4.

When the lens is absent, the isochrones are circular and the image is located at the central minimum. For a small lensing mass, the shape changes slightly and the minimum moves a little. But for large enough mass, a qualitative change occurs: contours become self-crossing and produce more and more images. Each self-crossing produces two new images, one saddle point and one minimum or maximum. Lensed quasars are typically in three or five-image configurations. Both cases have one maximum located at the center of the lensing galaxy. Since galaxies tend to have sharply-peaked central densities, the central maximum is highly demagnified and is almost always unobservable. Thus, the observed lensed quasars are mostly doubles or quads, with one incipient image hiding at the center of the lens.

Other image properties are related to the magnification factor  $\mu(\boldsymbol{\theta})$ , which is given by the following expression

$$\mu(\boldsymbol{\theta}) = \left[ \det \frac{\partial \boldsymbol{\beta}(\boldsymbol{\theta})}{\partial \boldsymbol{\theta}} \right]^{-1} = \frac{1}{(1 - \kappa)^2 - \gamma^2} .$$

The determinant can have either sign. This sign is called the parity of an image. Schneider et al. (1992) summarize the different characteristics of each of the three types of stationary points.

- Minima have positive parity, the smallest time delays,  $\gamma < 1 - \kappa \leq 1$ , and thus,  $\kappa < 1$  and  $\mu \geq 1$ . The last inequality indicates that an image located at a minimum is magnified. At a minimum, both eigenvalues of  $\mathcal{A}$  are positive.
- Saddle points have negative parity, i.e.  $(1 - \kappa)^2 < \gamma^2$ , and are therefore mirror-symmetric images of the source. At a saddle point, the matrix  $\mathcal{A}$  has one positive and one negative eigenvalue.
- Maxima have positive parity and the largest time delays. They verify  $(1 - \kappa)^2 > \gamma^2$  and  $\kappa > 1$ . At a maximum, both eigenvalues of  $\mathcal{A}$  are negative.

## 4.9 Critical curves and caustics

Critical curves define the positions in the image plane where the magnification  $\mu(\boldsymbol{\theta})$  is infinite. However, this divergence does not mean that the image of a source is actually

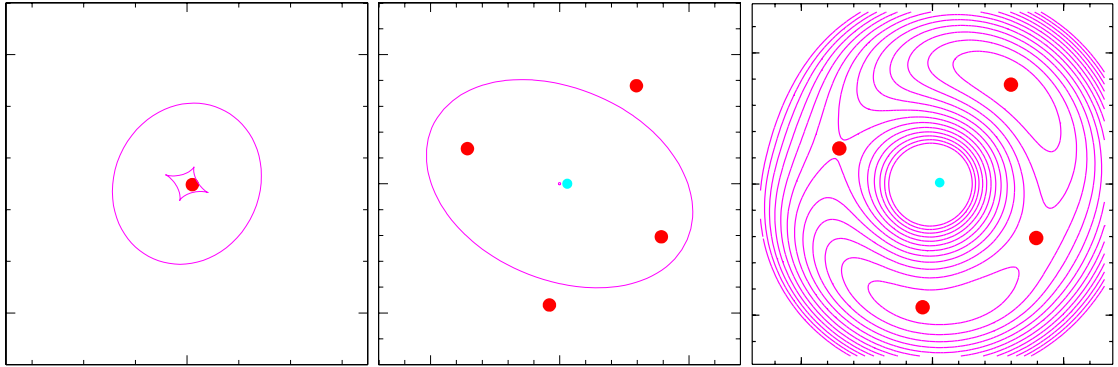


Figure 4.4: A model of the lensed quasar QSO 2237+0305. The panels are centered on the lens. *Left*: Source position and caustics. *Middle*: Image positions and critical curves. The central image is highly demagnified and is not observed. *Right*: Image positions and arrival-time contours (i.e. isochrones). The central image is located at the maximum of the arrival-time surface. Two images are located at minima and two others at saddle points of the arrival-time surface. The left panel (showing the source plane) has a scale half that of the other panels.

infinitely bright, because real sources are extended, i.e. for such source, the magnification is the weighted mean of  $\mu$  over the source (see Chapter 7). This always leads to finite magnifications.

If we map critical curves back to the source plane via the lens equation, we get caustic curves. Caustics separate regions on the source plane that give rise to different numbers of images. An illustration is given in Fig. 4.4. In this figure, the source is well within the inner caustic, and this results in five images. The image near the center is highly demagnified and observationally such a system would be a quad. Note that the inner caustic in the source plane maps the outer critical curve in the image plane.

For axially symmetric lenses (e.g., the point mass) the outer critical curve is a circle with radius of one Einstein angle  $\theta_E$ . This circle corresponds to the inner caustic that degenerates into a point: the origin  $\beta = \mathbf{0}$  in the source plane. This degeneracy occurs solely due to the highly symmetric situation of the lens model and thus, any slight perturbation of the mass distribution will unfold this caustic point into a caustic curve of finite extent. The inner critical curve has a corresponding outer caustic in the source plane, that is a circle.

## 4.10 The mass-sheet degeneracy

Modeling of a given lens is essential for most applications of gravitational lensing (e.g., the determination of  $H_0$ ). The models must fulfill several observational constraints that we briefly review in the case of strong lensing.

Suppose we observe a multiply-lensed source with  $N$  images, then the image positions  $\theta_i$  yield  $2(N - 1)$  independent constraints. If detected, the position  $\theta_l$  of the lensing galaxy adds 2 more constraints. Further constraints are the  $N - 1$  time-delays and  $N - 1$  flux ratios  $\mu_i/\mu_j$ . Note, however, that the measured flux ratios can not always be used because microlensing by stars in the lensing galaxy can produce additional (de-)magnification

of the lensed images. If we want to use the model to estimate  $H_0$  from the time-delay method, then at least one time delay has to be subtracted from the total number of constraints. Hence, in total there are  $4N - 3$  observational constraints at best. In practice, we may lack some of these constraints and the total number is often smaller than that.

Given the small number of observational constraints, especially for doubly-lensed sources, it is quite easy to find a model for the lens that fits the observations. The problem is that this model is generally not unique. A particular difficulty is the so-called mass-sheet degeneracy (Falco et al., 1985).

Let  $\kappa(\boldsymbol{\theta})$  be a mass distribution which provides a good fit to the observables. Then the whole family of lens models

$$\kappa_\lambda(\boldsymbol{\theta}) = (1 - \lambda) + \lambda\kappa(\boldsymbol{\theta})$$

provides an equally good fit to the data. The first term corresponds to adding a homogeneous mass density  $(1 - \lambda)$  to the mass distribution, whereas the second term is a rescaling of the initial mass distribution  $\kappa$ . The lens equation corresponding to  $\kappa_\lambda$  reads

$$\boldsymbol{\beta} = \boldsymbol{\theta} - \boldsymbol{\alpha}_\lambda(\boldsymbol{\theta}) \quad \text{with} \quad \boldsymbol{\alpha}_\lambda(\boldsymbol{\theta}) = (1 - \lambda)\boldsymbol{\theta} + \lambda\boldsymbol{\alpha}(\boldsymbol{\theta}) \quad \Rightarrow \quad \frac{\boldsymbol{\beta}}{\lambda} = \boldsymbol{\theta} - \boldsymbol{\alpha}(\boldsymbol{\theta})$$

so that the lens equation for  $\kappa_\lambda$  has the same form that for  $\kappa$ , except that the coordinates in the source are multiplied by  $1/\lambda$ . However, this rescaling has no consequence, since the unlensed source position is not observable. The magnifications behave as  $\mu_\lambda(\boldsymbol{\theta}) = \mu(\boldsymbol{\theta})/\lambda^2$ , but as only magnification ratios are observed, this can not be detected observationally. The shear is also rescaled  $\gamma_\lambda(\boldsymbol{\theta}) = \lambda\gamma(\boldsymbol{\theta})$ , but this also has no observable effects on the image geometries.

The only observables that are changed by the transformation  $\kappa \rightarrow \kappa_\lambda$  are the time delays. If we know the value of  $H_0$  from other cosmological observations, we can break the mass-sheet degeneracy and determine the absolute surface mass density. However, the situation becomes more problematic if the goal is to estimate  $H_0$ . If nothing sets an absolute scale for the source (e.g., we know its intrinsic luminosity) or an absolute mass scale (e.g., from its dynamics), one can not distinguish the model described by  $\kappa$  from the one described by  $\kappa_\lambda$ . One possible solution to break this mass-sheet degeneracy is given when sources with different distances  $D_s$  are lensed by the same object, because  $\Sigma_{\text{crit}}$  depends on  $D_s$ . This situation is rare for strongly lensed sources and there are only few examples (e.g., Gavazzi et al., 2008).

## 4.11 Modeling gravitational lenses

In Section 4.3, we have already described the point-mass lens and have shown that the deflection angle of a more general mass distribution can be computed from

$$\hat{\boldsymbol{\alpha}}(\boldsymbol{\xi}) = \frac{4G}{c^2} \int \frac{\Sigma(\boldsymbol{\xi}') (\boldsymbol{\xi} - \boldsymbol{\xi}')}{\|\boldsymbol{\xi} - \boldsymbol{\xi}'\|^2} d^2\xi'.$$

For some relatively simple mass distributions, analytical expressions can be obtained. The simplest lens models are obtained when their projected mass distribution is axially symmetric, i.e.  $\Sigma(\boldsymbol{\xi}) = \Sigma(\xi)$  with  $\xi = \|\boldsymbol{\xi}\|$ . In this case the deflection angle reads

$$\hat{\boldsymbol{\alpha}}(\boldsymbol{\xi}) = \frac{4G M(\xi)}{c^2 \xi} \frac{\boldsymbol{\xi}}{\|\boldsymbol{\xi}\|}$$



where  $M(\xi)$  is the mass enclosed within radius  $\xi$ . For more complicated lens models, the integral has to be solved numerically. There are two different families of models considered: parametric models (e.g., Keeton, 2001b) and pixelized models (e.g., Saha & Williams, 2004). We present first some of the most commonly used parametric models and describe some pixelized models afterwards.

### The Singular Isothermal Sphere

A simple lens model which applies, at least to first order, to the lensing properties of galaxies and galaxy clusters is the so-called Singular Isothermal Sphere (SIS). This model describes a spherical mass distribution where the velocity distribution at all radii is Maxwellian with a one-dimensional velocity dispersion  $\sigma_v$  (hence, the term isothermal). The spatial density and corresponding surface mass density are

$$\rho(r) = \frac{\sigma_v^2}{2\pi G r^2} \quad \Rightarrow \quad \Sigma(\xi) = \frac{\sigma_v^2}{2G} \frac{1}{\xi}$$

which yields the projected mass  $M(\xi)$  within radius  $\xi$ , and the deflection angle  $\hat{\alpha}(\xi)$

$$M(\xi) = 2\pi \int_0^\xi \Sigma(\xi') \xi' d\xi' = \frac{\pi \sigma_v^2 \xi}{G} \quad \Rightarrow \quad \hat{\alpha}(\xi) = 4\pi \left(\frac{\sigma_v}{c}\right)^2 \frac{\xi}{\|\xi\|}.$$

Note that the magnitude of  $\hat{\alpha}$  is constant. The Einstein angle of this lens model is

$$\theta_E = 4\pi \left(\frac{\sigma_v}{c}\right)^2 \frac{D_{ls}}{D_s} = 1.15'' \left(\frac{\sigma_v}{200 \text{ km/s}}\right)^2 \frac{D_{ls}}{D_s}$$

from which we conclude that the angular scale of the lens effect in galaxies is about an arcsecond. In terms of the Einstein angle we have

$$\kappa(\theta) = \gamma(\theta) = \frac{\theta_E}{2\|\theta\|}; \quad \hat{\alpha}(\theta) = \theta_E \frac{\theta}{\|\theta\|}; \quad \beta(\theta) = \theta - \theta_E \frac{\theta}{\|\theta\|}; \quad \mu(\theta) = \frac{\|\theta\|}{\|\theta\| - \theta_E}.$$

Limitations to the SIS are the central singularity and the infinite total mass. The SIS is therefore strictly speaking unphysical, but it is nevertheless commonly used in the literature due to the simplicity of its form, and to the fact that it reproduces the basic properties of lens systems (such as image separation) quite well.

### De Vaucouleurs model

De Vaucouleurs' law is perhaps the most widely used empirical law to describe the surface brightness profile of an elliptical galaxy (de Vaucouleurs, 1953). This law describes lens models where the mass distribution is assumed to follow the distribution of light. Thus, these models have a constant mass-to-light ratio with a surface mass density

$$\Sigma(\xi) = \Sigma_e \exp \left( -7.67 \left[ \left( \frac{\xi}{r_e} \right)^{1/4} - 1 \right] \right).$$

The scale length  $r_e$ , known as the effective radius, contains half of the total mass (or light) of the galaxy. De Vaucouleurs' law, also known as the  $r^{1/4}$  law (because  $\log(\Sigma(\xi)) \propto \xi^{1/4}$ ), is empirical in nature, and does not necessarily fit all elliptical galaxies over all ranges.

## NFW model

Navarro, Frenk, & White (1996, 1997) performed  $N$ -body cosmological simulations to study the density profiles of dark matter halos. They found that all such profiles have the same shape independently of the halo mass, the initial density fluctuation spectrum, and the values of the cosmological parameters. Their profiles are well fitted by the simple formula

$$\rho(r) = \rho_s \left[ \frac{r}{r_s} \left( 1 + \frac{r}{r_s} \right)^2 \right]^{-1}.$$

This profile has a central singularity and a scale radius  $r_s$  at which the slope of the profile changes from  $\rho(r) \propto r^{-1}$  close to the center to  $\rho(r) \propto r^{-3}$  at larger radii.

## Non-axisymmetric models with external shear

More complicated non-axisymmetric profiles are often used to describe the mass profile of real lenses, even though the lens equation may no longer have analytical solutions. Breaking the symmetry leads to qualitatively new properties of the lens. Most obvious of them, the central caustic (which is degenerated in a point for axisymmetric models) gets unfolded into a curve of finite size. A source situated inside this curve can then have five images. Observationally this would be a quad, as the central fainter image is generally not observed.

Simple non-axisymmetric models are those with two lines of symmetry, such as an ellipse has. Examples are mass distributions where  $\kappa$  is constant on (confocal) ellipses (e.g., Bourassa & Kantowski, 1975; Schramm, 1990), i.e. the surface mass density has the form  $\kappa = \kappa(\zeta)$  with  $\zeta^2 = \theta_x^2 + \theta_y^2/q^2$ , where  $0 < q < 1$  is the projected axis ratio and  $\zeta$  is an ellipse coordinate<sup>1</sup>. For analytic simplicity, it is sometimes more convenient to put the elliptical symmetry in the potential, rather than in the density (e.g., Blandford & Narayan, 1986; Witt & Mao, 1997). However, one should keep in mind that elliptical potentials correspond to unphysical matter distributions if the ellipticity is large (Kormann et al., 1994).

In general, real gravitational lenses are rarely isolated (e.g., Momcheva et al., 2006; Williams et al., 2006) and local structures, such as a group of galaxies, can perturb the lensing potential. In most cases the disturbers are located far enough to only have small contributions to the lensing potential  $\psi(\boldsymbol{\theta})$ . The additional potential  $\psi_{\text{ext}}(\boldsymbol{\theta})$  induced by the external perturbations can therefore be Taylor expanded around the lens position. To the second order, the perturbations are approximated by (Keeton, 2001a)

$$\psi_{\text{ext}}(\boldsymbol{\theta}) \simeq \frac{1}{2} \|\boldsymbol{\theta}\|^2 (\kappa_{\text{ext}} - \gamma_{\text{ext}} \cos [2(\phi - \phi_\gamma)])$$

where  $\kappa_{\text{ext}}$  is the convergence of the external perturbation,  $\gamma_{\text{ext}}$  is the strength of the induced external shear and  $\phi_\gamma$  indicates the “direction” of the external shear. Note that this angle is not a standard polar angle, but it is inserted so that the shear angle points toward the mass concentration producing the shear. The constants  $\kappa_{\text{ext}}$ ,  $\gamma_{\text{ext}}$ , and  $\phi_\gamma$  are evaluated at the position of the lens. The term  $\kappa_{\text{ext}}$  is equivalent to a uniform mass sheet with density  $\Sigma/\Sigma_{\text{crit}} = \kappa_{\text{ext}}$ . The only observable effect of  $\kappa_{\text{ext}}$  is to rescale the time delays by  $(1 - \kappa_{\text{ext}})$ , which leads to the mass-sheet degeneracy discussed in the previous

<sup>1</sup>The ellipse is centered on the origin and aligned along the  $\theta_x$ -axis

section; hence, this term is often omitted from lens models and introduced a posteriori using independent mass constraints (e.g., Bernstein & Fischer, 1999).

The addition of an external shear improves noticeably the modeling of most gravitational lenses. However, it can be difficult to disentangle the effects of the external perturbations and those of the ellipticity, and it is important to understand any degeneracies between the two sources of angular structure before drawing conclusions from the models (Keeton et al., 1997).

## Non-parametric pixelized models

Gravitationally lensed quasars provide only few observational constraints, which are in general inadequate by themselves to provide a unique reconstruction of the galaxy mass. As a consequence, the usual methodology is to model the lens with simple parametric models, but this strongly limits the number of considered mass distributions of the lens and results in large systematic errors in the determination of the Hubble constant. An alternative approach is to use non-parametric models, such as pixelized models (Saha & Williams, 1997; Williams & Saha, 2000), where each pixel is an independent mass element. These models have a large number of degrees of freedom ( $\sim 1000$ ) and thus, can better explore physically plausible mass distributions, all of which reproduce the lensing observables exactly. The disadvantage of this technique lies in the fact that it is an underconstrained problem, and one ends up with a multitude of mass models reproducing the observables. However, one can treat this ensemble of models statistically and derive probability distribution for the parameters of interest (e.g.,  $H_0$ ). One can even go further and combine the probability distributions obtained from different lensed quasars to get a simultaneous determination of  $H_0$  (e.g., Coles, 2008).

## 4.12 Microlensing

In the previous sections, we have seen how a large mass distribution, like a galaxy, can act as a gravitational lens. But smaller masses like stars or compact objects (e.g., black holes, brown dwarfs, planets, etc.) can also act as lenses. The deflection of light and hence, the angular separation between the lensed images of a background source are proportional to the square-root of the mass of the lens. For stellar mass objects, this implies that the image separation is typically of the order of one milli- or micro-arcsecond, hence the term microlensing introduced by Paczyński (1986a). Such small angular separations can not be resolved with current instruments, and the micro-images form one single unresolved (de-)magnified image. The only observable effect of microlensing is the global (de-)magnification of the lensed source, which can reach several magnitudes. A very interesting property of microlensing is that it is a dynamical phenomenon. The relative motions between the observer, the source, and the microlens induce flux variations on time-scales of a few days to several months depending on the lensed system. These evolving brightness fluctuations are called microlensing events.

Microlensing occurs essentially on two different distance scales, either on galactic or cosmological scales. In the context of this thesis, we will focus on cosmological microlensing, but we briefly mention some applications of galactic microlensing that have conducted to recent impressive results. Galactic microlensing involves a compact object situated in our Galaxy passing in front of a background source, usually a star, located either in our

Galaxy or in a nearby galaxy, like the Large Magellanic Cloud. Paczyński (1986b) proposed to use such microlensing situations as a mean to detect dark matter candidates in the form of massive compact halo objects (MACHOs). MACHOs are bodies too small to produce their own energy by fusion and might be brown dwarfs, planets, neutron stars, old white dwarfs, or black holes. In 1993, three different teams (MACHO, EROS, and OGLE) obtained the first lightcurves of galactic microlensing events and found several low-mass stars acting as microlenses (Alcock et al., 1993; Aubourg et al., 1993; Udalski et al., 1993). The search for MACHOs is still going on, and thousands of microlensing events in our Galaxy have already been observed. The statistics of these detected dark objects rule out the possibility that low-mass stars make up a significant fraction of dark matter in our Galaxy. Another important application of galactic microlensing is the search for extrasolar planets, as first mentioned by Mao & Paczyński (1991). The advantage of microlensing over other methods (e.g., radial velocities or transits) is its higher sensitivity to low-mass planets. Recently, Beaulieu et al. (2006) detected one of the smallest known extrasolar planets with only 5.5 Earth masses.

Cosmological microlensing differs from galactic microlensing in the sense that it does not involve one but many microlenses simultaneously. The effect of a whole galaxy acting as a lens on a background source (e.g., a quasar) is usually described by a smooth potential created by a continuous mass distribution. This mass distribution produces the observed multiple (de-)magnified macro-images of the source. The individual stars and compact objects of the galaxy introduce a graininess into the potential, which influences the macro-images. As described above, the microlenses produce an additional (de-)magnification of the images, which varies in time due to the relative motion of the microlenses. These flux variations are extrinsic to the background source and affect each macro-image independently. As a consequence, microlensing is often regarded as a source of noise in studies where the goal is to measure the time delays between the macro-images (e.g., to determine the Hubble constant). However, cosmological microlensing can also be treated as a very interesting source of information from which one can determine the size (e.g., Wambsganss et al., 1990b; Yonehara, 2001) and shape (e.g., Mineshige & Yonehara, 1999) of the background source, as well as the transverse velocity of the lensing system (e.g., Gil-Merino et al., 2005) and mean mass of the microlenses (e.g., Kochanek, 2004). More details on these methods are given in Chapter 7.

**Part II**  
**COSMOGRAIL**



*“You may delay, but time will not.”*  
*Benjamin Franklin (1706 - 1790)*

# Chapter 5

## Measuring time delays

### 5.1 Introduction

The Hubble constant  $H_0$  is a particularly important parameter in Friedmann-Robertson-Walker (FRW) cosmologies (e.g., the concordance model), because it sets the length and timescale of the Universe. Cosmological distances are directly proportional to  $H_0^{-1}$ , and a large uncertainty in  $H_0$  implies that we are unable to precisely determine the distances to any distant extragalactic object. This has dramatic consequences on the estimation of other cosmological parameters such as the energy densities  $\Omega_{m0}$  and  $\Omega_{\Lambda0}$ . For instance, the analysis of the WMAP data provides a well defined relation between  $\Omega_{m0}$  and  $\Omega_{\Lambda0}$  (Spergel et al., 2007, see Fig 2.4), but the actual determination of these values depends on the value of  $H_0$ .

Numerous techniques have been developed to determine  $H_0$ , and we have reviewed some of the commonly used methods in section 2.10. The major drawback of these methods is that they use standard candles as distance calibrators, which increases the systematic errors of the inferred value of  $H_0$ . Currently, the best estimation of the Hubble constant using these techniques is obtained by the HST Key Project  $H_0 = 72 \pm 8 \text{ km s}^{-1} \text{ Mpc}^{-1}$  (Freedman et al., 2001) with uncertainties larger than 10%. Considering the efforts and amount of telescope time necessary to accomplish a program like the Key Project, it is clear that a better estimation of  $H_0$  will be very difficult to reach with methods based on secondary distance indicators.

An alternative approach is offered by gravitational lensing and has the potential to increase the precision of  $H_0$  determinations by as much as one order of magnitude (Kochanek & Schechter, 2004) through the so-called time-delay method (Refsdal, 1964a). This method is based on the property that any intrinsic variability of a lensed source is observed at different times in the lensed images, and that the observed time delays between the images are proportional to  $H_0^{-1}$ . Hence, the Hubble constant can be determined at truly cosmological distances and independently of any standard candles or local distance calibrators.

At the beginning of this thesis in 2004, there were ten lensed quasars with measured time delays, of which nine gave  $H_0$  estimates (see Kochanek & Schechter, 2004). Unfortu-

nately, these time delays had uncertainties of the order of 10%, and hence they could not give competitive  $H_0$  estimates. To fully exploit the potential of gravitational lensing, it is imperative to reduce the uncertainties of the measured time delays by devising a dedicated and long-term monitoring program, in order to increase both the frequency and quality of the observations.

### 5.1.1 Observational and theoretical challenges

Although the time-delay method was published in 1964 by Sjur Refsdal, no concerted and long-term program has succeeded to implement the method at a level of precision really competitive with other techniques. There are several reasons for this. In Section 4.6, we saw that the theoretical expression for the time delay between two lensed images A and B is given by

$$\Delta t_{B-A} = \frac{1+z_l}{c} \frac{D_l D_s}{D_{ls}} \left( \frac{1}{2}(\boldsymbol{\theta}_B - \boldsymbol{\beta})^2 - \frac{1}{2}(\boldsymbol{\theta}_A - \boldsymbol{\beta})^2 - \psi(\boldsymbol{\theta}_B) + \psi(\boldsymbol{\theta}_A) \right)$$

where the  $D$ 's are angular-diameter distances proportional to  $H_0^{-1}$ . From this equation, we immediately see that a precise determination of  $H_0$  from the time-delay method requires the following input

1. the astrometry  $\boldsymbol{\theta}_A$  and  $\boldsymbol{\theta}_B$  of the lensed images relative to the lens position,
2. the time delay  $\Delta t_{B-A}$  between the lensed images,
3. the redshifts  $z_s$  and  $z_l$  of the source and the lens, respectively,
4. the gravitational potential  $\psi(\boldsymbol{\theta})$  (i.e. the mass distribution) of the lens.

Note that the true position  $\boldsymbol{\beta}$  of the unlensed source is not an observable and is determined from the lens model  $\psi(\boldsymbol{\theta})$ , which should reproduce the observed image positions.

An accurate determination of  $H_0$  is only possible if all four points are addressed. Although the astrometry of most gravitational lenses is now sufficiently well measured, with precisions reaching a few milli-arcseconds (Kochanek, 2003a), the other three points remain challenging. The required precision for time-delay measurements is of the order of a few percents, whereas the typical accuracy reached by past monitoring programs is five to ten times larger. Reasons for this are the high spatial resolution required to separate the quasar images, extrinsic variability induced by stellar microlensing, and the small amplitude of quasar intrinsic variability (a few tenths of a magnitude). An additional difficulty is the measurement of the lens redshift  $z_l$ , because the lens is often hidden by the glare of the much brighter quasar images. In these cases, deep spectroscopy with high spatial resolution is necessary (see Chapter 6).

Besides these observational challenges, there are also theoretical ones. The modeling of the lens potential has proven to be difficult, because of the paucity of observational constraints, and because of the perturbations induced by nearby structures like galaxy groups (Schechter, 2005). The non-uniqueness of lens models reproducing the observables is also an important issue, as it has led to contradictory results known as the central concentration problem (see Chapter 8).

To summarize and in order to reach the target accuracy of a few percent on  $H_0$ , it is mandatory to : (1) increase the precision of time-delay measurements, (2) determine the lens and source redshifts, and (3) improve the lens models. We will discuss each of these points more specifically in the following chapters.



### 5.1.2 The COSMOGRAIL project

The COSmological MOnitoring of GRAvItational Lenses (COSMOGRAIL, Courbin et al., 2005) started in April 2004 with the aim of measuring time delays for over twenty known lensed quasars and to evaluate  $H_0$  with a precision of a few percent. Accurate time-delay measurements are particularly demanding observationally, because the quasar images have small angular separations (typically of one arcsecond). Such separations require a spatial resolution of a few tenths of an arcsecond, which is reached by space telescopes like the Hubble Space Telescope (HST) or by large ground-based telescopes like the Very Large telescope (VLT). However, conducting a large monitoring program like COSMOGRAIL on such highly demanded telescopes is unrealistic, and smaller telescopes of the 1m or 2m class should be considered. The lower resolution of these telescopes imply that accurate photometry of blended objects, sometimes with several quasar images plus the lensing galaxy within the seeing disk, has to be performed. This difficult task is overcome with numerical methods such as the MCS deconvolution algorithm (Magain et al., 1998) described in Section 6.2. This algorithm increases the spatial resolution and assures that the quasar images are spatially separated and deblended, leading to accurate photometry.

A monitoring campaign like COSMOGRAIL requires large amounts of observing time, which are acquired with five different telescopes all located on sites with exceptional observing conditions (see Fig. 5.1). Before starting the observations, there are several issues that need to be addressed. The first one is the selection of the targets. Not every lensed quasar is suited for an accurate time-delay measurement. To determine which lens systems are best suited for the project, Saha et al. (2006) modeled fourteen lensed quasars using pixelized lens models. These models give an estimation of the expected time delay, which helps to optimize the observational strategy, i.e. at which frequency a given lensed quasar should be observed to use the available telescope time in the most optimal way.

Once the targets and observational strategy are defined, the observation campaign can start and, after a few months or years of monitoring, accurate lightcurves are obtained for the lensed quasar images. These curves are then cross-correlated to determine the time delays and evaluate  $H_0$  from the time-delay method.

## 5.2 Determination of the optimal sampling of observations

The lightcurves of the images of a lensed quasar are generally shifted in time and in magnitude due to both the different geometrical paths followed by the light and the time dilation caused by the gravitational potential of the lensing galaxy (see Section 4.6). Measuring the time delay is, for several reasons, not a trivial task. First it requires regular monitoring of the target over a long period (substantially longer than the time delay). Second, most objects are not observable during the whole year, i.e., they will be below the horizon for certain periods of the year. Third, there are nights with bad weather conditions when no data can be obtained. Fourth, variations in lensed quasars may not only be due to intrinsic fluctuations of the quasar, but also to microlensing by compact objects along the line of sight. Such a microlensing signal, depending on its timescale and amplitude, can be used to constrain the spatial structure in the quasar (see Chapter 7). But as long as these extrinsic variations are not clearly distinguished from the intrinsic variations, microlensing remains a nuisance for time delay measurements. Finally, the sampling of the observations is crucial and has to be determined on basis of the intrinsic variations in the quasar and the time delay estimated from the lens models (e.g., Saha et al., 2006).

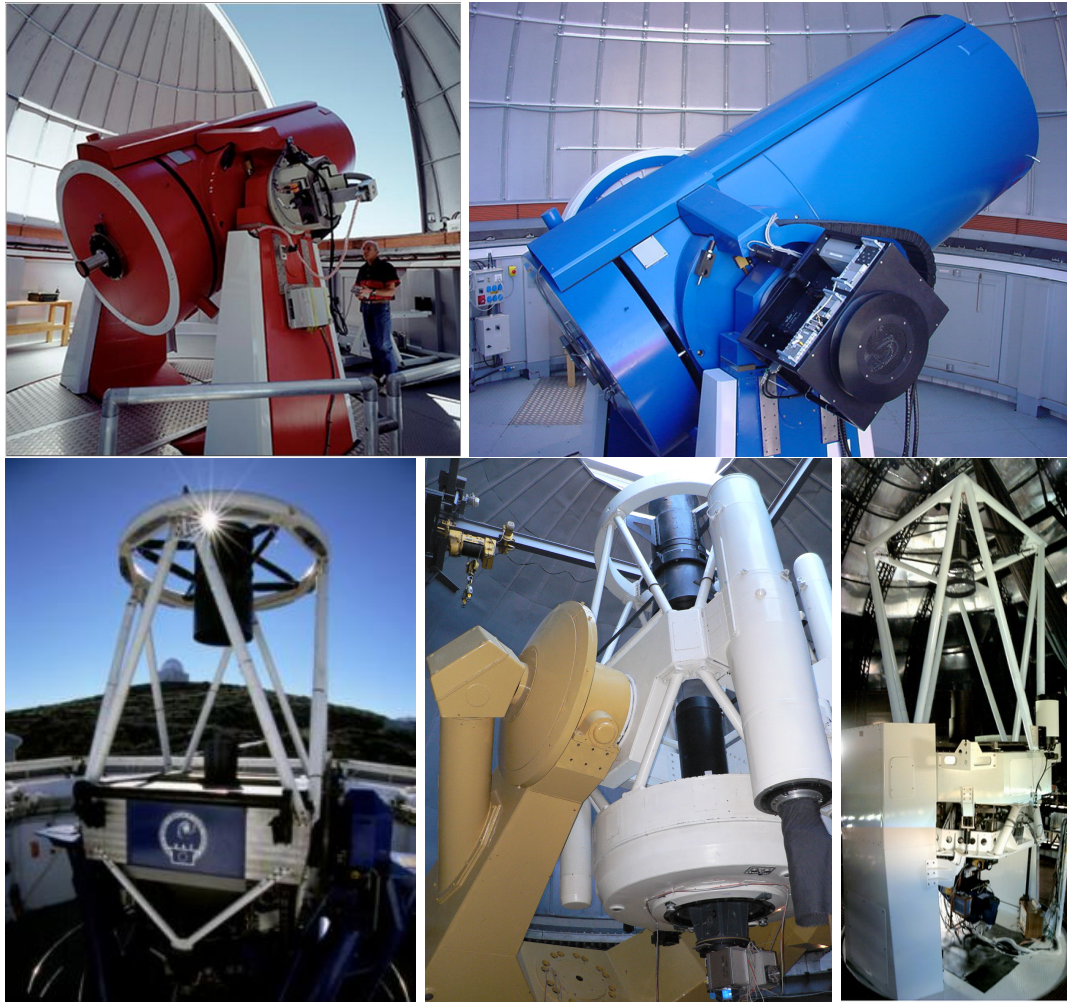


Figure 5.1: The five telescopes involved in the COSMOGRAIL project. *From left to right, and top to bottom:* (1) the Swiss 1.2m Euler telescope located at the European Southern Observatory of La Silla, Chile, (2) the Swiss-Belgian 1.2m Mercator telescope located on the Canarian island of La Palma, Spain, (3) the 2m robotic telescope of the Liverpool University (UK) also on La Palma, (4) the 1.5m telescope of the Maidanak Observatory in Uzbekistan, (5) the 2m Himalayan Chandra Telescope of the Indian Astronomical Observatory in Hanle.

Even though large amounts of telescope time are available for the COSMOGRAIL project, it is of great interest to use this time in the most optimal way, as this increases the number of lensed quasars that can be monitored simultaneously. Thus, for each individual target a specific optimal temporal sampling has to be adopted for the observations. This optimal sampling is determined from numerical simulations, which create artificial datasets that allow to test the efficiency of various observing strategies. The goal is to obtain, with the smallest number of observations, a time-delay estimation with a precision of a few percent.

### 5.2.1 Simulation of lightcurves

In order to produce realistic simulations we define several parameters, starting with the characteristics of the quasar lightcurves, which are the amplitude and timescale of the intrinsic variability. Typical values are found from the observed variability of unlensed quasars (e.g., Hook et al., 1994). Based on these values, we create a continuous lightcurve simulating the intrinsic variability of a quasar. We then shift this lightcurve by a given time delay  $\Delta t_{in}$ , and interpolate the shifted and unshifted lightcurves at selected observing dates. This produces the simulated lightcurves of two lensed quasar images.

The dates of the observations are determined following both a selected observing strategy and a chosen visibility of the object along the year. We test four observing strategies with different sampling rates: every three days, every seven days, every fifteen days, and a fourth irregular one. The visibility of a lensed quasar depends on its declination, e.g., equatorial objects are visible during roughly 5 months, whereas circumpolar objects are visible all year. Finally, and, to be more realistic, we add some noise to the simulated observations in the form of a Gaussian deviate having 0.01 mag standard deviation. This is a reliable estimate of the expected accuracy of the COSMOGRAIL telescopes (Vuissoz et al., 2007).

### 5.2.2 Extracting the time delay

Once, the lightcurves of the quasar images are simulated, we want to recover the input time delay  $\Delta t_{in}$ . Many techniques are available for this task, with a variety of technical subtleties dealing with unstable solutions, sparse sampling, and the effect of additional perturbations of the lightcurves such as those caused by microlensing (e.g., Press et al., 1992; Pelt et al., 1994; Beskin & Oknyanskij, 1995; Kundić et al., 1997; Burud et al., 2001). The aim of the present study is to decide which observing strategy will assure to recover the value of the input time delay within a few percent, rather than testing the techniques themselves. For this reason, we have adopted the cross-correlation method of Pelt et al. (1994, 1996), also called the minimum dispersion ( $D^2$ ) method. This method is widely used and combines robustness, simplicity, and low cost in terms of computing time. More elaborated methods may be more efficient, so that our results can be considered as lower limits on the accuracy that can actually be achieved by using a given set of lightcurves.

The minimum dispersion method can be summarized as follows: the lightcurve  $b(t)$  of one image, e.g., image B, is shifted by a trial time delay  $\Delta t$  and compared to the lightcurve  $a(t)$  of the other image, e.g., image A. The point is to find which curve  $b(t - \Delta t)$  best matches the curve  $a(t)$  within the overlap region. For any curve  $b(t - \Delta t)$  the overlap region is defined as the set of points for which there exist points in curve  $a(t)$ , both before and after in time. Curve  $a(t)$  is then linearly interpolated to these points, and the dispersion  $D^2(\Delta t)$  in the magnitude differences between the two curves provides the measure of goodness of fit. The time delay  $\Delta t_{out}$  between the curves is defined as the value that minimizes the dispersion  $D^2$ .

### 5.2.3 Results

For every input time delay  $\Delta t_{in}$ , we explore a range of different combinations of observing conditions and strategies. For each combination, we run  $10^5$  simulations, each time changing the artificial quasar lightcurve and adding randomly distributed errors to the simulated observations, i.e. normally distributed deviates of 0.01 mag variance. From

these  $10^5$  simulations, we obtain a distribution of the measured time delay  $\Delta t_{out}$ . The ratio between the standard deviation and the mean of this distribution defines the accuracy that can be expected for the adopted observing strategy in the chosen observing conditions.

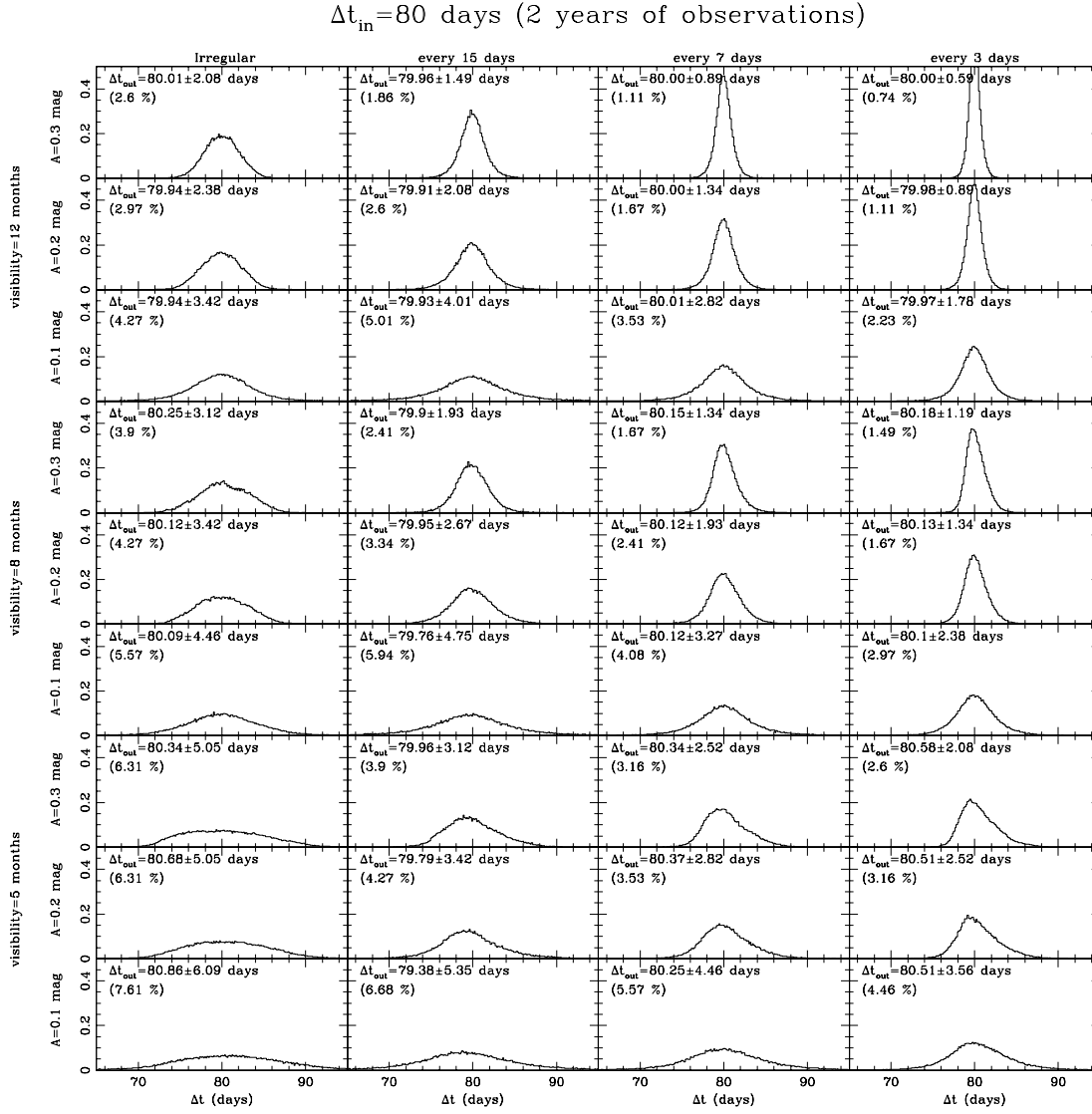


Figure 5.2: Histograms exploring the observational parameter space for the determination of a time delay of 80 days. Each curve is the probability density function for the time delay, obtained from  $10^5$  simulations, for a particular combination of the three parameters: (1) *sampling interval*, four columns, from left to right: irregular, 15 days, 7 days, 3 days), (2) *visibility period*, three bands from top to bottom: 12, 8, and 5 months, and (3) *peak-to-peak variation*  $A$  of the quasar lightcurve, three rows within each band, from top to bottom, : 0.3, 0.2, 0.1 mag. Each panel is labeled with the mean and standard deviation of the measured time delay, as well as the percentage error. The effect of microlensing is not included in these simulations.

We apply this procedure to input time delays  $\Delta t_{in}$  from 5 to 120 days. The results for  $\Delta t_{in} = 80$  days are illustrated in Fig. 5.2, where the 36 panels correspond to the different combination of the parameters. In each panel, the measured time delays  $\Delta t_{out}$  are plotted in histogram form, with the measured mean and standard deviation quoted.

This first set of simulations is performed without considering the effect of microlensing by stars in the lensing galaxy. However, most quasars with measured time delays have proved to be affected by microlensing. It is hence mandatory to introduce this effect into our artificial lightcurves and to estimate how the time-delay measurements are modified. Microlensing can be simulated as an additional lightcurve with a different length scale and amplitude. We express the peak-to-peak microlensing amplitude  $A_\mu$  as a simple function of the quasar lightcurve amplitude  $A$ . We take it as  $A_\mu = \alpha \cdot A$ , with  $\alpha = 0.01, 0.05, 0.10$ , in order to mimic a microlensing amplitude of respectively 1, 5 and 10% of the amplitude of the quasar lightcurve. The microlensing curve is smoothed using a convolution kernel of 100 days, i.e. about three times slower than the intrinsic variations of the quasar, and is added to the lightcurve of one of the quasar images. The choice of this image is irrelevant because only relative differences between the lightcurves of the two components are considered to extract the time delay. We then repeat the cross-correlation analysis. The complete results of this study are given in the paper at the end of this chapter (Eigenbrod et al., 2005).

### 5.3 Discussion

We have undertaken a set of simple but realistic numerical simulations in order to optimize the observing strategy of the COSMOGRAIL monitoring program. The predicted error bars on time delays compare very well with the ones obtained in optical wavelengths with real data (see Fig. 4 in Eigenbrod et al., 2005).

From our simulations, we conclude that short time delays will never be measured with a precision better than 2%, unless the intrinsic quasar variability is substantially larger than 0.3 mag. We find that time delays between 40 and 100 days are best suited for accurate time-delay measurements, even in the presence of microlensing, and especially in the case of circumpolar objects, where one can easily achieve a 2% accuracy. We also show that, when the time delay is comparable to the visibility window of the object, a logarithmic sampling can significantly improve the time delay determination. This is no longer true when the time delay is shorter than the visibility window, where the logarithmic sampling even degrades the results.

As expected, microlensing increases the error of the measured time delays. With 5% microlensing (as defined here), the estimated error on the time delay is twice that of the no-microlensing case. Moreover, equatorial objects should be avoided. Although they are accessible from the north and south, they are visible under good conditions for only 5-6 months along the year. This makes it impossible to measure time delays larger than 100 days. For shorter time delays, the estimated error for an equatorial object is twice that of the same object if it were circumpolar.

A point that is not discussed in our study is the influence of the magnitude shift between the lightcurves of the two lensed quasar images. This shift can have a significant effect on the determination of the time delay, especially when using the minimum dispersion method (e.g., Vuissoz et al., 2007). Any measurement of a “real” time delay should therefore be concerned about this issue, and more sophisticated methods should also be considered for

the extraction of the time delay.

The present study helps to define the optimal combinations of predicted time delay, object visibility and temporal sampling, to reach a target accuracy of a few percent. In particular, it was used to define the observing strategies of the COSMOGRAIL targets. Recent results are the determination of the time delay  $\Delta t = 49.5 \pm 1.9$  days in the lensed quasars SDSS J1650+4251 (Vuissoz et al., 2007), and the time delays  $\Delta t_{(B-A)} = 35.5 \pm 1.4$  days and  $\Delta t_{(B-C)} = 62.6^{+4.1}_{-2.3}$  days in WFI 2033–4723 (Vuissoz et al., 2008). These measurements have a precision below 4%, which is twice better than the accuracy reached by previous time-delay measurements. Furthermore, as the monitoring continues, these values will improve further, together with several other COSMOGRAIL time delays that will be published soon.

Increasing the number of known time-delay lenses is important because they can be combined to yield better estimates of  $H_0$  as when they are considered individually. For instance, Oguri (2007) developed a statistical method to examine the dependence of time delays on the complexity of lens potentials. They applied their method to sixteen published time-delay quasars and found  $H_0 = 68 \pm 6$  (stat.)  $\pm 8$  (syst.)  $\text{km s}^{-1} \text{Mpc}^{-1}$ . With a different approach, Coles (2008) used pixelized models to simultaneously reconstruct eleven time-delay lenses. He inferred  $H_0 = 71^{+6}_{-8} \text{ km s}^{-1} \text{Mpc}^{-1}$ . Adding more lenses to these studies will reduce the uncertainties and should in the foreseeable future provide a new determination of  $H_0$  with unprecedented accuracy.

- 5.4 Paper presenting how to sample the lightcurves of gravitationally lensed quasars to measure accurate time delays

*COSMOGRAIL: the COSmological MONitoring  
of GRAvItational Lenses*

*I. How to sample the lightcurves of gravitationally lensed  
quasars to measure accurate time delays*

A. Eigenbrod, F. Courbin, C. Vuissoz, G. Meylan, P. Saha, and S. Dye

*Astronomy & Astrophysics, 2005, 436, 25*





## COSMOGRAIL: The COSmological MONitoring of GRAVItational Lenses

### I. How to sample the light curves of gravitationally lensed quasars to measure accurate time delays

A. Eigenbrod<sup>1</sup>, F. Courbin<sup>1</sup>, C. Vuissoz<sup>1</sup>, G. Meylan<sup>1</sup>, P. Saha<sup>2</sup>, and S. Dye<sup>3</sup>

<sup>1</sup> École Polytechnique Fédérale de Lausanne, Laboratoire d'Astrophysique, Observatoire, 1290 Chavannes-des-Bois, Switzerland

e-mail: alexander.eigenbrod@epfl.ch

<sup>2</sup> Astronomy Unit, School of Mathematical Sciences, Queen Mary and Westfield College, University of London, Mile End Road, London E1 4NS, UK

<sup>3</sup> School of Physics and Astronomy, Cardiff University, 5 The Parade, Cardiff, CF24 3YB, UK

Received 23 November 2004 / Accepted 16 February 2005

**Abstract.** We use numerical simulations to test a broad range of plausible observational strategies designed to measure the time delay between the images of gravitationally lensed quasars. Artificial quasar light curves are created along with Monte-Carlo simulations in order to determine the best temporal sampling to adopt when monitoring the photometric variations of systems with time delays between 5 and 120 days, i.e., always shorter than the visibility window across the year. Few and realistic assumptions are necessary on the quasar photometric variations (peak-to-peak amplitude and time-scale of the variations) and on the accuracy of the individual photometric points. The output of the simulations is the (statistical) relative error made on the time delay measurement, as a function of 1- the object visibility over the year; 2- the temporal sampling of the light curves; and 3- the time delay. Also investigated is the effect of long term microlensing variations which must be below the 5% level (either intrinsically or by subtraction) if the goal is to measure time delays with an accuracy of 1–2%. However, while microlensing increases the random error on the time delay, it does not significantly increase the systematic error, which is always a factor 5 to 10 smaller than the random error. Finally, it is shown that, when the time delay is comparable to the visibility window of the object, a logarithmic sampling can significantly improve the time delay determination. All results are presented in the form of compact plots to be used to optimize the observational strategy of future monitoring programs.

**Key words.** gravitational lensing – cosmological parameters – cosmology: observations

#### 1. Measuring time delays

Measuring time delays in gravitationally lensed quasars is difficult, but not as difficult as it first appeared in the late eighties when the first monitoring programs were started. Obtaining regular observing time on telescopes in good sites was (and is still) not easy and the small angular separations between the quasar images require to perform accurate photometry of blended objects, sometimes with several quasar images plus the lensing galaxy within the seeing disk.

##### 1.1. COSMOGRAIL

The COSMOGRAIL project (COSmological MONitoring of GRAVItational Lenses), started in April 2004, addresses both issues of carrying out photometry of faint blended sources and of obtaining well sampled light curves of lensed quasars.

The project involves 5 telescopes: (1) the Swiss 1.2 m *Euler* telescope located at La Silla, Chile; (2) the Swiss-Belgian 1.2 m *Mercator* telescope, located in the Canaria islands (La Palma, Spain); (3) the 2 m robotic telescope of the Liverpool University (UK), also located at La Palma; (4) the 1.5 m telescope of Maidanak observatory in Uzbekistan; and (5) the 2 m Himalayan Chandra Telescope (HCT).

All 5 telescopes, and others that will join the collaboration, are used in order to follow the photometric variations of most known gravitationally lensed quasars that are suitable for a determination of  $H_0$ . The sample of targets is described further in Saha et al. (2005), as well as the non-parametric models and predicted time delays for all of them. Our target accuracy on individual photometric points is 0.01 mag, well within the reach of a 1–2 m class telescope and average seeing (1") in a good site. This accuracy is reached even for the blended components

of lensed quasars, thanks to image deconvolution algorithms such as the MCS algorithm (Magain et al. 1998).

The results presented in the following were obtained to optimize the observations of the COSMOGRAIL project, which aims at measuring time delays, with an accuracy close to 1% within 2 years of observations (per lensed quasar).

Although large amounts of time are available for COSMOGRAIL on each telescope, optimizing the time spent on each lensed quasar, depending on its luminosity and expected time delay, remains very important. The present paper aims at optimizing the temporal sampling to adopt in order to derive accurate time delays for as many lensed quasars as possible.

The paper is organized in the following way. Section 2 describes how we simulate the light curves of the quasar images. In Sect. 3, we present which parameters of the simulated light curves are varied and in which range they are varied. In Sect. 4, we explain how the time delays are extracted from the simulated light curves. The results of these simulations are discussed in Sect. 5. Since most lensed quasar light curves are probably affected by microlensing events, it is important that our simulations include such effects in order to evaluate their influence on the determination of the time delay. This is treated in Sect. 6. Finally, Sect. 7 investigates the effect of logarithmic sampling on the light curves and shows how this irregular sampling can improve the time delay measurements when it is of the order of the visibility window of the object. Note that we consider here only the time delays measured from optical light curves. Radio observations have characteristics that are completely different from the present simulations: noise properties, better spatial resolution, less sensitivity to microlensing.

### 1.2. Which accuracy?

Not all lensed quasars are suited to an accurate determination of  $H_0$ , first because not all of them have nice lens models with little influence of degeneracies and, second, because the error on the time delay propagates linearly into the error budget on  $H_0$ . While the latter is not the dominant component in the error budget it can (and should) be made almost negligible compared with the other sources of uncertainty. A precision of a few percent should be the goal of the photometric monitoring programs aimed at measuring time delays, if  $H_0$  is to be measured with an accuracy competitive with other methods. So far, very few time delays are known with very high accuracy. Among the best examples are the double Q 0957+561 (Colley et al. 2003), measured in optical wavelengths, and the quadruple B 1608+656 (Fassnacht et al. 2002), measured in radio wavelengths. Most other lensed quasars have time delays known with a precision of about 10%.

The accuracy of the time delays depends critically on the temporal sampling, on the visibility of the object over the year, on the influence of microlensing, and on the good will of the quasar source to show photometric variations at all. Using numerical simulations on artificial quasar light curves, we try in the present work to define the optimal observational strategy to adopt in order to reach a desired accuracy on the time delay.

We consider only the time delay between two quasar images. Our simulations remain applicable to multiple time delays in quads, but the errors on the photometric measurements of the 4 (or more) components must be uncorrelated.

## 2. Simulated light curves

The first step of the process is to generate artificial quasar light curves whose properties mimic quasar variations in a realistic way. A useful benchmark here is the analysis by Hook et al. (1994), of the variability properties of a sample of some 300 quasars.

They find that the variability  $\delta m$  of optically selected quasars can be represented by a function of the form:

$$|\delta m| = (0.155 + 0.023(M_B + 25.7)) \left( \frac{\delta t}{1+z} \right)^{0.18}$$

where  $M_B$  is the absolute  $B$  magnitude,  $z$  is the redshift, and  $\delta t$  is the time interval, in days, over which  $\delta m$  applies. We plot this relation in Fig. 1, for different luminosities ( $M_B = -26, -28$ ), and redshifts ( $z = 1, 2, \text{ and } 3$ ), which are typical for lensed quasars. The curves in the figure show a variation time-scale of 10 to 100 days for a typical change of a few tenths of a magnitude. Realistic simulated light curves should show a time-scale for the variations, and a total ‘‘peak-to-peak’’ amplitude  $A = \delta m$  of the variation that are in accord with these results.

In order to mimic these variations we first consider a time series of  $N$  points spanning the total duration of the observation. For each of these points we define a simulated magnitude in such a way that the artificial light curve follows a random walk with an arbitrary peak-to-peak amplitude. We next smooth the light curve with a Gaussian kernel that has a Full-Width-Half-Maximum ( $FWHM$ ) of 30 days to ensure that the typical variation time-scale matches that of real quasars. Finally, the curve is renormalized so that its maximum variation is equal to a specified peak-to-peak amplitude  $A$ .

A second light curve is then obtained, by applying a time shift  $\Delta t_{\text{in}} > 0$ . The two sets of points ( $t_A, m_A$ ) for image A and ( $t_B, m_B$ ) for image B obtained in this way are the final simulated light curves, both sampled with 10 points per 24 h. This sampling, very small compared with the sampling that will be adopted to carry out the actual observations, ensures that no interpolation is necessary when shifting curve B relative to curve A. The precision on the shift is, then, 0.1 day, 50 times smaller than the smallest time delay we wish to simulate.

The curves are used to produce artificial observations, this time with a much sparser sampling. We define  $N_{\text{obs}}$  observing points at the observing dates  $t_{\text{obs}}$ . For each of these dates we define the observed magnitude by selecting the closest value in time among the pairs ( $t_A, m_A$ ) for image A and ( $t_B, m_B$ ) for image B, resulting in noise free, sampled, artificial light curves. Finally, simulated photon noise is added to the data. This is achieved by adding to each observing point a normally distributed deviate of zero mean and variance  $\sigma_{\text{obs}}$ . Thus one has defined a combined set of  $N_{\text{obs}}$  observations, ( $t_{\text{obs}}, m_{A,\text{obs}}$ ) for image A and ( $t_{\text{obs}}, m_{B,\text{obs}}$ ) for image B. Typical light curves are shown in Fig. 2.

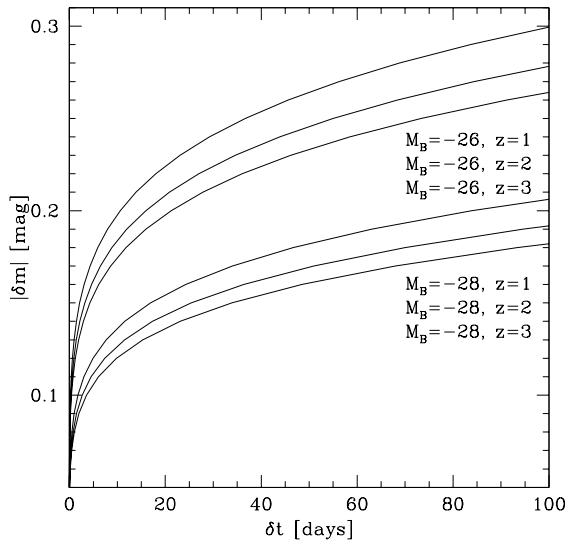


**Fig. 1.** Expected quasar variations  $\delta m$  in magnitudes as a function of the time interval  $\delta t$  (see text). The curves are plotted for 2 different absolute magnitudes  $M_B$  and for 3 quasar redshifts.

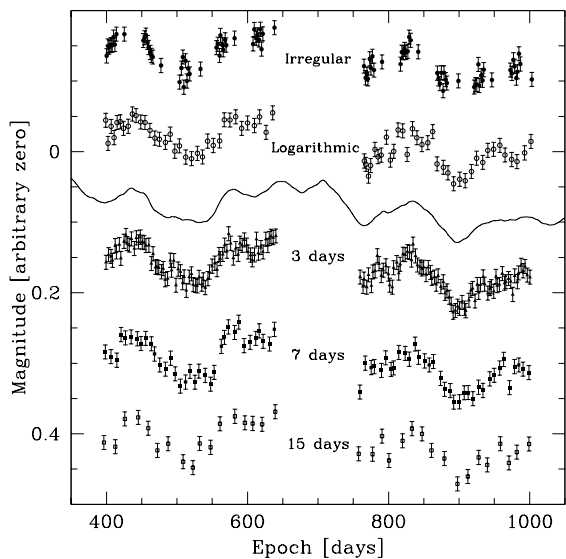


**Fig. 2.** Example of simulated light curve, for a 2-year long observation and a peak-to-peak amplitude  $A = 0.1$  mag. The continuous light curve is shown as a solid line. It has been smoothed on a length scale of 30 days. The four samplings used in the simulations are shown (plus the logarithmic sampling, see text), along with the error bars of 0.01 mag. The figure is constructed for an object with a visibility of 8 consecutive months, hence the size of the gap in the center of the curves is 4 months. The curve plotted for the logarithmic sampling has the same number of data points as the curve for the 7-day sampling.

### 3. Parameter space

In the simulations presented below, some parameters are imposed on us by technical limitations. This is the case of the maximum accuracy on the photometry of the individual quasar images. We assume that a good goal is 0.01 mag for a typical

lensed quasar, or a signal-to-noise of 100 integrated over the quasar image. We have tested some cases where the points have larger error bars, and this led to the conclusion that the adopted 0.01 mag error is a requirement to meet in order to carry out the project successfully. Doubling the error bars also doubles the error on the time-delay determination. Errors above 0.05 are likely to compromise the whole feasibility of the project. We also suppose that the algorithm used to carry out the photometry on the real data actually yields photon noise limited measurements. Second, we fix the total duration of the observations to two years, since one probably wants to measure  $H_0$  in a reasonable amount of telescope time.

Other parameters cannot be fixed in advance. They define the parameter space we want to explore through the simulations, and include:

1. The temporal sampling of the curves. We consider regularly spaced sampling intervals of 3, 7, and 15 days ( $\pm 30\%$  due, e.g., to bad weather). Also, in some observatories, large chunks of time are allocated rather than regularly spaced dates. To model this, as an example, we also carry out our experiment with a sampling of one observing point taken every other day during 15 days, followed by 1 single point taken in the middle of the next month, and again one point every other day for 15 days, and so on. We refer to this type of sampling as “irregular sampling”.
2. The visibility of the object. An equatorial object is seen no more than 5 months in a row in good conditions. A circumpolar object is by definition visible the entire year. We also choose an intermediate visibility of 8 months. It should be noted that we do not allow for large losses of data points, e.g. non allocation of time to the project during a full semester, which would simply hamper even a rough estimate of the time delay.
3. The amplitude  $A$  of variation of the quasar. We choose three typical peak-to-peak variations of  $A = 0.1, 0.2, 0.3$  mag over the two years of simulated observations, as suggested by Fig. 1.

Determining the best combination of these parameters is the goal of the present work, for a broad range of time delays, from 5 to 120 days. For each time delay there are 4 temporal samplings  $\times$  3 visibilities  $\times$  3 amplitudes = 36 different possible combinations of parameters.

### 4. Extracting the time delay

Using the light curves constructed in the previous section, we now try to recover the time delay  $\Delta t_{in}$  chosen in the simulated data. Many cross-correlation techniques are available for this task, with a variety of technical subtleties dealing with unstable solutions, sparse sampling, and the effects of additional perturbations to the light curves (such as those caused by microlensing).

The aim of the present experiment is to decide which observing strategy will assure us that the present typical 10% error bar on optical time delays decreases below 2%, rather than testing the cross-correlation techniques themselves. For this

reason, without further discussion, we have adopted the cross-correlation method of Pelt et al. (1994), which is in wide use, and which combines robustness, simplicity, and low cost in terms of computing time. No other correlation technique was used in the present simulations. More elaborated methods may be more efficient, so that our results can be considered as lower limits on the accuracy that can be actually achieved using a given set of light curves.

Although the Pelt method is well known, we briefly review the main steps followed to determine the time delay.

We first define an interval of time delays  $[\Delta t_{\min}, \Delta t_{\max}]$ , which contains the true value of the time delay  $\Delta t_{\text{in}}$ . Note that with real data, predicted time delays for lenses are accurate enough to follow this approach, especially in cases where the redshifts of the lens and source are known. We then define  $N_d$  equally spaced time delays over the range  $[\Delta t_{\min}, \Delta t_{\max}]$ , with interval  $\leq 0.1$  days i.e.  $N_d \geq (\Delta t_{\max} - \Delta t_{\min})/0.1 + 1$ . The interval is small compared with the input time delay  $\Delta t_{\text{in}}$  and ensures that the precision of the results, even for  $\Delta t_{\text{in}} = 5$  days, is not limited by the time resolution adopted in the simulations.

The light curve of image B is then shifted, successively, through the set of  $N_d$  time delays,  $\Delta t$ . The problem is to find which curve  $B(\Delta t)$  best matches curve A, within the overlap region. For any curve  $B(\Delta t)$  the overlap region is defined as the set of points for which there exist points in curve A, both before and after in time. Curve A is then linearly interpolated to these points, and the dispersion  $D^2(\Delta t)$  in the magnitude differences between the two curves provides the measure of goodness of fit. Data points for which the distance from the interpolated date to the closest date in curve A, is greater than some specified limit (i.e. where the interpolation is unreliable) are ignored in this calculation. The search is limited, obviously, to time delays for which the two curves overlap. Time delays of the order of half a year are thus only accessible for circumpolar objects.

This procedure yields the dispersion spectrum  $D^2(\Delta t)$ . The true time delay  $\Delta t_{\text{out}}$  between the images should be evident as a minimum in the dispersion spectrum  $D^2(\Delta t)$ . This minimum is determined by fitting a parabola to the dispersion spectrum.

## 5. Results

For every time delay  $\Delta t_{\text{in}}$  to be simulated, we explored the full range of 36 different combinations of the three parameters, detailed in Sect. 3. For each combination, we ran 100 000 simulations, each time changing the quasar light curve, and modifying the observed points by adding randomly distributed errors (i.e. normally distributed deviates of 0.01 mag variance). The results for  $\Delta t_{\text{in}} = 80$  days are summarized in Fig. 3, where the 36 panels correspond to the different parameter combinations. In each panel the measured time delays of the simulations are plotted in histogram form, with the measured mean and standard deviation (established by computing the range containing 68% of the results) quoted. The histograms are mostly symmetrical about their mean value, indicating that no strong systematic error is introduced. The slight shift (0.5 days in the worst case) of the mean of the histogram relative to value of  $\Delta t_{\text{in}}$  is small compared with the width of the histogram, i.e., the random error dominate the error budget.

**Table 1.** Published time delays and  $1\text{-}\sigma$  uncertainties for four lensed quasars, measured from their optical light curves. The percentage errors are given in parentheses.

Object	Time delay [days]	Reference
RXJ 0911+0551	$146 \pm 4$ (2.7%)	Hjorth et al. (2002)
FBQ 0951+2635	$16 \pm 2$ (13%)	Jakobsson et al. (2004)
PG 1115+080	$23.7 \pm 3.4$ (14%)	Schechter et al. (1997)
SBS 1520+530	$130 \pm 3$ (2.3%)	Burud et al. (2002a)
B 1600+434	$51 \pm 2$ (3.9%)	Burud et al. (2000)
HE 2149-2745	$103 \pm 12$ (12%)	Burud et al. (2002b)

The results for the percentage error, for the 36 parameter combinations, for all the simulated time delays, are presented in a compact way in Fig. 4. Here each panel shows the results for 12 parameter combinations, which are the 4 temporal samplings  $\times$  the 3 visibilities, and the three columns correspond to the 3 amplitudes. Each row is for a different time delay. In this figure are also shown the values of the quoted relative errors for six published time delays of quasars monitored in optical wavelengths. These values are summarized in Table 1, and have been plotted at a sampling of 15 days, which roughly correspond to their effective sampling. Although the observational strategy used for these quasars is not strictly the same as any of the ones we have defined, the predicted errors lie rather close to the real ones, with the exception of the double quasar HE 2149-2745, but this quasar had very smooth variations over the two years of observations, much smoother than the typical variations used in our simulations (see Fig. 2). We do not include the twin quasar Q 0957+561 because it has a 10-year long light curve, much longer than the two years considered in our simulations. Moreover its time delay of  $423 \pm 6$  days (Pelt et al. 1996) is much larger than the highest time delay used (i.e. 120 days).

Although the predicted relative errors on the time delay are very close to the published values, they are usually slightly more optimistic than the measured relative errors. The small discrepancies can be explained by differences in the parameters we use, compared with the characteristics of actual monitoring data, e.g.:

- a shorter or longer monitoring period than the supposed two years;
- different photometric errors than the supposed 0.01 mag;
- a temporal sampling that differs in detail from our idealized scheme.

The most likely explanation for the simulations being too optimistic however remains the presence of microlensing in the light curves of real quasars, which is the subject of the next section.

## 6. Influence of “slow” microlensing

Not all the photometric variations observed in the light curves of the quasar images are intrinsic to the quasar. Microlensing

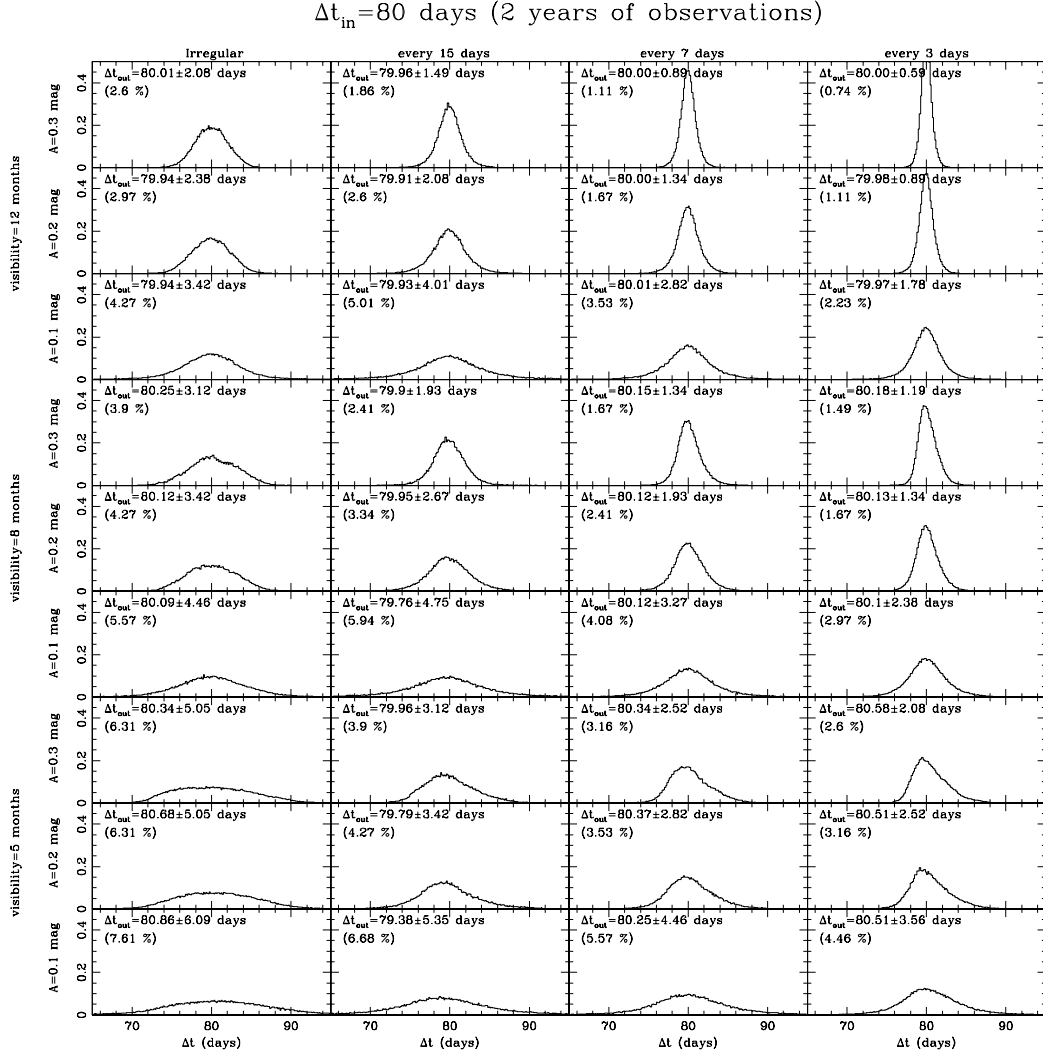


**Fig. 3.** Histograms exploring the observational parameter space described in the text for the determination of a time delay of 80 days. Each curve is the probability density function for the time delay, obtained from 100 000 simulations, for a particular combination of the three variables. These are: 1- *sampling interval*, four columns, *from left to right*: irregular, 15 days, 7 days, 3 days; 2- *visibility period*, three bands *from top to bottom*: 12, 8, and 5 months; 3- *peak-to-peak variation*, A, three rows within each band, *from top to bottom*: 0.3, 0.2, 0.1 mag. Each panel is labeled with the mean and standard deviation of the measured time delay, as well as the percentage error. The effect of microlensing is not included in these simulations, and is treated later.

by stars in the lensing galaxy introduces amplification events that contaminate the light curves.

The severity of such events depends not only on the location of the images relative to the lens but also on whether the image considered is a minimum, maximum or a saddle point in the arrival time surface (Schechter & Wambsganss 2002). Consequently, the image closest to the lens, in projection on the plane of the sky, and hence with the larger density of potential microlenses, is not necessarily the one with more microlensing. The doubly lensed quasar HE 1104-1805 is a typical example, where the image the further away from the lens is the one with the largest microlensing events.

Microlensing can act on different time scales, “slow” or “fast”, as compared with the time scale of the quasar’s intrinsic variations. A nice example of fast microlensing has been found in the light curve of HE 1104-1805 (e.g., Schechter et al. 2003). Since the temporal sampling used in past quasar monitoring programmes has been rather sparse, there is no other known example of fast microlensing. Slow microlensing, with smooth variations spanning several months or even years are more common, or are at least better detected with existing data. The slow variations in the four images of the Einstein Cross are the clearest examples of slow microlensing (e.g., Wozniak et al. 2000).

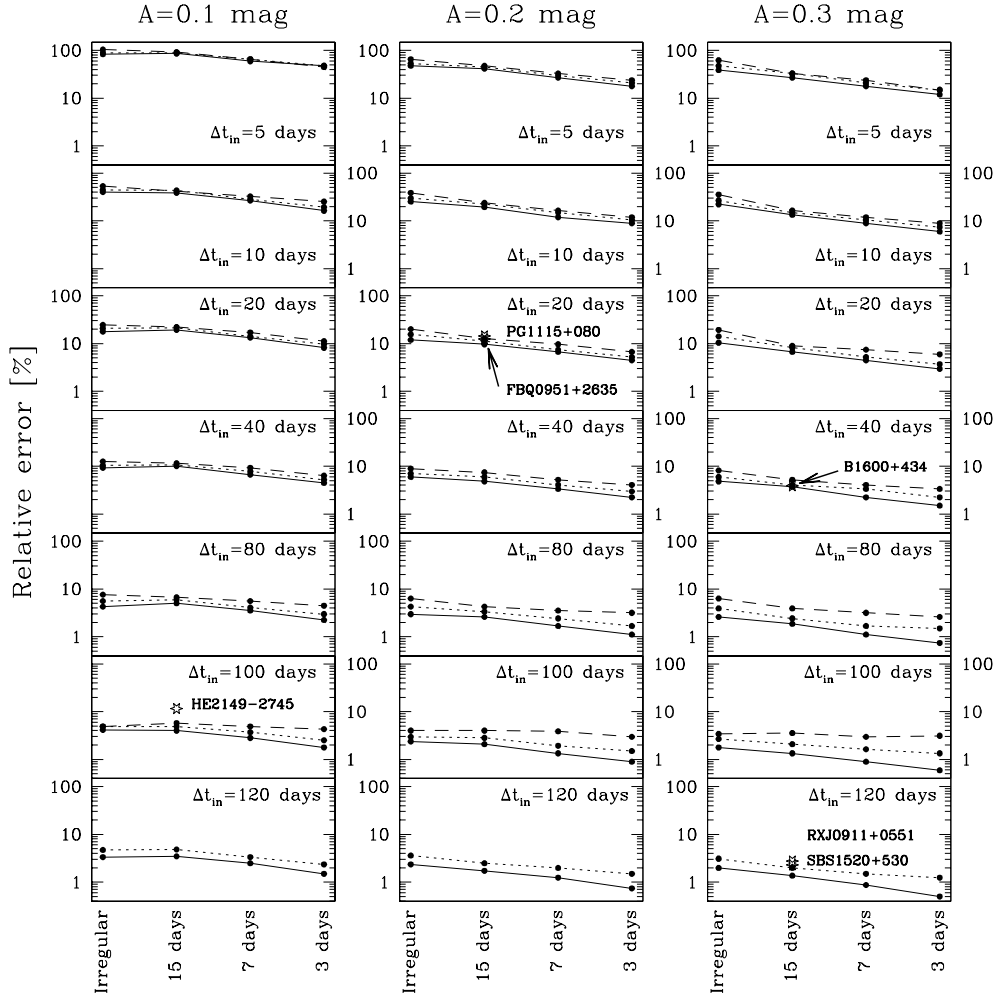


**Fig. 4.** Summary of the estimated percentage error on the measured time delay as a function of the observational parameters: 1- *peak-to-peak* variation,  $A$ ; 2- *sampling interval* ( $x$ -axis of each panel); 3- *visibility period*. Each panel corresponds to one value of the input time delay  $\Delta t_{\text{in}}$ . The percentage error on the time delay, plotted on the  $y$ -axis, is calculated from 100 000 simulations. The lines connecting the points correspond to different periods of visibility. The solid lines are for circumpolar objects, the dotted lines are for the 8-month visibility, and the long dashed lines are for the 5-month visibility. We have used three peak-to-peak values of the amplitudes  $A$  for the simulated light curves, which increases from left to right in the three columns. The curve for the 5-month visibility and 120-day time delay has not been computed, as there are almost no data points in common between the curves of image A and image B. The star-shaped symbols plot the percentage errors for quasars with real measured optical time delays published in the literature. See text for further details.

Since most quasars with measured time delays have been shown to be affected by slow microlensing, it is mandatory to introduce this effect into our artificial light curves and to estimate how the time-delay measurement is modified. The slow microlensing events can be simulated by creating a *microlensing* light curve in the same manner as we did for the intrinsic variations of the quasar (i.e. by using a smooth random walk model), but with a different length scale and amplitude. We express the peak-to-peak microlensing amplitude  $A_{\mu}$  as a simple function of the quasar amplitude. We take it as  $A_{\mu} = \alpha \cdot A$ , with  $\alpha = 0.01, 0.05, 0.10$ , in order to mimic a microlensing amplitude of respectively 1, 5 and 10% of the amplitude of the quasar light curve. The microlensing curve is smoothed using a convolution kernel of 100 days, i.e.  $\sim 3$  times slower than the

intrinsic variations of the quasar, and is added to the light curve of one of the quasar images. The choice of this image is irrelevant, because only relative differences between the lightcurves of the two components are considered to extract the time delay.

We then repeat the cross-correlation analysis. The microlensing event, thus, acts as an additional source of noise. Fast microlensing is not considered here. Introducing it is equivalent to artificially increase the 0.01 mag error bar on the individual points.

Figure 5 plots the results for the case of the 80-day time delay, and 3-day sampling, with different amplitudes of microlensing. The format is the same as in Fig. 3. It can be seen that no strong systematic variations are introduced. In each case the returned time delay is consistent with the input value,

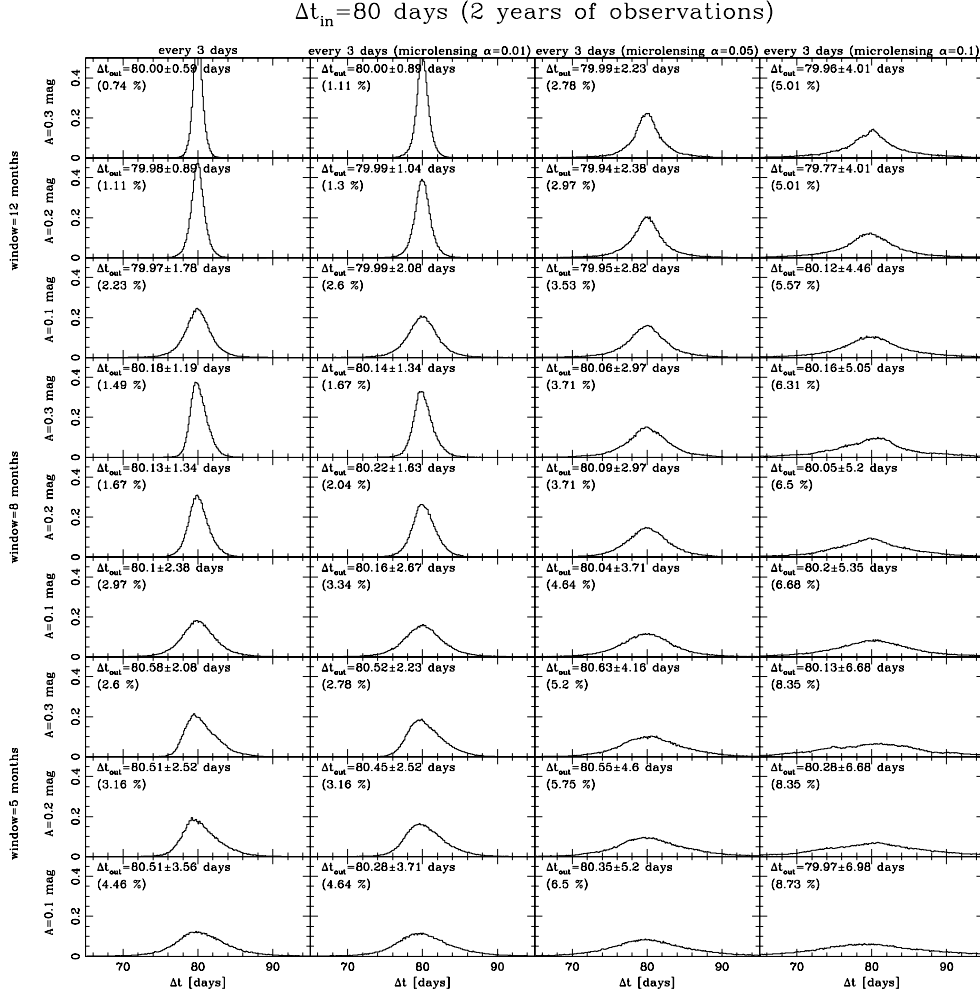


**Fig. 5.** Histograms exploring the observational parameter space described in the text for the determination of a time delay of 80 days, including the effects of microlensing. Each curve is the probability density function for the time delay, obtained from 100 000 simulations, for a sampling interval of 3 days, and for a particular combination of the variables. These are: 1- microlensing amplitude,  $A_\mu = \alpha \cdot A$ , four columns, from left to right:  $\alpha = 0, 0.01, 0.05, 0.1$ ; 2- visibility period, three bands from top to bottom: 0.3, 0.2, 0.1 mag. Each panel is labeled with the mean and standard deviation of the measured time delay, as well as the percentage error. While no strong systematic drifts of the histograms are seen relative to the input time delay  $\Delta t_{\text{in}} = 80$  days, the width of the histograms are significantly broadened as microlensing increases.

but microlensing substantially increases the uncertainty in the measurement, i.e. broadens the histograms. No distortion, i.e., skewness is apparent. The error on the time delay measurement without microlensing (left column) typically degrades by a factor of approximately 2 when 5% microlensing is present (i.e.,  $\alpha = 0.05$ ), and by up to a factor of 6 with 10% microlensing. However, the shift between the mean of the distribution and  $\Delta t_{\text{in}}$  is not much larger than in the no-microlensing case. Slow microlensing does not seem to introduce significant systematic errors.

Figures 6 and 7 summarize all the results of our simulations including microlensing, in a way similar to Fig. 4, showing how the error on the time delay degrades with increasing microlensing amplitude ( $\alpha$ , plotted on the  $x$ -axis in each of the column

plots). The figures are constructed for the irregular sampling as well as for the regular 3-day, 7-day and 15-day samplings.

We note that the time-delay determination is much more affected by microlensing with the 3-day sampling than with the 15-day or the “irregular” samplings: while changing  $\alpha$  from 0 to 0.1 increases the relative error by a factor of 8 for the 3-day sampling, it increases only by a factor of 3–4 with the 15-day or the irregular sampling. Microlensing has a stronger effect on well sampled light curves than on sparser samplings.

Similarly a light curve with large amplitude  $A$  will see its accuracy on the time-delay measurement slightly more degraded than one with a smaller amplitude. In both cases this may simply be due to the enhanced signal-to-noise of the light curves, either because more data points are available, or

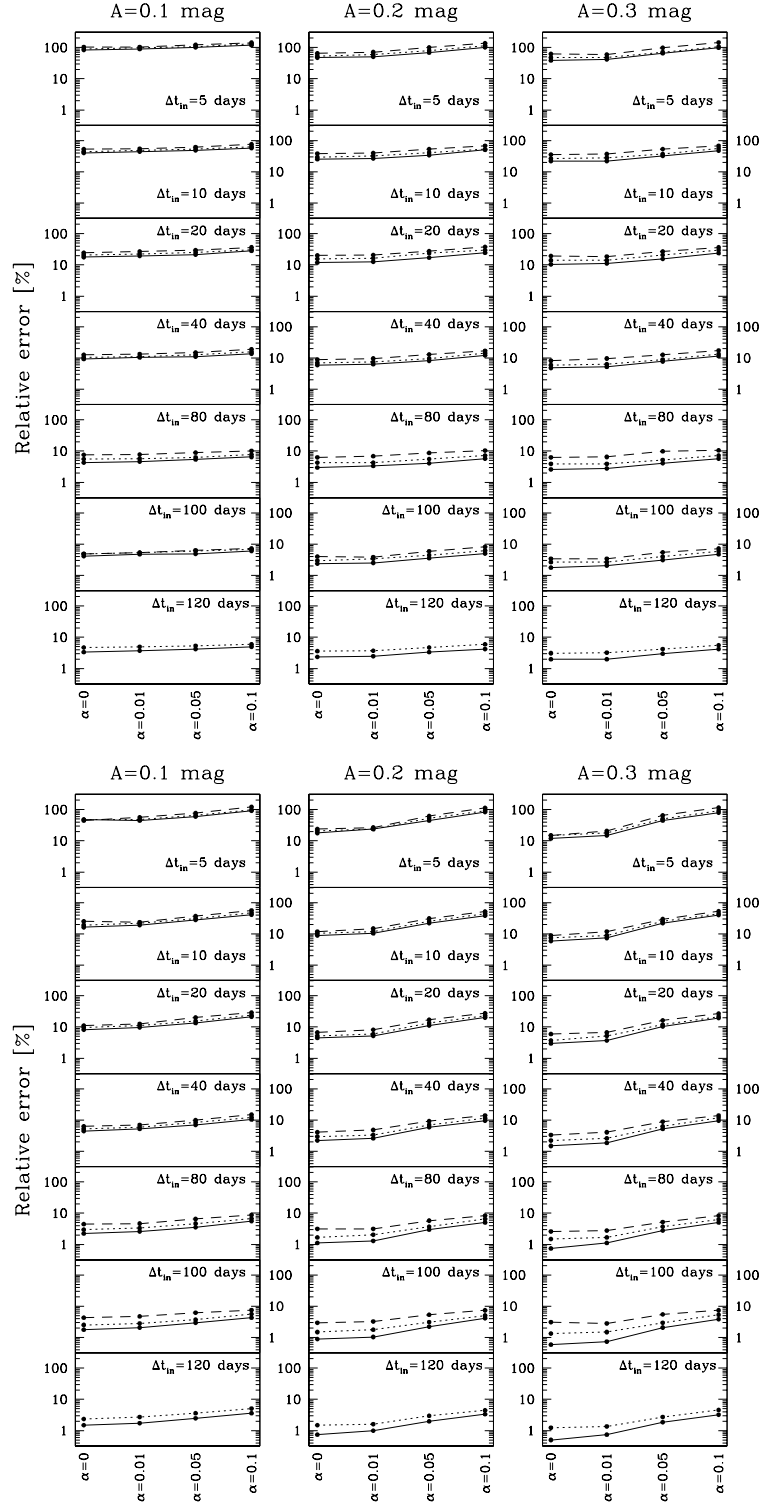


**Fig. 6.** *Top:* percentage error on the time delay for the *irregular sampling* and for three amplitudes  $A$ . In each column the results are shown for four microlensing amplitudes  $A_{\mu} = \alpha \cdot A$ , starting on the left with  $\alpha = 0$ , i.e., no microlensing. The different types of curves correspond to the three visibilities, as in Fig. 4. The solid lines are for circumpolar objects, the dotted lines are for the 8-month visibility, and the long dashed lines are for the 5-month visibility. *Bottom:* same plot as above but for the *3-day sampling*.



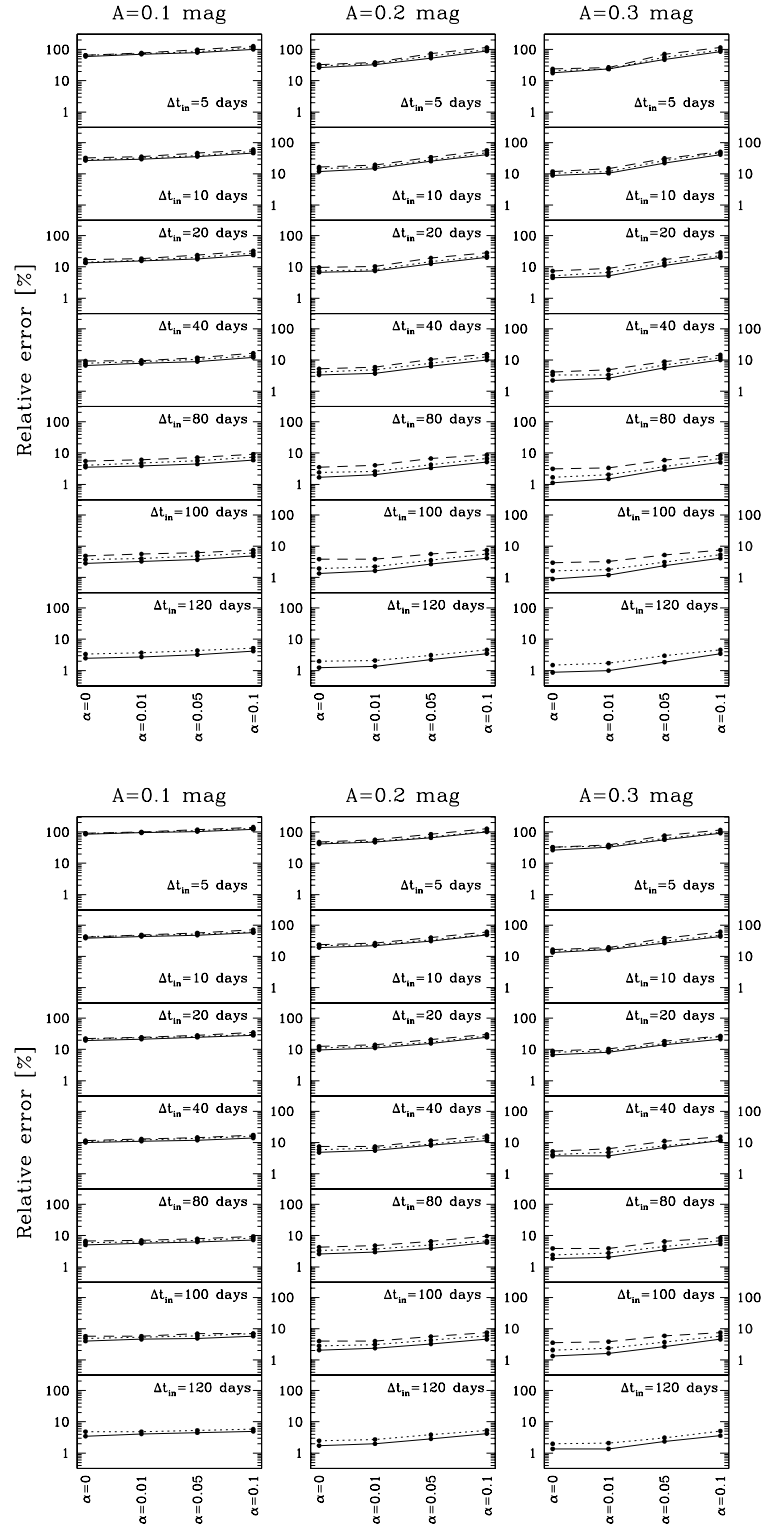
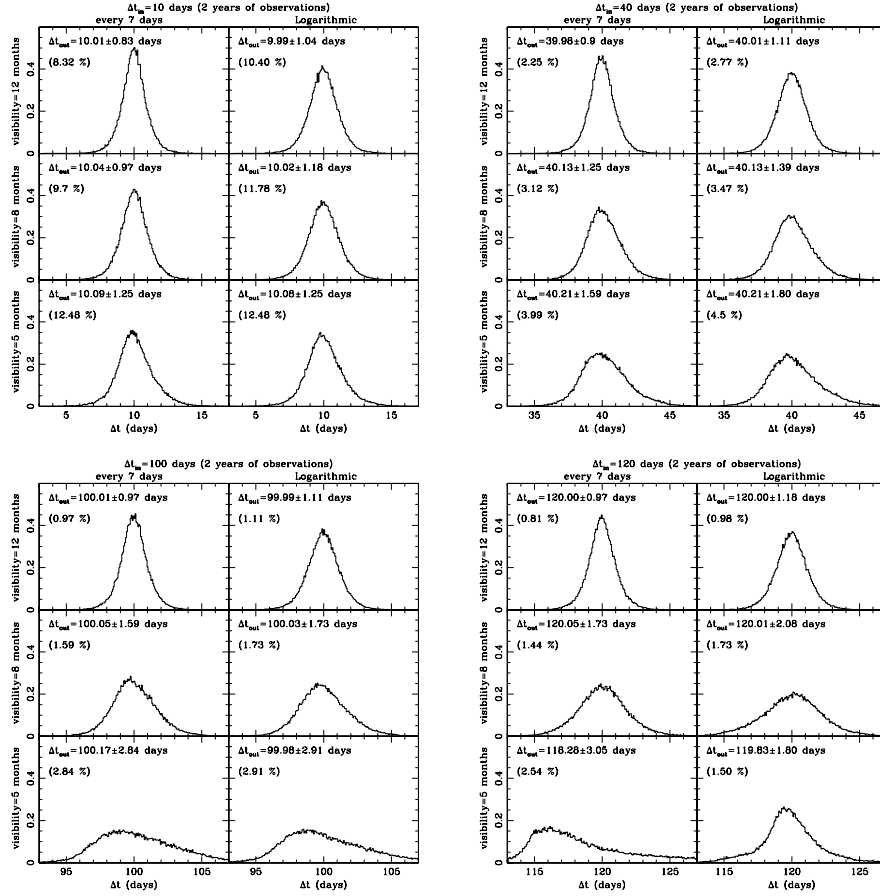


Fig. 7. Same as Fig. 6, but for the 7-day sampling (top) and for the 15-day sampling (bottom).



**Fig. 8.** Time delay distributions for four different values of  $\Delta t_{in}$ , each time for 3 visibilities and a peak-to-peak variation  $A = 0.3$ . We compare the distributions obtained for the logarithmic sampling (without microlensing), with the results for the 7-day sampling. Clear distortions of the histograms are seen when the time delay is close to the visibility window of the object, when a regular sampling is adopted (left column in the four panels). The histograms obtained with the logarithmic sampling are well symmetrical and narrow. The systematic error is also reduced. This effect is not so evident when the time delay is much shorter than the visibility window, where the logarithmic sampling even degrades the results.

because the quasar variations are stronger with respect to the photon noise of the individual photometric points.

In general we can conclude that the more accurate the time-delay determination is in the case without microlensing, the more it degrades when a given amount  $\alpha$  of microlensing is added: better data are more sensitive to microlensing. On the other hand, the data allowing accurate time delay determinations in the absence of microlensing are usually also better suited to the accurate subtraction of the microlensing events.

## 7. When the time delay becomes close to the length of the visibility window

So far we have compared light curves sampled with regular samplings, plus one irregular sampling. The main difference between these samplings was the number of data points within the period of 2 years of observations. It is then not surprising that finer sampling leads to better results. The simulations we

have done allow us to quantify the error bar on the time delay for each sampling.

Another natural question arising is: is there an optimal way to distribute a fixed number of sampling points, in order to reach the best possible accuracy on the time delay? This has been explored in other areas of astronomy, for example by adopting a logarithmic sampling of the data. We have tested the effect of such a sampling on quasar light curves. Figure 8 shows the results of the simulations, where we compare the (regular) 7-day sampling to a sampling adopting the exact same number of data points but distributed in a logarithmic way. As for the regular case, we have introduced a small randomly distributed error ( $\pm 0.4$  days) on each observing data to account for weather conditions and scheduling. As shown in Fig. 2 the curve starts with a very high frequency of observations and continues with a sampling getting close to regular. An important consequence is that objects that have a time delay of the order of the visibility period will be well sampled exactly where the two quasar light curves significantly overlap after correcting for the time

delay. In other words, the logarithmic scale allows to sample very well the (short) parts of the curves that will overlap after the time delay is applied.

The result in Fig. 8 is striking. As soon as the time delay is close to the length of the visibility window, the regular method fails to produce symmetrical histograms, whereas the histograms obtained with the logarithmic scale are narrower and more symmetrical about their mean. Their mean is also closer to  $\Delta t_{\text{in}}$  than with the regular method. This is no longer true when the time delay is shorter than the visibility window, where the logarithmic sampling even degrades the results.

## 8. Conclusions

We have undertaken a set of simple but realistic numerical simulations in order to optimize the observing strategy of our COSMOGRAIL photometric monitoring programs aimed at measuring  $H_0$ . The predicted error bars on time delays compare very well with the ones obtained in optical wavelengths with real data.

It is immediately seen from Figs. 6 and 7 that short time delays will never be measured accurately, i.e., with a precision better than 2%, unless the quasar amplitude  $A$  is substantially larger than 0.3 mag. Even with no microlensing and the 3-day sampling, time delays shorter than 10 days are measurable with 10% accuracy, at best. Time delays between 40 and 100 days seem optimal, especially in the case of circumpolar objects, where one can easily achieve 2% accuracy, even with the 7-day sampling.

Equatorial objects should be avoided. Although they are accessible from the north and south, they are visible under good conditions for only 5–6 months along the year. This makes it impossible to measure time delays larger than 100 days (hence the corresponding long-dashed curve is not represented in the relevant figures). For shorter time delays, e.g., 80 days, the estimated error for an equatorial object is twice that of the same object if it were circumpolar.

Microlensing complicates the situation. With 5% microlensing (as defined here), the estimated error on the time delay is twice that of the no-microlensing case. Again, optimal time delays are around 100 days, with a visibility of at least 8 months. Assuming an amplitude  $A = 0.2$  mag and 5% microlensing, an accuracy of 2% on the time delay is still possible for these objects. The long time delays also allow a sampling as long as 7 days to be adopted.

While microlensing increases the random error on the time delay, it does not increase significantly the systematic error (i.e.,  $|\Delta t_{\text{in}} - \Delta t_{\text{out}}|$ ), which remains low, usually 5 to 10 times lower than the random error, with or without microlensing.

Finally, adopting a logarithmic sampling step can improve the accuracy on the time delay when the time delay is close to the length of the visibility window of the object. However, this logarithmic sampling usually degrades the results for all other combinations of time delays and visibility windows.

The game of defining what could be a “golden” lens, at least in terms of quality of the time delay measurement, is not an easy one. This is why we have attempted in this paper to provide a grid of predicted error bars on the time delay, based on simple assumptions. The results are presented in a compact way in Figs. 6 and 7. We will use these plots to choose optimal combinations of 1- predicted time delay; 2- object visibility and 3- temporal sampling, to reach a target accuracy on the time delay. Even with large amounts of telescope time, the number of new lensed quasars is increasing quickly and one has to select the best possible cases. We hope that the present work will be useful for the task of identifying the objects that are the most likely to be measured accurately, so that the only significant remaining source of uncertainty on  $H_0$  will be the lens model.

## References

- Burud, I., Hjorth, J., Jaunsen, A. O., et al. 2000, *ApJ*, 544, 117  
 Burud, I., Hjorth, J., Courbin, F., et al. 2002a, *A&A*, 391, 481  
 Burud, I., Courbin, F., Magain, P., et al. 2002b, *A&A*, 383, 71  
 Colley, W., Schild, R. E., Abajas, C., et al. 2003, *ApJ*, 587, 71  
 Fassnacht, C. D., Xanthopoulos, E., Koopmans, L. V. E., et al. 2002, *ApJ*, 581, 823  
 Hjorth, J., Burud, I., Jaunsen, A. O., et al. 2002, *ApJ*, 572, 11  
 Hook, I., McMahon, R. G., Boyle, B. J., & Irwin, M. J. 1994, *MNRAS*, 268, 305  
 Jakobsson, P., Hjorth, J., Burud, I., et al. 2004  
 [arXiv:astro-ph/0409444]  
 Magain, P., Courbin, F., & Sohy, S. 1998, *ApJ*, 494, 452  
 Pelt, J., Hoff, W., Kayser, R., et al. 1994, *A&A*, 286, 775  
 Pelt, J., Kayser, R., Refsdal, S., et al. 1996, *A&A*, 305, 97  
 Refsdal, S. 1964, *MNRAS*, 128, 307  
 Saha, P., et al. 2005, in preparation  
 Schechter, P. L., & Wambsganss, J. 2002, *ApJ*, 580, 685  
 Schechter, P. L., Bailyn, C. D., Barr, R., et al. 1997, *ApJ*, 475, 85  
 Schechter, P. L., Udalski, A., Szymanski, M., et al. 2003, *ApJ*, 584, 657  
 Wozniak, P. R., Udalski, A., Szymanski, M., et al. 2000, *ApJ*, 540, 65



*“There are two kinds of light - the glow that illuminates, and the glare that obscures.”  
James Grover Thurber (1894 - 1961)*

## Chapter 6

# The redshift of lensing galaxies

## 6.1 Introduction

For the majority of all known gravitationally lensed quasars, the “distance” to the quasar is already well determined from spectroscopy by measuring the cosmological redshift affecting the spectrum of the quasar. On the opposite, the redshift of the much fainter lensing galaxy is usually poorly constrained or even completely unknown.

The determination of the lens redshift is essential for several reasons. First, detailed modeling of any gravitational lensing system requires the distance to the lens as an input. If a time delay has been measured for a given lensed quasar, it would be hopeless to infer an accurate estimate of the Hubble constant without knowing the redshift of the lens. Hence, it is absolutely necessary for a program like COSMOGRAIL to know the lens redshift of the monitored objects. Second, if a sufficiently large number of gravitational lenses with measured redshift is established, one can compute statistics to constrain the density  $\Omega_{\Lambda 0}$  of dark energy (e.g., Fukugita et al., 1990; Turner, 1990). Indeed, the probability that a distant object is strongly lensed is proportional to the number of possible lensing objects along the line of sight and thus, quite sensitive to dark energy. Increasing the number of lensed quasar with known lens redshifts will therefore improve the statistics and hence, the precision of the results.

The measurement of lens redshifts is difficult because of the small angular separation between the lensing galaxy and the lensed quasar images (typically one arcsecond), and because of the contamination of the much brighter quasar images. As a consequence, these measurements require deep spectroscopic observations using large telescopes in combination with advanced deconvolution methods to separate the spectrum of the lens from the glare of the much brighter quasar images. In this chapter, we present our spectroscopic survey conducted at the Very Large Telescope (VLT) of the European Southern Observatory (ESO) with the aim of measuring unknown lens redshifts. We combine the high quality VLT data with the MCS deconvolution method (Magain et al., 1998; Courbin et al., 2000) to further increase the spatial resolution and hence, retrieve the lens spectra

and determine the corresponding redshifts.

## 6.2 Spatial deconvolution

### 6.2.1 The MCS deconvolution algorithm

The resolution of astronomical images is limited by the resolution of the instruments and by the turbulence of Earth’s atmosphere. The resolution of a telescope improves with increasing size and when shorter wavelength are observed. Unfortunately, the resolution of ground-based optical telescopes does not improve without limit as its size is increased. This is due to atmospheric turbulence that produces the well-known “twinkling” of stars. As a consequence, the image of a point source (e.g., a star) is not a point, but is blurred. The observed blurring is described by the Point Spread Function (PSF), which depends on both the instrumental response and atmospheric turbulence present at the time of observation. Mathematically, the observed light distribution  $\mathcal{D}(\mathbf{x})$  of a given source can be considered as the convolution of the original light distribution  $\mathcal{F}(\mathbf{x})$  with the PSF  $\mathcal{T}(\mathbf{x})$ , plus some noise  $\mathcal{N}(\mathbf{x})$ .

$$\mathcal{D}(\mathbf{x}) = (\mathcal{T} * \mathcal{F})(\mathbf{x}) + \mathcal{N}(\mathbf{x})$$

where the symbol “\*” stands for the convolution. The aim of deconvolution is to invert this equation by deconvolving the data  $\mathcal{D}(\mathbf{x})$ , to recover the original light distribution  $\mathcal{F}(\mathbf{x})$ . However, there is no unique solution to this problem, especially in the presence of noise, and regularization techniques have to be used in order to select a plausible solution among the possible ones. A large variety of deconvolution methods have been proposed, depending on the way this particular solution is chosen.

One of these methods is the “MCS image deconvolution algorithm” (Magain et al., 1998). Unlike other traditional deconvolution methods, MCS is not violating the sampling theorem. This theorem determines the maximal sampling interval allowed so that an entire function can be reconstructed from sampled data (e.g., pixelized images). In other words, sampled data can not be fully reconstructed without violating the sampling theorem. Sampled images should not be deconvolved with the observed PSF  $\mathcal{T}(\mathbf{x})$ , but with a narrower function  $\mathcal{S}(\mathbf{x})$ , chosen so that the final deconvolved image is compatible with the sampling of the data. This means that an improved resolution rather than an infinite one is aimed at, overcoming the well known problem of “deconvolution artefacts”, which happen when retrieving spatial frequencies forbidden by the sampling theorem. Examples of common deconvolution methods are illustrated in Fig. 6.1. Only the MCS algorithm is unaffected by deconvolution artefacts.

Another strong advantage of MCS over other deconvolution methods is that it conserves the relative intensities of different parts of the image (e.g., different stars). Hence, it allows the user to perform accurate astrometry and photometry.

### 6.2.2 The MCS deconvolution algorithm for spectra

The method for spatial deconvolution of spectra (Courbin et al., 2000) follows the same fundamental principles as the “MCS image deconvolution algorithm”. In particular, a sampled image should not be deconvolved with the observed PSF  $\mathcal{T}(\mathbf{x})$ , but with a narrower function  $\mathcal{S}(\mathbf{x})$ , chosen so that the final deconvolved image can be properly sampled. For this purpose, one defines the final PSF  $\mathcal{R}(\mathbf{x})$  of the deconvolved spectrum and computes the PSF  $\mathcal{S}(\mathbf{x})$ , which should be used to perform the deconvolution instead of the

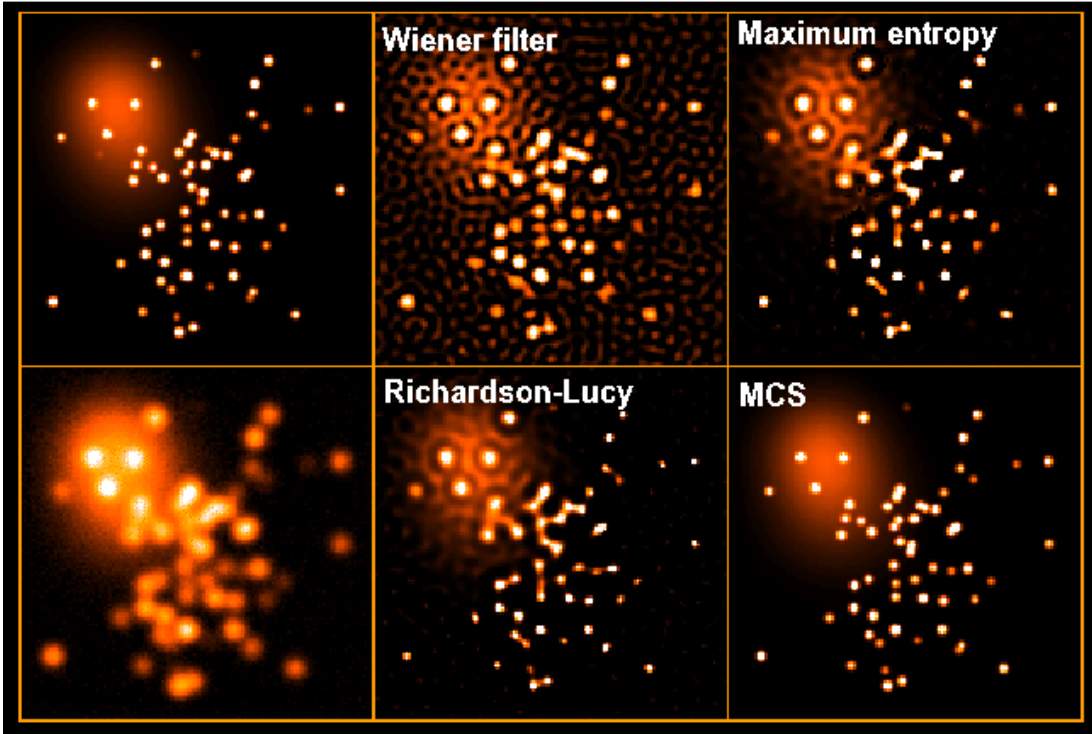


Figure 6.1: Deconvolution of a simulated image of a star cluster partly superimposed on a background galaxy using different methods. *Top left:* True light distribution with 2 pixels FWHM resolution. *Bottom left:* Observed image with 6 pixels FWHM and noise. *Top middle:* Wiener filter deconvolution of the observed image. *Bottom middle:* Fifty iterations of the accelerated Richardson-Lucy algorithm. *Top right:* Maximum entropy deconvolution. *Bottom right:* Deconvolution with the MCS algorithm.

observed PSF  $\mathcal{T}(\mathbf{x})$ . The profile  $\mathcal{S}(\mathbf{x})$  is obtained by inverting the equation

$$\mathcal{T}(\mathbf{x}) = (\mathcal{S} * \mathcal{R})(\mathbf{x}) .$$

A straightforward consequence of choosing the shape of the PSF  $\mathcal{R}(\mathbf{x})$  is that it is, indeed, exactly known. Such prior knowledge can be used to decompose the data into a sum of point sources with known analytical spatial profile and a deconvolved numerical background, so that the spectrum of extended sources in the immediate vicinity of bright point sources may be accurately extracted and sharpened.

### Computing the deconvolved spectra

A two dimensional spectrum is described by  $M$  spectral resolution elements (e.g.,  $M$  lines of pixels), each composed of  $N$  spatial resolution elements (e.g.,  $N$  columns of pixels). Each spectral resolution element of the spectrum can be approximated as a quasi-monochromatic one-dimensional image. This image has a deconvolved light distribution  $\mathcal{F}_j(x)$  that can be written

$$\mathcal{F}_j(x) = \mathcal{H}_j(x) + \sum_{k=1}^{N_*} a_{k,j} \mathcal{R}(x - c_{k,j}) .$$

The right hand side of the equation is the sum of a numerical background  $\mathcal{H}_j(x)$  and of  $N_*$  profiles  $\mathcal{R}(x)$  with intensities  $a_{k,j}$  and centers  $c_{k,j}$ . The profile  $\mathcal{R}(x)$  is chosen to be Gaussian, with fixed width (i.e. resolution) all along the spectral direction. The final deconvolved spectrum is therefore corrected for seeing variations with wavelength. Moreover, the spectra may suffer from slit misalignment with respect to the physical dimensions of the detector and from atmospheric refraction. As a consequence, the position of a given point source on the detector is wavelength dependent. The deconvolved two dimensional spectrum which best matches the data is obtained by minimizing the function

$$\mathcal{C}_{\chi^2} = \sum_{j=1}^M \sum_{i=1}^N \left( \frac{1}{\sigma_{i,j}} [(\mathcal{S}_j * \mathcal{F}_j)(x) - \mathcal{D}_j(x)]_{x=x_i} \right)^2$$

where  $\sigma_{i,j}$  is the error representative of the noise affecting the  $j^{\text{th}}$  spectral resolution element  $\mathcal{D}_j$  at position  $x_i$ , and  $\mathcal{S}_j(x)$  is the narrower PSF at the  $j^{\text{th}}$  spectral resolution element.

By definition, the profile  $\mathcal{R}(x)$  can not contain spatial frequencies above the Nyquist frequency  $f_N = 1/(2\Delta x)$  of the adopted spatial sampling step  $\Delta x$ , hence the deconvolved background  $\mathcal{H}_j(x)$  may be affected by noise enhancement. Such noise amplification might give rise to structures with frequencies forbidden by the sampling theorem. They should therefore be filtered out by regularization. This ensures that the deconvolved background  $\mathcal{H}_j(x)$  is smooth (in the spatial direction) on the length scale of the final resolution represented by the profile  $\mathcal{R}(x)$ . This is done by minimizing

$$\mathcal{L}_1 = \sum_{j=1}^M \sum_{i=1}^N \left( [\mathcal{H}_j(x) - (\mathcal{R} * \mathcal{H}_j)(x)]_{x=x_i} \right)^2 .$$

In spectroscopy, one may take advantage of the additional prior knowledge that the position of a given point source at a given spectral resolution element is highly correlated with its position in the neighbouring elements. We introduce this prior as a second constraint

$$\mathcal{L}_2 = \sum_{k=1}^{N_*} \sum_{j=1+W/2}^{M-W/2} \left[ c_{k,j} - \sum_{j'=-W/2}^{W/2} g_{j'} c_{k,j+j'} \right]^2$$

where  $g$  is a Gaussian function for simplicity. It is defined over a box of  $W$  spectral resolution elements centered on the  $j^{\text{th}}$  element. Its full width at half maximum  $w_g = 2\sqrt{\ln 2/b_g}$  defines the typical scale length where the correlation applies. The function is normalized to a total flux of one and is simply written as

$$g_j = \frac{1}{G} e^{-b_g j^2} \quad \text{where} \quad G = \sum_{j=-W/2}^{W/2} g_j .$$

The final algorithm for the spatial deconvolution of spectra therefore involves the minimization of the function

$$\mathcal{C} = \lambda \mathcal{C}_{\chi^2} + \mathcal{L}_1 + \mu \mathcal{L}_2 .$$

The optimal choice of the different Lagrange multipliers to be used is guided by the visual inspection of the residuals. The residuals are the difference between the deconvolved



image re-convolved by the PSF  $\mathcal{S}_j(x)$  and the raw data, in units of the noise. An accurate deconvolution should therefore leave a flat residual map with a mean value of 1.

The parameter  $\lambda$  is proportional to the smoothing of the deconvolved background  $\mathcal{H}_j(x)$  in the spatial direction. On the one hand, a too low  $\lambda$  produces a background which cannot correctly fit steep extended source profiles. On the other hand, a too high  $\lambda$  may create a “wave-shaped” background.

The parameter  $\mu$  expresses the strength of the correlation of the position of a given point source at a given wavelength with its position in the neighbouring spectral resolution elements. Choosing a too small  $\mu$  multiplier leads to over-fitting of the data and to a “noisy” deconvolved spectrum, while a larger  $\mu$  leads to under-fitting. The  $\mu$  multiplier has to be chosen in order to maximize the signal-to-noise ratio.

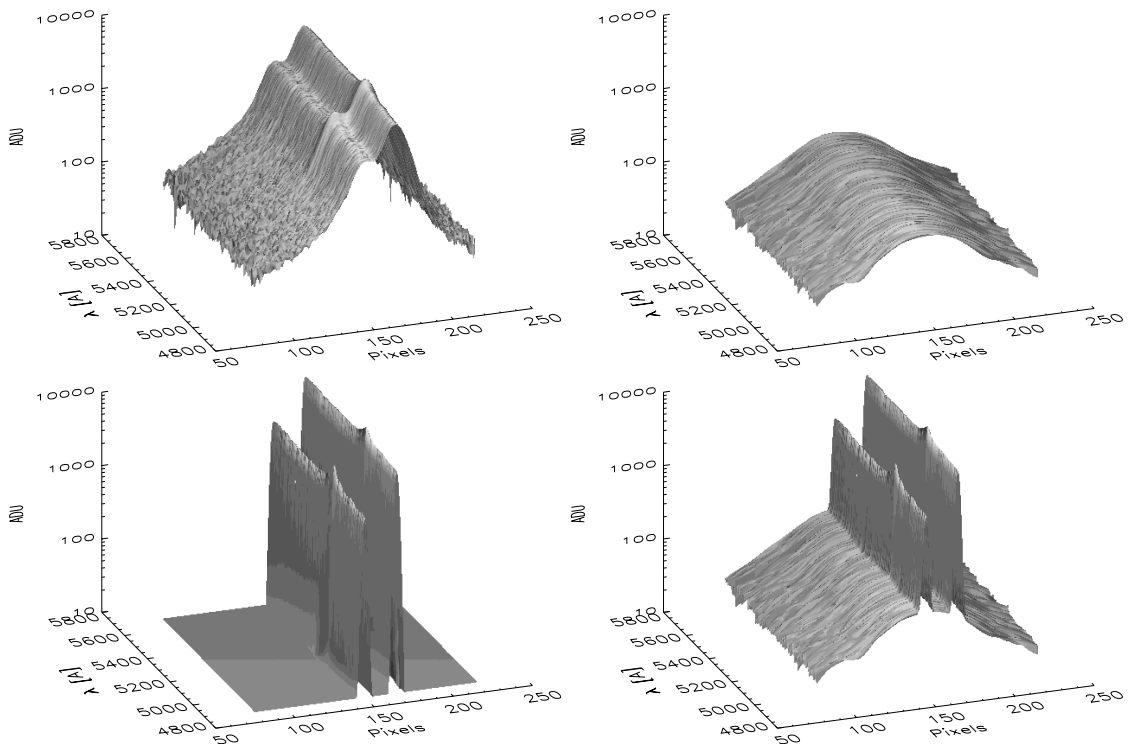


Figure 6.2: An example of the spatial deconvolution of a two-dimensional spectrum. *From left to right and top to bottom:* The original data  $\mathcal{D}_j(x_i)$ , the extended numerical background  $\mathcal{H}_j(x_i)$ , the punctual sources  $\mathcal{R}(x_i)$  and the result of the deconvolution, which is the sum of the extended background and the punctual sources.

### Computing the PSF $\mathcal{S}$

Deconvolving spectra requires a good knowledge of the instrumental PSF all along the wavelength range available. This condition is fulfilled as soon as the spectrum of a star or any other point source is recorded together with the spectrum of scientific interest. The construction of the PSF is carried out as with the image deconvolution algorithm, i.e., the PSF  $\mathcal{S}_j(x)$  is modeled as the sum of a one dimensional analytical Moffat profile  $\mathcal{M}_j(x)$  and of a numerical image  $\mathcal{Z}_j(x)$  containing all small residual differences between the Moffat

and the observed PSF  $\mathcal{T}_j(x) = (\mathcal{S}_j * \mathcal{R})(x)$

$$\mathcal{S}_j(x) = \mathcal{M}_j(x) + \mathcal{Z}_j(x) .$$

### The analytical component of the PSF $\mathcal{S}$

The analytical spatial profile at wavelength  $j$  is simply written as

$$\mathcal{M}_j(x) = a_j [1 + b_j (x - c_j)^2]^{-\beta_j}$$

where  $a_j$  is the intensity of the profile,  $b_j$  defines its width,  $c_j$  is its center along the spatial direction and  $\beta_j$  characterizes the wings of the profile.  $\mathcal{M}_j(x)$  is obtained by minimizing the  $\chi_{\mathcal{M}}^2$  between the observed PSF  $\mathcal{T}_j(x)$  and  $(\mathcal{M}_j * \mathcal{R})(x)$ . As a reminder,  $\mathcal{R}(x)$  is the chosen profile of the PSF after deconvolution. We have

$$\chi_{\mathcal{M}}^2 = \sum_{j=1}^M \sum_{i=1}^N \left( \frac{1}{\sigma_{i,j}} [(\mathcal{M}_j * \mathcal{R})(x) - \mathcal{T}_j(x)]_{x=x_i} \right)^2$$

where the  $i$  and  $j$  indices are respectively running along the spatial and spectral directions. As for the deconvolution, the center  $c_j$  of the spectrum at wavelength  $j$  is highly correlated to the position at neighbouring wavelengths. The same constraint can be applied to  $b_j$  and  $\beta_j$

$$\begin{aligned} \mathcal{L}_1 &= \sum_{j=1+W/2}^{M-W/2} \left[ c_j - \frac{1}{G} \sum_{j'=-W/2}^{W/2} g_{j'} c_{j+j'} \right]^2 \\ \mathcal{L}_2 &= \sum_{j=1+W/2}^{M-W/2} \left[ b_j - \frac{1}{G} \sum_{j'=-W/2}^{W/2} g_{j'} b_{j+j'} \right]^2 \\ \mathcal{L}_3 &= \sum_{j=1+W/2}^{M-W/2} \left[ \beta_j - \frac{1}{G} \sum_{j'=-W/2}^{W/2} g_{j'} \beta_{j+j'} \right]^2 \end{aligned}$$

where the function  $g$  is the same as before. Constructing the analytical Moffat component of the PSF can therefore be done by minimizing the function

$$\mathcal{C}_1 = \chi_{\mathcal{M}}^2 + \mu_1 \mathcal{L}_1 + \mu_2 \mathcal{L}_2 + \mu_3 \mathcal{L}_3 .$$

The choices of the three Lagrange multipliers  $\mu_1$ ,  $\mu_2$ ,  $\mu_3$  are not critical, in the sense that a PSF is never a perfect Moffat profile and an additional numerical component is mandatory to build  $\mathcal{S}_j(x)$  with the the required accuracy.

### The numerical component of the PSF $\mathcal{S}$

The small residual differences between the computed model  $\mathcal{M}_j(x)$  and the observed PSF  $\mathcal{T}_j(x)$  are given by

$$\mathcal{K}_j(x) = \mathcal{T}_j(x) - (\mathcal{M}_j * \mathcal{R})(x) .$$

These residuals are used to compute the numerical component  $\mathcal{Z}_j(x)$  by minimizing

$$\chi_{\mathcal{Z}}^2 = \sum_{j=1}^M \sum_{i=1}^N \left( \frac{1}{\sigma_{i,j}} [(\mathcal{R} * \mathcal{Z}_j)(x) - \mathcal{K}_j(x)]_{x=x_i} \right)^2 .$$

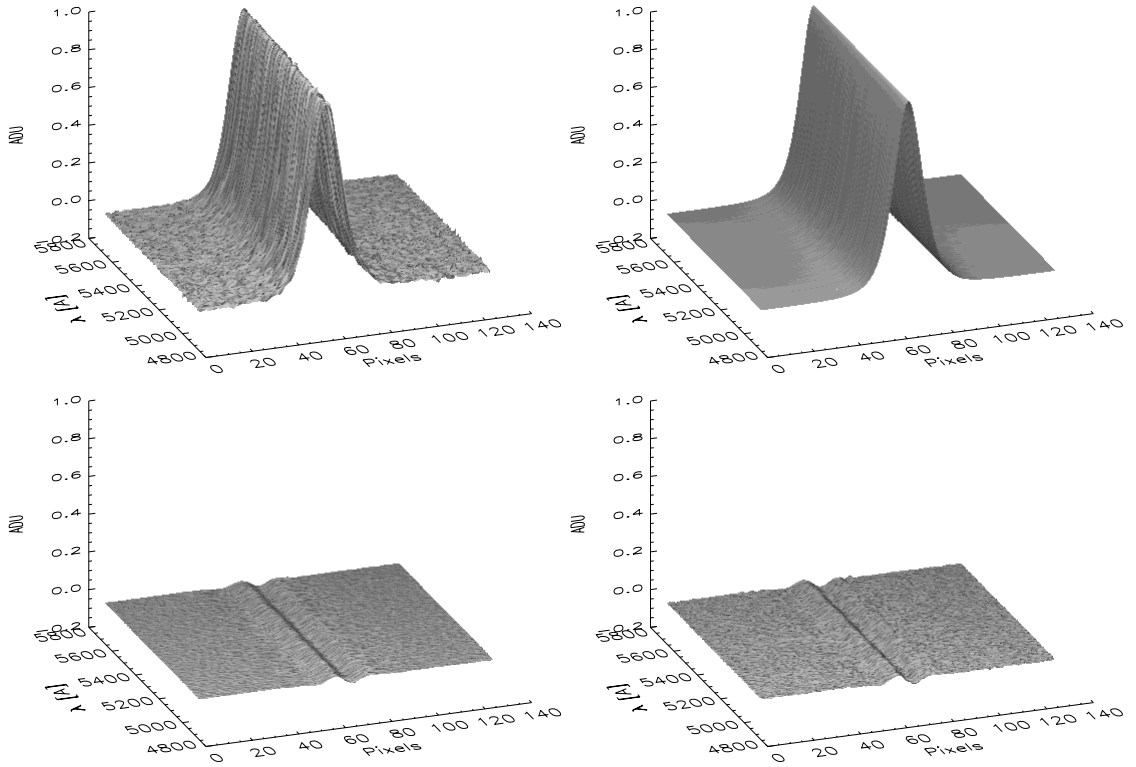


Figure 6.3: *From left to right and top to bottom:* The observed PSF  $\mathcal{T}_j(x_i)$  of a star, the fitted analytical Moffat profile  $\mathcal{M}_j(x_i)$ , the residuals  $\mathcal{K}_j(x_i)$ , and the slightly smoothed residuals  $\mathcal{Z}_j(x_i)$ . The final PSF  $\mathcal{S}_j(x_i)$  is the sum of the profile  $\mathcal{M}_j(x_i)$  and the residuals  $\mathcal{Z}_j(x_i)$ .

The residuals  $\mathcal{Z}_j(x)$ , just like the numerical background  $\mathcal{H}_j(x)$ , may be affected by noise enhancements with spatial frequencies forbidden by the sampling theorem. In order to filter these out and to ensure that  $\mathcal{Z}_j(x)$  is smooth on the length scale of the final resolution represented by the profile  $\mathcal{R}(x)$ , we need to minimize

$$\mathcal{L}_1 = \sum_{j=1}^M \sum_{i=1}^N \left( [\mathcal{Z}_j(x) - (\mathcal{R} * \mathcal{Z}_j)(x)]_{x=x_i} \right)^2 .$$

Because the PSF profile  $\mathcal{S}_j(x)$  is not expected to vary too much between neighbouring spectral resolution elements, we will also minimize

$$\mathcal{L}_2 = \sum_{j=1}^M \sum_{i=1}^N \left( \left[ \mathcal{Z}_j(x) - \frac{1}{G} \sum_{j'=-W/2}^{W/2} g_{j'} \mathcal{Z}_{j+j'}(x) \right]_{x=x_i} \right)^2 .$$

The determination of the numerical component of the PSF is then done by minimizing the function

$$\mathcal{C}_2 = \lambda \chi_{\mathcal{Z}}^2 + \mathcal{L}_1 + \mu \mathcal{L}_2 .$$

The Lagrange parameter  $\lambda$  is chosen so that  $\mathcal{Z}_j(x) * \mathcal{R}(x)$  matches at best  $\mathcal{K}_j(x)$  in the sense of a  $\chi^2$  and the final PSF  $\mathcal{S}_j(x)$  is simply the sum of  $\mathcal{M}_j(x)$  and  $\mathcal{Z}_j(x)$ .

The result of the process is a PSF  $\mathcal{S}_j(x)$  which incorporates seeing variations as a function of wavelength and takes into account atmospheric refraction. Observing with a Multi Object Spectrograph (MOS) will in most cases not only allow to observe the blended objects, but also to obtain simultaneously the spectra of one or more foreground stars. Observing several stars has the further advantage of allowing substantial improvement of the spatial sampling. Higher spatial resolution can then be achieved as well as a more accurate point source/background separation. In any case, either in long-slit spectroscopy or MOS, particular care should be paid to the centering of objects on the slits. The slit edges clip the PSF's wings. Although the deconvolution procedure can handle this, clipping has to be similar in the object spectrum and in the star spectra.

### 6.3 Spectroscopy with the Very Large Telescope

An essential piece of information still missing for numerous gravitationally lensed quasars is the redshift of the lensing galaxy. In order to change this situation, we devised a spectroscopic survey to measure these missing redshifts. The proposed survey was reviewed and accepted by the Observing Programs Committee (OPC) of the European Southern Observatory (ESO), which allocated us a total of 57 hours of observing time for three programs (074.A-0563, 075.A-0377, and 077.A-0155) at the Very Large Telescope (VLT) situated at Mount Paranal in Chile, see Fig. 6.4.



Figure 6.4: *Right:* The four 8m telescopes of the Very Large Telescope (VLT) of the European Southern Observatory (ESO) located at Mount Paranal, Chile. *Left:* The FOcal Reducer and low dispersion Spectrograph (FORs1) mounted on Kueyen, the second Unit Telescope (UT2) of the ESO-VLT. Image credit: ESO.

#### 6.3.1 Instrumental setup

The technical requirements for such a survey are high and demand both a good spatial sampling and deep exposures. Such requirements can only be reached with large telescopes like the VLT. Deep exposures are needed because of the faintness of the lensing galaxies which have typical apparent I-band magnitudes of 18 – 20 mag. Good spatial sampling

is necessary to extract the light of the faint galaxy from the glare of the much brighter quasar images. The angular separation of the quasar images is roughly  $1''$  with the lensing galaxy lying in between. Consequently, we need spectra with a spatial sampling of at least  $0.1''$  per pixel. The exposures should also be taken in good, but not exceptional, seeing conditions ( $0.8 - 1.0''$ ), which are best guaranteed in service mode. Finally, we should mention that the observations do not require photometric conditions and thin cirrus are acceptable. As we are mainly limited by photon noise introduced by the quasar images on the lensing galaxy, observing with one quarter of the moon is tolerable.

Our strategy is to later improve the spatial resolution of the spectra with the MCS deconvolution algorithm. As presented in Section 6.2, the algorithm requires the simultaneous observation of stars to compute the PSF. This is why we select the Multi-Object Spectroscopy (MOS) mode of the FOcal Reducer and low dispersion Spectrograph (FORs1, see Fig. 6.4). We choose the high resolution collimator to improve the spatial resolution. This instrumental configuration allows the simultaneous observation of a total of 9 objects over a field of view of  $3.4' \times 3.4'$  with a pixel scale of  $0.1''$ . Several slits are centered on foreground stars, and one is centered on the lensed system. The FORs spectrographs are equipped with an efficient atmospheric dispersion corrector (Avila et al., 1997) that allows to keep the same slit centering (within  $0.15''$ ) from  $4450$  to  $8650 \text{ \AA}$ . The mask is rotated to a Position Angle (PA) that corresponds to the alignment of two quasar images. This avoids clipping of the lensed images, which is important for the later spatial deconvolution of the spectra. The slits of the MOS mask are all  $19''$  long and  $0.7''$  or  $1.0''$  wide. The width is chosen in function of the quasar image configuration in order to minimize the lateral contamination by the quasar. This is particularly important for quadruply imaged quasars, where two images are aligned with the slit, while the two others lie outside but very close to the slit.

Our aim is to determine unknown redshifts, we therefore select the low dispersion grism G300V in combination with the GG435 order sorting filter. This favors wavelength coverage rather than high spectral resolution. This setup has a useful wavelength range  $4450 \text{ \AA} < \lambda < 8650 \text{ \AA}$  and a scale of  $2.69 \text{ \AA}$  per pixel in the spectral direction. The spectral resolution is given by the measured width  $\Delta\lambda$  of the sky emission lines, which yield a resolution  $R = \lambda/\Delta\lambda \simeq 300$  at the central wavelength  $\lambda = 5900 \text{ \AA}$ . This translates in velocity space to  $\Delta v = c\Delta\lambda/\lambda \simeq 1000 \text{ km s}^{-1}$ , which defines the expected accuracy of the measured redshifts  $z_l \simeq v_r/c$  of the order of  $\Delta z_l \simeq 0.001$ . This setup is hence well adapted for the measurement of redshifts lying in the range  $0.2 < z_l < 0.8$ , which corresponds to the most probable values for lensing galaxies.

In practice, our observation sequence consists of an acquisition image, a “through-slit” image to check the alignment of the objects in the slits, and a spectroscopic exposure. In order to reach a sufficiently high signal-to-noise we repeat this sequence several times for each gravitational lens. An example of one of the raw frames obtained for the target SDSS J0924+0219 is given in Fig. 6.5.

### 6.3.2 Data reduction

The spectra are bias subtracted and flat fielded using IRAF<sup>1</sup> standard routines. The flat fields for each slit are created from 5 dome exposures using cosmic ray rejection. They

<sup>1</sup>IRAF is distributed by the National Optical Astronomy Observatories, which are operated by the Association of Universities for Research in Astronomy, Inc., under cooperative agreement with the National Science Foundation.

are normalized by averaging 60 lines along the spatial direction, rejecting the 20 highest and 20 lowest pixels, then block replicating the result to match the physical size of the individual flat fields.

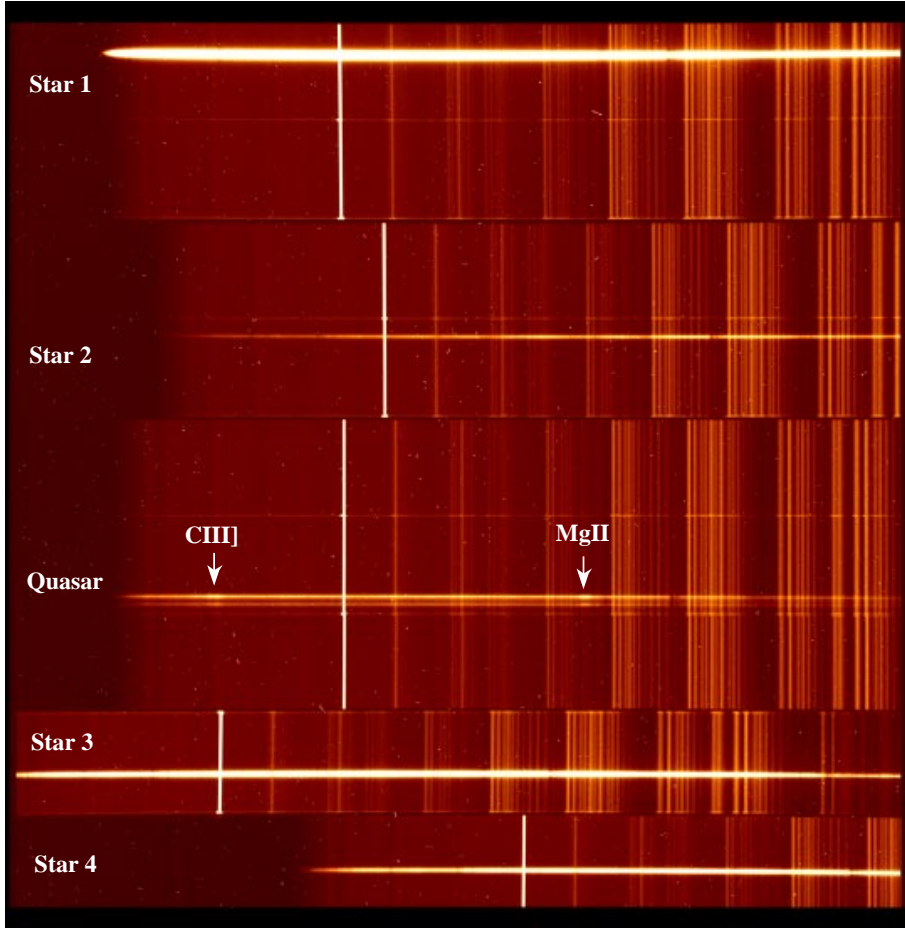


Figure 6.5: A raw frame obtained for the lensed quasar SDSS J0924+0219 with FORS1 in the MOS mode. There are nine slits in total. Four are centered on foreground stars and one on the images A and B of the lensed quasar. The C III] and Mg II broad emission lines of the quasar are well visible.

Wavelength calibration is obtained from the emission lines in the spectrum of helium-argon lamps. The wavelength solution is fitted in two dimension to each slit of the MOS mask. The fit uses a fifth-order Chebyshev polynomial along the spectral direction and a third-order Chebyshev polynomial fit along the spatial direction. Each spectrum is interpolated following this fit, using a cubic interpolation. This procedure ensures that the sky lines are well aligned with the columns of the CCD after wavelength calibration. The sky background is removed by subtracting a second-order Chebyshev polynomial fitted in the spatial direction to the areas of the spectrum that are not illuminated by the object.

Finally, we perform the cosmic ray removal. First, we shift the spectra in order to align them spatially (this shift is only a few tenths of a pixel). Second, we create a combined spectrum for each object (i.e. for the stars and for the lens) from the multiple exposures,

removing the 2 lower and 2 higher pixels, after applying appropriate flux scaling. The combined spectrum obtained in that manner is cosmic ray cleaned and used as a reference template to clean the individual spectra. We always check that neither the variable seeing, nor the variability of the quasar causes artificial loss of data pixels.

### 6.3.3 Flux calibration

The object spectra are taken in slightly different observing conditions, e.g., the airmass and seeing change, or thin cirrus appear. This can obviously affect the observed flux of the objects, but it can also induce color terms in the spectra. Before combining the different exposures of a given gravitational lens, these effects have to be corrected.

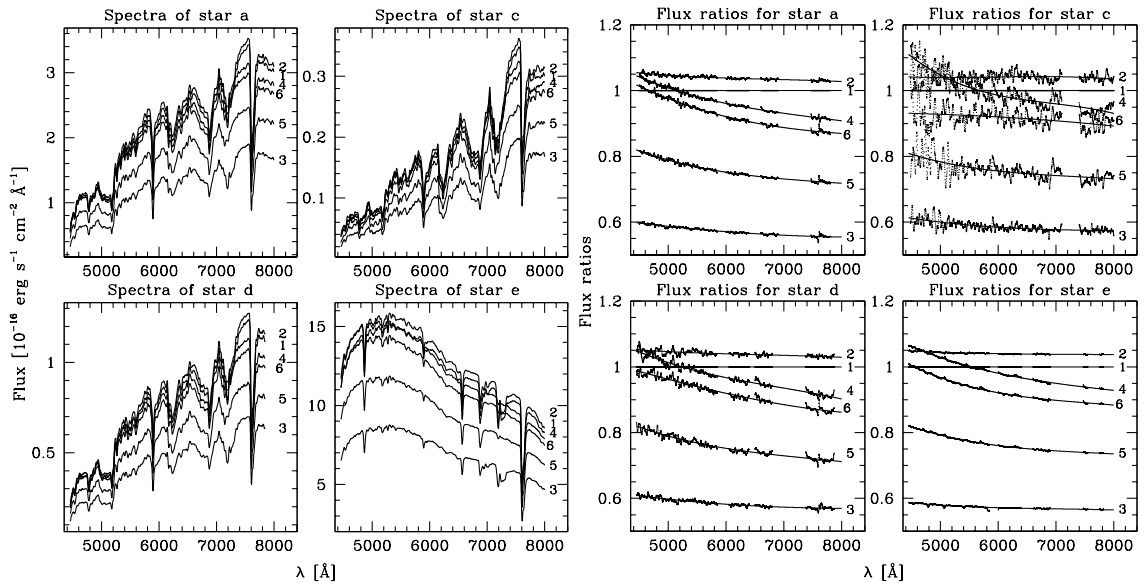


Figure 6.6: *Left:* The spectra of the four foreground stars observed simultaneously with SDSS J0924+0219. The index on the right of each spectrum indicates the exposure number. *Right:* The flux ratios between the first exposure and the 5 others, along with the third-order polynomial fits.

The task is not as easy as it may seem, because the lensed quasar images are expected to vary in time due to the intrinsic variability of the quasar, and/or extrinsic variability caused by microlensing. We therefore base our calibration method on the spectra of the foreground stars observed simultaneously with the lens (see Fig. 6.6). For each star, we compute the ratios between its spectra and the spectrum from a chosen reference exposure. The reference exposure is the one obtained in the best observing conditions. A third-order polynomial is then fit to the ratio spectra where we mask the small parts that are affected by strong atmospheric absorption. The derived ratio spectra and their corresponding polynomial fits are depicted in Fig. 6.6. For a given exposure, the ratio spectra are very similar from one star to another proving that the stars are not variable. We use the ratio spectra to compute the mean ratio spectrum corresponding to that exposure. For this calculation we exclude very faint stars having particular noisy spectra. The mean ratio spectrum is used to correct the spectrum of the objects. By repeating this for all

exposures, we perform an accurate relative flux calibration of the object spectra. Once this is done, we can combine the individual spectra of each object.

The final absolute flux calibration is based on the observation of spectrophotometric standard stars obtained with the same instrumental setup as the gravitational lenses. The spectra of the standard stars are used to determine the response curve of the instrument. The object spectra are finally corrected from the response curve and from atmospheric extinction using tabulated extinction curves.

### 6.3.4 Spatial deconvolution of the spectra

Even though the seeing on most spectra is good, the lensing galaxy is close enough to the bright quasar images to be affected by significant contamination from the wings of the PSF. For this reason, the spectral version of MCS deconvolution algorithm (Magain et al., 1998; Courbin et al., 2000) is used. This efficiently separates the spectrum of the lensing galaxy from the spectra of the quasar images. As described in Section 6.2, the algorithm uses the spatial information contained in the spectrum of a reference PSF, which is obtained from the slits positioned on the foreground stars. Using this reference PSF, the algorithm recovers the spectra of the quasar images, as well as the spectrum of the lensing galaxy.

### 6.3.5 Deconvolution without PSF stars

The VLT archives contain several spectroscopic data of lensed quasars, that can potentially be used to determine the redshift of the lensing galaxies. Most of these data are obtained with long-slit spectroscopy. Examples of such data are the observations acquired during the ESO-VLT program 077.A-0197 (PI: H.-W. Rix). This program was conducted simultaneously to our program 077.A-0155, but with a different instrumental setup. The main difference was that our program used the MOS mode, while the latter was based on long-slit spectroscopy. Long slits have the evident drawback that only the lensed system is observed and hence, there are no spectra of foreground stars in the data. Spectra of stars have proven to be very useful in the data processing described in Section 6.3, as they are used to determine both the relative flux calibration between different exposures and the reference PSF  $\mathcal{S}_j(x_i)$  necessary for the MCS deconvolution. Without stellar spectra, the task is more complicated and, indeed, Ofek et al. (2006) could only determine the redshift of the lensing galaxy in those objects where either the lensed quasar images are well separated ( $\Delta\theta > 1.4''$ ), or where the lensing galaxy is bright. The other more difficult cases require spatial deconvolution to extract the faint spectra of the lens.

In the following, we show how the spectrum of a gravitational lens can be recovered with the MCS algorithm even in the case of long-slit spectroscopy, where no stellar spectrum is available. Fortunately, in most cases the long slit of the spectrograph is aligned on two lensed quasar images with the galaxy lying in between. The idea is thus to use the spectra of the bright quasar images to infer the reference PSF. We present two test cases, where we have successfully applied this technique: the two lensed quasars QJ 0158–4325 and HE 0230–2130, see Fig. 6.7.

#### The lensing galaxy in QJ 0158–4325

The doubly imaged quasar QJ 0158–4325 has a redshift  $z_s = 1.290$  and an image separation of  $1.22''$ . It was first discovered in the Calán-Tololo Quasar survey (Maza et al.,



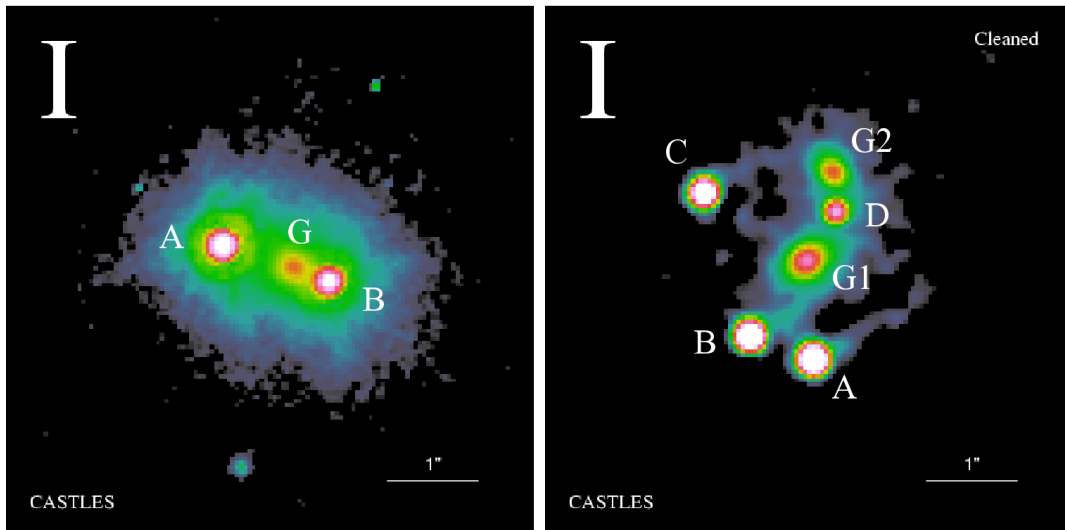


Figure 6.7: HST images of the lensed quasars QJ 0158–4325 (left) and HE 0230–2130 (right) obtained by Kochanek (2003a) in the I-band. North is up, and East to the left.

1995) and was called CTQ 414. It was confirmed to be a lensed quasar by Morgan et al. (1999). From the VLT archives we have retrieved a set of four long-slit spectra centered on the quasar images and on the lensing galaxy. The data were acquired during the program 077.A-0197 with the FOcal Reducer and low dispersion Spectrograph (FORS2) on 2006 September 19th and 22nd. The spectra were taken through an  $0.7''$  slit, under a mean seeing of  $1.28''$ . The pixel scale in the spatial direction is  $0.11''/\text{pixel}$ . Each spectrum has an exposure time of 1300 s, leading to a total time of 5200 s. The standard collimator is used in combination with the grism G200I without any filter. This gives a scale of  $4.86 \text{ \AA}/\text{pixel}$ , from 5500 to 11000  $\text{\AA}$ . The spectra were reduced using the method detailed in Section 6.3.

The FORS2 data do not contain any stars, and the lensing galaxy is weak and lies at  $0.4''$  of the quasar image B. This makes it particularly difficult to disentangle the light of the lens from the glare of the quasar images. We therefore modify our deconvolution strategy. We do not use stars, but rather the two bright quasar images to compute the PSF reference. To do so, we proceed in an iterative way. First, we mask the inner parts of the quasar images in the two-dimensional spectra, i.e. the parts where we expect the lens spectrum. We also attribute artificially large errors to the masked parts, and use these masked spectra to determine a first estimate of the reference PSF  $\mathcal{S}_j(x)$ . An illustration is given in Fig. 6.8. The quasar image B defines the left wing of the PSF, while quasar image A defines the right wing.

We take the HST astrometry of Morgan et al. (1999) as a first guess of the position of the lens relative to the quasar images. We then deconvolve the original data considering three point sources. Two are for the quasar images A and B, and one is for the lensing galaxy. Given the small apparent extent of the lens in the HST images, we do not expect a strong signal in the extended numerical background  $\mathcal{H}_j(x_i)$  and rather choose to model the lens as a point source. Along the deconvolution, the MCS algorithm optimizes the positions and intensities of the three point sources and, at the end, yields their individual spectra. We then start the iterative process, i.e. we re-convolve the retrieved two-dimensional lens

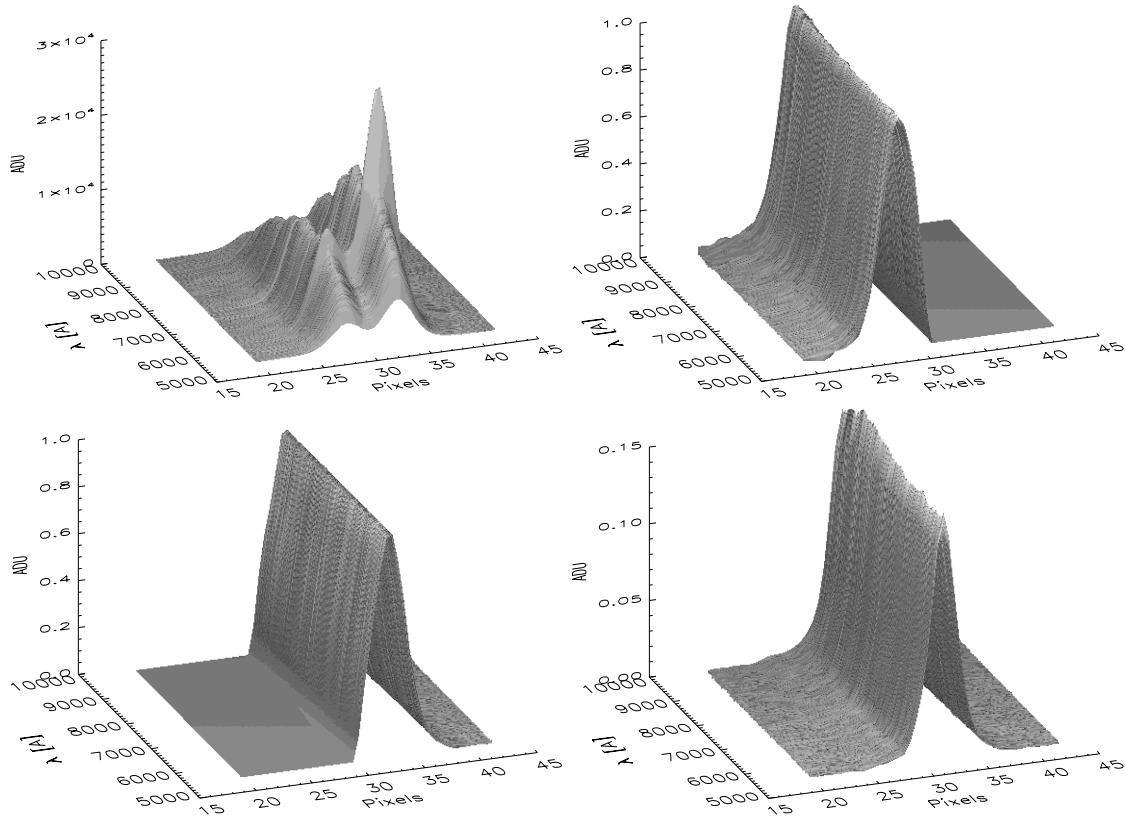


Figure 6.8: Computing the reference PSF  $\mathcal{S}_j(x_i)$  from the spectra of the quasar images. *From left to right and top to bottom:* The original data  $\mathcal{D}_j(x_i)$ , where the Mg II broad emission line of QJ 0158–4325 is well visible, the normalized spectrum of quasar image B (where image A is masked) used as a PSF  $\mathcal{T}_j(x_i)$ , the normalized spectrum of image A (where image B is masked) used as a second PSF  $\mathcal{T}_j(x_i)$ , and the derived reference PSF  $\mathcal{S}_j(x_i)$  used for the MCS deconvolution.

spectrum with the first guess PSF  $\mathcal{S}_j(x_i)$  and subtract it from the raw two-dimensional data. This provides us with a spectrum of the quasar images that is less affected by the lensing galaxy. We recompute  $\mathcal{S}_j(x_i)$  from these lens-subtracted data and proceed to a new deconvolution based on this new PSF. We repeat this procedure three times. We show in Fig. 6.9 the final one-dimensional spectrum of the lensing galaxy, smoothed with a  $24 \text{ \AA}$  box. The accuracy of the spectral decomposition is supported by the fact that no residual light of the quasar Mg II broad emission line is seen in the spectrum of the lensing galaxy. The lensing galaxy spectrum exhibits typical absorption lines of an elliptical galaxy, i.e. the G band,  $H\beta$ , Mg band, Fe II, Na D and  $H\alpha$ . Based on the position of these lines, we infer the redshift  $z_l = 0.317 \pm 0.001$  of the lens in QJ 0158–4325. This value is well compatible with the strong absorption line visible in the spectrum of quasar image B at about  $7767 \text{ \AA}$ , but absent in the spectrum of A. This feature is hence identified as being due to the Na D absorption (at  $5892 \text{ \AA}$ ) from the lens.

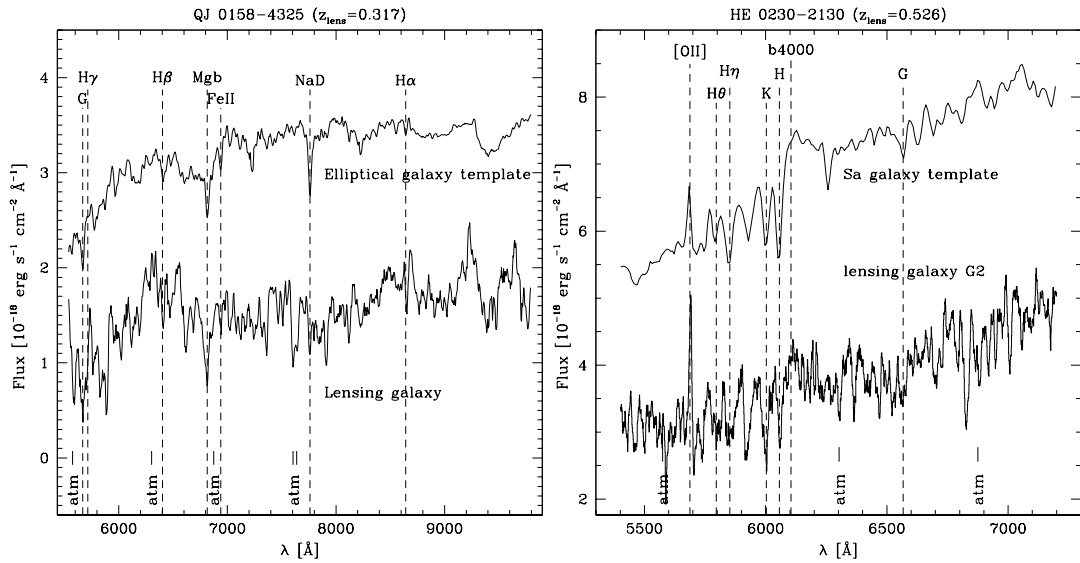


Figure 6.9: *Left*: Spectrum of the lensing galaxy in QJ 0158–4325. The template spectrum of a redshifted elliptical galaxy at  $z_l = 0.317$  is shown for comparison (Kinney et al., 1996). *Right*: Spectrum of the lens G2 in HE 0230–2130 with prominent [O II] emission. The template spectrum of a redshifted Sa spiral galaxy at  $z_l = 0.526$  is shown (Kinney et al., 1996). Atmospheric absorptions are indicated by the label *atm*.

### The second lensing galaxy in HE 0230–2130

In addition to the data of QJ 0158–4325, we retrieve VLT/FORS1 data from the archives for HE 0230–2130. This quadruply imaged  $z_s = 2.162$  quasar was discovered by Wisotzki et al. (1999). It has a maximum image separation of  $2.15''$  and two lensing galaxies. The main lensing galaxy, G1, is located between the four quasar images. We have already determined its redshift from our VLT/FORS1 MOS data. The second, fainter lens is located outside the area defined by the quasar images, close to the faint quasar image D (see Fig. 6.7). We show in the following how we determine the redshift of this second lens.

The archived data were acquired on October 18th 1999 for program 64.O-0259 (PI: L. Wisotzki) in the long-slit mode with the standard resolution collimator ( $0.2''$  per pixel), the G600R grism, and the order sorting filter GG435. The useful wavelength range is  $5250 < \lambda < 7450 \text{ \AA}$  with a pixel scale of  $1.08 \text{ \AA}$  in the spectral direction. The long slit is  $0.7''$  wide and aligned on quasar images B and D. We compute the approximate PSF  $\mathcal{S}_j(x_i)$  from the isolated quasar image B, and follow the same iterative procedure as described for QJ 0158–4325. After three iterations, we obtain the final lens spectrum shown in Fig. 6.9 and determine the redshift  $z_l = 0.526 \pm 0.002$  of the galaxy G2. The spectrum has a lower signal-to-noise than our MOS spectra and less accurate flux calibration, but it allows to measure well the redshift of lens G2, which displays prominent [O II] emission, contrary to lens G1.

### 6.3.6 Results

We have shown how the MCS deconvolution algorithm can be used to recover the spectrum of faint lensing galaxies that are hidden in the glare of bright quasar images. Once

these spectra are obtained, the redshifts of the galaxies are easily determined from the characteristic features present in the spectra. The Ca II H & K absorption lines are obvious in most cases, as well as the 4000 Å break, the G band typical for CH absorption, the Mg band, and the H $\beta$  and Fe II absorption lines. These features, except the 4000 Å break, are used to compute the redshift. The  $1\sigma$  error is inferred from the standard deviation between all the measurements on the individual lines. We summarize the determined redshifts in Table 6.1. All of them, except the redshift of the lens in Q 0158–4325, have been published (Eigenbrod et al., 2006a,b, 2007). The corresponding papers are attached at the end of this chapter.

Table 6.1: Results for the redshift determination of the lensing galaxies of sixteen lensed quasars. We also give the lens redshift estimates that were published prior to our analysis. We indicate if these redshifts are determined from absorption features (*abs.*) observed in the spectra of the lensed quasar or if they are estimated from photometry (*phot.*).

	Object	$z_l$	Previously published $z_l$
1	HE 0047–1756	$0.407 \pm 0.001$	$\gtrsim 0.6$ <i>phot.</i> (Wisotzki et al., 2004)
2	Q 0142–100 $\equiv$ UM 673	$0.491 \pm 0.001$	0.493 <i>abs.</i> (Surdej et al., 1988)
3	Q 0158–4325 $\equiv$ CTQ 414	$0.317 \pm 0.001$	none
4	HE 0230–2130, G1	$0.523 \pm 0.001$	$\lesssim 0.6$ <i>phot.</i> (Wisotzki et al., 1999)
	HE 0230–2130, G2	$0.526 \pm 0.002$	none
5	SDSS J0246–0825	$0.723 \pm 0.002$	0.724 <i>abs.</i> (Inada et al., 2005)
6	HE 0435–1223	$0.454 \pm 0.001$	0.3 – 0.4 <i>phot.</i> (Wisotzki et al., 2002)
7	SDSS J0806+2006	$0.573 \pm 0.001$	0.573 <i>abs.</i> (Inada et al., 2006)
8	SDSS J0924+0219	$0.394 \pm 0.001$	0.4 <i>phot.</i> (Inada et al., 2003)
9	FBQ 0951+2635	$0.260 \pm 0.002$	0.21 <i>phot.</i> (Kochanek et al., 2000)
10	BRI 0952–0115	$0.632 \pm 0.002$	0.41 <i>phot.</i> (Kochanek et al., 2000)
11	SDSS J1138+0314	$0.445 \pm 0.001$	none
12	SDSS J1226–0006	$0.517 \pm 0.001$	none
13	SDSS J1335+0118	$0.440 \pm 0.001$	$\lesssim 0.5$ <i>phot.</i> (Oguri et al., 2004)
14	Q 1355–2257 $\equiv$ CTQ 327	$0.702 \pm 0.001$	0.4 – 0.6 <i>phot.</i> (Morgan et al., 2003)
15	WFI J2033–4723	$0.661 \pm 0.001$	0.4 <i>phot.</i> (Morgan et al., 2004)
16	HE 2149–2745	$0.603 \pm 0.001$	0.4 – 0.5 <i>phot.</i> (Kochanek et al., 2000)

## 6.4 The lensed quasar SDSS J0924+0219

In Section 6.3, we have presented our spectroscopic survey with a specific focus on the determination of the lens redshifts. However, in most cases we have centered the slit of the spectrograph on both the lensing galaxy and the quasar images. Hence, additional results of this survey are the spectra of the lensed quasar images. Our observing strategy consists of multiple spectroscopic exposures taken at different epochs. The exposures for a single lensed quasar are sometimes a few weeks to months apart and are hence, interesting to detect potential flux variations induced by microlensing. These fluctuations are expected to occur on typical time scales of a few months and can produce chromatic effects in the

spectra of the quasar images (see Chapter 7).

In the present section, we focus on the lensed quasar SDSS J0924+0219 discovered in the course of the Sloan Digital Sky Survey (SDSS) and having a redshift  $z_s = 1.524$  (Inada et al., 2003). This object is particularly interesting in several aspects. First, it has an anomalous image flux ratios, the origin of which is unclear. It has been argued that the faintest image of SDSS J0924+0219, which is located at a saddle point of the arrival-time surface, could be demagnified either from star microlensing (Schechter et al., 2004; Keeton et al., 2006) or subhalos microlensing (Kochanek & Dalal, 2004). Second, we spatially deconvolve HST images of SDSS J0924+0219, which reveal a double Einstein ring. One ring corresponds to the lensed host galaxy of the quasar, while the other bluer ring corresponds to another source. It is not excluded that this second source is at a different redshift than the quasar. If this is true, SDSS J0924+0219 might be a unique object to break the mass-sheet degeneracy (see Section 4.10).

From our spectroscopic data we have already determined the redshift  $z_l = 0.394 \pm 0.001$  of the lensing galaxy. These data have been acquired on two epochs separated by two weeks. This is an interesting time span for studying the quasar variability and for the potential detection of microlensing. For the two dates, the flux ratio between quasar images A and B remain mostly the same in the continuum and in the broad emission lines. However, there are obvious and asymmetric changes in some of the quasar broad emission lines. Microlensing of the broad emission line region is the most probable explanation for this. These variations give interesting information on the geometry of the broad emission line region. For example and based on our data, Popović (2006) describes a two-component model with one region contributing to the broad line cores and one additional emitting region contributing to the broad line wings.

We have also retrieved existing HST/NICMOS and ACS images of the object from the HST archives. We deconvolve these images with the MCS algorithm (Magain et al., 1998) to better unveil the double Einstein ring. The lensed host galaxy adds further constraints for the modeling of the lens, which has proven to be difficult. The lens ellipticity and position angle measured in the HST images are hard to reconcile with simple models without external shear. We also notice a discrepancy between the models constrained by the rings only and the ones constrained solely by the positions of the quasar images. These facts support the presence of substructures in the lens of SDSS J0924+0219 situated toward the demagnified image D. Finally, the range of time delays predicted by the different lens models is large and sensitive to the presence of external shear and to the main lens ellipticity and position angle. The measurement of the time delays might therefore prove extremely useful to better determine the mass distribution in this lens. The detailed analysis of this lensed quasar is published (Eigenbrod et al., 2006a) and the corresponding paper can be found at the end of this chapter.

## 6.5 Discussion

We have determined the redshift of the lensing galaxies in sixteen gravitationally lensed quasars using both data of our spectroscopic survey and data from the VLT archives. Our procedure combines the high quality VLT data with the MCS deconvolution algorithm, and shows how a lens redshift can be determined even in the difficult cases where the lens is faint and lies close to the bright quasar images.

If we compare our results with the previously published estimates of the lens redshifts,

we see that photometric redshift estimates are in general not very accurate indicators of the true redshift. Absorption lines seen in the spectra of the lensed quasar images are much better indicators, especially when several lines are observed. However, caution should be used in the identification of the lines, particularly when several absorption systems are present along the line-of-sight of the quasar.

Our lens redshifts for the two time-delay lenses FBQ 0951+2635 and HE 2149–2745 are not compatible with previous estimates. We find  $z_l = 0.260 \pm 0.002$  instead of  $z_l = 0.21$  for the first and  $z_l = 0.603 \pm 0.001$  for the second, instead of  $z_l = 0.495 \pm 0.010$ . These new lens redshifts have a direct impact on several previous studies. Indeed, HE 2149–2745 is one of lens systems that has been used to argue possible low  $H_0$  values from the time-delay method (e.g., Kochanek, 2002, 2003b). The new redshift significantly increases the derived  $H_0$  thereby weakening the possible low  $H_0$  problem (e.g., Oguri, 2007).

After submission of our results, Ofek et al. (2006) reported redshift measurements for a number of lensed quasar systems, five of which overlap with our sample. In all five cases, their measurements confirm ours. Their results are HE 0047–1756,  $z_l = 0.408$ , HE 0230–2130,  $z_l = 0.522$ , HE 0435–1223,  $z_l = 0.455$ , SDSS J0924+0219,  $z_l = 0.393$ , and WFI J2033–4723,  $z_l = 0.658$ , all with uncertainties of 0.001.

The absence of emission lines in the spectra of the lensing galaxies indicate that all the observed lenses, except maybe for the secondary lens G2 in HE 0230–2130 which has strong [O II] emission, are gas-poor early-type galaxies. This is not surprising as it is well known that strong lensing favors early-type over late-type galaxies, and massive galaxies over dwarfs (e.g., Turner et al., 1984; Fukugita & Turner, 1991). Elliptical galaxies, despite their smaller number, are hence several times more important as lens systems than spiral galaxies.

In analyzing data of the VLT archives, we have shown that multi-object spectroscopy should definitely be preferred to long-slit spectroscopy, if the data is planned to be spatially deconvolved. The additional spatial information contained in the two-dimensional spectra of foreground stars is essential for an accurate deconvolution of the data, and can easily be obtained in multi-object spectroscopy. Furthermore, the stars can be used to perform a relative flux calibration between different exposures, leading to an accurate final flux calibration of the lens spectra. In this context, integral-field spectroscopy is also not a good alternative to multi-object spectroscopy, because of the weaker sensitivity of integral-field spectroscopy, which is problematic for this kind of project.

During our spectroscopic survey and analysis, we have focused on the spectra of the lensing galaxies. However, in most cases we have centered the slit of the spectrograph on both the lensing galaxy and two quasar images. Hence, additional results of this survey are the spectra of the lensed quasar images. The spectroscopic exposures are taken at different epochs, and are sometimes a few weeks apart. Hence, as shown for SDSS J0924+0219, these observations can be used to study the quasar variability and potentially also chromatic flux variations induced by microlensing. The latter provide information on the geometry and dimension of the broad-line and continuum emitting regions (e.g., Richards et al., 2004; Popović, 2006).

The problem of unknown lens redshifts is still not solved. Even though we could contribute a little to its resolution, there are continuously new lensed quasars that are discovered (e.g., the five new lensed quasars found by Inada et al., 2008), and not all of them have a determined lens redshift. It will be important in the future to repeat the experience for other lensing galaxies and hence, increase the sample of lenses with known

---

lens redshifts. This is important for several applications. For instance, Vuissoz et al. (2008) measured the time delays in WFI J2033–4723, and inferred an estimate of  $H_0$  via the time-delay method, which requires a well determined lens redshift. Similarly, in the near future several other lensed quasars, that are currently monitored by the COSMOGRAIL project, will benefit from the redshift measurements. This will finally provide a robust determination of  $H_0$ , since several time-delay lenses can be combined to infer a better estimate of  $H_0$  (e.g., Oguri, 2007; Coles, 2008).

Another application using lens redshifts is possible, if a sufficiently large number of gravitational lenses with measured redshifts is established. Such a lens sample can be used to compute statistics that constrain the density of dark energy (e.g., Fukugita et al., 1990; Turner, 1990). Indeed, the probability that a distant object is strongly lensed is proportional to the number of possible lensing objects along the line of sight and thus, quite sensitive to dark energy. This method has been applied in several studies (e.g., Kochanek, 1996; Falco et al., 1998; Chiba & Futamase, 1999), but their results have been limited by the small size of existing lens samples, as well as poor knowledge of source and lens populations (Maoz, 2005). Increasing the number of lensed quasars with known lens redshifts is therefore imperative. (e.g., Kochanek, 1996; Falco et al., 1998; Chiba & Futamase, 1999). Recently, Oguri et al. (2008) considered a larger sample of lens redshifts (including those determined in this thesis) and obtained a better constrained value of  $\Omega_{\Lambda 0} = 0.74^{+0.11}_{-0.15}$  (stat.)  $^{+0.13}_{-0.06}$  (syst.) for a cosmological constant model ( $w = -1$ ). Increasing the number of known lens redshifts will further improve the accuracy of this application, and will help to obtain better estimates of cosmological parameters.





**6.6 Paper presenting the determination of the redshift of the lensing galaxy, the quasar spectral variability, and the Einstein rings in SDSS J0924+0219**

*COSMOGRAIL: the COSmological MONitoring  
of GRAvItational Lenses*

*II. SDSS J0924+0219: the redshift of the lensing galaxy,  
the quasar spectral variability, and the Einstein rings*

A. Eigenbrod, F. Courbin, S. Dye, G. Meylan, D. Sluse, P. Saha, C. Vuissoz, &  
P. Magain

*Astronomy & Astrophysics, 2006, 451, 747*



## COSMOGRAIL: the COSmological MONitoring of GRAVitational Lenses

### II. SDSS J0924+0219: the redshift of the lensing galaxy, the quasar spectral variability and the Einstein rings<sup>\*</sup>

A. Eigenbrod<sup>1</sup>, F. Courbin<sup>1</sup>, S. Dye<sup>2</sup>, G. Meylan<sup>1</sup>, D. Sluse<sup>1</sup>, C. Vuissoz<sup>1</sup>, and P. Magain<sup>3</sup>

<sup>1</sup> Laboratoire d'Astrophysique, École Polytechnique Fédérale de Lausanne (EPFL), Observatoire, 1290 Sauverny, Switzerland  
 e-mail: alexander.eigenbrod@epfl.ch

<sup>2</sup> School of Physics and Astronomy, Cardiff University, 5 The Parade, Cardiff, CF24 3YB, UK

<sup>3</sup> Institut d'Astrophysique et de Géophysique, Université de Liège, Allée du 6 août 17, Sart-Tilman, Bât. B5C, 4000 Liège, Belgium

Received 26 October 2005 / Accepted 7 February 2006

#### ABSTRACT

**Aims.** To provide the observational constraints required to use the gravitationally lensed quasar SDSS J0924+0219 for the determination of  $H_0$  from the time delay method. We measure here the redshift of the lensing galaxy, we show the spectral variability of the source, and we resolve the lensed host galaxy of the source.

**Methods.** We present our VLT/FORS1 deep spectroscopic observations of the lensed quasar SDSS J0924+0219, as well as archival HST/NICMOS and ACS images of the same object. The two-epoch spectra, obtained in the Multi Object Spectroscopy (MOS) mode, allow for very accurate flux calibration and spatial deconvolution. This strategy provides spectra for the lensing galaxy and for the quasar images A and B, free of any mutual light contamination. We deconvolve the HST images as well, which reveal a double Einstein ring. The mass distributions in the lens, reconstructed in several ways, are compared.

**Results.** We determine the redshift of the lensing galaxy in SDSS J0924+0219:  $z_{\text{lens}} = 0.394 \pm 0.001$ . Only slight spectral variability is seen in the continuum of quasar images A and B, while the C III], Mg II and Fe II emission lines display obvious changes. The flux ratio between the quasar images A and B is the same in the emission lines and in the continuum. One of the Einstein rings found using deconvolution corresponds to the lensed quasar host galaxy at  $z = 1.524$  and a second bluer one, is the image either of a star-forming region in the host galaxy, or of another unrelated lower redshift object. A broad range of lens models give a satisfactory fit to the data. However, they predict very different time delays, making SDSS J0924+0219 an object of particular interest for photometric monitoring. In addition, the lens models reconstructed using exclusively the constraints from the Einstein rings, or using exclusively the astrometry of the quasar images, are not compatible. This suggests that multipole-like structures play an important role in SDSS J0924+0219.

**Key words.** gravitational lensing – cosmology: cosmological parameters – quasars: individual: SDSSJ0924+0219 – dark matter

### 1. Introduction

COSMOGRAIL is a multi-site optical monitoring campaign of lensed quasars. Following the original work by Refsdal (1964), its goal is to measure, with an accuracy close to one percent (Eigenbrod et al. 2005), the so-called time delay between the images of most gravitationally lensed quasars. These time delays are used in combination with lens models and detailed observations of individual systems to infer the value of the Hubble parameter  $H_0$ , independent of any standard candle (e.g., reviews by Courbin et al. 2002; Kochanek 2005a).

The present work is devoted to the quadruply imaged quasar SDSS J0924+0219 (Inada et al. 2003) at  $z = 1.524$ , discovered

in the course of the Sloan Digital Sky Survey (SDSS). This object is particularly interesting because of its anomalous image flux ratios, the origin of which is unclear. It has been argued that the faintest image of SDSS J0924+0219, which is located at a saddle point of the arrival-time surface, could be demagnified either from star microlensing (Schechter et al. 2004; Keeton et al. 2006) or subhalos microlensing (Kochanek & Dalal 2004).

We analyse here our deep optical spectra of SDSS J0924+0219 obtained with the ESO Very Large Telescope (VLT). These spectra are used to: 1- measure the redshift of the lensing galaxy; 2- estimate the spectral variability of the quasar; 3- measure the flux ratio between images A and B of SDSS J0924+0219, in the continuum and the broad emission lines. Hubble Space Telescope (HST) ACS and NICMOS images from the STScI archives are deconvolved using the MCS algorithm (Magain et al. 1998) which unveils two Einstein rings. One of the rings corresponds to the host galaxy of the quasar source and is used to constrain the lens models. The second one

<sup>\*</sup> Based on observations made with the ESO-VLT Unit Telescope 2 Kueyen (Cerro Paranal, Chile; Program 074.A-0563, PI: G. Meylan) and on data obtained with the NASA/ESA Hubble Space Telescope (Program HST-GO-9744, PI: C. S. Kochanek) and extracted from the data archives at the Space Telescope Science Institute, which is operated by the Association of Universities for Research in Astronomy, Inc., under NASA contract NAS 5-26555.

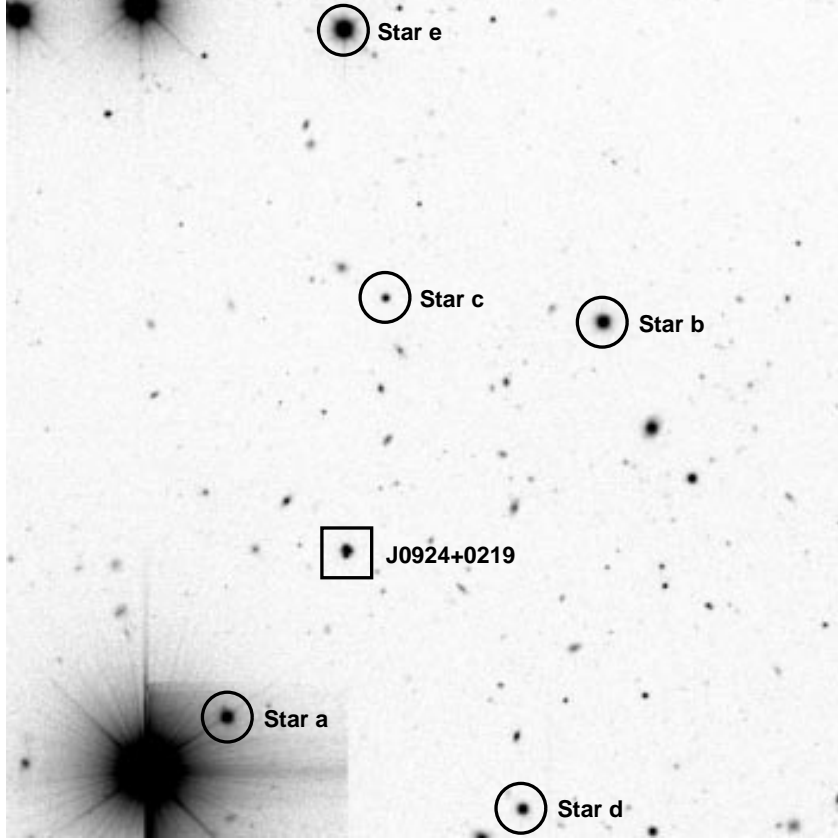


**Fig. 1.** *R*-band VLT image of SDSS J0924+0219, where objects are labeled following Inada et al. (2003). The stars a, c, d, and e are used to compute the PSF spectrum (see text). Only stars a, d and e are used to derive the relative flux calibration between each MOS mask. The field of view is  $3.4' \times 3.4'$ , North is to the top, East to the left.

is probably due to a star-forming region in the host galaxy of the quasar source or to another unrelated object.

## 2. VLT spectroscopy

### 2.1. Observations

Our spectroscopic observations of SDSS J0924+0219 are part of a low dispersion spectroscopic survey aimed at measuring all unknown lens redshifts. They are acquired with the FOcal Reducer and low dispersion Spectrograph (FORs1), mounted on the ESO Very Large Telescope, used the MOS mode (Multi Object Spectroscopy) and the high resolution collimator. This configuration allows the simultaneous observation of a total of 8 objects over a field of view of  $3.4' \times 3.4'$  with a pixel scale of  $0.1''$  (Fig. 1). The G300V grism, used in combination with the GG435 order sorting filter, leads to the useful wavelength range  $4450 \text{ \AA} < \lambda < 8650 \text{ \AA}$  and to a scale of  $2.69 \text{ \AA}$  per pixel in the spectral direction. This setup has a spectral resolution  $R = \lambda/\Delta\lambda \approx 300$  at the central wavelength  $\lambda = 5900 \text{ \AA}$ , which translates in velocity space to  $\Delta v = c\Delta\lambda/\lambda \approx 1000 \text{ km s}^{-1}$ .

The slitlets of the MOS mask are all  $19''$  long and  $0.7''$  wide, which both avoids lateral contamination by the quasar image C and matches well the seeing values during the observations. Four slits were centered on the foreground stars a, c, d, e, while a fifth slit is centered on images A and B of SDSS J0924+0219, after rotation of the mask to a suitable Position Angle (PA) (Fig. 2).

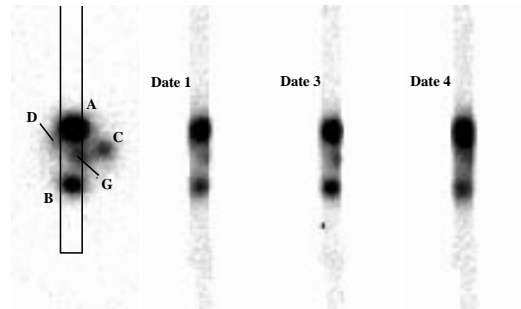


**Fig. 2.** *R*-band images of SDSS J0924+0219. A short 30 s exposure is shown on the left, where the quasar images A, B, C and D as well as the lensing galaxy, are indicated. The seeing is  $0.37''$  in this image and the pixel scale is  $0.10''$ . The position of the  $0.70''$  slitlets is also indicated. They correspond to three epochs of observations with very different seeing (see Table 1). The slit has not moved at all between the exposures, even when taken 15 days apart.

The spectra of the stars are used both to compute the reference Point Spread Function (PSF) needed for the deconvolution and to carry out a very accurate relative flux calibration. “Through-slit” images acquired just before exposures #1, #3, #4 in order to check the mask alignment are displayed in Fig. 2.

## 2.2. Reduction and deconvolution

The spectra are bias subtracted and flat-fielded using IRAF<sup>1</sup>. The flat fields for each slitlet are created from 5 dome exposures, using cosmic ray rejection. They are normalized by averaging 60 lines along the spatial direction, rejecting the 20 highest and 20 lowest pixels, then block replicating the result to match the physical size of the individual flat fields.

Wavelength calibration is obtained from numerous emission lines in the spectrum of Helium-Argon lamps. The wavelength solution is fitted in two dimension to each slitlet of the MOS mask. The fit uses a fifth-order Chebyshev polynomial along the spectral direction and a third-order Chebyshev polynomial fit along the spatial direction. Each spectrum is interpolated following this fit, using a cubic interpolation. This procedure ensures that the sky lines are well aligned with the columns of the CCD after wavelength calibration. The wavelength solution with respect to the reference lines is found to be very good, with an rms scatter better than 0.2 Å for all spectra.

The sky background is then removed by fitting a second-order Chebyshev polynomial in the spatial direction to the areas of the spectrum that are not illuminated by the object.

Finally, we perform the cosmic ray removal as follows. First, we shift the spectra in order to align them spatially (this shift is only a few tenths of a pixel). Second, we create a combined spectrum for each object from the 6 exposures, removing the 2 lower and 2 higher pixels, after applying appropriate flux scaling. The combined spectrum obtained in that way is cosmic ray cleaned and used as a reference template to clean the individual spectra. We always check that neither the variable seeing, nor the variability of the quasar causes artificial loss of data pixels.

Even though the seeing on most spectra is good, the lensing galaxy is close enough to the brightest quasar images A and B to be affected by significant contamination from the wings of the PSF. For this reason, the spectral version of MCS deconvolution algorithm (Magain et al. 1998; Courbin et al. 2000) is used in order to separate the spectrum of the lensing galaxy from the spectra of the quasar images. The MCS algorithm uses the spatial information contained in the spectrum of a reference PSF, which is obtained from the slitlets positioned on the four isolated stars a, c, d, and e (Fig. 1). The final normalized PSF is a combination of the four PSF spectra. The six individual spectra are deconvolved separately, extracted, flux calibrated as explained in Sect. 2.3 and combined. The spectrum of the lensing galaxy is extracted from the “extended channel” of the deconvolved data, while the spectra of the quasar images are extracted from the “point-source channel” (see Courbin et al. 2000).

## 2.3. Flux calibration

Our absolute flux calibration is based on the spectrum of the spectrophotometric standard star Feige 66 taken on the night of 2005 January 16. The response function of the grism is determined for this single epoch. It is cross calibrated using stars observed in each MOS mask in order to obtain a very accurate calibration across all epochs. The spectra of four stars are displayed in Fig. 3, without any deconvolution and having used a 4” aperture for extraction. We find significant differences in flux between the six epochs, that need to be corrected for. The

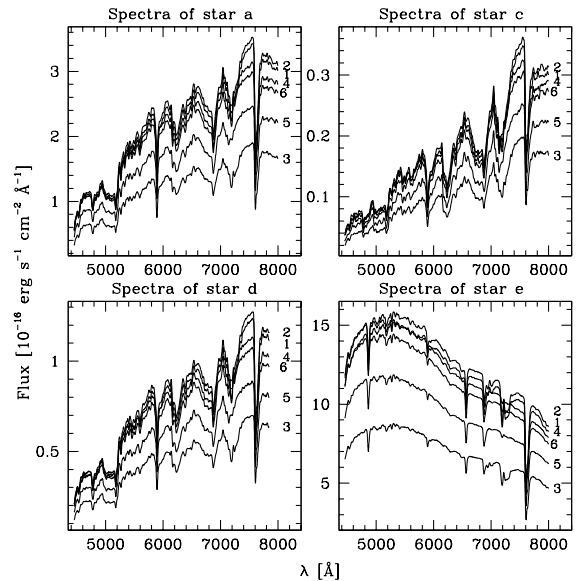


**Fig. 3.** The spectra of the foreground stars. The index on the right of each spectrum indicates the exposure number, following Table 1. Flux differences are mainly due to the presence of light clouds on observation dates #3, #5 and #6.

**Table 1.** Journal of the VLT spectroscopic observations of SDSS J0924+0219. The seeing is measured on the spectrum of the PSF stars. The exposure time is 1400 s for each of the 6 epochs.

ID	Date	Seeing ["]	Airmass	Weather
1	14/01/2005	0.66	1.188	Photometric
2	14/01/2005	0.59	1.150	Photometric
3	14/01/2005	0.46	1.124	Light clouds
4	01/02/2005	0.83	1.181	Photometric
5	01/02/2005	0.97	1.146	Light clouds
6	01/02/2005	0.84	1.126	Light clouds

main causes for these differences are variable seeing and variable extinction due to thin cirrus during some of the observations (Table 1). The effect of mask misalignment is excluded, as can be seen from the image-through-slit of Fig. 2.

Assuming that the intrinsic flux of the foreground stars has not varied between the six exposures, and taking the data #1 of Table 1 as a reference, we derive the flux ratio between this reference epoch and the six other dates, for each star. These curves, fitted with a third-order polynomial, are shown in Fig. 4. The corrections computed in this way are found to be very stable across the mask: the curves obtained for two different stars only showed slight oscillations with an amplitude below 2%. This is also the accuracy of the flux correction between different epochs. A mean correction curve is then computed for each epoch from all stars, except star c which is much fainter than the others, and is applied to the deconvolved spectra of the quasars and of the lensing galaxy.

## 3. Extracted spectra

### 3.1. The lensing Galaxy

The six deconvolved spectra of the lensing galaxy are extracted, combined, and smoothed with a 5 Å box (2 pixels). Figure 5 shows the final one-dimensional spectrum, where the Ca II H & K absorption lines are obvious, as well as the 4000 Å break,

<sup>1</sup> IRAF is distributed by the National Optical Astronomy Observatories, which are operated by the Association of Universities for Research in Astronomy, Inc., under cooperative agreement with the National Science Foundation.

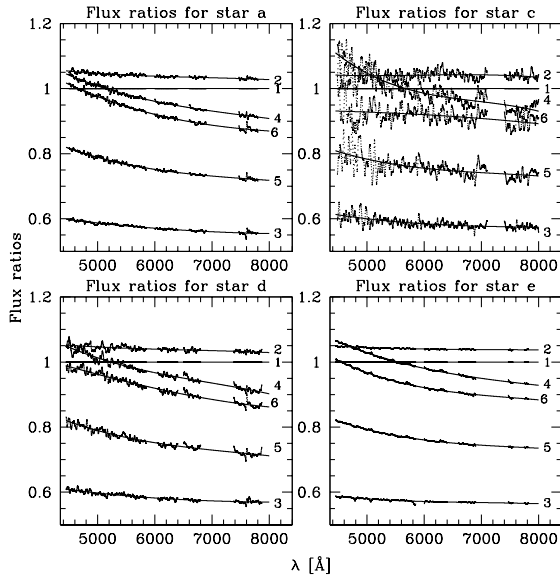


**Fig. 4.** Flux ratios between Date #1 and the 5 others, along with the third-order polynomial fits. We use the ratios of the 3 stars: a, d and e to determine the mean correction applied to the quasar. Star c, which is much fainter than the others, is excluded from the final calibration. The (small) parts of the spectra with strong atmospheric absorption are masked during the polynomial fit. The peak-to-peak differences between the ratios computed using star a, d and e, differ by less than 2%.

the G-band typical for CH absorption, the Mg band, and the  $H\beta$ , and Fe II absorption lines. These features yield a mean redshift of  $z_{\text{lens}} = 0.394 \pm 0.001$ , where the  $1-\sigma$  error is the standard deviation between all the measurements on the individual lines, divided by the square root of the number of lines used. We do not consider the 4000 Å break in these calculations. This spectroscopic redshift falls very close to the photometric estimate of  $z = 0.4$  by Inada et al. (2003), and agrees with the spectroscopic redshift of Ofek et al. (2005). In addition, the absence of emission lines confirms a gas-poor early-type galaxy. No trace of the quasar broad emission lines is seen in the spectrum of the lensing galaxy, indicative of an accurate decomposition of the data into the extended (lens) and point source (quasar images) channels.

### 3.2. The quasar images

The mean spectra of quasar images A and B are shown in Fig. 6, smoothed with a 5 Å box. The Al III], Si III], C III], [Ne IV] and Mg II broad emission lines are clearly identified. A Gaussian fit to these 5 lines yield a mean redshift of  $1.524 \pm 0.001$  for image A and  $1.524 \pm 0.002$  for the fainter image B. The standard deviation between the fits to the individual lines, divided by the square root of the number of lines used, is taken as the error bar. These results are in excellent agreement with the values obtained by Inada et al. (2003), as well as the redshift from the SDSS database, who both report  $z = 1.524$ .

### 3.3. Variability of the quasar images

The spectra of quasar images A and B are shown in Fig. 7 for 2005 January 14 and February 1. These are the mean of

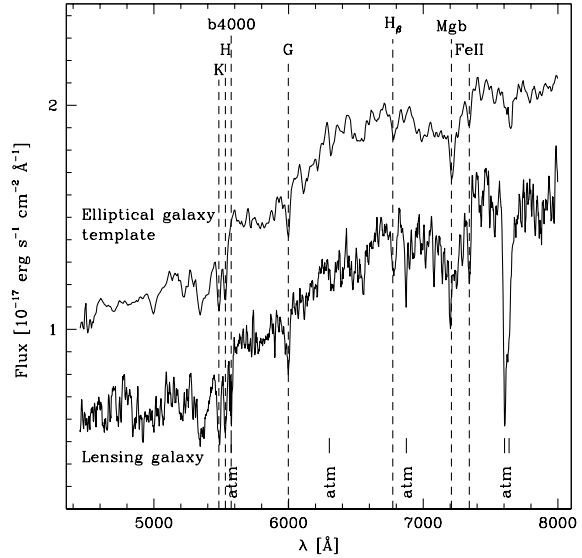


**Fig. 5.** Spectrum of the lensing galaxy in SDSS J0924+0219, as obtained by combining the data for the 6 epochs, i.e., a total integration time of 8400s. The template spectrum of an elliptical galaxy at  $z = 0.394$  is also shown for comparison (Kinney et al. 1996). All main stellar absorption lines are well identified. Prospects for a future determination of the galaxy’s velocity dispersion are therefore excellent.

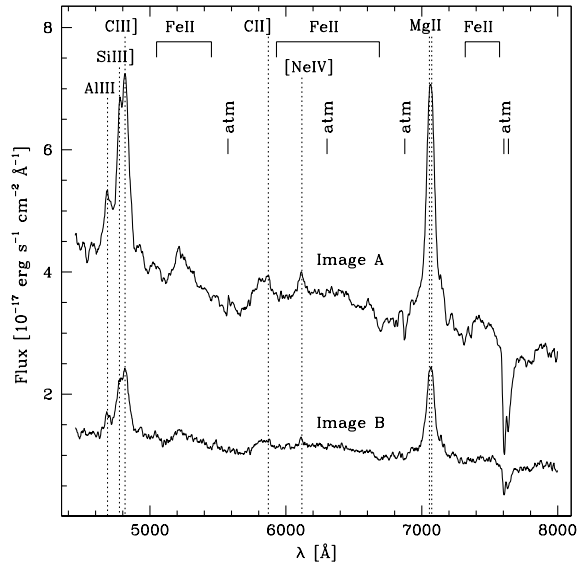


**Fig. 6.** Spectra of the quasar images A and B of SDSS J0924+0219, as extracted from the deconvolved data. These figure shows the mean of the 6 spectra taken for the 6 epochs, after the flux calibration described in Sect. 2.3.

the three spectra obtained on each date, smoothed with a 5 Å box. Although the continuum shows little variation (only B has faded slightly between our two observing dates), there are obvious changes in the broad emission lines of each quasar image. In image A, the red wing of the Mg II emission line has brightened, as well as the C II] emission line, while in image B, the center of the C III] emission line has become double peaked and the Fe II feature redwards of Mg II has faded. A zoom on these lines

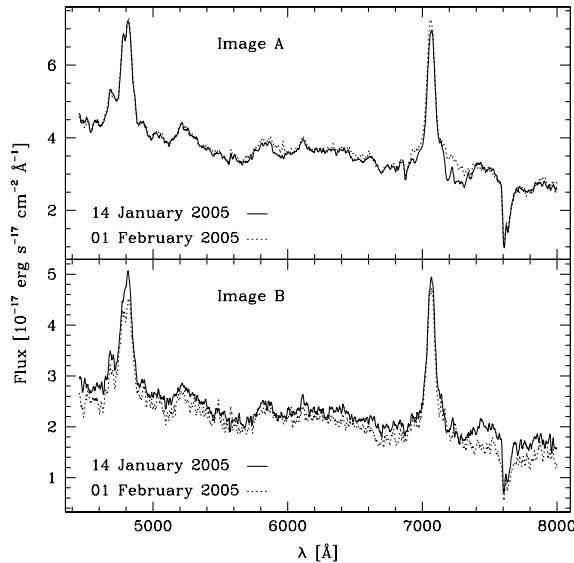


**Fig. 7.** The spectra of images A and B on 14 January and 1 February 2005 show a stable continuum for both images, but the broad emission lines do vary on a time-scale of two weeks (see Fig. 8).

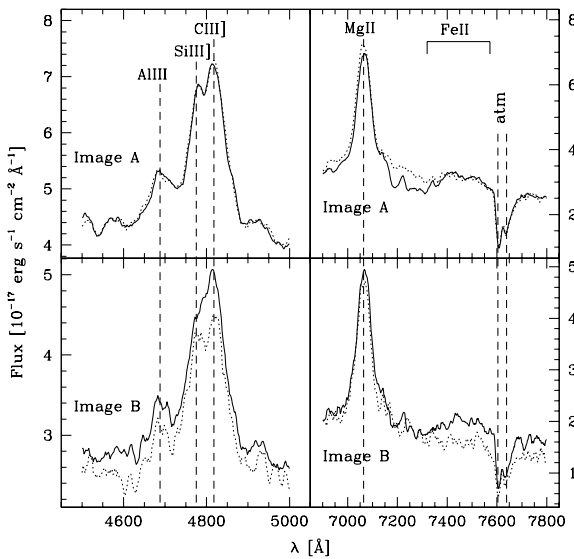


**Fig. 8.** Enlargements of Fig. 7 comparing the broad emission lines of images A and B on 14 January (solid curve) and 1 February 2005 (dotted curve). Obvious variations are seen in the red wing of the Mg II in image A, in the center of the C III] in image B. The Fe II feature redwards of Mg II in image B has also changed by 20%. These variations are asymmetric about the center of the lines. The asymmetry is different in C III] and Mg II.

is shown in Fig. 8. The line variations are already visible before averaging the 3 individual spectra at a given date and in the not-so-blended quasar images of the raw un-deconvolved spectra. We can therefore safely rule out any deconvolution artefacts due to PSF variations in the MOS mask. In addition, the residual images after deconvolution (see Courbin et al. 2000, for more details) are particularly good, indicative of little or no PSF variations across the slitlet mask.

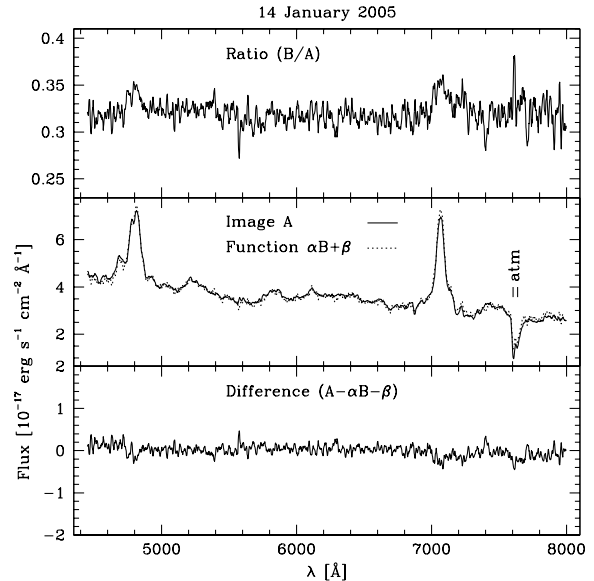


**Fig. 9.** Comparison between the spectra of images A and B taken on 14 January 2005. *The top panel* shows the dimensionless ratio B/A. The mean ratio is 0.32. *In the middle panel*, a first-order polynomial  $\alpha B + \beta$  is fit to the spectra of image A. The best fit is obtained with  $\alpha = 2.80 \pm 0.05$  and  $\beta = 0.37$ . The difference in flux between A and the fitted  $\alpha B + \beta$  polynomial is displayed in *the bottom panel*, and does not exceed a few percent of the flux.

### 3.4. Image flux ratio

Keeton et al. (2006) have recently observed that the flux ratio between the images of SDSS J0924+0219 is different in the continuum and in the broad emission lines. In their slitless HST/ACS observations, the flux ratio between A and B is 2.60 in the emission lines, and about 3.5 in the continuum, i.e., the emission lines are 30% different from the continuum.

We plot the flux ratio between quasar image B and A as a function of wavelength at a given date (top panels in Figs. 9 and 10). This ratio is close to flat, with some small differences in the broad emission lines.

We construct the spectrum  $\alpha B + \beta$  and adjust the parameters using a linear least squares fit so that it matches the spectrum of quasar A. The result is shown in the middle panels of Figs. 9 and 10. Almost no trace of the emission lines are seen in the difference spectra in the bottom panels of the figure. Our spectra indicate no strong differential amplification of the continuum and broad emission lines in the components A and B of SDSS J0924+0219, and the small residual seen in the emission lines in the bottom panels of Figs. 9 and 10 are an order of magnitude smaller than reported in Keeton et al. (2006).

In the 15 days separating the observations,  $\alpha$  has changed by only 2%. For both dates the residuals of the fit are almost perfectly flat, indicating no continuum change. Only asymmetric changes in the emission lines are seen.

Finally, the flat flux ratio between image A and B shows that there is no significant extinction by interstellar dust in the lensing galaxy.

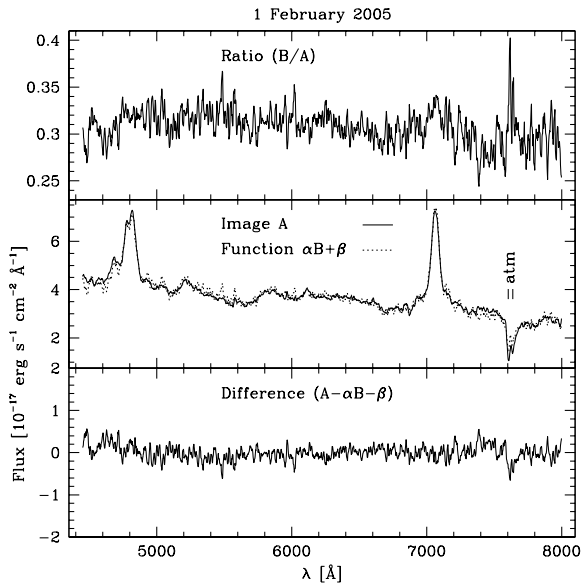


**Fig. 10.** Same as in Fig. 9 but for the spectra taken on 1 February 2005. The mean B/A ratio is 0.31, and the best fit of image A is obtained with  $\alpha = 2.86 \pm 0.05$  and  $\beta = 0.43$ .

### 3.5. Intrinsic variations vs. microlensing

It is hard, with only two observing points, to infer the origin of the spectral variations observed in SDSS J0924+0219. Nevertheless, we see rapid (15 days) and asymmetric changes in the emission lines of the quasar images, and no strong changes in the continuum. Intrinsic variations of quasars are usually stronger in the continuum than in the emission lines, and they are also longer than the two-week span we observe here. Such rapid variations due to microlensing have been seen in at least one other lensed quasar: HE 1104-1805 (Schechter et al. 2003). SDSS J0924+0219 might be a second such case. Microlensing variability is supported by the photometric broad-band data by Kochanek et al. (2005b), showing that A and B have very different light curves that are hard to match even after shifting them by the expected time delay. However, microlensing usually acts on the continuum rather than on the emission lines of quasar spectra, because of the much smaller size of the continuum region. Differential amplification of the continuum relative to the emission lines, as observed by Keeton et al. (2006), would be a strong support to the microlensing hypothesis. Our spectra do not show such a differential amplification, but we note that our wavelength range is very different from that of Keeton et al. (2006) and that they observed in May 2005, i.e., 3 months after our observations.

Assuming microlensing is the correct interpretation of the data, its strength depends upon the scale-size of the source, with smaller sources being more susceptible to large magnification (e.g. Wambsgans & Paczynski 1991). The continuum emitting region and the broad-line region (BLR) of a quasar can appear small enough to undergo significant magnifications. The limiting source size for microlensing to occur is given by the Einstein radius projected onto the source plane. This means that only structures in the source with sizes comparable to or smaller than this radius will experience appreciable amplification. The Einstein radius, projected onto the source plane for microlenses with masses in the range  $0.1 M_{\odot} < M < 10 M_{\odot}$  is  $7 < R_E < 70$  light-days for a cosmology with  $\Omega_m = 0.3$ ,  $\Omega_{\Lambda} = 0.7$  and  $h_{100} = 0.65$ .

Kaspi et al. (2000) derived sizes for active galaxy nuclei from reverberation mapping of the Balmer lines. As a function of intrinsic luminosity, they found a global scaling of the broad-line region (BLR) ranging from approximately 1 to 300 light days, which compares well with the Einstein radius of the microlenses in the lensing galaxy of SDSS J0924+0219.

The observations also reveal that the broad emission lines and the continuum do not vary on the same time scale. Indeed, the continuum of image A remains constant over the 15-day time span of the observations, while the broad emission lines vary.

Detailed microlensing simulations by Lewis & Iбата (2004) show that the correlation between the magnification of the BLR and the continuum source exists, but is weak. Hence variations in the broad emission lines need not be accompanied by variations in the continuum. This argument has been confirmed through observations of other gravitationally lensed quasars (Chartas et al. 2002; Richards et al. 2004).

Another observational fact that needs some enlightening is the asymmetric amplification of the broad emission lines (see Fig. 8). Such an amplification occurs for the C II] and Mg II emission lines in the spectra of image A. The red wings of these lines are significantly more amplified than the blue ones. An explanation for this is given by Abajas et al. (2002) and Lewis & Iбата (2004), who show that emission lines can be affected by substantial centroid shifts and modification of the line profile. Asymmetric modification of the line profile can be indicative of a rotating source. Microlensing of the part of the BLR that is rotating away from us would then explain the observed asymmetric line amplifications. This would imply that a microlensing caustic is passing at the edge of the broad line region, and is far enough from the continuum to leave it unaffected.

## 4. HST imaging

Optical and near-IR images of SDSS J0924+0219 are available from the HST archive in the *F555W*, *F814W* and *F160W* filters. The *F555W* and *F814W* observations have been obtained on 18 November 2003 with the Advanced Camera for Surveys (ACS) and the Wide Field Channel (WFC). The *F555W* data consist of two dithered 1094 s exposures, each one being split in two (CRSPLIT = 2) in order to remove cosmic rays. Two consecutive 1148 s exposures have been taken through the *F814W* filter, one hour later, again splitting the exposure time in two. Finally, the NICMOS2 observations, taken on 2003 November 23, consist of 8 dithered exposures, for a total of 5312 s. The 5-day period separating the optical and near-IR observations is of the order of the expected time delay between images A and B of the quasar.

### 4.1. Image deconvolution

The MCS algorithm (Magain et al. 1998) is used to deconvolve all images. This algorithm sharpens the images and preserves the flux of the original data. It also decomposes the data into a set of analytical point sources (the quasar images) and a numerical “extended channel” which contains all the features other than point sources, i.e., the lensing galaxy and the Einstein ring. All images are rebinned to a common pixel scale prior to deconvolution and combined with cosmic ray rejection. The reference image adopted to carry out the whole deconvolution work is the first image taken through the *F814W* filter, i.e., image j80i33031 in the HST archive. The position angle of this reference image relative to the North is  $PA = -2.67^{\circ}$ . All the astrometry in the following is given in the coordinate system of this image.



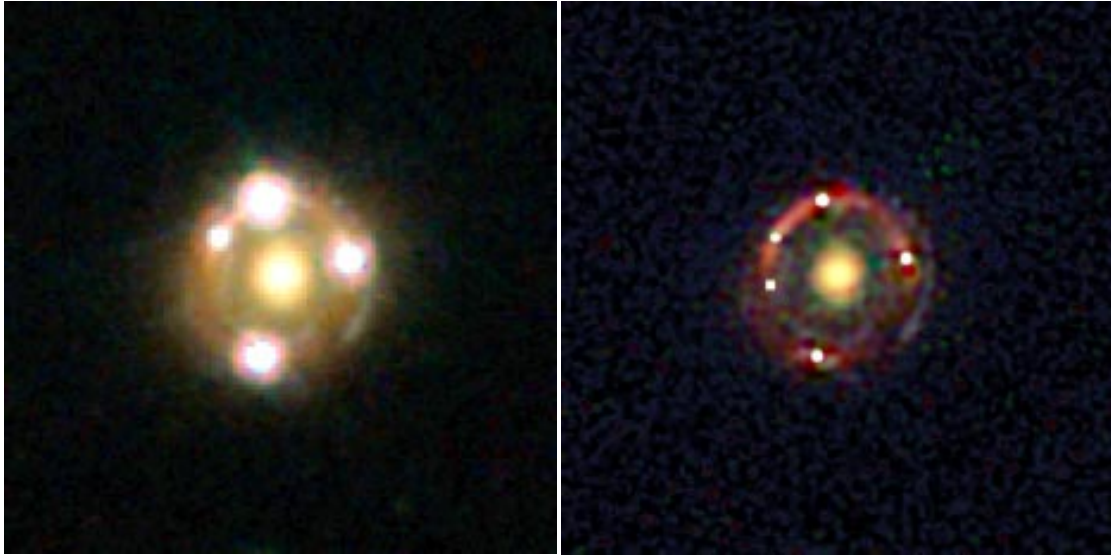


**Fig. 11.** *Left:* composite HST image using the observations through the  $F555W$ ,  $F814W$  and  $F160W$  filters. The resolution is respectively  $0.10''$  in  $F555W$  and  $F814W$ , and  $0.15''$  in  $F160W$ . *Right:* deconvolved image. It has a pixel size of  $0.025''$  and a resolution of  $0.05''$ . The lensed host galaxy of the quasar is clearly seen as red arcs well centered on the quasar images. A second set of bluer arcs inside and outside the area delimited by the red arcs is also revealed. The field of view is  $3.0''$  on a side. The image is slightly rotated relative to North, which is at  $PA = -2.67^\circ$ . East is to the left. The white square shows the position of the perturber found for the SIE and NFW models of Sect. 5.2.

The data used here are the pipeline-drizzled images available from the archive. The pixel scale in the deconvolved image is half that of the original image, i.e.,  $0.025'' \times 0.025''$ . The spatial resolution is the same in all deconvolved images, i.e.,  $0.05''$  Full-Width-Half-Maximum ( $FWHM$ ).

As the HST PSF has significant spatial variations across the field of view, stars located far away from SDSS J0924+0219 on the plane of the sky are not ideal for use in the image deconvolution. To circumvent this problem we have devised an iterative procedure. We first deconvolve the images with a fixed PSF, directly measured from stars. This gives a deconvolved image of the lens and Einstein ring, that we reconvolve with the PSF and subtract from the original data. A second PSF is re-computed from this new lens- and ring-subtracted image, directly from the quasar images, following the procedure described in Magain et al. (2005). This is similar to a blind-deconvolution, where the PSF is modified during the deconvolution process. A new deconvolved image is created with the improved PSF, as well as a new lens- and ring-subtracted image. We repeat 4 times in a row the procedure until the residual map (Magain et al. 1998; Courbin et al. 1998) is flat and in average equal to  $1\sigma$  after deconvolution, i.e., until the deconvolved image becomes compatible with the data in the  $\chi^2$  sense.

#### 4.2. Results

The deconvolved images through the three filters are shown in Fig. 11, as a colour composite image. Two sets of arcs are clearly seen, corresponding to the host galaxy of the source quasar, and to a bluer object not centered on the images of the quasar. This arc is well explained by a second lensed source (see Sect. 5.2) which is either a star-forming region in the source, or another unrelated object.

Instead of using the conventional version of the MCS deconvolution algorithm, we use a version that involves a semi-analytical model for the lensing galaxy. In this procedure, the

**Table 2.** Astrometry of SDSS J0924+0219 and flux ratio between the images. All positions are given relative to the lensing galaxy in the coordinate system of our reference HST image j80i33031. The  $1-\sigma$  error bar on the astrometry is  $0.005''$ , mainly dominated by the error on the position of the lensing galaxy. The error bar on the flux ratio is of the order of 10% for images B, C and 20% for image D, and includes the systematic errors due to the presence of the Einstein ring (see text).

Object	$X$ ( $''$ )	$Y$ ( $''$ )	$F555W$	$F814W$	$F160W$
Lens	+0.000	+0.000	–	–	–
A	–0.185	+0.859	1.00	1.00	1.00
B	–0.246	–0.948	0.51	0.46	0.44
C	+0.782	+0.178	0.39	0.34	0.32
D	–0.727	+0.430	0.06	0.06	0.03

analytical component of the lensing galaxy is either a two-dimensional exponential disk, or a de Vaucouleurs profile. All slight departures from these two profiles are modeled in the form of a numerical array of pixels which includes the arcs as well.

In all bands, we find that an exponential disk fits the data much better than a de Vaucouleurs profile, which is surprising for an elliptical galaxy, as indicated by the VLT spectra. Table 2 gives a summary of our astrometry, relative to the center of the fitted exponential disk. The mean position angle of the lensing galaxy, in the orientation of the HST image, is  $PA = -61.3 \pm 0.5^\circ$  (positive angles relative to the North in a counter-clockwise sense) and the mean ellipticity is  $e = 0.12 \pm 0.01$ , where the error bars are the dispersions between the measurements in the three filters. We define the ellipticity as  $e = 1 - b/a$ , where  $a$  and  $b$  are the semi-major and semi-minor axis respectively. Note that although the formal error on the lens ellipticity and PA is small, the data show evidence for isophote twisting. The effective radius of the galaxy is  $R_e = 0.50 \pm 0.05''$ .

The flux ratios of the quasar images are derived from the deconvolved images. The MCS algorithm provides the user with the intensities of all point sources in the image, decontaminated

**Table 3.** Best-fit parametric models for SDSS J0924+0219, obtained with the LENSMODEL package (Keeton 2001). The position angles of the lens  $\theta_c$  and of the external shear  $\theta_\gamma$  are given in degrees, positive angles being counted counter-clockwise relative to the North. The coordinates  $(x, y)$  of the centres of the models are given in arcseconds, and the time delays  $\Delta t$  are expressed in days relative to the leading image B. The extreme values for the time delays within the smallest  $1\text{-}\sigma$  region of Fig. 12 are also given. We adopt a  $(\Omega_m, \Omega_\Lambda) = (0.3, 0.7)$  cosmology and  $h_{100} = 0.65$ . All models have one degree of freedom.

Model	Parameters	$(x, y)$	$e$	$\theta_c$	$\gamma$	$\theta_\gamma$	$\Delta t_{AB}$	$\Delta t_{CB}$	$\Delta t_{DB}$	$\chi^2$
SIE	$b' = 0.87$	(-0.003, 0.002)	0.13	-73.1	0.053	65.4	$5.7^{6.7}_{5.1}$	$9.1^{10.4}_{8.2}$	$6.2^{7.2}_{5.5}$	0.91
de Vaucouleurs	$b = 2.64$ $R_c = 0.50$	(-0.004, 0.002)	0.16	-70.1	0.096	77.3	$8.6^{8.9}_{8.1}$	$13.8^{14.4}_{12.9}$	$9.4^{9.7}_{8.8}$	1.41
NFW	$\kappa_s = 0.70$ $r_s = 1.10$	(-0.003, 0.001)	0.10	-72.0	0.047	65.4	$4.9^{8.0}_{3.6}$	$7.8^{12.7}_{5.8}$	$5.4^{8.7}_{4.0}$	0.72

from the light of the extended features, such as the ring in SDSS J0924+0219 and the lensing galaxy. The error on the quasar flux ratio is dominated by the contamination by the Einstein ring. If the intensity of a quasar image is overestimated, this will create a “hole” in the deconvolved Einstein ring at the quasar image position. If it is underestimated, the local  $\chi^2$  at the position of the quasar image will become much larger than  $1\sigma$ . The flux ratios in Table 2 are taken as the ones giving at the same time a continuous Einstein ring without any “hole”, and leading to a good  $\chi^2$ , close to 1, at the position of the quasar images. The error bars quoted in Table 2 are taken as the difference between these two extreme solutions, divided by 2. They include both the random and systematic errors.

## 5. Modeling

Constraining the mass distribution in SDSS J0924+0219 is not trivial. Firstly, we do not have access to the true image magnifications due to contamination by microlensing and secondly, the light distribution of the lensing galaxy is not very well constrained. The ellipticity and position angle of the lens change with surface brightness, indicative of isophote twisting. Measuring the faintest isophotes on the HST data leads to  $PA \approx -25^\circ$ , as is adopted by Keeton et al. (2006) in his models. However, brighter isophotes and fitting of a PSF-deconvolved exponential disk profile yields  $PA = -61.3^\circ$ .

As a blind test for the shape of the mass distribution underlying the light distribution, and without using any constraint on the ellipticity or PA of the lens, we use the non-parametric models of Saha & Williams (2004). Fitting only the image positions returns an asymmetric lens whose major axis is aligned approximately East-West (i.e.,  $PA = 90^\circ$ ). Given the discrepancy between this simple model and the observed light distribution, we test in the following a range of models with differing levels of observational constraints, in order to predict time delays.

### 5.1. Parametric models

#### 5.1.1. Using the flux ratios

The LENSMODEL package (Keeton 2001) is used to carry out an analytical modeling of the lensing galaxy. Three lensing galaxy models are considered: the Singular Isothermal Ellipsoid (SIE), the Navarro et al. (1997) profile (NFW), and the de Vaucouleurs (1948) profile. In a first attempt, we constrain these models with the lensing galaxy position, the relative positions of the lensed images (Table 2) and their flux ratios (taken as the mean of the ratios measured in the three *F555W*, *F814W*, *F160W*

filters). If no external shear is included in the models, we find a lens ellipticity of  $e \approx 0.3$  with a PA  $\theta_c \approx 85^\circ$  and an associated  $\chi^2 \approx 200$ . The ellipticity and PA agree well with the models obtained from the semi-linear inversion method of Warren & Dye (2003) (see Sect. 5.2).

Next, we include external shear to the model. The lens position angle  $\theta_c$ , coordinates, and ellipticity agree better with the measured values in the HST images. The  $\chi^2$  values remain bad ( $\chi^2 \approx 30$ ), although improved with respect to the models without external shear. The shear orientation is  $\theta_\gamma \sim 60^\circ$  which is about in the direction of a bright galaxy located  $9.5''$  away from SDSS J0924+0219 and at  $PA = 53^\circ$ .

The main contribution to the total  $\chi^2$  is the anomalous flux ratios between the images of SDSS J0924+0219. In particular, the extreme flux ratio between image A and image D of  $\sim 15$ , when these two images are predicted to have approximately the same brightness. This is not surprising because of the evidence of microlensing in image A (Sect. 3.5) and of possible millilensing induced by massive substructures. This lead us to the considerations presented in the next section.

#### 5.1.2. Discarding the flux ratios

The modeling is similar to that of Sect. 5.1.1. External shear is included but the flux ratios are discarded. In order to use only models that have one degrees of freedom (DOF), we have fixed the effective radius of the de Vaucouleurs model to the observed value. Given the number of observational constraints, the NFW model would have zero DOF if all its parameters were left free during the fit. We have therefore fixed the orientation of the external shear in this model to the value we found in the SIE+shear model. The best fit models are presented in Table 3, with (reduced)  $\chi^2$  improved to values close to 1.

We map the lens ellipticity vs. external shear plane in order to estimate the degree of degeneracy between these two parameters. The results are displayed in Fig. 12. It is immediately seen that the  $1\text{-}\sigma$  ellipses of the different models only marginally overlap. This is confirmed by the time delay values summarized in Table 3 where we also give the extreme values of the time delays within the 68% confidence interval. The minimum difference between the extreme time delays predicted with a constant mass-to-light ratio galaxy (de Vaucouleurs) and by the more physically plausible SIE model is about 8%. Since the error measurement on the time delay propagates linearly in the error budget, even a rough estimate of the three time delays in SDSS J0924+0219, with 8% accuracy will already allow to discriminate efficiently between flat M/L models and SIE. Distinguishing between SIE and NFW is more difficult as time

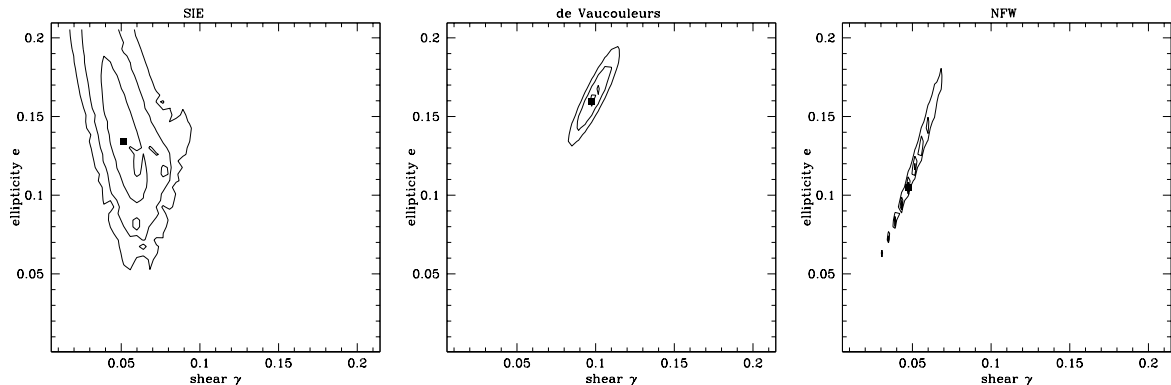


**Fig. 12.** The three plots give the reduced  $\chi^2$  as a function of lens ellipticity  $e$  and external shear  $\gamma$  for the three analytic models used in the LENSMODEL package. No constraint is used on the image flux ratios. The contours correspond to the 1, 2 and 3- $\sigma$ , confidence levels. The degeneracy between ellipticity and shear is clear. Only the NFW models are (marginally) compatible with no external shear at all, as also suggested by the semi-linear inversion of Sect. 5.2. The black square in each panel indicated the best fit model, which parameters are given in Table 3.

delays predicted by NFW models differ by only 1% from the SIE time delays. Such an accuracy will be hard to reach in SDSS J0924+0219, that has short time delays and a short visibility period given its equatorial position on the plane of the sky (see Eigenbrod et al. 2005).

### 5.2. Using the arcs of the lensed sources

The HST images of SDSS J0924+0219 reveal two sets of arcs. One is prominent in the near-IR (in red in Fig. 11) and is well centered on the quasar images. It is the lensed image of the quasar host galaxy. A second set of bluer arcs is best seen in  $F555W$ . It is off-centered with respect to the quasar images, indicating either a companion to the quasar host, or an independent intervening object along the line of sight.

We apply the semi-linear inversion method of Warren & Dye (2003) to the arcs observed in the  $F555W$  and  $F160W$  data. The method incorporates a linear matrix inversion to obtain the source surface brightness distribution that gives the best fit to the observed lensed image for a given lens model. This linear step is carried out per trial lens parametrisation in a standard non-linear search for the global best fit.

Dye & Warren (2005) successfully apply this technique to the Einstein ring system 0047–2808. They demonstrate that the extra constraints provided by the image of the ring results in smaller errors on the reconstructed lens model, compared to using only the centroids of the principal images as constraints in this system.

In the case of 0047–2808, the source is a star forming galaxy without any point-like emission whereas the image of SDSS J0924+0219 is clearly dominated by the QSO’s central point source. To prevent the reconstruction of SDSS J0924+0219 from being dominated by the point source and because in this section only the reconstruction of the QSO host emission is of interest, we masked out the four point source images in the  $F555W$  and  $F160W$  data supplied to the semi-linear inversion code. The astrometry of the quasar images is not used as a constraint. Figure 13 shows the masked ring images.

#### 5.2.1. Reconstruction results

The deconvolved  $F160W$  and  $F555W$  data are reconstructed with 6 different parametric lens models. Three of these are single

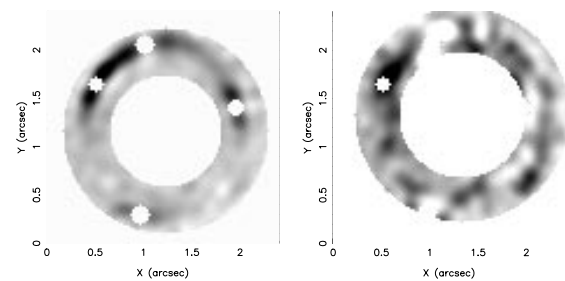


**Fig. 13.** Annular mask applied to the  $F160W$  (left) and  $F555W$  (right) data with point sources masked out. The annulus in the  $F555W$  image is shifted by  $0.1''$  to the left and  $0.2''$  to the top with respect to the  $F160W$  image, to properly encompass the blue arc seen in Fig. 11.

mass component models: the singular isothermal ellipsoid (SIE), the elliptical NFW, and the elliptical NFW with external shear. The remaining three test for asymmetry in the lens model by including a secondary singular isothermal sphere (SIS) mass component that is also free to move around in the lens plane and vary in normalization in the minimization. These models are the dual SIS model, the SIE+SIS model and the NFW+SIS model.

Since the  $F160W$  data have the highest signal to noise arcs, we base our lens modeling on these data and applied our overall best fit model to the  $F555W$  data to reconstruct the source. In all cases, we reconstruct with a  $0.5'' \times 0.5''$  source plane comprising  $10 \times 10$  pixels. The reconstruction is not regularised, except in Fig. 14 where first order regularisation (see Warren & Dye 2003) is applied to enhance visualization of the source.

Table 4 lists the minimized parameters for each model and the corresponding values of  $\chi^2$ . The SIE+SIS and NFW+SIS models clearly fare better than their single component counterparts, implying the lens is asymmetric. For the SIE+SIS, a decrease in  $\chi^2$  of  $\Delta\chi^2 = 33$  for 3 fewer degrees of freedom has a significance of  $5.1\sigma$ . The decrease of  $\Delta\chi^2 = 40$  for the NFW+SIS has a significance of  $5.7\sigma$ . Both models consistently place the secondary SIS mass component around  $(-0.80'', -0.05'')$  with a normalization of only  $\sim 2.5\%$  of the main component.

Interestingly, the elliptical models listed in Table 4 have ellipticities close to those obtained with the LENSMODEL

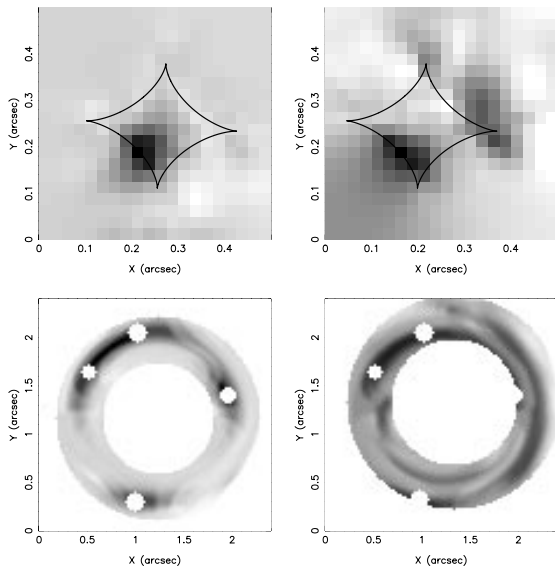


**Fig. 14.** Reconstructed source from  $F160W$  data (top left) and its lensed image (bottom left). A second source lying on the rightmost cusp caustic (top right) is reconstructed from the  $F555W$  image corresponding to the blue arc (bottom right).

software, when no external shear is considered. When external shear is added to the NFW model, we do indeed obtain a significantly better fit compared to the NFW on its own, but the results differ from those listed in Table 3. While the ellipticity remains almost the same as in Table 3, its PA differs by approximately  $25^\circ$ . Moreover, we find a ten times smaller amplitude for the shear using the semi-linear inversion than using LENSMODEL. Note, however, that the observed quasar image astrometry is used in the LENSMODEL analysis, whereas it is not in the present semi-linear inversion. If we use the lens model found by the semi-linear inversion to predict the position of the quasar images, we find poor agreement between the predicted and the measured positions. The global, large scale shape of the lens found by the semi-linear inversion is well adapted to model the Einstein rings, which are very sensitive to azimuthal asymmetry in the lens, but additional smaller scale structures are needed to slightly modify the positions of the quasar images and make them compatible with the measured astrometry. The disagreement between the astrometry predicted by LENSMODEL and the one predicted by the semi-linear inversion adds support to the presence of multipole-type substructures in the lens (e.g., Congdon & Keeton 2005).

The top left plot in Fig. 14 shows the reconstructed source corresponding to the best fit NFW+SIS model for the  $F160W$  data. The observed arcs are explained by a single QSO host galaxy. Note that in this figure, purely to aid visualization, we have regularised the solution and plotted the surface brightness with a pixel scale half that used in the quantitative reconstruction. The bottom left corner of Fig. 14 shows the image of the reconstructed source lensed by the best fit NFW+SIS model.

We then take the best fit NFW+SIS model in order to reconstruct the  $F555W$  data shown on the right in Fig. 13. Note that the annular mask is shifted slightly compared to the  $F160W$  data, to properly encompass the blue arc. The reconstructed source and corresponding lensed image are shown on the right hand side of Fig. 14.

There are two distinct sources now visible. The QSO host identified previously has again been reconstructed. This is because its dominant image, the bright arc in the top left quadrant of the ring, is still present in the  $F555W$  data. A second source, more diffuse and lying on the rightmost cusp caustic is also visible. This second source is responsible for the blue arcs.

The redshift of the second source remains unknown. It could be a star forming object/region lying  $0.2'' \cdot D_s \approx 1200 h_{100}^{-1}$  pc away from the quasar, i.e., it would be part of the host galaxy. It is, however, not excluded that this second source is at a different redshift than the quasar, e.g. located between the quasar and the lens, as it is bluer than the quasar host galaxy. If the latter is true, SDSS J0924+0219 might be a unique object to break the mass sheet degeneracy. Unfortunately, the lens modeling alone, does not allow to infer a redshift estimate.

### 5.3. Note on the different types of models

The two methods used above differ in several respects. LENSMODEL has a limited number of free parameters but uses only the constraints on the astrometry of the quasar images. While a qualitative representation of the lensed host galaxy of the quasar source can be attempted, the method does not allow a genuine fitting of the Einstein rings assuming a (simplified) shape for the quasar host.

The semi-linear inversion carries out a direct reconstruction of the lensed source as a whole, where each pixel of the HST image is a free parameter. As the quasar images largely dominate the total flux of the source, they need to be masked before the reconstruction. For this reason it is not possible with this method, at the present stage of its development, to constrain the lens model using *simultaneously* the astrometry of the quasar images and the detailed shape of the Einstein rings.

Although the two methods used in the present work are fundamentally different and although they use very different observational constraints, they agree on the necessity to bring extra mass near image D of SDSS J0924+0219. Smooth lenses like the ones implemented in LENSMODEL have PAs that differ by  $10^\circ$  from the one measured in the HST images. In the orientation of Fig. 11, the mass distribution found by LENSMODEL is closer to horizontal (PA =  $-90^\circ$ ) than the light distribution, hence giving larger masses next to image D. In the semi linear inversion, the optimal position found for the SIS perturber is also close to image D.

Given the above discussion, the poor determination of the lens PA is a main limitation to the interpretation of the time delays in SDSS J0924+0219. An alternative route is to determine the dynamical rotation axis of the lens, a challenge which is now within the reach of integral field spectroscopy with large telescopes and adaptive optics.

## 6. Conclusions

We have spatially deconvolved deep sharp VLT/FORS1 MOS spectra of SDSS J0924+0219, and measured the redshift of the lensing galaxy,  $z_{\text{lens}} = 0.394 \pm 0.001$ , from numerous stellar absorption lines. The spectrum beautifully matches the elliptical galaxy template of Kinney et al. (1996).

The flux ratio between image A and B is  $F_A/F_B = 2.80 \pm 0.05$  on 2005 January 14, and  $F_A/F_B = 2.86 \pm 0.05$  on 2005 February 1, i.e., it has not changed between the two dates given the uncertainties on the flux ratios (Table 1). For each date, this ratio is mostly the same in the continuum and in the broad

**Table 4.** Minimized lens model parameters and corresponding  $\chi^2$ . Model parameters are:  $\kappa_0$  = mass normalization in arbitrary units,  $(x, y)$  = offset of lens model centre from lens optical axis in arcseconds,  $e$  = ellipticity,  $\gamma$  = external shear,  $\theta_e$  and  $\theta_\gamma$  = PA in degrees counted counter-clockwise from North. In the case of the NFW, the scale radius is held fixed at  $6''$  in the minimization. The third column gives the number of degrees of freedom (NDOF). Subscript “b” refers to the secondary SIS in the dual component models (see text).

Model	$\chi^2_{\min}$	NDOF	Minimized parameters
SIE	4280	3975	$\kappa_0 = 100.0$ , $(x, y) = (0.02, 0.04)$ , $e = 0.270$ , $\theta_e = 86.0$
NFW	4011	3974	$\kappa_0 = 100.0$ , $(x, y) = (0.06, 0.06)$ , $e = 0.187$ , $\theta_e = 84.9$
Dual SIS	4385	3974	$\kappa_0 = 49.2$ , $(x, y) = (0.00, 0.28)$ , $\kappa_{0b} = 51.6$ , $(x, y)_b = (-0.06, -0.33)$
SIE+SIS	4247	3972	$\kappa_0 = 99.4$ , $(x, y) = (0.04, 0.04)$ , $e = 0.265$ , $\theta_e = 85.1$ , $\kappa_{0b} = 2.1$ , $(x, y)_b = (-0.79, -0.03)$
NFW+SIS	3971	3971	$\kappa_0 = 98.0$ , $(x, y) = (0.05, 0.08)$ , $e = 0.206$ , $\theta_e = 83.1$ , $\kappa_{0b} = 2.8$ , $(x, y)_b = (-0.80, -0.09)$
NFW+ $\gamma$	3992	3972	$\kappa_0 = 100.0$ , $(x, y) = (0.06, 0.06)$ , $e = 0.168$ , $\theta_e = 86.0$ , $\gamma = 0.010$ , $\theta_\gamma = 78.3$

emission lines of the quasar images A and B. This may seem in contradiction with Keeton et al. (2006) who see differential amplification of the continuum relative to the lines, but our observing dates and setup are very different from theirs.

While the continuum of images A and B has not changed in 15 days, there are obvious and asymmetric changes in some of the quasar broad emission lines. Microlensing of both A and B is compatible with this, although somewhat ad hoc assumptions must be done on the position of the microcaustics relative to the quasar, as well as on the relative sizes of the continuum and broad line regions.

Deep HST imaging reveals two sets of arcs. One corresponds to the red lensed host galaxy of the quasar and defined an Einstein ring connecting the quasar images. The other, fainter and bluer is off-centered with respect to the quasar images. It is either a star-forming region in the quasar source host galaxy, or another intervening object.

The lens ellipticity and PA measured in the HST images are hard to reconcile with simple models without external shear. The model fits improve when external shear is added, even though the predicted PA differs from the measured one by approximately  $25^\circ$ .

Models of Sect. 5.2, involving an additional small (SIS) structure to the main lens always place it along the East-West axis, about  $0.8''$  to the East of the main lens, i.e., towards the demagnified image D. In addition, the models reconstructed using only the Einstein rings do not predict the correct astrometry for the quasar images. Einstein rings constrain the overall, large scale of the lens. Small deviations from this large scale shape are needed to match the quasar images astrometry. The discrepancy between the models using the rings and the ones using the quasar image positions therefore adds support to the presence of multipole-like substructures in the lens of SDSS J0924+0219.

Finally, the range of time delays predicted by the different lens models is large and is very sensitive to the presence of external shear and to the determination of the main lens ellipticity and PA. The time delay measurement and the lens modeling, combined with integral field spectroscopy of the lens in SDSS J0924+0219 might therefore prove extremely useful to map the mass-to-light ratio in the lens, by comparing the

lensing and dynamical masses, to the light distribution inferred from the HST images.

*Acknowledgements.* The authors would like to thank Dr. Steve Warren for useful discussions and the ESO staff at Paranal for the care taken with the crucial slit alignment necessary to carry out the spectra deconvolutions. The HST archive data used in this article were obtained in the framework of the CfA-Arizona Space Telescope LENS Survey (CASTLES, HST-GO-9744, PI: C. S. Kochanek). P.M. acknowledges support from the PSS Science Policy (Belgium) and by PRODEX (ESA). COSMOGRAIL is financially supported by the Swiss National Science Foundation (SNSF).

## References

- Abajas, C., Mediavilla, E., Muñoz, J. A., et al. 2002, *ApJ*, 576, 640  
 Chartas, G., Agol, E., Eracleous, M., et al. 2002, *ApJ*, 658, 509  
 Congdon, A. B., & Keeton, C. R. 2005, *MNRAS*, 364, 1459  
 Courbin, F., Lidman, C., Frye, B. L., et al. 1998, *ApJ*, 499, L199  
 Courbin, F., Magain, P., Kirkove, M., et al. 2000, *ApJ*, 529, 1136  
 Courbin, F., Saha, P., & Schechter, P. L. 2002, *Lecture Note in Physics*, ed. Courbin, & Minniti (Springer Verlag: Berlin), 608, 1  
 de Vaucouleurs, G. 1948, *Ann. Astrophys.*, 11, 247  
 Dye, S., & Warren, S. J. 2005, *ApJ*, 623, 31  
 Eigenbrod, A., Courbin, F., Vuissoz, C., et al. 2005, *A&A*, 436, 25  
 Faber, S. M., Tremaine, S., Ajhar, E. A., et al. 1997, *AJ*, 114, 1771  
 Hernquist, L. 1990, *ApJ*, 356, 359  
 Inada, N., Becker, R. H., Burles, S., et al. 2003, *AJ*, 126, 666  
 Jaffe, W. 1983, *MNRAS*, 202, 995  
 Kaspi, S., Smith, P. S., Netzer, H., et al. 2000, *ApJ*, 533, 631  
 Keeton, C. R. 2001 [arXiv:astro-ph/0102340]  
 Keeton, C. R., Burles, S., Schechter, P. L., & Wambsganss, J. 2006, *ApJ*, 639, 1  
 Kinney, A. L., Calzetti, D., Bohlin, R. C., et al. 1996, *ApJ*, 467, 38  
 Kochanek, C. S. 2005a, in *Proceedings of the 33rd Saas Fee advanced course, Gravitational Lensing: Strong, Weak & Micro*, ed. G. Meylan, P. Jetzer, & P. North (Springer Verlag: Berlin)  
 Kochanek, C. S. 2005b, in *Impact of Gravitational Lensing on Cosmology*, ed. Y. Mellier, & G. Meylan, IAU Symp., 225, 205 [arXiv:astro-ph/0412089]  
 Kochanek, C. S., & Dalal, N. 2004, *ApJ*, 610, 69  
 Lewis, G. F., & Ibata, R. A. 2004, *MNRAS*, 348, 24  
 Magain, P., Courbin, F., & Sohy, S. 1998, *ApJ*, 494, 452  
 Magain, P., Courbin, F., Sohy, S., & Gillon, M. 2005, in preparation  
 Moore, B., Governato, F., Quinn, T., et al. 1998, *ApJ*, 499, L5  
 Muñoz, J. A., Kochanek, C. S., & Keeton, C. R. 2001, *ApJ*, 558, 657  
 Navarro, J. F., Frenk, C. S., & White, S. D. M. 1997, *ApJ*, 490, 493  
 Ofek, E. O., Maoz, D., Rix, H.-W., et al. 2005 [arXiv:astro-ph/0510465]  
 Refsdal, S. 1964, *MNRAS*, 128, 307  
 Richards, G. T., Keeton, C. R., Bartosz, P., et al. 2004, *ApJ*, 610, 679  
 Saha, P., & Williams, L. L. R. 2004, *AJ*, 127, 2604  
 Schechter, P. L., Udalski, A., Szymanski, M., et al. 2003, *ApJ*, 584, 657  
 Schechter, P. L., Wambsganss, J., & Lewis, G. F. 2004, *ApJ*, 613, 77  
 Wambsganss, J., & Paczynski, B. 1991, *AJ*, 102, 864  
 Warren, S. J., & Dye, S. 2003, *ApJ*, 590, 673



**6.7 Paper presenting the determination of the redshift of the lensing galaxy in eight gravitationally lensed quasars**

*COSMOGRAIL: the COSmological MONitoring  
of GRAvItational Lenses*

*III. Redshift of the lensing galaxy in eight gravitationally  
lensed quasars*

A. Eigenbrod, F. Courbin, G. Meylan, C. Vuissoz, & P. Magain

*Astronomy & Astrophysics, 2006, 451, 759*





## COSMOGRAIL: the COSmological MONitoring of GRAVitational Lenses

### III. Redshift of the lensing galaxy in eight gravitationally lensed quasars<sup>\*</sup>

A. Eigenbrod<sup>1</sup>, F. Courbin<sup>1</sup>, G. Meylan<sup>1</sup>, C. Vuissoz<sup>1</sup>, and P. Magain<sup>2</sup>

<sup>1</sup> Laboratoire d’Astrophysique, École Polytechnique Fédérale de Lausanne (EPFL), Observatoire, 1290 Sauverny, Switzerland

<sup>2</sup> Institut d’Astrophysique et de Géophysique, Université de Liège, Allée du 6 août 17, Sart-Tilman, Bat. B5C, 4000 Liège, Belgium

Received 1 November 2005 / Accepted 21 December 2005

#### ABSTRACT

**Aims.** We measure the redshift of the lensing galaxy in eight gravitationally lensed quasars in view of determining the Hubble parameter  $H_0$  from the time delay method.

**Methods.** Deep VLT/FORS1 spectra of lensed quasars are spatially deconvolved in order to separate the spectrum of the lensing galaxies from the glare of the much brighter quasar images. A new observing strategy is devised. It involves observations in Multi-Object-Spectroscopy (MOS) which allows the simultaneous observation of the target and of several PSF and flux calibration stars. The advantage of this method over traditional long-slit observations is a much more reliable extraction and flux calibration of the spectra.

**Results.** For the first time we measure the redshift of the lensing galaxy in three multiply-imaged quasars: SDSS J1138+0314 ( $z_{\text{lens}} = 0.445$ ), SDSS J1226–0006 ( $z_{\text{lens}} = 0.517$ ), SDSS J1335+0118 ( $z_{\text{lens}} = 0.440$ ), and we give a tentative estimate of the redshift of the lensing galaxy in Q 1355–2257 ( $z_{\text{lens}} = 0.701$ ). We confirm four previously measured redshifts: HE 0047–1756 ( $z_{\text{lens}} = 0.407$ ), HE 0230–2130 ( $z_{\text{lens}} = 0.523$ ), HE 0435–1223 ( $z_{\text{lens}} = 0.454$ ) and WFI J2033–4723 ( $z_{\text{lens}} = 0.661$ ). In addition, we determine the redshift of the second lensing galaxy in HE 0230–2130 ( $z_{\text{lens}} = 0.526$ ). The spectra of all lens galaxies are typical for early-type galaxies, except for the second lensing galaxy in HE 0230–2130 which displays prominent [OII] emission.

**Key words.** gravitational lensing – cosmological parameters – quasars: general

## 1. Introduction

Gravitationally lensed quasars have become a truly efficient source of new astrophysical applications, since the discovery of the first case by Walsh et al. (1979). These objects are potentially useful for measuring the Hubble parameter  $H_0$  from the time delay between their lensed images (Refsdal 1964), assuming a model for the mass distribution in the lensing galaxy. Conversely, for an assumed or measured value of  $H_0$ , the mass distribution in the lens can be reconstructed from the time delay measurement. The study of lensed quasars is therefore a “no-lose” game, either because of its cosmological implications ( $H_0$ ) or for the study of galaxy formation and evolution through the determination of detailed mass maps for lensing galaxies, especially their dark matter content.

The second most important application of quasar lensing involves microlensing by stars in the lensing galaxy. Microlenses produce chromatic magnification events in the light curve of the images of the source, as they cross their line of sight. The amplitude, duration and frequency of the events depend on the transverse velocity of stars in the lensing galaxy, on their surface density, and on the relative sizes of the microlensing caustics with respect to the regions of the source affected by

microlensing. Photometric monitoring of lensed quasars in several bands or, better, spectrophotometric monitoring can therefore yield constraints on the energy profile of quasar accretion disks and on the size of the various emission line regions (e.g. Agol & Krolik 1999; Mineshige & Yonehara 1999; Abajas et al. 2002).

All the above applications of quasar lensing require the knowledge of the redshift of the lensing galaxy, which is frequently hidden in the glare of the quasar images. The present paper is part of a larger effort to carry out long term photometric monitoring of lensed quasars in the context of COSMOGRAIL (e.g. Eigenbrod et al. 2005). In this paper we focus on the determination of the redshifts of the lensing galaxies in several gravitationally lensed quasars, using deep spectra obtained with the ESO Very Large Telescope (VLT). The targets were simply selected in function of their visibility during the period of observation.

## 2. VLT spectroscopy

### 2.1. Observations

We present observations for eight gravitationally lensed quasars, in order to determine the redshift of the lensing galaxy. The targets are HE 0047–1756, HE 0230–2130, HE 0435–1223, SDSS J1138+0314, SDSS J1335+0118, Q 1355–2257 (also known as CTQ 327), SDSS J1226–0006 and WFI J2033–4723.

Our spectroscopic observations are acquired with the FOCal Reducer and low dispersion Spectrograph (FORS1), mounted

<sup>\*</sup> Based on observations made with the ESO-VLT Unit Telescope 2 Kueyen (Cerro Paranal, Chile; Programs 074.A-0563 and 075.A-0377, PI: G. Meylan), and on archive data taken with the ESO-VLT Unit Telescope 1 Antu (Cerro Paranal, Chile; Program 064.O-0259(A), PI: L. Wisotzki).

**Table 1.** Journal of the observations of HE 0047–1756. Grism and filter: G300V+GG435. HR collimator: 0.1'' per pixel. Slitlets width: 1.0'' ( $R = 210$  at 5900 Å).

ID	Date	Seeing ["]	Airmass	Weather
1	18/07/2005	0.49	1.281	Photometric
2	18/07/2005	0.53	1.191	Photometric

**Table 2.** Journal of the observations of HE 0230–2130. Grism and filter: G600R+GG435. SR collimator: 0.2'' per pixel. Slitlets width: 0.5'' ( $R = 1910$  at 6200 Å).

ID	Date	Seeing ["]	Airmass	Weather
1	15/12/2004	0.60	1.166	Light clouds
2	15/12/2004	0.58	1.248	Light clouds
3	01/03/2005	0.78	1.800	Photometric

on the ESO Very Large Telescope. Very importantly, all the observations are carried out in the MOS mode (Multi Object Spectroscopy). This strategy allows the simultaneous observation of the main target and of several stars used both as flux calibrators and as reference PSF to spatially deconvolve the data.

Most of our targets are observed with the high-resolution collimator, allowing us to observe simultaneously eight objects over a field of view of  $3.4' \times 3.4'$  with a pixel scale of 0.1''. However, because few suitable PSF stars are visible in the vicinity of SDSS J1226–0006 and HE 0230–2130, the observations for these two objects use the standard-resolution collimator, which has a field of view of  $6.8' \times 6.8'$  and a pixel size of 0.2''.

We use the GG435 order sorting filter in combination with the G300V grism for all objects, except HE 0230–2130 for which we use the G600R grism. The G300V grism gives a useful wavelength range  $4450 < \lambda < 8650$  Å and a scale of 2.69 Å per pixel in the spectral direction. This setup has a spectral resolution  $R = \lambda/\Delta\lambda \approx 200$  at the central wavelength  $\lambda = 5900$  Å for a 1.0'' slit width in the case of the high resolution collimator. The choice of this grism favors spectral coverage rather than spectral resolution as the observations are aimed at measuring unknown lens redshifts. The combination of the G600R grism with the GG435 filter used for HE 0230–2130 has a wavelength range of  $5250 < \lambda < 7450$  Å with a pixel scale of 1.08 Å in the spectral direction. This gives a higher spectral resolution of  $R \approx 1200$  at the central wavelength  $\lambda = 6270$  Å for a slit width of 1.0'' and with the standard resolution collimator.

We choose slitlets of various widths, depending on the brightness of the target and on the configuration of the quasar images. The slit width is chosen so that it matches the seeing requested for the service-mode observations and minimizes lateral contamination by the quasar images. Our observing sequences consist of a short acquisition image, an “image-through-slit” check, followed by one or two consecutive deep spectroscopic exposures. All individual exposures for all objects are 1400 s long. The journals of the observations are given in Tables 1 to 8. The through-slit images are displayed in Figs. 1 to 8, where the epochs refer to the exposure numbers in Tables 1 to 8.

For every object we center at least three slitlets on foreground stars and one slitlet on the lensing galaxy. The mask is rotated to a Position Angle that avoids clipping of any quasar image. This is mandatory to carry out spatial deconvolution of the spectra. The spectra of the PSF stars are also used to cross-calibrate the flux scale as the data are taken at different airmasses and at different dates. Three spectrophotometric standard stars are used to carry out the relative flux calibration, i.e. EG 21, LTT 3218, and LTT 6248.

**Table 3.** Journal of the observations for HE 0435–1223. Grism and filter: G300V+GG435. HR collimator: 0.1'' per pixel. Slitlets width: 1.0'' ( $R = 210$  at 5900 Å).

ID	Date	Seeing ["]	Airmass	Weather
1	11/10/2004	0.47	1.024	Photometric
2	11/10/2004	0.45	1.028	Photometric
3	12/10/2004	0.46	1.024	Photometric
4	12/10/2004	0.53	1.028	Photometric
5	11/11/2004	0.57	1.093	Photometric
6	11/11/2004	0.56	1.145	Photometric

**Table 4.** Journal of the observations for SDSS J1138+0314. Grism and filter: G300V+GG435. HR collimator: 0.1'' per pixel. Slitlets width: 1.0'' ( $R = 210$  at 5900 Å).

ID	Date	Seeing ["]	Airmass	Weather
1	10/05/2005	0.82	1.191	Photometric
2	11/05/2005	0.70	1.155	Photometric
3	11/05/2005	0.67	1.133	Photometric
4	11/05/2005	0.66	1.132	Photometric
5	11/05/2005	0.64	1.148	Photometric

**Table 5.** Journal of the observations for SDSS J1226–0006. Grism and filter: G300V+GG435. SR collimator: 0.2'' per pixel. Slitlets width: 1.0'' ( $R = 400$  at 5900 Å).

ID	Date	Seeing ["]	Airmass	Weather
1	16/05/2005	0.85	1.109	Photometric
2	16/05/2005	0.84	1.099	Photometric
3	16/05/2005	0.92	1.105	Photometric
4	16/05/2005	1.02	1.125	Photometric
5	16/05/2005	0.78	1.221	Photometric
6	16/05/2005	0.89	1.299	Photometric
7	16/05/2005	0.82	1.422	Photometric
8	16/05/2005	0.88	1.576	Photometric

**Table 6.** Journal of the observations for SDSS J1335+0118. Grism and filter: G300V+GG435. HR collimator: 0.1'' per pixel. Slitlets width: 1.0'' ( $R = 210$  at 5900 Å).

ID	Date	Seeing ["]	Airmass	Weather
1	03/02/2005	0.73	1.167	Photometric
2	03/02/2005	0.71	1.133	Photometric
3	03/03/2005	0.69	1.112	Photometric
4	03/03/2005	0.77	1.123	Photometric
5	03/03/2005	0.68	1.153	Photometric
6	03/03/2005	0.62	1.198	Photometric

**Table 7.** Journal of the observations for Q 1355–2257. Grism and filter: G300V+GG435. HR collimator: 0.1'' per pixel. Slitlets width: 1.0'' ( $R = 210$  at 5900 Å).

ID	Date	Seeing ["]	Airmass	Weather
1	05/03/2005	0.68	1.016	Photometric
2	05/03/2005	0.73	1.040	Photometric
3	20/03/2005	0.63	1.038	Photometric
4	20/03/2005	0.54	1.015	Photometric
5	20/03/2005	0.57	1.105	Photometric
6	20/03/2005	0.56	1.166	Photometric

**Table 8.** Journal of observations for WFI J2033–4723. Grism and filter: G300V+GG435. HR collimator: 0.1'' per pixel. Slitlets width: 1.4'' ( $R = 160$  at 5900 Å).

ID	Date	Seeing ["]	Airmass	Weather
1	13/05/2005	0.50	1.256	Light clouds
2	13/05/2005	0.58	1.198	Light clouds
3	13/05/2005	0.60	1.148	Light clouds
4	13/05/2005	0.48	1.117	Light clouds
5	13/05/2005	0.53	1.095	Light clouds

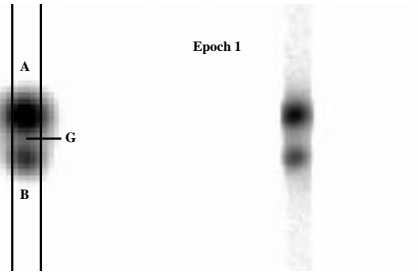


**Fig. 1.** HE 0047–1756. Slit width: 1.0''. Mask PA: 10°.

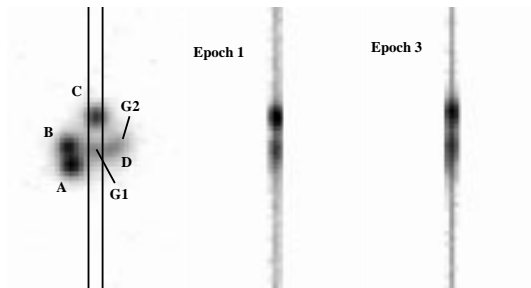


**Fig. 2.** HE 0230–2130. Slit width: 0.5''. Mask PA: –60°.

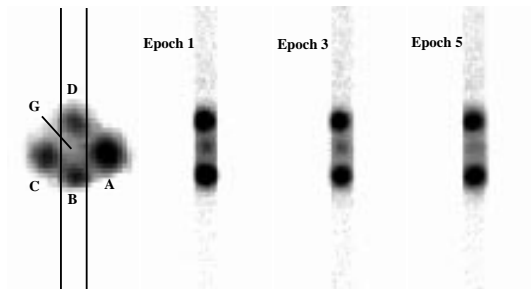


**Fig. 3.** HE 0435–1223. Slit width: 1.0''. Mask PA: –164°.

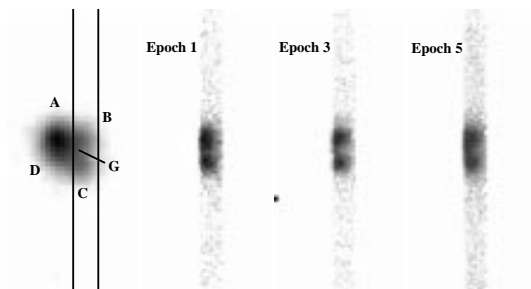


**Fig. 4.** SDSS J1138+0314. Slit width: 1.0''. Mask PA: –84°.

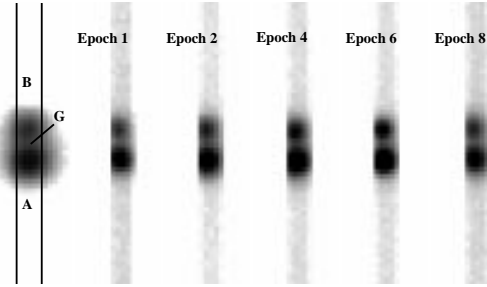


**Fig. 5.** SDSS J1226–0006. Slit width: 1.0''. Mask PA: –90°.

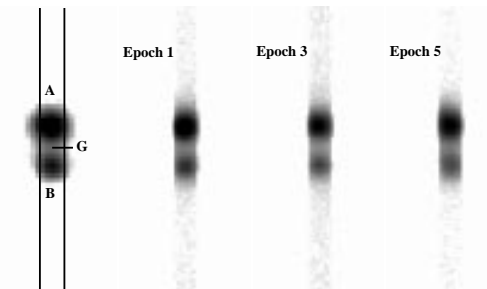


**Fig. 6.** SDSS J1335+0118. Slit width: 1.0''. Mask PA: 43°.

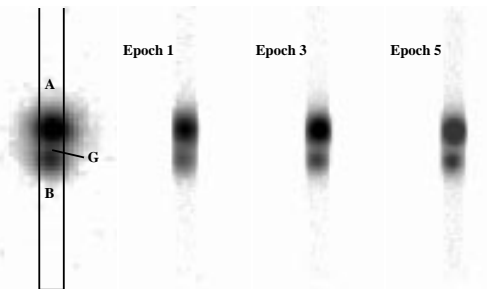


**Fig. 7.** Q 1355–2257. Slit width: 1.0''. Mask PA: –78°.

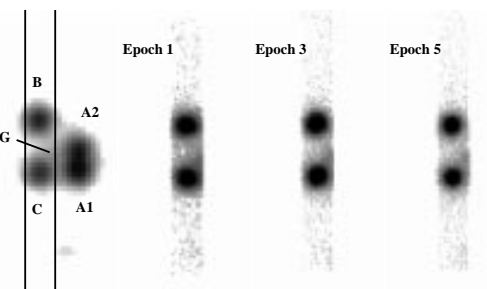


**Fig. 8.** WFI J2033–4723. Slit width: 1.4''. Mask PA: –82°.

In addition to our own data, we retrieve VLT/FORS1 data from the archive for HE 0230–2130. These data were acquired on 18 October 1999 for program 064.O-0259(A). They used the long slit mode with the standard resolution collimator (0.2'' per pixel), the G600R grism, and the order sorting filter GG435. The useful wavelength range is the same as for the MOS observations, i.e.,  $5250 < \lambda < 7450$  Å with a pixel scale of 1.08 Å in the spectral direction.

## 2.2. Reduction and deconvolution

We carry out the standard bias subtraction and flat field correction of the spectra using IRAF<sup>1</sup>. The flat field is created for each slitlet from five dome exposures using cosmic ray rejection. It is then normalized by averaging 45 lines along the spatial direction, rejecting the 20 highest and 20 lowest pixels. The result is then block replicated to match the physical size of the individual flat fields.

Wavelength calibration is obtained from numerous emission lines in the spectrum of helium-argon lamps. The wavelength solution is fitted in two dimensions to each slitlet of the MOS mask. The fit uses a fifth order Chebyshev polynomial along the spectral direction and a fourth order Chebyshev polynomial fit along the spatial direction. Each spectrum is interpolated following this fit using a cubic interpolation. This procedure ensures that the sky lines are well aligned with the columns of the CCD after wavelength calibration.

The sky background is then removed by fitting and subtracting a second order Chebyshev polynomial in the spatial direction to the areas of the spectrum that are not illuminated by the object.

Finally, we remove the cosmic rays as follows. First we shift the spectra in order to align them spatially (this shift is only a few tenths of a pixel). Second, we create a combined spectrum for each object from all exposures, removing the lower and higher pixels, after applying appropriate flux scaling. The combined spectrum obtained in that way is cosmic ray cleaned and is used as a reference template to clean the individual spectra. For each MOS mask the object slitlet and the PSF slitlets are reduced exactly in the same way.

A flux cross-calibration of the spectra taken at different airmasses or dates is needed before combining them into one final spectrum. This is done efficiently using the spectra of the PSF stars as references, as described in Eigenbrod et al. (2006). The reference stars are assumed to be non-variable and a ratio spectrum is created for each star, i.e. we divide the spectrum of the star by the spectrum of the same star in the other exposures. This is done for at least two stars in each mask and we check that the response curves derived using different stars are compatible. The dispersion between the response curves obtained in that way is about 2%. A mean correction curve is then computed and applied to each two-dimensional spectrum. The individual spectra for each object are finally combined.

The archive data of HE 0230–2130 consist of one single long slit spectrum. The bias subtraction, flatfielding, wavelength calibration and background removal are done in exactly the same way as for the MOS spectra. The cosmic ray removal is done using the IRAF packages for single-image data. The flux calibration is done using three standard stars: G93–48, LTT 7987, LTT 9239, taken on the same night as the science frame.

## 2.3. Deconvolution and extraction of the MOS spectra

Even though the seeing values are good for most spectra, the lensing galaxy is often close enough to the brighter quasar images to be affected by significant contamination from the wings of the PSF. For this reason, the spectral version of the MCS deconvolution algorithm (Magain et al. 1998; Courbin et al. 2000) is used in order to separate the spectrum of the lensing

galaxy from the spectra of the quasar images. The MCS algorithm uses the spatial information contained in the spectrum of a reference PSF, which is obtained from the slitlets positioned on the isolated stars. The final normalized PSF is a combination of at least three different PSF spectra. The deconvolved spectra are not only sharpened in the spatial direction, but also decomposed into a “point-source channel” containing the spectra of the quasar images, and a “extended channel” containing the spectra of everything in the image which is not a point-source, i.e. in this case the spectrum of the lensing galaxy.

The deconvolved spectra of the lensing galaxies are extracted and smoothed with a 10 Å box. Figures 9 to 16 display the final one-dimensional spectra, where the Ca II H & K absorption lines are obvious, as well as the 4000 Å Balmer break, and the G-band typical for CH absorption. In some cases, we identify a few more features that are labeled in the individual figures. The identified lines are used to determine the redshift of the lensing galaxies given in Table 9. We compute the 1- $\sigma$  error as the standard deviation between all the measurements of the individual lines. The absence of emission lines in all spectra indicates that the observed lensing galaxies are gas-poor early-type galaxies.

In most cases, no trace of the quasar broad emission lines is seen in the spectrum of the lensing galaxy, indicative of an accurate decomposition of the data into the extended (lens) and point source (quasar images) channels. Only our VLT spectrum of the lensing galaxy of HE 0230–2130 is suffering from residuals of the quasar broad emission lines, probably due to lateral contamination by images A and B of the quasar. This additional source of contamination is circumvented by subtracting a scaled version of the spectrum of quasar image C to the spectrum of the lensing galaxy. The flux calibration of this particular lens might therefore be less accurate than for the other objects. Note, however, that this procedure was only applied to HE 0230–2130.

## 3. Notes on individual objects

**HE 0047–1756:** a doubly imaged quasar discovered by Wisotzki et al. (2004). It has a redshift of  $z = 1.67$  and a maximum image separation of 1.44". The redshift of the lensing galaxy has recently been measured by Ofek et al. (2005) at  $z_{\text{lens}} = 0.408$ . We confirm this result, with  $z_{\text{lens}} = 0.407 \pm 0.001$ , and present a much higher signal-to-noise spectrum in Fig. 9. An elliptical galaxy template matches well the spectrum of the lens.

**HE 0230–2130:** this quadruply imaged  $z = 2.162$  quasar was discovered by Wisotzki et al. (1999). It has a maximum image separation of 2.15" and two lensing galaxies. The main lensing galaxy, G1, is located between the four quasar images. A second, fainter lens is located outside the area defined by the quasar images, close to the faint quasar image D (Fig. 17). The spectrum of G1 is shown in Fig. 10. Our redshift ( $z_{\text{lens}} = 0.523 \pm 0.001$ ) is in very good agreement with the result  $z_{\text{lens}} = 0.522$  of Ofek et al. (2005). The spectrum matches well that of an early-type galaxy. The spectrum of the second lensing galaxy G2 is extracted from the archive long-slit spectrum presented in Sect. 4.

**HE 0435–1223:** this quadruply imaged quasar, discovered by Wisotzki et al. (2002), has a redshift of  $z = 1.689$  and has a maximum image separation of 2.56", hence with little contamination of the lens spectrum by the quasar images. The redshift of the lensing galaxy has already been measured (Morgan et al. 2005; Ofek et al. 2005) at  $z_{\text{lens}} = 0.455$ . We confirm this result, with  $z_{\text{lens}} = 0.454 \pm 0.001$ , and present a much higher signal-to-noise spectrum in Fig. 11. A S0 galaxy template matches well the spectrum of the lens.

<sup>1</sup> IRAF is distributed by the National Optical Astronomy Observatories, which are operated by the Association of Universities for Research in Astronomy, Inc., under cooperative agreement with the National Science Foundation.

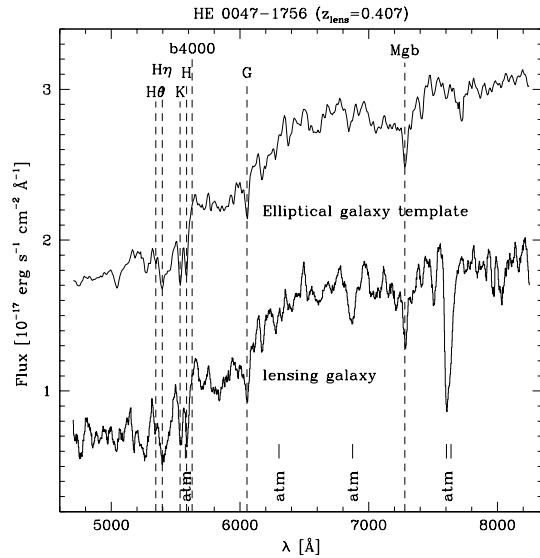


**Fig. 9.** Spectrum of the lens in HE 0047–1756. The total integration time is 2800 s. The template spectrum of a redshifted elliptical galaxy is shown for comparison (Kinney et al. 1996).

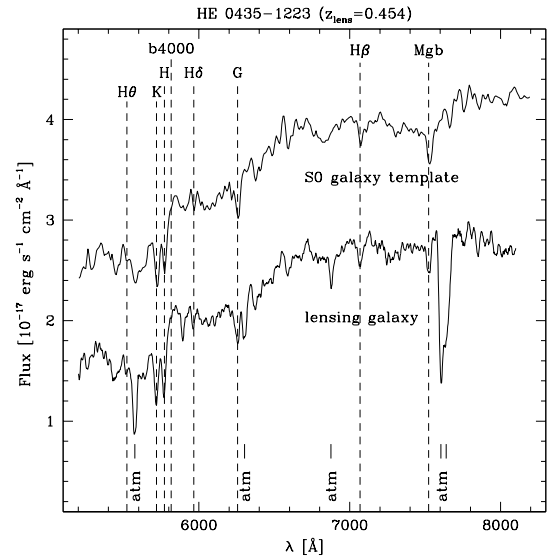


**Fig. 11.** Spectrum of the lens in HE 0435–1223. The total integration time is 8400 s. The template spectrum of a redshifted S0 galaxy is shown (Kinney et al. 1996).

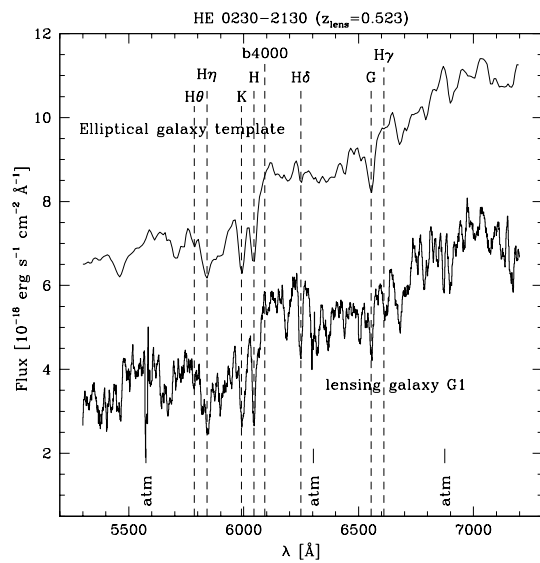


**Fig. 10.** Spectrum of the lensing galaxy G1 in HE 0230–2130, as obtained by combining the data for the three epochs, i.e. a total integration time of 4200 s. A scaled version of the spectrum of quasar image C is subtracted to the spectrum of the lensing galaxy, in order to remove lateral contamination by the quasar images A and B (see text).

**SDSS J1138+0314:** this quadruply imaged quasar was discovered in the course of the Sloan Digital Sky Survey (SDSS) by Burles et al. (2005). This lensed quasar has a maximum image separation of  $1.46''$ . We obtain high signal-to-noise spectra of the quasar and determine its redshift  $z = 2.438$ . There is very little doubt that this system is lensed. The lensing galaxy is seen on archival HST/NICMOS images. We measure  $z_{\text{lens}} = 0.445 \pm 0.001$  (Fig. 12).

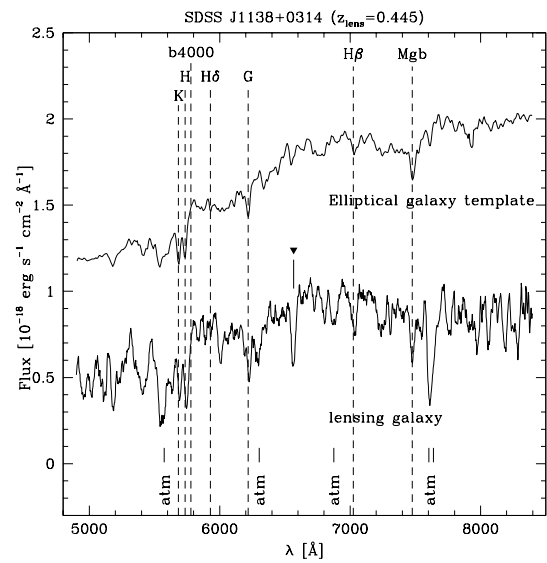


**Fig. 12.** Spectrum of the lens in SDSS J1138+0314. The total integration time is 7000 s. The absorption feature marked by the black triangle is probably residual light of the quasar images. The C III] emission of the quasar falls exactly at this wavelength.

**SDSS J1226–0006:** a doubly imaged quasar at  $z = 1.120$  found in the course of the Sloan Digital Sky Survey (SDSS) by Inada et al. (2005). This system is doubtlessly lensed, as the lensing galaxy is seen on archival HST/ACS images, between both quasar images, at only  $0.4''$  away from image A. We measure  $z_{\text{lens}} = 0.516 \pm 0.001$  (Fig. 13). The spectrum of the lensing galaxy is well matched by the spectrum of an elliptical galaxy.

**SDSS J1335+0118:** a doubly imaged quasar with a  $1.56''$  separation, discovered by Oguri et al. (2004). The quasar is at



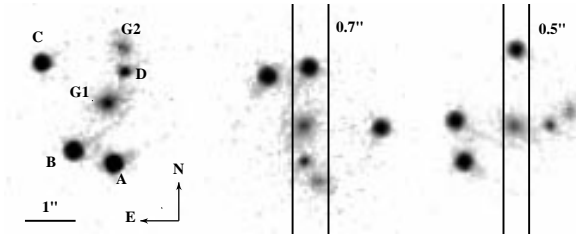


**Fig. 17.** *Right:* HST image of HE 0230–2130 taken with the WFPC2 instrument in the F814W filter. The pixel scale is  $0.05''$ . *Middle:* same image but with a position angle of  $-160^\circ$ . We show in overlay a  $0.7''$  slit which corresponds to the observational setup used to take the long-slit spectrum (program 064.O-0259(A) archive data). *Left:* for comparison, we show the slit used for our MOS observations. The position angle is  $-60^\circ$  and the slit has a width of  $0.5''$ . Negative angles are counted clockwise from North.

**Table 9.** Redshift values determined for the lensing galaxies in the eight gravitational lenses. Only a tentative redshift is given for Q 1355–2257. See Section 4 for more details about the second lens G2 in HE 0230–2130.

Object	$z_{\text{lens}}$
HE 0047–1756	$0.407 \pm 0.001$
HE 0230–2130, G1	$0.523 \pm 0.001$
HE 0230–2130, G2	$0.526 \pm 0.002$
HE 0435–1223	$0.454 \pm 0.001$
SDSS J1138+0314	$0.445 \pm 0.001$
SDSS J1226–0006	$0.517 \pm 0.001$
SDSS J1335+0118	$0.440 \pm 0.001$
Q 1355–2257	$0.701(?)$
WFI J2033–4723	$0.661 \pm 0.001$

redshift is compatible with but slightly higher than the one reported by Ofek et al. (2005).

#### 4. The second lens in HE 0230–2130

The long-slit archive FORS1 spectrum of HE 0230–2130 is taken with the slit centered on the quasar images B and D (middle panel in Fig. 17). The two-dimensional sky-subtracted spectrum is shown in Fig. 18, where a hint of an emission line can already be seen at the spatial location of lens G2 along the slit.

As no PSF star is available the data have to be deconvolved in a different way than the MOS spectra. We proceed in an iterative way. First, we cut the spectrum in two along the spectral direction and determine a first estimate of the reference PSF spectrum from the brighter quasar image B directly. During this first step, the PSF is constructed from the upper half of the spectrum in Fig. 18 containing the spectrum of image B. We then deconvolve the original data, we take the extended-channel part of the deconvolution, reconvolve it with the approximate PSF and subtract it from the data. This provides us with a spectrum of the quasar image that is much less affected by the lensing galaxy. A second PSF is constructed from these new lens-cleaned spectra and a new deconvolution is carried out. We perform this cycle twice to obtain the final spectrum presented in Fig. 19. This spectrum has a lower signal-to-noise than our MOS spectra and less accurate flux calibration but it allows to measure well the redshift of lens G2, which displays prominent [OII] emission, contrary to lens G1. Fig. 18 shows that the emission comes from an object lying outside the region delimited by the quasar image. It therefore clearly corresponds to lens G2.

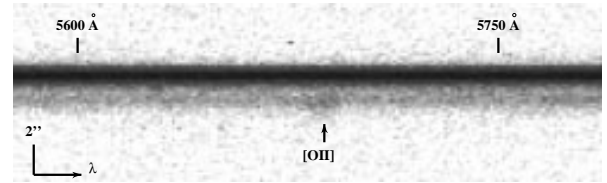


**Fig. 18.** Spectra of quasar image B and D of HE 0230–2130 (slit as in the middle panel of Fig. 17). A strong emission feature is seen “below” the quasar image D. It extends well beyond the area delimited by the quasar images, and corresponds to the [OII] emission of galaxy G2.

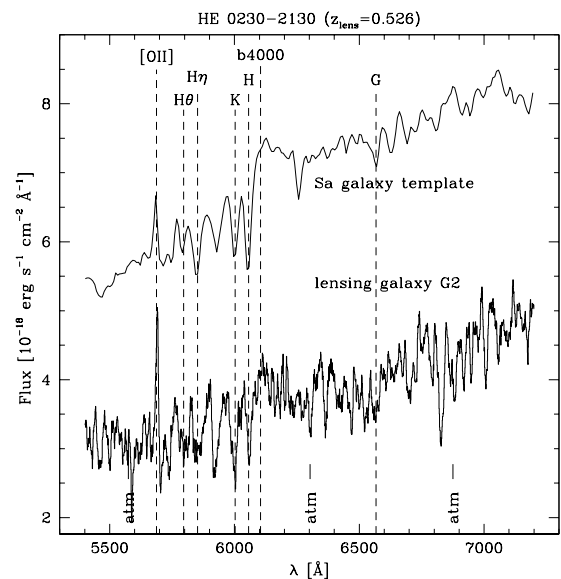


**Fig. 19.** Spectrum of the second lensing galaxy G2 in HE 0230–2130, obtained from the FORS1 long-slit spectrum. The exposure time is 3000 s. Note the prominent [OII] emission lines, absent from the spectrum of G1 (Fig. 10).

The redshift of lens G2 is  $z_{\text{lens}} = 0.526 \pm 0.002$ . It is measured using the [OII] emission, the Ca II H & K absorption lines, the G-band, and the hydrogen H $\theta$  and H $\eta$  absorption lines. The deconvolved spectrum of G2 is shown in Fig. 19. Although the flux calibration is not optimal without a good knowledge of the PSF, the spectrum resembles that of a Sa spiral galaxy.

As can be seen in the middle panel of Fig. 17, G2 is not well centered in the slit but lies at  $0.4''$  away from the slit center. This small *spatial* misalignment of the object within the slit mimics a spectral shift of  $\sim 2 \text{ \AA}$  to the red. This translates into a redshift change of less than  $\Delta z = 0.0004$  at  $6000 \text{ \AA}$  and has no effect on the redshift determination of galaxy G2. We conclude that the observed difference in redshift  $\Delta z = 0.003$  between galaxy G1 and G2 is real. It translates into a velocity difference of  $\Delta v = 900 \pm 450 \text{ km s}^{-1}$  typical for a galaxy group. HE 0230–2130 might therefore be lensed by a group of physically related galaxies of which G1 and G2 are two of the main members.

## 5. Summary and conclusions

We present here the previously unknown redshifts of the lensing galaxies in three gravitationally lensed quasars and confirm four others, already presented in Ofek et al. (2005). We also measure the redshift of a second lensing galaxy in HE 0230–2130 and give a tentative estimate of the lens redshift in Q 1355–2257.

The MOS mode in which all observations are taken and the subsequent observation of several PSF stars is crucial to carry out a reliable decontamination of the lens spectrum by those of the quasar images. The PSF stars are also used to carry out a very accurate flux calibration of the spectra.

Contrary to long-slit observations where no PSF stars are available (Ofek et al. 2005), we do not need to iteratively remove a scaled version of the quasar spectra from the data. Because microlensing can produce significant differences between the spectra of the quasar images, such a procedure may result in biased continuum slopes and wrong conclusions about the presence of dust in the lens. For this reason we fully base our extraction on a spatial decomposition using independent PSF spectra.

We find that all the lensing galaxies in our sample are early-type ellipticals or S0, except for the second lensing galaxy in HE 0230–2130, which displays prominent [OII] emission. And we do not find any evidence for significant extinction by dust in their interstellar medium.

*Acknowledgements.* The authors are very grateful to the ESO staff at Paranal for the particular care paid to the slit alignment necessary to perform the spectra deconvolutions. P.M. acknowledge financial support from PRODEX (Belgium). COSMOGRAIL is financially supported by the Swiss National Science Foundation (SNSF). The image shown in Fig. 17 was obtained with the NASA/ESA Hubble Space Telescope (Program # 9744, PI: C. S. Kochanek) and extracted from the data archives at the Space Telescope Science Institute, which is operated by the Association of Universities for Research in Astronomy, Inc., under NASA contract NAS 5-26555.

## References

- Abajas, C., Mediavilla, E., Muñoz, J. A., Popović, L. Č., & Osoz, A. 2002, *ApJ*, 576, 640  
 Agol, E., & Krolik, J. 1999, *ApJ*, 524, 49  
 Burles, S., et al. 2005, in preparation  
 Courbin, F., Magain, P., Kirkove, M., & Sohy, S. 2000, *ApJ*, 529, 1136  
 Eigenbrod, A., Courbin, F., Vuissoz, C., et al. 2005, *A&A*, 436, 25  
 Eigenbrod, A., Courbin, F., Dye, S., et al. 2006, 451, 747  
 Inada, N., et al. 2005, in preparation  
 Kinney, A. L., Calzetti, D., Bohlin, R. C., et al. 1996, *ApJ*, 467, 38  
 Magain, P., Courbin, F., & Sohy, S. 1998, *ApJ*, 494, 452  
 Mineshige, S., & Yonehara, A. 1999, *PASJ*, 51, 497  
 Morgan, N. D., Gregg, M. D., Wisotzki, L., et al. 2003, *AJ*, 126, 696  
 Morgan, N. D., Cardwell, J. A. R., Schechter, P. L., et al. 2004, *AJ*, 127, 2617  
 Morgan, N. D., Kochanek, C. S., Pevunova, O., & Schechter, P. L. 2005, *AJ*, 129, 2531  
 Ofek, E. O., Maoz, D., Rix, H.-W., Kochanek, C. S., & Falco, E. E. 2005  
 [arXiv:astro-ph/0510465]  
 Oguri, M., Inada, N., Castander, F. J., et al. 2004, *PASJ*, 56, 399  
 Refsdal, S. 1964, *MNRAS*, 128, 307  
 Saha, P., et al. 2005, *A&A*, submitted  
 Walsh, D., Carswell, R. F., & Weymann, R. J. 1979, *Nature*, 279, 381  
 Wisotzki, L., Christlieb, N., Liu, M. C., et al. 1999, *A&A*, 348, L41  
 Wisotzki, L., Schechter, P. L., Bradt, H. V., Heinmüller, J., & Reimers, D., et al. 2002, *A&A*, 395, 17  
 Wisotzki, L., Schechter, P. L., Chen, H.-W., et al. 2004, *A&A*, 419, L31



**6.8 Paper presenting the determination of the redshift of the lensing galaxy in seven gravitationally lensed quasars**

*COSMOGRAIL: the COSmological MONitoring  
of GRAvItational Lenses*

*VI. Redshift of the lensing galaxy in seven gravitationally  
lensed quasars*

A. Eigenbrod, F. Courbin, & G. Meylan

*Astronomy & Astrophysics, 2007, 465, 51*



## COSMOGRAIL: the COSmological MONitoring of GRAVitational Lenses

### VI. Redshift of the lensing galaxy in seven gravitationally lensed quasars<sup>\*</sup>

A. Eigenbrod, F. Courbin, and G. Meylan

Laboratoire d’Astrophysique, École Polytechnique Fédérale de Lausanne (EPFL), Observatoire, 1290 Sauverny, Switzerland  
 e-mail: alexander.eigenbrod@epfl.ch

Received 15 December 2006 / Accepted 12 January 2007

#### ABSTRACT

**Aims.** The knowledge of the redshift of a lensing galaxy that produces multiple images of a background quasar is essential to any subsequent modeling, whether related to the determination of the Hubble constant  $H_0$  or to the mass profile of the lensing galaxy. We present the results of our ongoing spectroscopic observations of gravitationally lensed quasars in order to measure the redshift of their lensing galaxies. We report on the determination of the lens redshift in seven gravitationally lensed systems.

**Methods.** Our deep VLT/FORS1 spectra are spatially deconvolved in order to separate the spectrum of the lensing galaxies from the glare of the much brighter quasar images. Our observing strategy involves observations in Multi-Object-Spectroscopy (MOS) mode which allows the simultaneous observation of the target and of several crucial PSF and flux calibration stars. The advantage of this method over traditional long-slit observations is that it allows a much more reliable extraction and flux calibration of the spectra.

**Results.** We obtain the first reliable spectra of the lensing galaxies in six lensed quasars: FBQ 0951+2635 ( $z_{\text{lens}} = 0.260$ ), BRI 0952–0115 ( $z_{\text{lens}} = 0.632$ ), HE 2149–2745 ( $z_{\text{lens}} = 0.603$ ), Q 0142–100 ( $z_{\text{lens}} = 0.491$ ), SDSS J0246–0825 ( $z_{\text{lens}} = 0.723$ ), and SDSS J0806+2006 ( $z_{\text{lens}} = 0.573$ ). The last three redshifts also correspond to the Mg II doublet seen in absorption in the quasar spectra at the lens redshift. Our spectroscopic redshifts of HE 2149–2745 and FBQ 0951+2635 are higher than previously reported, which means that  $H_0$  estimates from these two systems must be revised to higher values. Finally, we reanalyse the blue side of our previously published spectra of Q 1355–2257 and find Mg II in absorption at  $z = 0.702$ , confirming our previous redshift estimate. The spectra of all lenses are typical of early-type galaxies.

**Key words.** gravitational lensing – cosmology: cosmological parameters

## 1. Introduction

About 100 gravitationally lensed quasars have been found since the discovery of the first case by Walsh et al. (1979). An advantage of lensed quasars resides in their possible variability, potentially leading to the measurement of the so-called time delay between the lensed images of the source. This quantity is directly related to the Hubble constant  $H_0$  and to the slope of the mass profile of the lensing galaxy at the position of the quasar images projected on the plane of the sky. Assuming a model for the mass distribution in the lensing galaxy, and measuring the time delay, one can infer the value of  $H_0$  (Refsdal 1964). Conversely, for a given  $H_0$  estimate, the mass distribution in the lens can be reconstructed from the time delay measurement. In both cases, one wishes to construct a large, statistically significant sample of lensed quasars, either to reduce the random errors on  $H_0$ , or to build a large sample of massive early-type galaxies, the mass profile of which can be strongly constrained, thanks to gravitational lensing.

For whatever subsequent application of quasar lensing, some of the key measurements to carry out in each individual system are (i) the value of the time delay; (ii) the astrometry of all quasar images with respect to the lensing galaxy; and (iii) the redshift of the lensing galaxy.

The main goal of COSMOGRAIL (e.g. Eigenbrod et al. 2005) is to measure a large number of time delays from a photometric monitoring campaign based on a few 2-m class telescopes. While this goal can be reached only in the long run, it is possible to pave the way to accurate modeling of the systems by obtaining the redshift of the lensing galaxies in all the systems currently monitored. This is the goal of the present paper, which is the continuation of our spectroscopic study of lensed quasars, undertaken at the VLT with FORS1 (e.g. Eigenbrod et al. 2006b).

## 2. VLT spectroscopy

### 2.1. Observations

We present new observations of six gravitationally lensed quasars, in order to determine the redshift of the lensing galaxy, plus a re-analysis of one object previously published in Eigenbrod et al. (2006b). The details of the observational setup and of the data reduction can be found in Eigenbrod et al. (2006a,b), but we remind in the following some of the most important points.

Our observations are acquired with the Focal Reducer and low dispersion Spectrograph (FORS1), mounted on the ESO Very Large Telescope at the Observatory of Paranal (Chile). All the observations are carried out in the MOS mode (Multi Object Spectroscopy). This strategy is the most convenient to get

<sup>\*</sup> Based on observations made with the ESO-VLT Unit Telescope 2 Kueyen (Cerro Paranal, Chile; Programs 077.A-0155, PI: G. Meylan).

simultaneous observations of the main target and of several stars used both as flux calibrators and as reference point-spread functions (PSF) in order to spatially deconvolve the spectra. We choose these stars to be located as close as possible to the gravitationally lensed quasars with similar apparent magnitudes.

All targets are observed with the high-resolution collimator, allowing us to observe simultaneously eight objects over a field of view of  $3.4' \times 3.4'$  with a pixel scale of  $0.1''$ . The GG435 order sorting filter in combination with the G300V grism is used for all objects, giving a useful wavelength range  $4450 < \lambda < 8650 \text{ \AA}$  and a scale of  $2.69 \text{ \AA}$  per pixel in the spectral direction. This setup has a spectral resolution  $R = \lambda/\Delta\lambda \approx 200$  at the central wavelength  $\lambda = 5900 \text{ \AA}$  for a  $1.0''$  slit width in the case of the high resolution collimator. The choice of this grism favors spectral coverage rather than spectral resolution as we aim at measuring unknown lens redshifts.

We choose slitlets of  $1.0''$  width, matching the seeing requested for these service-mode observations. Our observing sequences consist of a short acquisition image, an “image-through-slit” check, followed by two consecutive deep spectroscopic exposures. All individual exposures for all objects are 1400 s long. The journals of the observations are given in Table 1. The through-slit images are displayed in Figs. 1 to 6, where the epochs refer to the exposure numbers in Table 1.

For every object we center at least two slitlets on foreground stars and one slitlet along the lensed images of the quasar. The mask is rotated to a Position Angle that avoids clipping of any quasar image. This is mandatory to carry out spatial deconvolution of the spectra. The spectra of the PSF stars are also used to cross-calibrate the flux scale as the data are taken at different airmasses and at different epochs (see Eigenbrod et al. 2006a). Six spectrophotometric standard stars are used to carry out the relative flux calibration, i.e. GD 108, HD 49798, LTT 377, LTT 1020, LTT 1788, and LTT 7987.

## 2.2. Reduction and deconvolution

We follow exactly the same procedure as described by Eigenbrod et al. (2006b). We carry out the standard bias subtraction, flat field correction and sky background subtraction using IRAF<sup>1</sup>. The wavelength calibration is obtained from the spectrum of helium-argon lamps. The cosmic rays are removed using multiple exposures.

A flux cross-calibration of the spectra is applied before combining them into one final spectrum. This is done efficiently using the spectra of the PSF stars as references.

In order to separate the spectrum of the lensing galaxy from the spectra of the much brighter quasar images, we use the spectral version of the MCS deconvolution algorithm (Magain et al. 1998; Courbin et al. 2000)

This software uses the spatial information contained in the spectra of several reference PSF stars. The deconvolved spectra are sharpened in the spatial direction, and also decomposed into a “point-source channel” containing the spectra of the quasar images, and an “extended channel” containing the spectra of everything in the image which is not a point-source, i.e. in this case the spectrum of the lensing galaxy.

The deconvolved spectra of the lensing galaxies are extracted and smoothed with a  $10\text{-\AA}$  box. Figures 7 to 12 display the

<sup>1</sup> IRAF is distributed by the National Optical Astronomy Observatories, which are operated by the Association of Universities for Research in Astronomy, Inc., under cooperative agreement with the National Science Foundation.

**Table 1.** Journal of the observations.

ID	Date	Seeing ["]	Airmass	Weather
Q 0142–100				
1	11/08/2006	0.83	1.119	Photometric
2	11/08/2006	0.77	1.078	Photometric
3	19/08/2006	0.78	1.709	Photometric
4	19/08/2006	0.79	1.507	Photometric
SDSS J0246–0825				
1	22/08/2006	0.76	1.490	Photometric
2	22/08/2006	0.67	1.350	Photometric
3	22/08/2006	0.60	1.234	Photometric
4	22/08/2006	0.58	1.161	Photometric
5	22/08/2006	0.61	1.103	Photometric
6	22/08/2006	0.59	1.069	Photometric
SDSS J0806+2006				
1	22/04/2006	0.86	1.442	Photometric
2	22/04/2006	0.90	1.494	Photometric
3	23/04/2006	0.93	1.590	Photometric
4	23/04/2006	0.95	1.714	Photometric
FBQ 0951+2635				
1	31/03/2006	0.68	1.600	Photometric
2	31/03/2006	0.74	1.593	Photometric
3	01/04/2006	0.59	1.598	Photometric
4	01/04/2006	0.57	1.629	Photometric
BRI 0952–0115				
1	23/04/2006	0.67	1.097	Photometric
2	24/04/2006	0.58	1.087	Photometric
3	24/04/2006	0.56	1.094	Photometric
4	24/04/2006	0.50	1.116	Photometric
5	24/04/2006	0.42	1.165	Photometric
6	24/04/2006	0.45	1.225	Photometric
Q 1355–2257				
1	05/03/2005	0.68	1.016	Photometric
2	05/03/2005	0.73	1.040	Photometric
3	20/03/2005	0.63	1.038	Photometric
4	20/03/2005	0.54	1.015	Photometric
5	20/03/2005	0.57	1.105	Photometric
6	20/03/2005	0.56	1.166	Photometric
HE 2149–2745				
1	04/08/2006	0.66	2.004	Photometric
2	04/08/2006	0.62	1.724	Photometric
3	04/08/2006	0.62	1.461	Photometric
4	04/08/2006	0.69	1.328	Photometric
5	04/08/2006	0.52	1.204	Photometric
6	04/08/2006	0.59	1.134	Photometric

final one-dimensional spectra, where the Ca II H & K absorption lines are obvious, as well as the  $4000\text{-\AA}$  Balmer break, and the G band typical for CH absorption. In some cases, we identify a few more features that are labeled in the individual figures. The identified lines are used to determine the redshift of the lensing galaxies given in Table 2. We compute the  $1\text{-}\sigma$  error as the standard deviation between all the measurements of the individual lines. The absence of emission lines in all spectra indicates that these observed lensing galaxies are gas-poor early-type galaxies.

In most cases, no trace of the quasar broad emission lines is seen in the spectrum of the lensing galaxy, indicative of an accurate decomposition of the data into the extended (lens) and point source (quasar images) channels. Only our VLT spectrum of the lensing galaxy of BRI 0952–0115 is suffering from residuals of the quasar Ly $\alpha$  emission: the presence of the strong Ly $\alpha$  in the blue side of the spectrum complicates the deconvolution process.

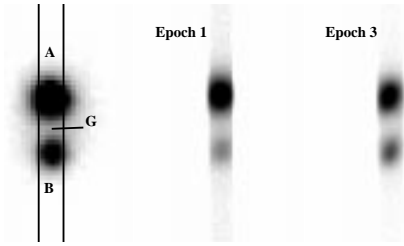


Fig. 1. Q 0142–100. Slit width:  $1.0''$ . Mask PA:  $+75^\circ$ .

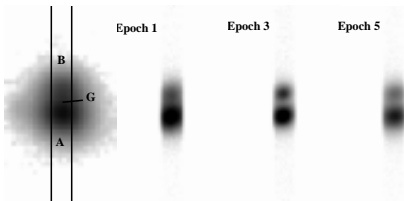


Fig. 2. SDSS J0246–0825. Slit width:  $1.0''$ . Mask PA:  $+55^\circ$ .

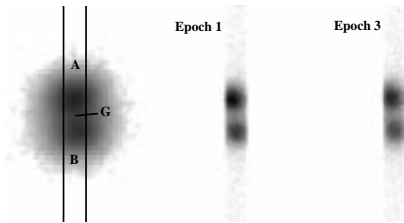


Fig. 3. SDSS J0806+2006. Slit width:  $1.0''$ . Mask PA:  $-56^\circ$ .

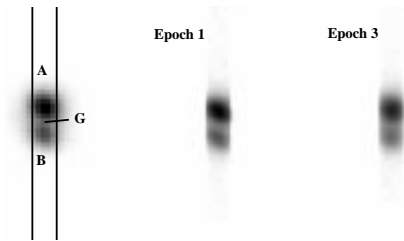


Fig. 4. FBQ 0951+2635. Slit width:  $1.0''$ . Mask PA:  $+53^\circ$ .

### 3. Notes on individual objects

Q 0142–100 (UM 673 or PHL 3703): this object was first discovered by Macalpine & Feldman (1982) as a high redshift quasar with  $z = 2.719$ . A few years later Surdej et al. (1987) identified Q 0142–100 as a gravitational lens with two quasar components separated by  $2.2''$ . No spectrum of the lensing galaxy has ever been obtained, but Ca II and Na I absorption lines are detected in the spectrum of the fainter quasar image B, suggesting that it is located at a redshift  $z_{\text{lens}} = 0.493$  (Surdej et al. 1988). From our spectrum of the lensing galaxy we confirm that it is the object responsible for the quasar absorption lines. Our best estimate of the redshift is  $z_{\text{lens}} = 0.491 \pm 0.001$ . The observed galaxy spectrum is typical for an early type galaxy.

SDSS J0246–0825: this double-image quasar was discovered in the course of the Sloan Digital Sky Survey (SDSS) by Inada et al. (2005). The quasar has a redshift  $z = 1.68$  and an image separation of  $1.04''$ . From the Mg II and Mg I absorption lines observed in the spectra of the two quasar

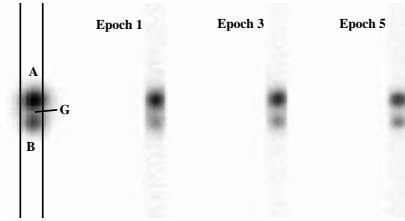


Fig. 5. BRI 0952–0115. Slit width:  $1.0''$ . Mask PA:  $-45^\circ$ .

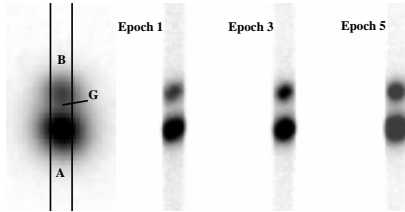


Fig. 6. HE 2149–2745. Slit width:  $1.0''$ . Mask PA:  $-32^\circ$ .

components, Inada et al. (2005) estimate the redshift of the lensing galaxy to be  $z_{\text{lens}} = 0.724$ . Our direct redshift measurement  $z_{\text{lens}} = 0.723 \pm 0.002$  is in very good agreement with this value. The spectrum matches well that of an elliptical galaxy.

SDSS J0806+2006: this two-image gravitationally lensed quasar ( $z = 1.540$ ) was recently discovered by Inada et al. (2006). The two quasar images are separated by  $1.40''$ . Several absorption lines are found in the quasar spectra, such as the (Mg II, Ca II H&K and Fe II) lines, at a redshift of  $z_{\text{lens}} = 0.573$ . The redshift we obtain from our spectrum is  $z_{\text{lens}} = 0.573 \pm 0.001$ . The spectrum (see Fig. 9) matches very well the template spectrum of an elliptical galaxy.

FBQ 0951+2635: a double-image quasar at  $z = 1.246$  with  $1.1''$  image separation found in the course of the FIRST Bright QSO Survey (FBQS) by Schechter et al. (1998). A time delay estimate of  $\Delta t = 16 \pm 2$  days between the quasar images is given by Jakobsson et al. (2005), but the redshift of the lensing galaxy, by the same authors, is found to be elusive. Schechter et al. (1998) detect absorption lines attributed to Mg II at  $z = 0.73$  and  $z = 0.89$  in both spectra of the quasar components. From the position of the lens on the fundamental plane, Kochanek et al. (2000) suggest  $z_{\text{lens}} \approx 0.21$ . We measure  $z_{\text{lens}} = 0.260 \pm 0.002$  for this early-type lensing galaxy. This also corresponds to the photometric redshift of 0.27 measured by Williams et al. (2006) for a group of galaxies in the field of the lensing galaxy.

BRI 0952–0115: this gravitational lens was discovered by McMahon et al. (1992) as a pair of  $z = 4.50$  quasars separated by  $0.9''$ . Kochanek et al. (2000) found that the lens galaxy appears to be a typical early-type lens galaxy, with a fundamental plane redshift estimate of  $z_{\text{lens}} \approx 0.41$ . We measure a significantly higher value, namely  $z_{\text{lens}} = 0.632 \pm 0.002$  (Fig. 11), and the spectrum of the lensing galaxy is well matched by that of an elliptical galaxy. With this new redshift, the lensing galaxy can no longer be considered as a member of the group of galaxies identified by Momcheva et al. (2006), but possibly of another small group in the field at  $z \approx 0.64$ .

Q 1355–2257 (CTQ 327): this two-image quasar, discovered by Morgan et al. (2003), has a redshift of  $z = 1.373$ , and an image separation of  $1.23''$ . The redshift of the lensing galaxies has been estimated by Morgan et al. (2003) to lie in the range  $0.4 < z_{\text{lens}} < 0.6$ . Ofek et al. (2005) note that their spectrum of the quasar component B shows an excess of emission longward

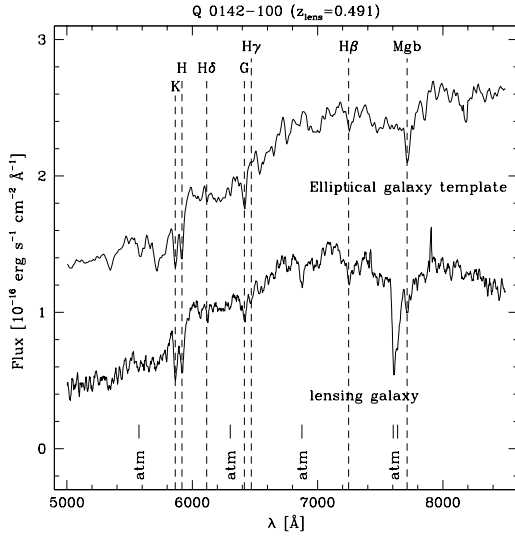


**Fig. 7.** Spectrum of the lens in Q 0142–100. The total integration time is 5600 s. The template spectrum of a redshifted elliptical galaxy is shown for comparison (Kinney et al. 1996). Atmospheric absorptions are indicated in all figures by the label atm.

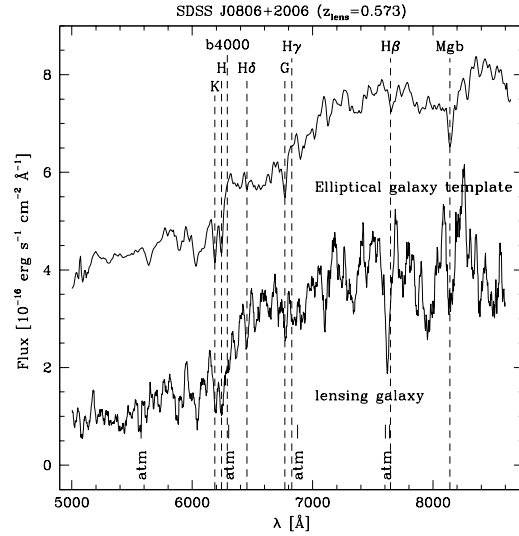


**Fig. 9.** Spectrum of the lens in SDSS J0806+2006. The total integration time is 5600 s.

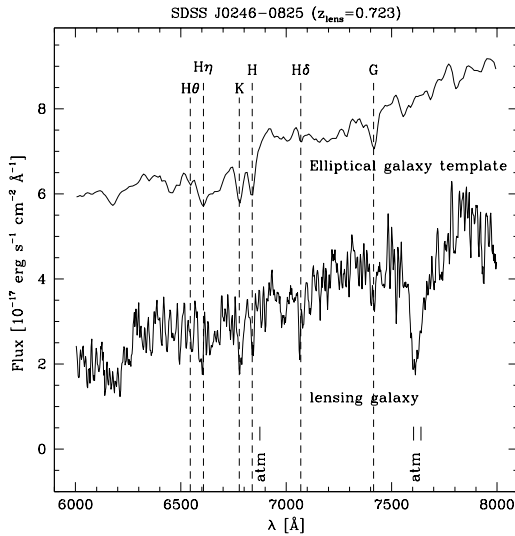


**Fig. 8.** Spectrum of the lens in SDSS J0246–0825. The total integration time is 8400 s.

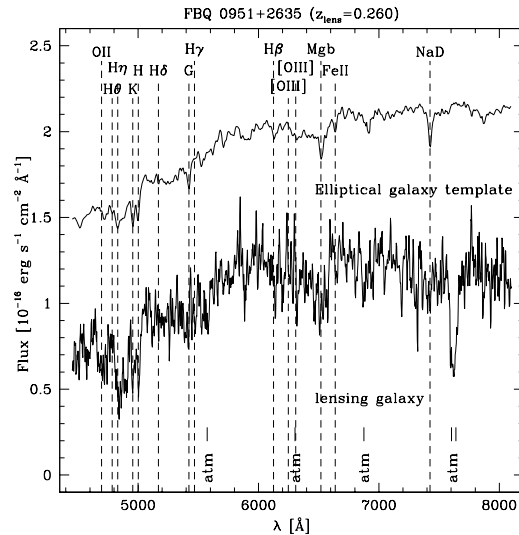


**Fig. 10.** Spectrum of the lens in FBQ 0951+2635. The total integration time is 5600 s.

of  $\sim 5870$  Å. They associate the location of this emission excess to the  $4000$ -Å break of the lensing galaxy leading to a redshift of  $z_{\text{lens}} = 0.48$ . In a previous paper (Eigenbrod et al. 2006b), we gave a significantly higher tentative redshift value of  $z_{\text{lens}} = 0.701$ . A re-analysis of our data allows to extend slightly our spectra to the blue side and to unveil the Mg II absorption line in the spectrum of the quasar component B. The absorption is seen at the redshift we estimate for the spectrum of the lens, i.e.  $z_{\text{lens}} = 0.702 \pm 0.001$ . Figure 13 displays the new quasar spectrum with an enlargement on the region around the Mg II absorption.

HE 2149–2745: Wisotzki et al. (1996) found this bright gravitationally lensed quasar at  $z = 2.033$ , with two images separated by  $1.71''$ . They gave first estimates of the redshift of the lensing galaxy, refined later by Lopez et al. (1998), who infer

a probable redshift range of  $\sim 0.3$ – $0.5$ . Kochanek et al. (2000) give a fundamental plane redshift estimate of  $0.37 \leq z_{\text{lens}} \leq 0.50$ . Burud et al. (2002) measure the time delay between the two images ( $\Delta t = 103 \pm 12$  days) and report a tentative redshift of  $z_{\text{lens}} = 0.495 \pm 0.010$  by cross-correlating the lens spectrum with a template spectrum of an elliptical galaxy, but they notice that the signal-to-noise of the correlation function is poor. Our direct spectroscopic result disagrees with all previous estimates, with the new value of  $z_{\text{lens}} = 0.603 \pm 0.001$ . This value corresponds to the photometric redshift  $z \approx 0.59$  (later spectroscopically confirmed at  $z = 0.603$ ) of a galaxy group in the field (Williams et al. 2006; Momcheva et al. 2006). Faure et al. (2004) also reported this group of galaxies at the photometric redshift  $z = 0.7 \pm 0.1$ .

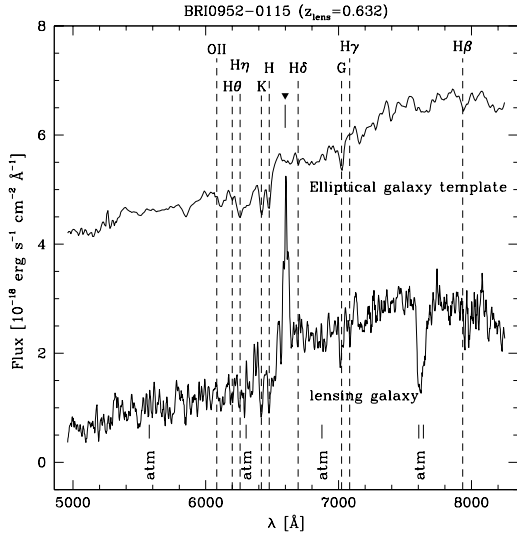


**Fig. 11.** Spectrum of the lens in BRI 0952–0115. The total integration time is 8400 s. The emission feature marked by the black triangle is residual light of the quasar images. The Ly $\alpha$  emission of the quasar falls exactly at this wavelength.

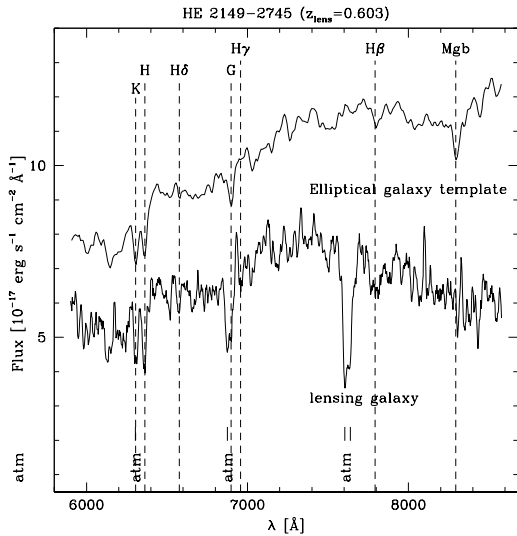


**Fig. 12.** Spectrum of the lens in HE 2149–2745. The total integration time is 8400 s.

#### 4. Summary and conclusions

We present straightforward VLT spectroscopic observations of six gravitationally lensed quasars and we measure the redshift of the lensing galaxy directly from the continuum light spectrum and several sets of absorption lines. The MOS mode in which all observations are taken and the subsequent observation of several PSF stars are crucial to carry out a reliable decontamination of the lens spectrum by those of the quasar images. The PSF stars are also used to carry out a very accurate flux calibration of the spectra.

Three of our redshifts measurements also correspond to absorption lines seen in the quasar spectrum. Following the work of Williams et al. (2006) and Momcheva et al. (2006), we

**Table 2.** Redshift values determined for the lensing galaxies in the seven gravitational lenses.

Object	$z_{\text{lens}}$
Q 0142–100	$0.491 \pm 0.001$
SDSS J0246–0825	$0.723 \pm 0.002$
SDSS J0806+2006	$0.573 \pm 0.001$
FBQ 0951+2635	$0.260 \pm 0.002$
BRI 0952–0115	$0.632 \pm 0.002$
Q 1355–2257	$0.702 \pm 0.001$
HE 2149–2745	$0.603 \pm 0.001$

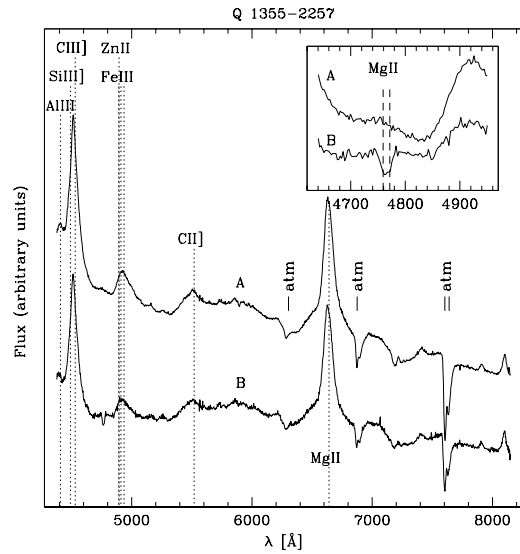


**Fig. 13.** Spectrum of the images of quasar Q 1355–2257. The total integration time is 8400 s. In the inset, we show the Mg II absorption lines present in the spectrum of component B and which is due to the lensing galaxy.

identify three lensing galaxies as members of small groups of galaxies. A re-analysis of the spectra of Q 1355–2257, which lens spectrum has a low signal-to-noise ratio in Eigenbrod et al. (2006b), allows to detect the Mg II doublet in absorption in the quasar spectrum and confirm our previous redshift estimate, i.e.  $z_{\text{lens}} = 0.702 \pm 0.001$ .

Finally, our probably most exciting results are our new redshift measurements for the two lensed quasars with time-delay determinations FBQ 0951+2635 and HE 2149–2745, that are not compatible with previous estimates. We find  $z_{\text{lens}} = 0.260 \pm 0.002$  instead of  $z_{\text{lens}} = 0.21$  for the first and  $z_{\text{lens}} = 0.603 \pm 0.001$  for the second, instead of  $z_{\text{lens}} = 0.495 \pm 0.010$ . This implies that previous estimates of  $H_0$  based on these two systems must be revised to higher values, for a given lens model. While the impact of the change in redshift is negligible for FBQ 0951+2635 given the present uncertainties on the measured time delay (Jakobsson et al. 2005), it is sufficiently large in the case of HE 2149–2745 (Burdud et al. 2002) to justify some new modeling of the system.

These new lens redshifts have a direct impact on several previous studies. More specifically the inferred value for  $H_0$  from the multiple-lens models of Saha et al. (2006) should be updated with these new redshifts, as well as with the recently measured time delay of SDSS J1650+4251 by Vuissoz et al. (2007). In other studies (e.g. Kochanek 2002, 2003; Oguri 2006), HE 2149–2745 is one of lens systems that has been used to

argue possible low  $H_0$  values from time delays. The new lens redshift significantly increases the derived  $H_0$ , thereby weakening the possible low  $H_0$  problem.

*Acknowledgements.* The authors are very grateful to the ESO staff at Paranal for the particular care paid to the slit alignment necessary to perform the spectra deconvolutions. COSMOGRAIL is financially supported by the Swiss National Science Foundation (SNSF).

## References

- Burud, I., Courbin, F., Magain, P., et al. 2002, *A&A*, 383, 71  
 Courbin, F., Magain, P., Kirkove, M., & Sohy, S. 2000, *ApJ*, 529, 1136  
 Eigenbrod, A., Courbin, F., Vuissoz, C., et al. 2005, *A&A*, 436, 25  
 Eigenbrod, A., Courbin, F., Dye, S., et al. 2006a, *A&A*, 451, 747  
 Eigenbrod, A., Courbin, F., Meylan, G., et al. 2006b, *A&A*, 451, 759  
 Faber, S. M., & Jackson, R. E. 1976, *ApJ*, 204, 668  
 Faure, C., Alloin, D., Kneib, J. P., et al. 2004, *A&A*, 428, 741  
 Inada, N., Burles, S., Gregg, M. D., et al. 2005, *AJ*, 130, 1967  
 Inada, N., Oguri, M., Becker, R. H., et al. 2006, *AJ*, 131, 1934  
 Jakobsson, P., Hjorth, J., Burud, I., et al. 2005, *A&A*, 431, 103  
 Kinney, A. L., Calzetti, D., Bohlin, R. C., et al. 1996, *ApJ*, 467, 38  
 Kochanek, C. S. 2002, *ApJ*, 578, 25  
 Kochanek, C. S. 2003, *ApJ*, 583, 49  
 Kochanek, C. S., Falco, E. E., Impey, C. D., et al. 2000, *ApJ*, 543, 131  
 Lopez, S., Wucknitz, O., & Wisotzki, L. 1998, *A&A*, 339, L13  
 Macalpine, G. M., & Feldman, F. R. 1982, *ApJ*, 261, 412  
 Magain, P., Courbin, F., & Sohy, S. 1998, *ApJ*, 494, 452  
 McMahon, R., Irwin, M., & Hazard, C. 1992, *Gemini*, 36, 1  
 Momcheva, I., Williams, K. A., Keeton, C. R., et al. 2006, *ApJ*, 641, 169  
 Morgan, N. D., Gregg, M. D., Wisotzki, L., et al. 2003, *AJ*, 126, 696  
 Morgan, N. D., Cardwell, J. A. R., Schechter, P. L., et al. 2004, *AJ*, 127, 2617  
 Ofek, E. O., Maoz, D., Rix, H.-W., et al. 2006, *ApJ*, 641, 70  
 Oguri, M. 2006 [[arXiv:astro-ph/0609694](https://arxiv.org/abs/astro-ph/0609694)]  
 Refsdal, S. 1964, *MNRAS*, 128, 307  
 Saha, P., Coles, J., Maccio', A. V., et al. 2006, *ApJ*, 650, L17  
 Schechter, P. L., Gregg, M. D., Becker, R. H., et al. 1998, *AJ*, 115, 1371  
 Surdej, J., Swings, J.-P., Magain, P., et al. 1987, *Nature*, 329, 695  
 Surdej, J., Magain, P., Swings, J.-P., et al. 1988, *A&A*, 198, 49  
 Vuissoz, C., Courbin, F., Sluse, D., et al. 2007, *A&A*, 464, 845  
 Walsh, D., Carswell, R. F., & Weymann, R. J. 1979, *Nature*, 279, 381  
 Williams, K. A., Momcheva, I., Keeton, C. R., et al. 2006, *ApJ*, 646, 85  
 Wisotzki, L., Koehler, T., Lopez, S., et al. 1996, *A&A*, 315, 405



**Part III.**  
**The Einstein Cross**



*“Where the telescope ends the microscope begins,  
and who can say which has the wider vision?”  
Victor Hugo (1802 - 1885)*

## Chapter 7

# Microlensing: a natural telescope

In section 4.12, we gave a brief introduction about microlensing on cosmological scales, and described how microlenses (i.e. stars and other compact objects) located in a strong lensing galaxy can produce extrinsic and uncorrelated flux variations in the images of a lensed background quasar. We will now describe in more detail, how this phenomenon can be used as a natural telescope to probe the central emission region of a lensed quasar.

### Extended sources

In the previous chapters, we have generally considered that the lensed background source is a point. This leads to lensed images which are also reduced to points. The total magnification  $\mu_p(\boldsymbol{\beta})$  of such a source located at  $\boldsymbol{\beta}$  is given by the sum of the magnifications over all its images, i.e.

$$\mu_p(\boldsymbol{\beta}) = \sum_{i=1}^n |\mu(\boldsymbol{\theta}_i)|$$

where  $n$  is the number of lensed images. The total magnification  $\mu_p(\boldsymbol{\beta})$  is a function of the source position and defines, in the source plane, the so-called magnification pattern. A magnification pattern obtained for a distribution of point-like microlenses is illustrated in the upper left panel of Fig. 7.1. An interesting point to investigate is the case of an extended source. Let us assume that the source is located at  $\boldsymbol{\beta}$  and that the surface brightness profile of the source is  $I(\boldsymbol{\beta})$ . The total magnification  $\mu(\boldsymbol{\beta})$  of this source is given by the weighted mean over the source area

$$\mu(\boldsymbol{\beta}) = \left( \int I(\boldsymbol{\beta}') d^2\beta' \right)^{-1} \int \mu_p(\boldsymbol{\beta}') I(\boldsymbol{\beta}' - \boldsymbol{\beta}) d^2\beta' .$$

The integral corresponds to the convolution of the surface brightness profile  $I(\boldsymbol{\beta})$  and the magnification pattern  $\mu_p(\boldsymbol{\beta})$ . This last equation is very interesting, because it shows that, for the same lens, different surface brightness profile will have different total magnifications

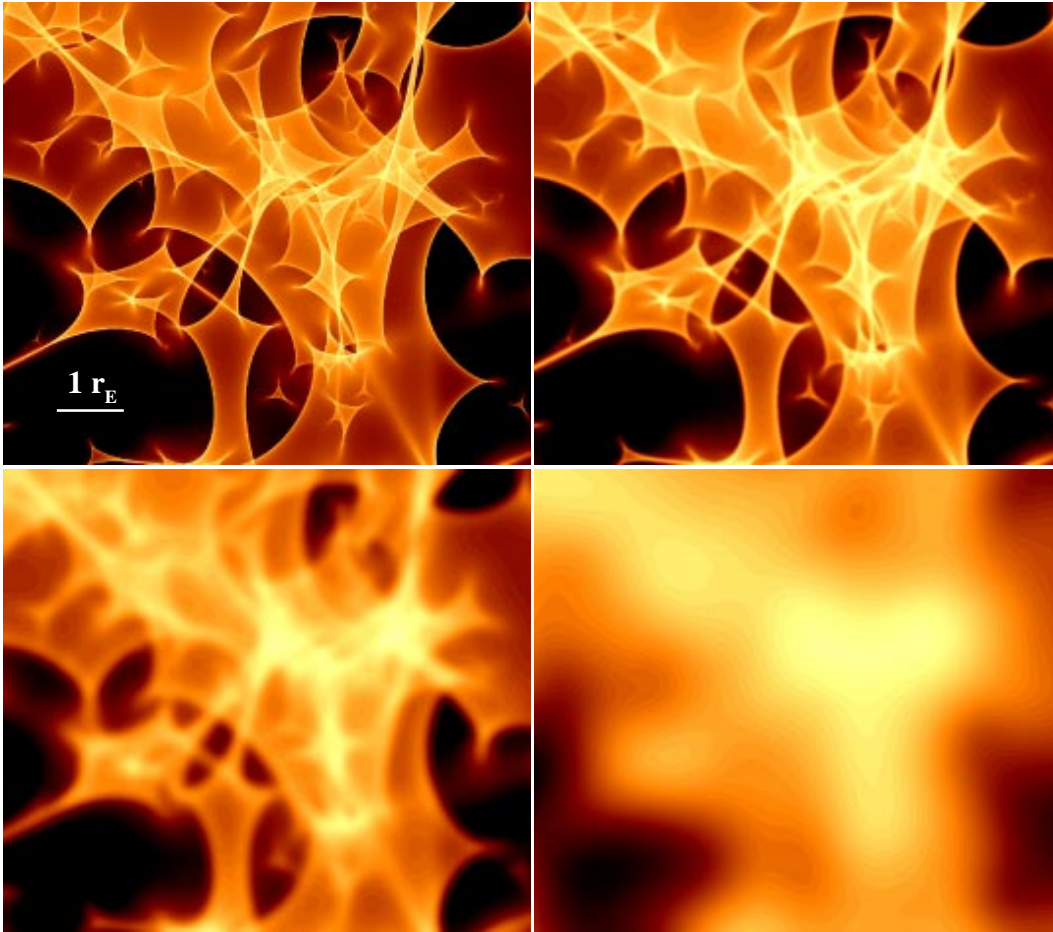


Figure 7.1: Example (top left) of a magnification pattern  $\mu_p(\beta)$  for a random distribution of  $1 M_\odot$  point-like lenses obtained with the inverse ray-shooting method (Wambsganss, 1999). The total magnification  $\mu(\beta)$  of an extended source is given by the convolution of the magnification pattern  $\mu_p(\beta)$  with the surface brightness profiles  $I(\beta)$  of the source. Displayed are the total magnification  $\mu(\beta)$  obtained for three different Gaussian source profiles with FWHM =  $0.05 r_E$  (top right),  $0.2 r_E$  (bottom left), and  $1 r_E$  (bottom right).

$\mu(\beta)$ . In Fig. 7.1, we illustrate this effect for Gaussian surface brightness profiles with different sizes, i.e. with different full widths at half maximum (FWHM).

### Chromatic effects

Whereas gravitational lensing is achromatic, because the deflection of photons does not depend on their wavelength, the magnification of an extended source can lead to color terms in practice, since the surface brightness profile  $I(\beta)$  might be different at different wavelengths (e.g., Kayser et al., 1986; Wambsganss & Paczyński, 1991). A typical example for such a source is a quasar accretion disk, where high-energy photons are emitted closer to the quasar's center than low-energy photons. For example, we have seen in Section 3.3, that for a standard thin accretion disk, the expected source size  $R_s$  emitting at wavelength  $\lambda$  scales as  $R_s(\lambda) \propto \lambda^{4/3}$ .

An important point is that these chromatic effects can only be observed if the magnification pattern  $\mu_p(\boldsymbol{\beta})$  varies on scales comparable with the source size. The scale on which the magnification pattern varies is given, to the first order, by the Einstein radius in the source plane

$$r_E \doteq D_s \theta_E = D_s \sqrt{\frac{4GM}{c^2} \frac{D_{ls}}{D_s D_l}} \simeq 4 \times 10^{16} \sqrt{\frac{M}{M_\odot}} \text{ cm}$$

where typical lens and source redshift of  $z_l = 0.5$  and  $z_s = 2.0$  are assumed for the numerical value on the right-hand side.

As can be seen in Fig. 7.1, if  $R_s \gg r_E$ , the convolution of  $\mu_p(\boldsymbol{\beta})$  and  $I(\boldsymbol{\beta})$  will produce a total magnification  $\mu(\boldsymbol{\beta})$  that is strongly smoothed leading to  $\mu(\boldsymbol{\beta}) \simeq \langle \mu_p \rangle$ , where  $\mu(\boldsymbol{\beta})$  is independent on the source profile  $I(\boldsymbol{\beta})$ . In the other extreme case of  $R_s \ll r_E$ , the source profile can be assimilated to a ‘‘Dirac function’’, i.e.  $I(\boldsymbol{\beta}) \simeq \delta(\boldsymbol{\beta})$ . The total magnification is then given by the magnification pattern  $\mu(\boldsymbol{\beta}) \simeq \mu_p(\boldsymbol{\beta})$  and is, again, independent of the source profile. Hence, chromatic effects in the total magnification of an extended source are only possible if the source size  $R_s$  is comparable to  $r_E$ .

From the definition of  $r_E$ , we see that if the considered lens is a star (or a compact object) with a mass  $M$  comparable to the mass of the Sun, then the Einstein radius  $r_E$  has about the same size as a quasar accretion disk, i.e. about  $10^{15}$  cm. Accretion disks of lensed quasars are thus excellent candidates for the observation of chromatic microlensing.

### The effective relative transverse velocity

Because of the relative motion between the source, the lens and the observer, the source moves relatively to the magnification pattern and, consequently, the micro-magnifications vary in time. The velocity  $\mathbf{V}$  of the source measured by the observer is called the effective relative velocity and is given by (Kayser et al., 1986)

$$\mathbf{V} = \frac{1}{1+z_s} \mathbf{v}_s - \frac{1}{1+z_l} \frac{D_s}{D_l} \mathbf{v}_l + \frac{1}{1+z_l} \frac{D_{ls}}{D_l} \mathbf{v}_{obs}$$

where  $\mathbf{v}_s$  is the velocity of the source measured in the source frame,  $\mathbf{v}_l$  is the velocity of the lens measured in the lens frame, and  $\mathbf{v}_{obs}$  is the velocity of the observer measured in the observer frame.

Besides these velocities, there is a further dynamical effect that we have to consider, namely the individual motions of the microlenses in the lensing galaxy. These motions imply that the magnification pattern is changing while the source crosses it. In practice, this effect is difficult to simulate, because it requires time-evolving magnification patterns, which demand important computational resources. Kundić & Wambsganss (1993) and Wambsganss & Kundić (1995) have studied such time-evolving patterns and show that, in a statistical sense, the overall effect can be approximated by an increase of the motion of the lensing galaxy. If the microlens has a one-dimensional velocity dispersion  $\sigma_v$  and, if the bulk velocity of the galaxy is  $v_{bulk}$ , then

$$v_l = \sqrt{v_{bulk}^2 + (a \sigma_v)^2}$$

where  $a \simeq 1.3$  represents the effectiveness of microlensing produced by the velocity dispersion versus the bulk motion.

The transverse component of  $\mathbf{V}$  is noted  $V_{\perp}$  and is called the effective relative transverse velocity. This velocity describes how fast the source is moving through the magnification pattern, and can be used to estimate the time scale of the microlensing-induced flux variations. This time scale is given by the time it takes the source to cross a caustic line. The reason is that the sharp caustic lines separate regions of low and high magnification. Hence, if a source crosses such a caustic line, we can observe a large change in magnification. The crossing time  $t_{cross}$  is the time it takes the source to cross its own diameter. In cosmological microlensing we have typically

$$t_{cross} = \frac{R_s}{V_{\perp}} \simeq 4 \left( \frac{R_s}{10^{15} \text{ cm}} \right) \left( \frac{V}{10^3 \text{ km/s}} \right)^{-1} \text{ months.}$$

This value shows that microlensing induced flux variations can only be observed if a given lensed quasar is monitored during several months or years.

### Microlensing techniques

The possibility for individual stars of a lensing galaxy to act as microlenses has been studied for the first time by Chang & Refsdal (1979). This study was limited to low optical depths, i.e. to cases where only one star strongly affects the properties of the macro-images, as this seemed to be the only case that could be treated analytically. However, in real cases, the optical depth at the image positions is of order unity, and numerous microlenses have to be considered simultaneously. The exact arrangement of these microlenses in a distant galaxy can not be determined. Thus, microlensing simulations have to deal with this problem in a statistical way. The microlenses are distributed randomly in the lens plane, according to a given surface mass density and shear, both being obtained from the macro-model of the lensed system.

Investigations of these situations necessarily require time consuming numerical simulations. Young (1981) was the first to study microlensing at large optical depth. He computed the shape of the image of an extended source viewed through the star field of a lensing galaxy. In a different approach, Paczyński (1986a) developed a method to numerically find all micro-images of a source lying behind a star field by solving the lens equation. Using this method, he derived the lightcurves of a point source that is moving relative to the microlenses. He showed that microlensing introduces considerable scatter in the intensity of the microlensed source, up to three magnitudes. One drawback of his method is that it only applies to point sources and that the computation must be done for every particular position of the source.

A significant improvement was achieved with the inverse ray-shooting method (Kayser et al., 1986; Schneider & Weiss, 1987), which has become, and still is, the workhorse for quasar microlensing studies. This method does not attempt to find the images of a point source, but instead shoots light-rays from the observer through the lens back to the source plane. The density of the collected rays at a certain position in the source plane is proportional to the magnification at this position. Hence, the method computes the total magnification for a whole range of source positions simultaneously (see, e.g., the magnification pattern illustrated in Fig. 7.1). One drawback of the ray-shooting technique is that no information about the positions of the micro-images is obtained, but this is not a major issue because micro-images are not resolved with current instruments. Wambsganss (1990) and Wambsganss et al. (1990a) further improved the inverse ray-shooting method by implementing a hierarchical tree code (Barnes & Hut, 1986), where stars are organized

into a nested hierarchy of cells, and weighted according to their distance to the ray. This greatly simplifies the calculations and improves the computing efficiency by a factor of one hundred.

An alternative and semi-analytical technique to simulate microlensing lightcurves, called the contouring method, was developed independently by Lewis et al. (1993) and Witt (1993). The basic idea of this method is that it is easier to find the images of a straight line than the images of a point. But in the case of extended sources, this technique rapidly becomes analytically intractable, and numerical approaches are required (Wyithe & Webster, 1999).

### Applications of quasar microlensing

Parallel to the growing complexity of microlensing techniques, the astrophysical applications of microlensing gained more and more interest. The amplitude, duration, and frequency of micro-magnifications depend on several parameters: the effective relative transverse velocity  $V_{\perp}$ , the surface density  $\kappa_{\star}$  of stars, the surface density  $\kappa_c$  of continuously distributed (dark) matter, the shear  $\gamma$ , and the relative sizes of the microlensing caustics with respect to the regions of the source affected by microlensing (e.g., Wambsganss et al., 1990b). We know that the typical size of the microlensing caustics is given by the Einstein radius  $r_E$ , which depends on the square root of the mass of the microlenses. The surface densities and the shear are usually determined from the macro-model and thus, there are essentially three unknown parameters for the microlensing simulations:

- the size  $R_s$  of the source,
- the effective relative transverse velocity  $V_{\perp}$ ,
- the masses  $M$  of the microlenses.

The aim of microlensing studies is to determine these three parameters through detailed investigations of the observed microlensing lightcurves. Roughly speaking, there are two different approaches to study microlensing lightcurves. One approach is to focus on one single high-magnification event, the other is statistical and based on the analysis of long-term monitoring data. The first approach consists in modeling the observed high-magnification event as a single caustic crossing (e.g., Wyithe et al., 2000b; Yonehara, 2001). It is assumed that only one single microlens plays a significant role in the high-magnification event and that contributions from other lens objects are negligible. This assumption is questionable as, even for relatively small values of the convergence and shear, the pattern of caustics is very complicated (e.g., Wambsganss et al., 1990b).

The second, statistical, approach is based on the study of the lightcurves of lensed quasar images spanning several years. There are different ways to interpret these lightcurves. It can be done by studying the structure or auto-correlation function (e.g., Seitz & Schneider, 1994; Lewis & Irwin, 1996), doing statistics of parameter variations over time intervals (e.g., Schmidt & Wambsganss, 1998; Wambsganss et al., 2000; Gil-Merino et al., 2005), or obtaining probability distributions with lightcurve derivatives (e.g., Wyithe et al., 1999). In general, the results of these methods are either probability distributions, or upper or lower limits for the source size, the effective transverse relative velocity, and the masses of the microlenses.

A third approach was developed by Kochanek (2004). He developed a general method for analyzing the lightcurves of microlensed quasars by fitting a large number of simulated lightcurves to the data, and by using Bayesian analysis to simultaneously infer the probability distributions for the effective transverse velocity, the average stellar mass, and the size of the quasar accretion disk. The advantage of his method is that it uses long lightcurves (spanning several observing seasons), rather than isolated high-magnification events. Furthermore, the entire lightcurves are used to infer the probability distribution of the parameters, instead of some of their statistical characteristics.

Besides the flux variations, microlensing can also induce chromatic effects in the images of a lensed quasar. As mentioned earlier, this is due to the variation of the spectrum of a quasar accretion disk from its center to its edge (Kayser et al., 1986). Photometric monitorings of lensed quasars in several bands or spectrophotometric monitorings can therefore yield constraints on the structure of quasar accretion disks (e.g., Agol & Krolik, 1999). This effect is also interesting when comparing the luminosity of the continuum with that in the emission lines. Since the continuum source is smaller than the emission line region, it should be affected differently by microlensing. Furthermore, if the emission line profile varies over the source (for instance due to rotation), the observed line profiles are also expected to vary in time (e.g., Agol & Krolik, 1999; Mineshige & Yonehara, 1999; Abajas et al., 2002).

## 7.1 The Einstein Cross QSO 2237+0305

The gravitational lens QSO 2237+0305, also known as the Einstein Cross or Huchra's lens, was discovered by Huchra et al. (1985) during the Center for Astrophysics redshift survey.

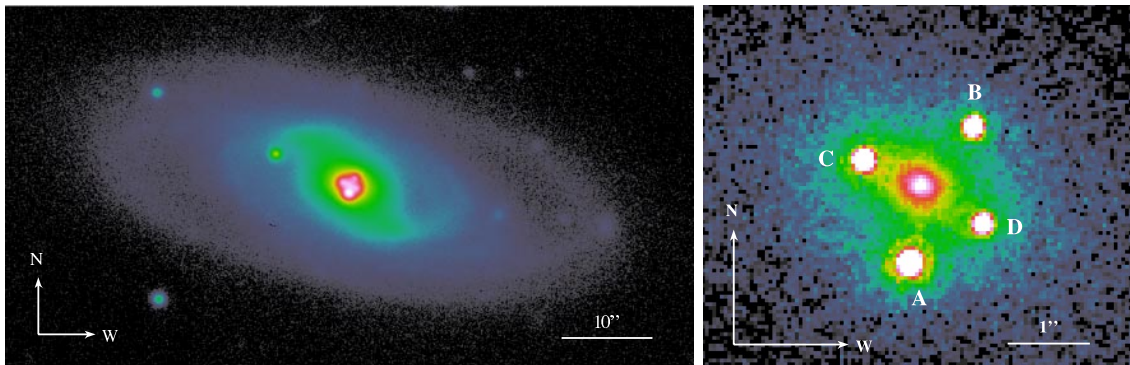


Figure 7.2: The Einstein Cross QSO 2237+0305 with the four lensed quasar images arranged in a cross-like pattern around the nucleus of the lensing galaxy. *Left*: an R-band image of the spiral lensing galaxy obtained with FORS1 of the ESO-VLT during the pre-imaging of our spectroscopic monitoring program. *Right*: an HST image of the center of the lensing galaxy obtained by Kochanek (2003a) in the V-band.

It consists of a  $z_s = 1.695$  quasar gravitationally lensed into four images arranged in a cross-like pattern around the nucleus of a  $z_l = 0.039$  barred Sab galaxy. The quasar images have a separation of about  $0.89''$  from the galaxy center. The corresponding Einstein



radius is

$$r_E = 5.77 \times 10^{16} \sqrt{\frac{M}{0.1 M_\odot}} \text{ cm}$$

for a concordance cosmology  $(\Omega_{m0}, \Omega_{\Lambda0}) = (0.3, 0.7)$  and  $H_0 = 70 \text{ km s}^{-1} \text{ Mpc}^{-1}$ . This is comparable to the typical size of quasar accretion disks and, therefore, makes microlensing in this object very likely.

Three years after its discovery, Schneider et al. (1988) and Kent & Falco (1988) computed first simple models of the system from which they drew several interesting conclusions. First, the time delays between the lensed images will be very difficult to measure because the delays are expected to be very short (only of the order of a day). This is an evident drawback if the goal is to measure  $H_0$  using the time-delay method, but it is a great advantage for microlensing studies. Indeed, the intrinsic variability of the quasar can be easily distinguished from the microlensing-induced variations as the former should appear almost at the same time in all four images, while microlensing does not. Second, the redshift of the lens being small, the quasar images are located very close to the center of the lensing galaxy. Lightrays from the background quasar pass through the bulge of the lens, where the density of stars is high, making microlensing very likely. The small lens redshift also leads to a large projected transverse velocity of the source relative to the magnification pattern resulting in a shorter timescale for microlensing. Given all these particularities, it is not surprising that an impressive number of observational and theoretical studies have been focused on this unique gravitational lens.

### The macro-model of the lensing galaxy

Many lens models have been proposed for the lensing galaxy in QSO 2237+0305 (see Table 2 in Wyithe et al., 2002, and references therein). Most of them are parametric models and are based on the galaxy and quasar image positions. Optical flux ratios cannot be used as model constraints because of microlensing and uncertain differential extinction. Measurements of the flux ratios in the radio or infrared should be more reliable because the more extended emission regions are less affected by microlensing, and because extinction is less important at these wavelengths. Unfortunately, the measured radio flux ratios (Falco et al., 1996) have large uncertainties and provide only weak constraints on the models. Infrared observations obtained by Agol et al. (2000, 2001) are compatible with the radio data and determine the flux ratios with an accuracy of about ten percent. These flux ratios provide three additional constraints, but there is still a large variety of lens models that describe the observables equally well.

On the one hand, these studies show that parametric lens models do not uniquely define the image magnifications, nor the total magnification. Indeed, different models predict total magnifications ranging from a few to a few hundred (e.g., Wambsganss & Paczyński, 1994; Witt et al., 1995; Chae et al., 1998). On the other hand, the total mass inside the Einstein ring is consistently measured at  $1.55 \times 10^{10} h_{70}^{-1} M_\odot$  with an accuracy of a few percent (e.g., Rix et al., 1992; Wambsganss & Paczyński, 1994; Chae et al., 1998).

In a more detailed analysis, Schmidt et al. (1998) used HST images to model the bulge and bar of the lensing galaxy. Their models assume a constant mass-to-light ratio, and the observed light distribution in the lensing galaxy is used to infer further constraints on the model. They derived a detailed model for the lens, and determined the values of the convergence  $\kappa$  and shear  $\gamma$  at the image positions. These values are comparable to several

other studies. We give some examples in Table 7.1.

Table 7.1: Macro-lensing parameters for the quasar images. Images C and D are saddle points, image A and B are minima (see also Fig. 4.4).

Image	$\kappa$	$\gamma$	$\mu$	Reference
A	0.36	0.44	4.63	Schneider et al. (1988)
B	0.45	0.28	4.46	
C	0.88	0.53	-3.75	
D	0.61	0.66	-3.53	
A	0.47	0.41	8.87	Wambsganss & Paczyński (1994)
B	0.46	0.40	7.60	
C	0.56	0.63	-4.92	
D	0.51	0.58	-10.38	
A	0.36	0.40	4.01	Schmidt et al. (1998)
B	0.36	0.42	4.01	
C	0.69	0.71	-2.45	
D	0.59	0.61	-4.90	
A	0.394	0.395	4.73	Kochanek (2004)
B	0.375	0.390	4.19	
C	0.743	0.733	-2.12	
D	0.635	0.623	-3.92	

### Photometric monitorings

Soon after the discovery of QSO 2237+0305, photometric monitoring of the individual quasar images revealed that they possessed uncorrelated variability. This was interpreted as an effect of gravitational microlensing and represents the first detection of microlensing in the lightcurves of a lensed quasar (Irwin et al., 1989). Despite broad interest in this object, the photometric data of QSO 2237+0305 remained sparse until the end of the 1990s. Typical lightcurves contained only a few epochs per season and covered at most five observing seasons (Corrigan et al., 1991; Ostensen et al., 1996). Reasons for that were the difficulties in measuring with reasonable accuracy the magnitudes of the lensed quasar images because of the proximity of the images, and because of significant blending due to the lensing galaxy.

At the end of the 1990s, several groups started to monitor QSO 2237+0305 more regularly. Data sets were obtained by Alcalde et al. (2002) on the Canary Islands for the Gravitational Lensing International Time Project (GLITP), by Vakulik et al. (1997) and Koptelova et al. (2005) at the Maidanak Observatory, and by Schmidt et al. (2002) at the Apache Point Observatory. The situation further improved in 1997, when the Optical Gravitational Lensing Experiment (OGLE) (Woźniak et al., 2000a,b; Udalski et al., 2006) started a very regular (i.e. every few nights) monitoring of the Einstein Cross. To date, the OGLE project provides the most homogeneous and extensive photometric coverage of the gravitational lens QSO 2237+0305, spanning more than ten years (see Fig. 7.3).

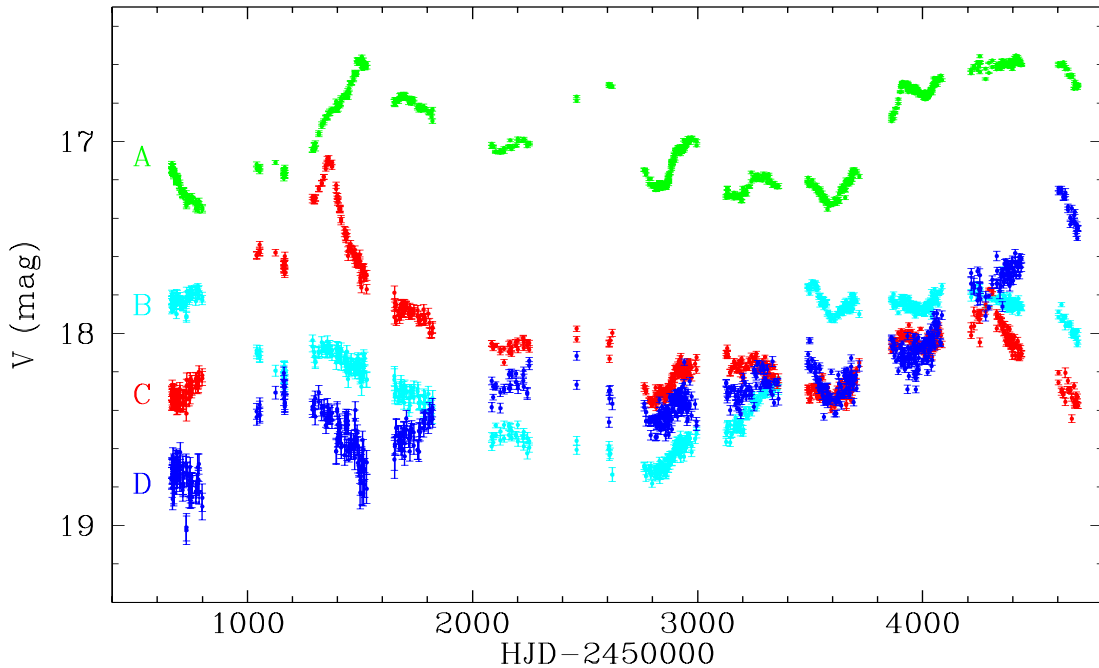


Figure 7.3: OGLE lightcurves in the V-band of the four images of QSO 2237+0305 spanning twelve observing seasons from 1997 to 2008 (Woźniak et al., 2000a,b; Udalski et al., 2006).

## 7.2 Spectrophotometric monitoring of QSO 2237+0305

Most of quasar microlensing studies are based exclusively on broad-band photometric monitorings (e.g., Woźniak et al., 2000a; Schechter et al., 2003; Colley et al., 2003). These data are usually obtained in one single broad photometric band. They can hence provide constraints on the source size, but not on its inner structure. In order to do so, monitoring in several bands or in spectroscopy are required. For this reason, we proposed to perform a spectrophotometric monitoring of the Einstein Cross at the Very Large Telescope (VLT). Our proposal was reviewed and accepted by the Observing Programs Committee (OPC) of the European Southern Observatory (ESO), which allocated us a total of 108 hours of observing time for four programs (073.B-0243, 074.B-0270, 075.B-0350, 076.B-0197) and one large program (177.B-0615) spanning 4 additional semesters.

Such a long-term monitoring program can only be conducted in service mode, which implies to spent some effort on communicating with the staff observing at the VLT in order to reach the necessary regularity of the observations, i.e. one observation every fifteen days. Regular observations are not trivial to obtain at highly demanded telescopes like the VLT, and require a detailed planning of the observations taking into account the position and phase of the moon, as well as the schedule of the service runs. This issue was problematic for the first observing semester, when our project was assigned a priority B, which led to only two observing epochs instead of the ten planned. The situation notably improved in the following semesters, when we were granted time in priority A, which helped getting data regularly.

A further difficulty rised in the beginning of the year 2007, when the CCD of FORS1

was replaced with a new one, which is more sensitive to the blue part of the optical spectrum. However, this change has only a limited influence on our data, since we perform a relative flux calibration between the observing epochs using foreground stars (see below) to minimize the effect of changing observational conditions.

At the end of our monitoring, we gathered a total of forty-three epochs, starting in October 2004 and ending in December 2007, with a mean sampling of one epoch every fifteen days.

### 7.2.1 Instrumental setup

The technical requirements for the spectrophotometric monitoring are very similar to those of our spectroscopic survey described in section 6.3, and demand both a good spatial sampling and relatively deep exposures. The chosen instrumental setup is essentially the same as the one used for the lens redshift measurements. One particular difficulty of the monitoring is to accurately deblend the quasar images from the light of the extended and bright lensing galaxy. This problem is the opposite of the one encountered with the lens redshift measurements, where the lenses were affected by the glare of the much brighter quasar images. The images of QSO 2237+0305 are separated by roughly one arcsecond, and we use the MCS deconvolution technique to both improve the spatial sampling and separate spatially the quasar images and the lensing galaxy.

Our observations are acquired with the FOcal Reducer and low dispersion Spectrograph (FORs1) in the Multi-Object Spectroscopy (MOS) mode using the high resolution collimator. Four slits are centered on foreground stars, and one is centered on the lensed system. Two masks are designed in order to observe the two pairs of quasar images. The stars observed in both masks are the same. The first mask is aligned on quasar images A and D, while the second is aligned on images B and C. The masks are rotated to position angles that avoid clipping of any quasar image, which is important for the spatial deconvolution of the spectra.

Our observing sequence consists of a short acquisition image, a “through-slit” image, followed by a consecutive deep spectroscopic exposure. All individual exposures are 1620 s long. We choose a slit width of  $0.7''$ , approximately matching the seeing (the mean seeing is  $0.8''$ ) and avoiding contamination of a quasar image by the others.

The G300V grism is used in combination with the GG375 order sorting filter. For our slit width, the spectral resolution is  $\Delta\lambda = 15 \text{ \AA}$ , as measured from the FWHM of night-sky emission lines, and the resolving power is  $R = \lambda/\Delta\lambda \simeq 400$  at the central wavelength  $\lambda = 5900 \text{ \AA}$ . The useful wavelength range is  $3900 < \lambda < 8200 \text{ \AA}$  with a scale of  $2.69 \text{ \AA}$  per pixel in the spectral direction. This configuration favors spectral coverage rather than spectral resolution, allowing to follow the continuum over a broad spectral range, starting with the very blue portion of the optical spectrum. In spite of  $R \simeq 400$ , a detailed profile of the BEL is still accessible. Finally, we observe spectrophotometric standard stars in order to remove the response of the telescope, CCD, and grism.

### 7.2.2 Data reduction

We use the same procedure as described in section 6.3. The spectra are bias subtracted and flat fielded. Wavelength calibration is obtained from the emission lines in the spectrum of helium-argon lamps. For the cosmic-ray rejection we use the L. A. Cosmic algorithm (van Dokkum, 2001). The cosmic-ray corrected images are inspected visually in order to

check that no data pixel is affected by the process, especially in the emission lines and in the data with the best seeing.

The sky background is removed in a different way in the spectra of the stars than in those of the lensed quasar. For the stars, which are small compared with the slit length ( $19''$ ), we proceed as described in section 6.3. We fit a polynomial in the spatial direction to the areas of the spectrum that are not illuminated by the object and subtract it from the data. As the lensing galaxy in QSO 2237+0305 is larger than the slit length, this procedure is not applicable. Instead, we use the slits positioned on empty sky regions located next to the quasar. The sky background is fitted to these slits and removed from the slit containing the images of QSO 2237+0305.

### 7.2.3 Flux calibration

We first apply a relative flux calibration to the spectra as described in section 6.3, using the four stars. This procedure corrects the effect of varying observational conditions (e.g., changes in airmass, seeing, or thin cirrus) that can induce color terms in the spectra. The high stability of the applied corrections across the field demonstrates that all residual chromatic slit losses due to the atmospheric refraction are fully corrected. The computation of the correction is eased by several facts. First, the position angle of the masks is the same for the quasar images and for the stars, i.e. the PSF clipping is the same for the target and the reference stars. Second, we avoid observations at large airmasses, i.e. never larger than 2.5. Finally, the atmospheric refraction corrector on FORS1 is very efficient (Avila et al., 1997). Again, the final absolute flux calibration is based on the spectra of spectrophotometric standard stars obtained with the same instrumental setup as QSO 2237+0305.

### 7.2.4 Spatial deconvolution of the spectra

The lensing galaxy in QSO 2237+0305 is extended and its nucleus has an apparent R-band magnitude of about 18 mag, which is comparable to the magnitudes of the quasar images. The quasar images are hence affected by significant contamination from the lensing galaxy. We use the spectral version of MCS deconvolution algorithm (Magain et al., 1998; Courbin et al., 2000) to efficiently remove the spectrum of the lensing galaxy from the spectra of the quasar images, as described in section 6.2.

### 7.2.5 Results

Our spectrophotometric monitoring started in October 2004 and lasted till December 2007. It has a mean sampling of about one epoch every fifteen days. We acquired the spectra of images A and D of QSO 2237+0305 on forty-two epochs, and the spectra of images B and C on forty epochs. The detailed journal of the observations is given in the two papers by Eigenbrod et al. (2008b,a), which are reproduced at the end of this chapter.

As a sanity check of our flux calibration, we compare our results with the OGLE-III photometry of QSO 2237+0305 (Udalski et al., 2006). We integrate our quasar spectra in the corresponding V-band to estimate, from the spectra, the photometric lightcurves as if they were obtained from imaging. The overall agreement is very good and verifies the quality of our flux calibration.

We know that spectral emission features coming from smaller regions in the source are more affected than features emitted in more extended regions. In order to study

the variation of each feature in our spectra independently, we decompose the spectra into their individual components following the multi-component decomposition (MCD) approach (Wills et al., 1985; Dietrich et al., 2003). This decomposes the spectra into a power-law continuum  $f_\nu \propto \nu^{\alpha_\nu}$ , a pseudo-continuum due to the merging of the Fe emission blends, and an emission spectrum due to the individual broad emission lines.

We find that all images of QSO 2237+0305 are affected by microlensing in both the continuum and the broad emission lines. On short timescales of a few months, images A and B are the most affected by microlensing during our monitoring campaign. Image C and especially D are more quiescent. Image A shows an important brightening episode in June 2006 (HJD  $\sim$  2453900 days), and image B in May 2005 (HJD  $\sim$  2453500 days). We show that the continuum of these two images becomes bluer as they get brighter, as expected from microlensing of an accretion disk.

We also report microlensing-induced variations of the broad emission lines, both in their integrated line intensities and in their profiles. Variations in the intensities are detected mainly in images A and B. Our measurements suggest that higher ionization lines like C IV and C III] are more magnified than lower ionization lines like Mg II. This is compatible with reverberation mapping studies and a stratified structure of the broad line region (e.g., Peterson, 1993; Kaspi et al., 2000). Variations in the line profiles are present but weak. In image A, we find that the profile of the C III] line is broadened during the brightening episode of June 2006. The C III] line profile in image C seems also to be broadened at several epochs. Broadening of the broad emission lines in image B is less obvious.

Finally, we estimate the differential extinction between pairs of quasar images due to dust in the lensing galaxy to be in the range 0.1 – 0.3 mag, with images C and D being the most reddened. This amount of differential extinction is too small to explain the large microlensing magnification ratios involving images A and C. Long-term microlensing, beyond the duration of our observations, is therefore present in these images.

The very different behaviors of the broad emission lines and the continuum, with respect to microlensing, offer considerable hope to infer quantitative information on the internal structure of the lensed quasar, and to probe the two types of regions independently (e.g., Kochanek, 2004). We show in the following sections how the observed variations in the continuum can be used to infer the spatial structure of the accretion disk in QSO 2237+0305.

### 7.3 Energy profile of the accretion disk

We already mentioned that microlensing depends on the surface densities of both stars  $\kappa_*$  and continuously distributed matter  $\kappa_c$ , on the shear  $\gamma$ , on the masses  $M$  of the microlenses, on the effective relative transverse velocity  $V_\perp$ , and on the source size  $R_s$ . We summarize in the following some important results concerning these quantities with a specific focus on the Einstein Cross. We then show how microlensing simulations fitting the data of our spectrophotometric monitoring can be used to infer the energy profile of the quasar accretion disk of QSO 2237+0305. The main difficulties reside in the degeneracies existing between  $M$ ,  $V_\perp$ , and  $R_s$ . Therefore, most studies use some priors limiting the values of at least one of these quantities, usually  $V_\perp$  based on what we know from general galaxy and cluster dynamics (e.g., Mould et al., 1993).

### 7.3.1 Previous studies

#### Smoothly distributed matter versus compact objects

The behavior of microlensing lightcurves depends on both the density  $\kappa_*$  of compact (stellar) objects and the density  $\kappa_c$  of the smoothly distributed (dark) matter (Paczynski, 1986a). Schechter & Wambsganss (2002) showed that, contrary to naive expectation, diluting the stellar component of a lensing galaxy with smoothly distributed matter increases rather than decreases the microlensing fluctuations caused by the remaining stars. They also demonstrated that for a bright pair of images straddling a critical curve, the negative parity image, i.e. the saddle point of the arrival time surface, is much more strongly affected by microlensing fluctuations than the associated minimum. This effect may explain the highly demagnified saddle points observed in some gravitational lenses (e.g., image D in SDSS J0924+0219). Congdon et al. (2007) extended these studies by considering various source sizes and a power-law mass function for the microlenses. They came to the conclusion that, for saddle points, diluting the stellar population with smoothly distributed matter increases the magnification dispersion for small sources and decreases it for large sources. This implies that the quasar continuum and broad-line regions may experience very different microlensing in negative-parity images.

The dependence of the image flux ratios on image parities suggest that in most lensed quasars, the stars must represent only a modest fraction of the total density (e.g., Schechter & Wambsganss, 2002; Kochanek & Dalal, 2004). Lewis & Gil-Merino (2006) found that depending on the size of the source, low-mass objects (with  $10^{-4} M_\odot$ ) can mimic the effect of a smooth component. However, in the case of the Einstein Cross the situation is different because the quasar images are located within the bulge of the lensing galaxy, where we do not expect a large contribution from smoothly distributed matter (Kochanek et al., 2007). The study of van de Ven et al. (2008) combines gravitational lensing with dynamics and shows that dark matter has only a small contribution to the central surface mass density. Thus, the density  $\kappa_c$  is small in QSO 2237+0305, and the convergence at the image positions is principally due to stars (i.e.  $\kappa = \kappa_*$ ).

#### The mass of the microlenses

Most investigations of microlensing at high optical depth that have explored the effect of multiple microlens mass components have led to the conclusion that the probability distribution of the micro-magnification is not very sensitive to the mass function of the microlenses (e.g., Wambsganss, 1992; Wyithe & Turner, 2001; Congdon et al., 2007). Lewis & Irwin (1995) found that the characteristic timescale for variability due to microlensing does also not depend on the detailed shape of the mass function. Thus, microlensing is relatively insensitive to the microlens mass spectrum, but it does depend on the mean microlens mass  $\langle M \rangle$ . The mean mass is a very important parameter because it sets the scale of the Einstein radius  $r_E \propto \langle M \rangle^{1/2}$  and hence, the characteristic size of the caustics. For example, a four times bigger  $\langle M \rangle$  yields a magnification pattern that is “zoomed in” by a factor two.

The determination of  $\langle M \rangle$  is not trivial because of the degeneracy existing between the effective transverse velocity and  $\langle M \rangle$ . Strong microlensing variability can be explained either by a large transverse velocity or a small  $\langle M \rangle$ . Wyithe et al. (2000a) studied the distribution of lightcurve derivatives and, by comparing the observed microlensing rate with their simulations, they determined lower limits for the average mass of the microlenses

in the bulge of QSO 2237+0305. Their study shows that a significant contribution of Jupiter-mass (i.e.  $10^{-4} M_{\odot}$ ) compact objects can unambiguously be ruled out with a lower mass limit of typically  $0.01 M_{\odot}$ . This result is confirmed by Lewis & Irwin (1996) and Wambsganss et al. (1990b) who found  $0.1 \leq (\langle M \rangle / M_{\odot}) (v_{l\perp} / 600 \text{ km/s})^2 \leq 1$ .

A comparable mass range is also obtained from studies of other lensed objects. Schmidt & Wambsganss (1998) investigated a lack of microlensing in the lightcurves of Q 0957+561 and ruled out microlenses having  $\langle M \rangle \ll 0.01 (v_{l\perp} / 600 \text{ km/s})^2 M_{\odot}$ . The MACHO collaboration (Alcock et al., 1997a,b) recorded microlensing events in the Milky Way. They derived  $0.1 \leq \langle M \rangle / M_{\odot} \leq 1.0$  towards the Galactic bulge and  $\langle M \rangle \geq 0.05 M_{\odot}$  in the halo. All these studies show that a likely value for  $\langle M \rangle$  is of the order  $0.1 M_{\odot}$ , which is well comparable with the mean mass of about  $0.3 M_{\odot}$  derived from the initial mass function of Kroupa (2002).

### The effective relative transverse velocity

We have already seen that the variability of microlensing is caused by relative motion between the observer, the lens and the source. For a concordance cosmology  $(\Omega_{m0}, \Omega_{\Lambda0}) = (0.3, 0.7)$  and  $H_0 = 70 \text{ km s}^{-1} \text{ Mpc}^{-1}$ , we get for QSO 2237+0305

$$\mathbf{V} = 0.37 \mathbf{v}_s - 10.3 \mathbf{v}_l + 9.9 \mathbf{v}_{obs} \quad (7.1)$$

Bennett et al. (2003) determined the Sun's motion relative to the cosmic microwave background and found that the Sun moves in a direction almost parallel to the direction to QSO 2237+0305, so that the last term on the right hand side of equation (7.1) can be neglected, because the transverse part is very small. Assuming that the peculiar velocities of the quasar and the lensing galaxy,  $v_s$  and  $v_l$ , are of the same order, the first term in equation (7.1) can be neglected as well, since its weight is only about 4% of the total. Hence, the effective relative transverse velocity is  $V_{\perp} \simeq 10.3v_{l\perp}$  and is expressed in distance per unit observed-frame time.

In number of microlensing studies, the lens velocity has been assumed to be  $v_{l\perp} \simeq 600 \text{ km/s}$  (e.g., Witt, 1993; Kundić & Wambsganss, 1993), a quantity obtained through probabilistic arguments based on general cluster dynamics (e.g., Mould et al., 1993). Wyithe et al. (1999) presented the first determination of an upper limit for the effective transverse velocity in QSO 2237+0305. They used photometric data with a monitoring spanning almost ten years, but with a poor sampling rate (61 points in total). They found  $v_{l\perp} < 500 \text{ km/s}$  based on considerations of the distribution of lightcurve derivatives. Later, Kochanek (2004) determined a higher upper limit of  $1800 \text{ km/s}$ , but the significant variability of the quasar images during the considered OGLE monitoring period may be the cause of the relatively high velocities found in his work. Gil-Merino et al. (2005) examined the distribution of quiescent periods in the lightcurves and found an upper limit of  $625 \langle M / 0.1 M_{\odot} \rangle^{1/2} \text{ km/s}$  (90 percent confidence) for  $v_{l\perp}$ .

Witt & Mao (1994) described a theoretical height-duration correlation during high magnification events. Considering observed high magnification events, they determined an upper limit of  $600 \text{ km/s}$ , but the correlation and hence the derived limit are dependent on the source size assumed. Indeed, a degeneracy exists between the source size and the velocity (Kochanek, 2004). When the source is large, the magnification pattern is heavily smoothed and a high velocity is required because the smoothing also increases the scale length of the variations in the magnification pattern. For smaller source sizes the scale length of the variations are shorter and the velocities correspondingly smaller.



Except for a few studies (e.g., Paczyński, 1986b; Kundić & Wambsganss, 1993; Schramm et al., 1993; Wambsganss & Kundić, 1995) the random star field is generally considered to be static, i.e. it is assumed that the proper motions of the stars is much smaller than the effective transverse velocity, which appears to be a good approximation in the case of QSO 2237+0305. As already mentioned, Kundić & Wambsganss (1993) and Wambsganss & Kundić (1995) show that the velocity dispersion of the stars can statistically be interpreted as a bulk velocity artificially increased by an efficiency factor  $a \simeq 1.3$ .

### The size and energy profile of the source

An important application of quasar microlensing is to infer the size of the emission region in the lensed quasar (e.g., Nemiroff, 1988; Grieger, 1990), as well as its spatial structure from color variations observed in the quasar images (e.g., Wambsganss et al., 1990b; Wambsganss & Paczyński, 1991). First analyses focused on isolated high magnification events. High magnification events occur when a compact source crosses a critical curve. The smaller the source, the higher the peak luminosity and the smaller the timescale for the sudden rise to (or fall from) maximum luminosity. Therefore one can determine the relative size of the source at different wavelengths by observing throughout the peak at the corresponding wavelengths. Furthermore, if the transverse velocity  $V_{\perp}$  is known, one can also estimate the “absolute” source size.

Following this method, several studies estimated the size of the optical continuum source in QSO 2237+0305 based on one poorly sampled high magnification event that was observed in image A during late 1988 (e.g., Wambsganss et al., 1990b; Rauch & Blandford, 1991; Wyithe et al., 2000b). The result of these studies is an upper limit for the source size of about  $2 \times 10^{15}$  cm assuming a transverse velocity of  $v_{l\perp} = 600$  km/s. Shalyapin et al. (2002) analyzed another high magnification event observed in late 1999 in image A of QSO 2237+0305 by the GLITP collaboration. They obtained a larger source size of  $3.7 \times 10^{16}$  cm. A further event in image C, this time, was observed in 1999 by the OGLE team, and Yonehara (2001) derived a conservative upper limit for the source size of  $5.7 \times 10^{16}$  cm assuming a mean microlens mass of  $0.1 M_{\odot}$ .

However, the mode of analysis of single high-magnification events is only valid in the case of a source that is much smaller than the typical caustic spacing, which is questionable in the case of QSO 2237+0305. With a much larger data set and a more sophisticated analysis of the microlensing lightcurves of QSO 2237+0305, Kochanek (2004) showed that thermal emission from an accretion disk is consistent with the size  $1.4 \times 10^{15} h^{-1}$  cm  $< R_s < 4.5 \times 10^{15} h^{-1}$  cm inferred from microlensing. Nevertheless, microlensing in a sample of gravitationally lensed quasars has led to a different conclusion: the size of the optical and ultraviolet emission region inferred from microlensing is too large compared to the predictions of accretion disk models based on the quasar luminosity (Pooley et al., 2007; Kochanek et al., 2007). This contradictory results indicate that additional observations and a more careful comparison to theory is required. In particular, the determination of the size as a function of wavelength will prove most useful.

Multi-wavelength or spectroscopic monitorings of lensed quasars used to be rare, but have recently begun to become more common. Wyithe et al. (2002) compared optical and mid-infrared data of QSO 2237+0305 and found that the mid-infrared emission region is mostly unaffected by microlensing, leading to the conclusion that the corresponding emission region must have a size  $\gtrsim 1 r_E$ , which demonstrated that the infrared emission in radio-quiet quasars is due to thermal emission by dust rather than to synchrotron emission.

More recently, Anguita et al. (2008) analyzed R and G-band lightcurves of the 1999 high-magnification event of image C of QSO 2237+0305 following the method of Kochanek (2004). They derived a relative size between the R and G-band emission regions of  $1.45^{+0.90}_{-0.25}$  based on the velocity prior determined by Gil-Merino et al. (2005). This value is in good agreement with the standard thin accretion disk model of Shakura & Sunyaev (1973). From photometric observations of HE 1104–1805 in 11 bands, Poindexter et al. (2008) derived the spatial structure (or energy profile) of the quasar accretion disk with  $\beta = 0.61^{+0.21}_{-0.17}$ , where  $\beta$  is the logarithmic slope of the temperature profile  $T \propto R^{-\beta}$ . Their result is consistent with the standard value  $\beta = 3/4$  (Shakura & Sunyaev, 1973), but is limited by the poor sampling and large uncertainties of the analyzed data.

Several other studies compared microlensing in the X-ray and optical domain, and further demonstrated the efficiency of microlensing in probing the inner emission region of lensed quasars. For instance, Morgan et al. (2008) analyzed the lightcurves of the lensed quasar PG 1115+080 and concluded that the effective radius of the X-ray emission is  $1.3^{+1.1}_{-0.5}$  dex smaller than that of the optical emission. They found that the X-ray emission is generated near the inner edge of the accretion disk, while the optical emission comes from scales slightly larger than those expected for a standard thin disk. Another example is given by Chartas et al. (2008), who combined X-ray and optical data of HE 1104–1805 and revealed that the X-ray emitting region is compact with a half-light radius smaller than  $2 \times 10^{15}$  cm.

Eventually, we should mention one important property concerning the source surface brightness profile. Several studies (e.g., Mortonson et al., 2005; Congdon et al., 2007) have shown that the microlensing-induced flux variations are relatively insensitive to the exact form of the source profile, and that they principally depend on its characteristic size. The size of the source controls the smoothing of the magnification pattern. For example, very large source sizes ( $> 5 r_E$ ) produce magnification patterns that are so strongly smoothed that they are unable to account for the amplitude ( $> 1$  mag) of the flux variations observed in QSO 2237+0305 (Refsdal & Stabell, 1993). On the contrary, very small source sizes ( $< 0.01 r_E$ ) give very moderately smoothed magnification patterns, which lead to sharp magnification events that are not observed in the lightcurves. The lower bound found in that way is  $0.01 r_E$  (e.g., Kochanek, 2004; Anguita et al., 2008).

To summarize the results of the numerous studies cited, we expect the optical/UV emission region of QSO 2237+0305 to have a size between  $10^{15}$  and  $10^{16}$  cm, and an energy profile that should resemble the profile predicted by the standard thin accretion disk model.

### About degeneracies

As mentioned earlier, the scales of the magnification patterns are defined in terms of the Einstein radius  $r_E$ , which depends on the square root of the mean mass of the microlenses. Thus, the computational variables for the source size and velocity are in fact the scaled source size  $\hat{R}_s = R_s / \langle M / M_\odot \rangle^{1/2}$  and the scaled transverse velocity  $\hat{V}_\perp = V_\perp / \langle M / M_\odot \rangle^{1/2}$ . Following these definitions,  $\hat{R}_s$  is the relative size of the source with respect to the Einstein radius, and  $\hat{V}_\perp$  is the velocity with which the source is moving across the magnification pattern.

The determination of the three parameters  $R_s$ ,  $V_\perp$  and  $\langle M \rangle$  is not easy because of the degeneracies existing between them. As reported by Kochanek (2004), there is a strong, essentially linear, correlation between  $\hat{R}_s$  and  $\hat{V}_\perp$ , i.e.  $\hat{R}_s \propto \hat{V}_\perp^x$  where  $x \simeq 1$ . Furthermore,

$\hat{R}_s$  and  $\hat{V}_\perp$  are both defined as functions of  $\langle M \rangle$ , which imply degeneracies between  $\langle M \rangle$ ,  $\hat{V}_\perp$ , and  $\hat{R}_s$ . However, since  $R_s = \hat{R}_s \langle M/M_\odot \rangle^{1/2}$  and  $\langle M \rangle \propto (V_\perp/\hat{V}_\perp)^2$ , the physical size of the source  $R_s \propto V_\perp \hat{V}_\perp^{-1} \simeq V_\perp$  depends essentially on our estimate of the physical velocity  $V_\perp$  and avoids the degeneracies between  $\langle M \rangle$ ,  $\hat{V}_\perp$ , and  $\hat{R}_s$ .

### 7.3.2 Inverse ray-shooting

The inverse ray-shooting method was first developed by Kayser et al. (1986) and Schneider & Weiss (1987) and has become very popular in microlensing studies. Wambsganss (1990) and Wambsganss et al. (1990a) further improved this method by implementing a hierarchical tree code (Barnes & Hut, 1986), which greatly improves the computing efficiency. The basic idea of the method is to shoot lighttrays from the observer through the star field of the lensing galaxy and back to the source plane.

The microlenses are distributed randomly according to the stellar density  $\Sigma_{\text{crit}} \kappa_\star$ . The deflection angle for a given lightray is computed from the sum of the deflection angles of  $N_\star$  individual stars acting like microlenses, plus the perturbing effect of the lensing galaxy. The gravitational field of the galaxy changes very little over the distance scale of the microlens distribution. It is thus natural to Taylor expand the field of the galaxy. Note that this perturbation is not assumed to be small. The lowest-order, non-trivial term in the expansion is the quadratic term (tidal field). The deflection angle for a given lightray at position  $\boldsymbol{\xi}$  is hence given by

$$\hat{\boldsymbol{\alpha}}(\boldsymbol{\xi}) = \frac{4G}{c^2} \sum_{i=1}^{N_\star} M_i \frac{\boldsymbol{\xi} - \boldsymbol{\xi}_i}{(\boldsymbol{\xi} - \boldsymbol{\xi}_i)^2} + \hat{\boldsymbol{\alpha}}_g + \frac{4\pi G}{c^2} \Sigma_{\text{crit}} \begin{pmatrix} \kappa_c + \gamma & 0 \\ 0 & \kappa_c - \gamma \end{pmatrix} \boldsymbol{\xi}$$

where the origin of the coordinate frame is chosen so that it coincides with the center of the microlens distribution. The orientation of the coordinate frame is chosen such that the shear  $\gamma$  acts along one of the coordinate axes. The first term on the right-hand side describes the deflection due to the  $N_\star$  microlenses. The second term is the deflection angle at the position of the macro-image due to the lensing galaxy, and the third term is the quadrupole contribution of the galaxy. We remind that  $\gamma$  is the shear and that  $\Sigma_{\text{crit}} \kappa_c$  is the smoothed or continuously distributed surface density, which contributes to the total deflection as an additional constant deflection. The parameters  $\kappa_\star$ ,  $\kappa_c$ , and  $\gamma$  are determined from the macro-model of the lensing galaxy. In the case of the Einstein Cross, we have  $\kappa_c \simeq 0$  and  $\kappa \simeq \kappa_\star$ . Some values of  $\kappa$  and  $\gamma$  for QSO 2237+0305 are given in Table 7.1. In the present study, we use the recent values given by Kochanek (2004).

The inverse ray-shooting method does have some drawbacks. The practical limitations inherent to the method are finite resolution and the problem of fair sampling of the source plane. Ideally, one would like to have a very large magnification pattern with side length of about 1000  $r_E$ , covered by many pixels (at least 100 pixels per Einstein radius  $r_E$ ) so that small sources, compared to the Einstein radius, can be considered. In order to be able to detect small fluctuations, these pixels should contain many lighttrays ( $> 1000$ ). It is of course not possible to meet all these requirements with current computing facilities, and one has to find an intermediate solution. We adopt a side length of  $10^4$  pixels that corresponds to  $10 r_E$ . The smallest possible source size,  $0.001 r_E$ , is determined from the pixel size. For magnification patterns with small side length, the mean magnification  $\langle \mu \rangle$  may not be exactly representative for the parameter set. Its value may differ a little from

the real one due to statistical fluctuations. In practice, these deviations are small (less than one percent), and are thus negligible for our analysis.

Once all these parameters are defined, we compute the deflection angle of the lightrays passing through the random star field using the numerical code of Wambsganss (1999). We have already seen that microlensing is relatively insensitive to the microlens mass spectrum and that it mainly depends on the mean microlens mass  $\langle M \rangle$ . We can hence consider the same mass  $\langle M \rangle$  for all microlenses in the field. A likely value for this mass is  $0.1 M_\odot$ . We will consider this value from now on. We shoot approximately  $10^{11}$  lightrays through the field of microlenses and collect the deflected rays in the  $10^4 \times 10^4$  pixel grid located in the source plane. The density of the collected rays is proportional to the magnification and thus, defines the magnification pattern  $\mu_p(\beta)$  (see Fig. 7.1 for a small cutout of the pattern). We compute the magnification patterns of all four images of QSO 2237+0305 based on the macro-model of Kochanek (2004), assuming  $\langle M \rangle = 0.1 M_\odot$ .

### 7.3.3 Observed microlensing lightcurves

Observations of microlensing-induced flux variations are usually obtained from long-term photometric monitorings like the OGLE experiment (Woźniak et al., 2000a,b; Udalski et al., 2006). The observed flux variations in the quasar images are due to both microlensing and intrinsic variations of the quasar. In order to extract the microlensing signal, we need to remove the intrinsic quasar fluctuations from the lightcurves. In practice, we do this by considering the difference between the lightcurves of two images as described below.

In the following, we focus exclusively on the lightcurves of image A and B of the Einstein Cross, because they are the two images undergoing the strongest flux variations within the time span of our spectrophotometric monitoring. We know that the observed flux  $F_i$  of a lensed quasar image  $i$  is the product of the unlensed flux  $F_0$  of the source, the extinction  $e^{-\tau_i}$ , and the macro and micro-magnification  $\mu_{macro,i}$  and  $\mu_{micro,i}$

$$F_i = \mu_{micro,i} \mu_{macro,i} e^{-\tau_i} F_0 .$$

In the case of QSO 2237+0305, we can neglect the time delays between the images, because they are expected to be of the order of one day or less (see Section 7.1). The difference in magnitude  $\Delta m$  between image A and B is hence simply given by  $\Delta m = -2.5 \log(F_A/F_B)$ . The extinction and macro-magnifications remain constant in time. As a consequence, the time variability that is observed in  $\Delta m$  is only due to microlensing

$$\Delta m = -2.5 \log \left( \frac{\mu_{micro,A}}{\mu_{micro,B}} \right) + m_0$$

where  $m_0$  is a constant due to the combined effect of the macro-magnifications and differential extinction between the quasar images.

We use two different data sets for the present study. The first one is the well sampled V-band lightcurves of the OGLE experiment (Udalski et al., 2006) and the second one is our deep spectrophotometric monitoring. In order to study in more detail the chromatic fluctuations in the continuum of the spectra of images A and B, we define six wavelength ranges that we will use as photometric bands. For each of these bands, we compute the observed lightcurve by integrating the continuum in the corresponding wavelength range. By subtracting the magnitude of image B from that of image A, we obtain six 39-epoch difference lightcurves  $\Delta m$ . More details can be found in the paper reproduced at the end of this chapter (Eigenbrod et al., 2008a).

### 7.3.4 Simulated microlensing lightcurves

We have already seen that in the case of an extended source, the magnification  $\mu(\beta)$  at the source position  $\beta$  is given by the convolution of the source surface brightness profile  $I(\beta)$  and the magnification pattern  $\mu_p(\beta)$ . As mentioned earlier, microlensing is relatively insensitive to the exact source profile. For simplicity, we choose a Gaussian surface brightness profile with a scaled source size  $\hat{R}_s$  specified by the Gaussian width  $\sigma$  or equivalently by the Full Width at Half Maximum ( $\text{FWHM} = 2.35\sigma$ ). Simulated microlensing lightcurves are then obtained from source trajectories (i.e. one-dimensional cuts) through the convolved magnification pattern.

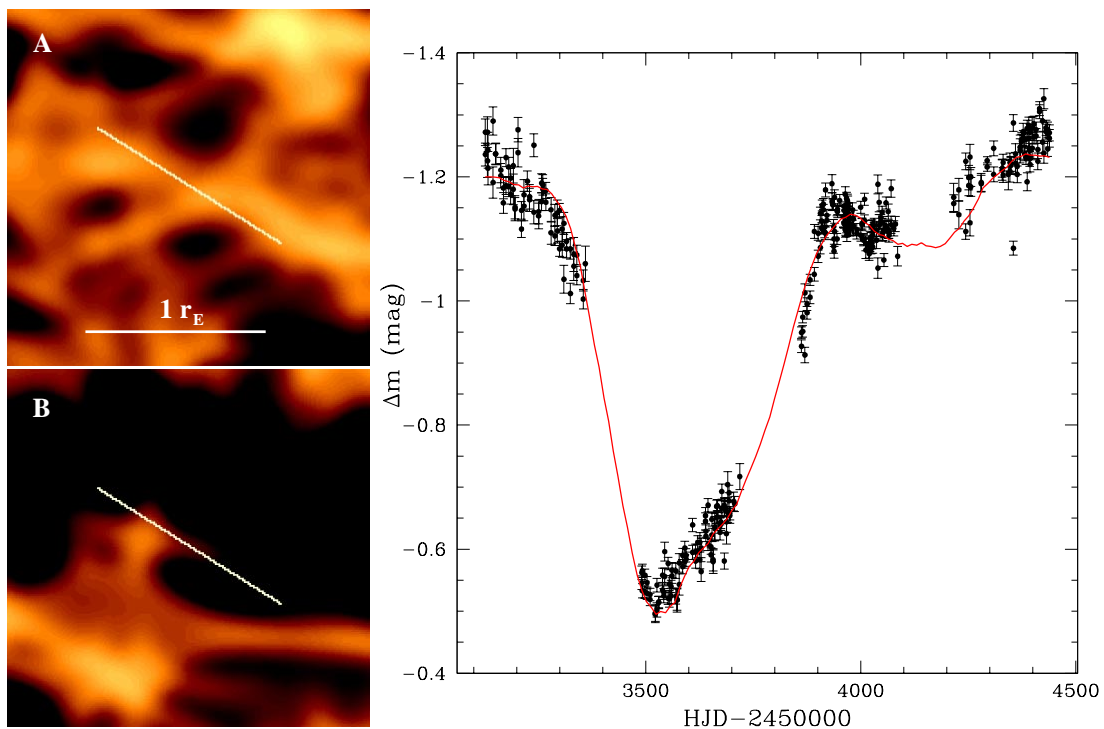


Figure 7.4: Example of a simulated microlensing difference lightcurve. *Left*: Source trajectory through the convolved magnification patterns of image A and B. The considered source has a Gaussian surface brightness profile with a FWHM of  $\hat{R}_s = 0.16 r_E$ . The masses of the microlenses are  $0.1 M_\odot$ . *Right*: The observed OGLE difference lightcurve  $\Delta m$  between image A and B of QSO 2237+0305 (black dots) and the simulated difference lightcurve  $\Delta m'$  (red curve).

Each of these simulated lightcurves is characterized by two kinds of parameters: physical and trajectory parameters. The physical parameters are the local magnification tensor  $\kappa$  and  $\gamma$ , the mass  $\langle M \rangle$ , the scaled source size  $\hat{R}_s$ , and the scaled effective transverse velocity  $\hat{V}_\perp$  of the source. The trajectory parameters are  $\theta$  and  $\beta_0$ , where  $\theta$  is the direction angle and  $\beta_0$  the coordinates of the starting point of the source trajectory.

In order to compare our microlensing simulations with the observed difference lightcurve  $\Delta m$  between image A and B of QSO 2237+0305, we first have to compute a simulated difference lightcurve. We do this by tracing the source trajectory through the convolved magnification patterns of both images, and by extracting the corresponding simulated mi-

cro-lensing lightcurves for A and B. We subtract the lightcurve of image B from that of image A and obtain a simulated difference lightcurve  $\Delta m'(p)$ , see Fig. 7.4.

The simulated difference lightcurve  $\Delta m'(p)$  is characterized by the chosen parameter set  $p = (\kappa, \gamma, \langle M \rangle, \hat{R}_s, \hat{V}_\perp, m_0, \theta, \beta_{0,A}, \beta_{0,B})$ , where  $\beta_{0,A}$  and  $\beta_{0,B}$  are the coordinates of the starting point in the convolved magnification pattern of image A and B, respectively. The trajectory is constrained to have identical directions  $\theta$  and velocities  $\hat{V}_\perp$  across the patterns of images A and B. The direction is set to be the same in both patterns since the shear direction between images A and B is approximately the same (Witt & Mao, 1994), and because we assume the motion of the source to be primarily due to the bulk motion of the lensing galaxy rather than to the individual motions of the stars.

### 7.3.5 Bayesian analysis

We have just seen how to generate a simulated difference lightcurves  $\Delta m'(p)$  from a particular choice of the parameters  $p$ . We now want to compare these simulations with the observations in order to estimate the source size and spatial structure of the quasar accretion disk. To do so, we follow the method developed by Kochanek (2004). His method, based on Bayesian analysis, compares large numbers of trial lightcurves with an observed data set to simultaneously estimate  $R_s$ ,  $V_\perp$ , and  $\langle M \rangle$ . The main idea of the method is to construct an ensemble of model (i.e. of simulated  $\Delta m'(p)$ ), which, given the data  $D = \Delta m$ , can then be used to infer the probability distributions of  $R_s$ ,  $V_\perp$ , and  $\langle M \rangle$ .

From Bayes' theorem, we know that the probability of the parameter set  $p$ , given the data  $D$ , is

$$P(p|D) = \frac{P(D|p) P(p)}{P(D)} = \frac{L(D|p)}{N} P(p)$$

where  $P(p)$  is the prior,  $L(D|p)$  is the likelihood and  $N$  is a normalization constant. We define each of these in more detail in the following. The prior probability  $P(p)$  refers to any information we have on the parameters  $p$  prior to our study. We define the relative likelihoods  $L(D|p)$  of the parameters  $p$  based on the  $\chi^2$  statistics. Usually, this is done following the standard approach for ensemble analysis (e.g., Sambridge, 1999), which uses the maximum likelihood estimator

$$L(D|p) = \exp\left(-\frac{\chi^2(p)}{2}\right)$$

where  $\chi^2(p)$  is determined by computing the  $\chi^2$  between the data  $D = \Delta m$  and the simulated lightcurve  $\Delta m'(p)$

$$\chi^2(p) = \sum_{k=1}^{n_{obs}} \left( \frac{\Delta m_k - \Delta m'_k(p)}{\sigma_k} \right)^2$$

where  $\sigma_k$  are the uncertainties of the OGLE data, and  $n_{obs}$  is the number of observations. Finally, all Bayesian parameter estimates have to be normalized by the requirement that the total probability is unity, i.e.  $\int P(p|D) dp = 1$  and hence

$$N = \int L(D|p) P(p) dp .$$

In practice, the integral is computed by summing the probabilities for our sampling of trajectories, which is equivalent to using Monte Carlo integration methods to compute

the integral over the ensemble of all possible trajectories. The sum over the random trajectories will converge to the true integral, provided we consider a sufficiently large number of trajectories. For instance, the probability of a particular trajectory  $j$  (defined by the set of parameters  $p_j$ ) given the data  $D$  is

$$P(p_j|D) = \frac{L(D|p_j) P(p_j)}{N} = \frac{L(D|p_j) P(p_j)}{\sum_{j=1}^n L(D|p_j) P(p_j)}$$

where  $n$  is the total number of simulated lightcurves.

We compute the probability distributions for the physical parameters of interest by marginalizing over the other parameters. For instance, the probability distribution of the scaled source size  $\hat{R}_s$  is obtained by integrating over all other parameters, that we write  $p'$ , hence,  $p = (\hat{R}_s, p')$  and

$$P(\hat{R}_s|D) \propto \int P(\hat{R}_s, p'|D) dp' = \sum_{j=1}^n P(\hat{R}_s, p'_j|D).$$

As already mentioned in Subsection 7.3.1, the physical size of the source  $R_s$  depends essentially on our estimate of the physical velocity  $V_\perp$ , and avoids the degeneracies between  $\langle M \rangle$ ,  $\hat{V}_\perp$ , and  $\hat{R}_s$ . Estimates of  $V_\perp$ , i.e. the prior  $P(V_\perp)$ , can be obtained from the observations of the motion of other galaxies or galaxy clusters (e.g., Benson et al., 2003). More details can be found in the paper at the end of this chapter (Eigenbrod et al., 2008a).

### 7.3.6 Results

We apply the Bayesian analysis to the OGLE difference lightcurve between image A and B, and compute the probability distributions of  $\hat{R}_s$  and  $\hat{V}_\perp$ . We derive a scaled source FWHM of  $\hat{R}_s = (0.16_{-0.10}^{+0.12}) r_E$ , and a scaled velocity of  $\hat{V}_\perp = (3.9_{-1.8}^{+3.0}) \times 10^3 \langle M/0.1M_\odot \rangle^{1/2}$  km/s.

We find a linear correlation  $\hat{R}_s \propto \hat{V}_\perp$ . This correlation determines the time scale of the observed microlensing-induced fluctuations, which is given by the half-light radius divide by the effective transverse velocity, i.e.  $0.5 \hat{R}_s / \hat{V}_\perp = 4.0 \pm 1.0$  months, and which is independent of  $\langle M \rangle$  and of the velocity prior  $P(V_\perp)$ .

Based on the six lightcurves computed from our spectroscopic data in six photometric bands, we infer the probability distribution of the source-size ratio  $\hat{R}_i / \hat{R}_{ref}$ , where  $R_i$  is the size of the source emitting at the mean wavelength  $\lambda_i$  of band  $i = 1, 2, \dots, 6$ . The reference radius  $\hat{R}_{ref}$  at the reference wavelength  $\lambda_{ref}$  can be chosen arbitrarily. We simply define the middle band #3 as our reference. We plot the ratio  $R_i / R_{ref}$  against the corresponding wavelength ratio  $\lambda_i / \lambda_{ref}$  in Fig 7.5, and determine the slope of the energy profile by fitting a power law  $R \propto \lambda^\zeta$ . The final energy profile obtained from the whole sample of source trajectories is shown in Fig. 7.5 and yields  $\zeta = 1.2 \pm 0.3$ .

## 7.4 Discussion

Our result for the source FWHM  $\hat{R}_s = (0.16_{-0.10}^{+0.12}) r_E$  is well compatible with the upper limit of  $0.98 r_E$  given by Yonehara (2001). It is also in good agreement with the FWHM derived by Anguita et al. (2008),  $\hat{R}_s = (0.06 \pm 0.01) r_E$  and by Kochanek (2004),  $\hat{R}_s = (0.20_{-0.12}^{+0.19}) r_E$ .

We confirm the linear correlation  $\hat{R}_s \propto \hat{V}_\perp$  found by Kochanek (2004) and determine the time scale of the observed microlensing-induced fluctuations to be  $4.0 \pm 1.0$  months. The

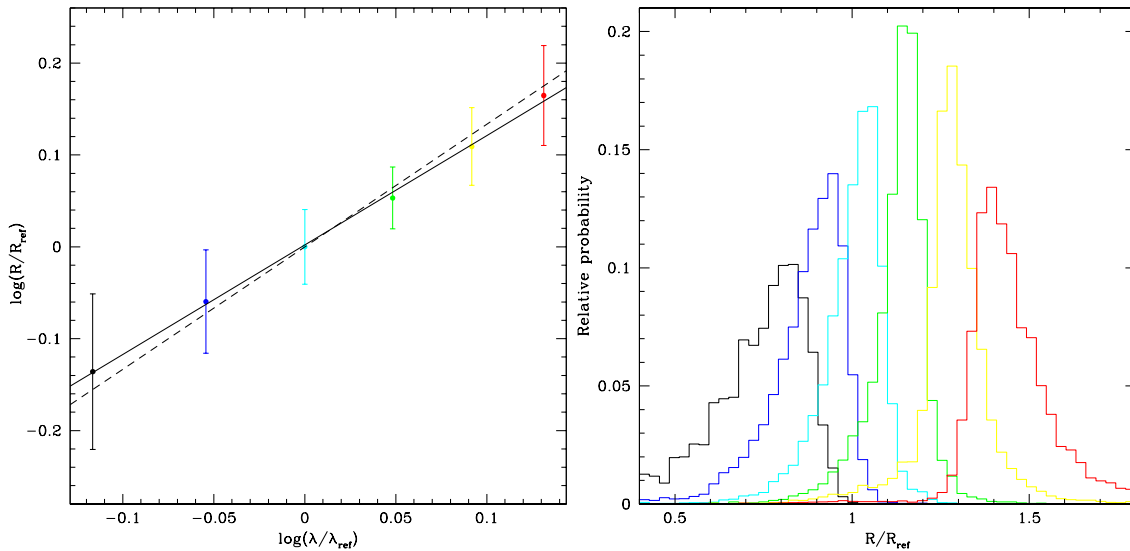


Figure 7.5: *Left* : The final energy profile obtained from the whole ensemble of source trajectories. The reference wavelength is  $\lambda_{ref} = 2125 \text{ \AA}$  measured in the source frame. The error bars give the  $1\sigma$  uncertainties. The solid line indicates the linear regression across the points. The dashed line shows the relation  $R \propto \lambda^{4/3}$  expected for the standard thin accretion disk of Shakura & Sunyaev (1973). *Right* : The corresponding probability distributions of the  $R_i$  values obtained in the six bands  $i = 1, 2, \dots, 6$ .

strong correlation between  $\hat{R}_s$  and  $\hat{V}_\perp$  implies that the choice of the velocity prior can bias our estimate of the source size because  $R_s \propto V_\perp$ . The selection of the observation period can also bias the derived source size. As reported by Kochanek (2004), if the considered period is very active in terms of microlensing, the simulations will favor high transverse velocities and/or small source sizes. One possible solution to minimize the bias induced by the selection of the observation period is to consider the longest possible lightcurves. This has the evident drawback of dramatically increasing the computing effort, making the problem rapidly intractable. However, as discussed in the following, the estimate of the physical source size  $R_s$  has only a limited effect on the determination of the index  $\zeta$ .

From the analysis of our spectroscopic data, we determine the energy profile  $R \propto \lambda^\zeta$  of the quasar accretion disk with  $\zeta = 1.2 \pm 0.3$ , which is in good agreement with the value of  $\zeta = 4/3$  expected from the standard thin accretion disk model (Shakura & Sunyaev, 1973). Our findings are also in good agreement with Anguita et al. (2008), who obtained  $\zeta = 1.2_{-0.6}^{+2.0}$  for QSO 2237+0305, and with  $\zeta = 1.64_{-0.46}^{+0.56}$  obtained by Poindexter et al. (2008) from multi-band photometry of the lensed quasar HE 1104–1805.

We observe that the determination of the power-law index  $\zeta$  is almost independent on the velocity prior used. This is easily explained by the fact that the scaling between  $R_s$  and  $\hat{R}_s$  is independent of the considered wavelength and hence,  $R_i/R_{ref} = \hat{R}_i/\hat{R}_{ref}$ . As a consequence, the determination of relative source sizes, and thus the energy profile, is not expected to depend on the assumed microlens mass  $\langle M \rangle$ . This is further confirmed by the fact that Anguita et al. (2008) obtain a value for  $\zeta$  which is in good agreement with ours, even though they consider a more restrictive velocity prior and derive a slightly smaller source size.



**7.5 Paper presenting the spectrophotometric monitoring of QSO 2237+0305 with the Very Large Telescope**

*Microlensing variability in the gravitationally lensed quasar QSO 2237+0305  $\equiv$  the Einstein Cross*

*I. Spectrophotometric monitoring with the VLT*

A. Eigenbrod, F. Courbin, D. Sluse, G. Meylan, & E. Agol

*Astronomy & Astrophysics, 2008, 480, 647*



## Microlensing variability in the gravitationally lensed quasar QSO 2237+0305 $\equiv$ the Einstein Cross<sup>★</sup>

### I. Spectrophotometric monitoring with the VLT

A. Eigenbrod<sup>1</sup>, F. Courbin<sup>1</sup>, D. Sluse<sup>1</sup>, G. Meylan<sup>1</sup>, and E. Agol<sup>2</sup>

<sup>1</sup> Laboratoire d’Astrophysique, École Polytechnique Fédérale de Lausanne (EPFL), Observatoire de Sauverny, 1290 Versoix, Switzerland

<sup>2</sup> Astronomy Department, University of Washington, Box 351580, Seattle, WA 98195, USA

Received 18 September 2007 / Accepted 20 December 2007

#### ABSTRACT

We present the results of the first long-term (2.2 years) spectroscopic monitoring of a gravitationally lensed quasar, namely the Einstein Cross QSO 2237+0305. The goal of this paper is to present the observational facts to be compared in follow-up papers with theoretical models to constrain the inner structure of the source quasar.

We spatially deconvolve deep VLT/FORS1 spectra to accurately separate the spectrum of the lensing galaxy from the spectra of the quasar images. Accurate cross-calibration of the 58 observations at 31-epoch from October 2004 to December 2006 is carried out with non-variable foreground stars observed simultaneously with the quasar. The quasar spectra are further decomposed into a continuum component and several broad emission lines to infer the variations of these spectral components.

We find prominent microlensing events in the quasar images A and B, while images C and D are almost quiescent on a timescale of a few months. The strongest variations are observed in the continuum of image A. Their amplitude is larger in the blue (0.7 mag) than in the red (0.5 mag), consistent with microlensing of an accretion disk. Variations in the intensity and profile of the broad emission lines are also reported, most prominently in the wings of the C III and center of the C IV emission lines. During a strong microlensing episode observed in June 2006 in quasar image A, the broad component of the C III is more highly magnified than the narrow component. In addition, the emission lines with higher ionization potentials are more magnified than the lines with lower ionization potentials, consistent with the results obtained with reverberation mapping. Finally, we find that the V-band differential extinction by the lens, between the quasar images, is in the range 0.1–0.3 mag.

**Key words.** gravitational lensing – galaxies: quasars: general – galaxies: quasars: emission line – quasars: individual: QSO 2237+0305, Einstein Cross

### 1. Introduction

The gravitational lens QSO 2237+0305, also known as “Huchra’s lens” or the “Einstein Cross”, was discovered by Huchra et al. (1985) during the Center for Astrophysics Redshift Survey. It consists of a  $z_s = 1.695$  quasar gravitationally lensed into four images arranged in a crosslike pattern around the nucleus of a  $z_l = 0.0394$  barred Sab galaxy. The average projected distance of the images from the lens center is  $0.9''$ .

A few years after this discovery, Schneider et al. (1988) and Kent & Falco (1988) computed the first simple models of the system, leading to the conclusion that this system was very promising to study microlensing. Indeed, the predicted time delays between the four quasar images are of the order of a day (Rix et al. 1992; Wambsganss & Paczyński 1994), meaning that intrinsic variability of the quasar can easily be distinguished from microlensing events. In addition, the particularly small redshift of the lensing galaxy implies large tangential velocities for the microlenses. Furthermore the quasar images form right in the bulge of the lens where the stellar density is the highest. The combination of these properties makes microlensing events very

likely in the Einstein Cross and very rapid, with timescales of a few weeks to a few months. Indeed, Irwin et al. (1989) reported significant brightness variations of the brightest quasar image A, which they interpreted as the first detection ever of microlensing in the images of a multiply-imaged quasar.

Since then, microlensing events have been observed in several other gravitationally lensed quasars, and are expected to occur in virtually any quadruply lensed quasar (Witt et al. 1995). Probably the most compelling examples of microlensing light curves are given by the Optical Gravitational Lensing Experiment (OGLE) (Woźniak et al. 2000a; Udalski et al. 2006). Started in 1997, this project monitors regularly the four quasar images of QSO 2237+0305, showing continuous microlensing-induced variations in the light curves.

Most of the quasar microlensing studies so far are based exclusively on broad-band photometric monitoring (e.g. Woźniak et al. 2000b; Schechter et al. 2003; Colley & Schild 2003). These observations, even though dominated by variations of the continuum, make it very difficult to disentangle variations in the continuum from variations in the broad emission lines (BELs). Both types of regions are affected by microlensing, but in different ways depending on their size.

Microlensing of an extended source can occur when its size is smaller than or comparable to the Einstein radius of a star, i.e. of the order of  $10^{17}$  cm or  $10^{-1}$  pc in the case of the Einstein

<sup>★</sup> Based on observations made with the ESO-VLT Unit Telescope # 2 Kueyen (Cerro Paranal, Chile; Proposals 073.B-0243(A&B), 074.B-0270(A), 075.B-0350(A), 076.B-0197(A), 177.B-0615(A&B), PI: F. Courbin).

Cross (Nemiroff 1988; Schneider & Wambsganss 1990). From reverberation mapping, the broad line region (BLR) was long estimated to be larger than this, of the order of  $10^{18}$  cm or 1 pc, hence leaving little room for BEL microlensing. However, more recent reverberation mapping studies revise this downwards, to  $10^{16}$  cm (Wandel et al. 1999; Kaspi et al. 2000), which is also consistent with the disk-wind model of Murray et al. (1995). Inspired by these numbers, Abajas et al. (2002) and Lewis & Ibata (2004) investigated BEL microlensing in further detail and computed possible line profile variations for various BLR models.

Observations of significant continuum and BEL microlensing have been reported in a number of systems (QSO 2237+0305, Filippenko 1989; Lewis et al. 1998; Wayth et al. 2005; HE 2149–2745, Burud et al. 2002a; HE 0435–1223, Wisotzki et al. 2003; H 1413+117, Chartas et al. 2004; SDSS J1004+4112, Richards et al. 2004; HE 1104–1805, Gómez-Álvarez 2004; HE 0047–1756, Wisotzki et al. 2004; SDSS J0924+0219, Eigenbrod et al. 2006a; Keeton et al. 2006; and RXJ 1131–1231, Sluse et al. 2007). These first observational indications of microlensing can be turned into a powerful tool to probe the inner parts of quasars, provided regular spectroscopic data can be obtained. Several theoretical studies show how multiwavelength light curves can constrain the energy profile of the quasar accretion disk and also the absolute sizes of the line-emitting regions (e.g., Agol & Krolik 1999; Mineshige & Yonehara 1999; Abajas et al. 2002; Kochanek 2004).

In this paper we present the results of the first long-term spectrophotometric monitoring of the Einstein Cross. The spectral variations of the four quasar images are followed under sub-arcsecond seeing conditions with the Very Large Telescope (VLT) of the European Southern Observatory for more than two years, from October 2004 to December 2006, with a mean temporal sampling of about one point every second week. This first paper describes the observations, the method used to separate the quasar spectra from that of the lensing galaxy, and the main observational results. Simple considerations of the properties of microlensing caustics and of the geometry of the central parts of the quasar already allow us to infer interesting constraints on the quasar energy profile in the Einstein Cross.

The full analysis of our monitoring data, still being acquired at the VLT, requires detailed microlensing simulations coupled with quasar models and will be the subject of future papers.

## 2. Observations

We acquired our observations with the FOcal Reducer and low dispersion Spectrograph (FORS1), mounted on Kueyen, the Unit Telescope # 2 of the ESO Very Large Telescope (VLT) located at Cerro Paranal (Chile). We performed our observations in the multi-object spectroscopy (MOS) mode. This strategy allowed us to get simultaneous observations of the main target and of four stars used as reference point-spread functions (PSFs). These stars were used to spatially deconvolve the spectra, as well as to perform accurate flux calibration of the target spectra from one epoch to another. We chose these stars to be located as close as possible to QSO 2237+0305 and to have similar apparent magnitudes as the quasar images. The PSF stars # 1, 2, 3, and 4 have *R*-band magnitudes of 17.5, 17.0, 15.5, and 17.5 mag, respectively. Figure 1 shows the field of view of our observations.

We used the high-resolution collimator of FORS1 to achieve the best possible spatial sampling of the data, i.e. 0.1'' per pixel. With this resolution, we observed a maximum of 8 objects simultaneously over a field of view of  $3.4' \times 3.4'$ . One slit was

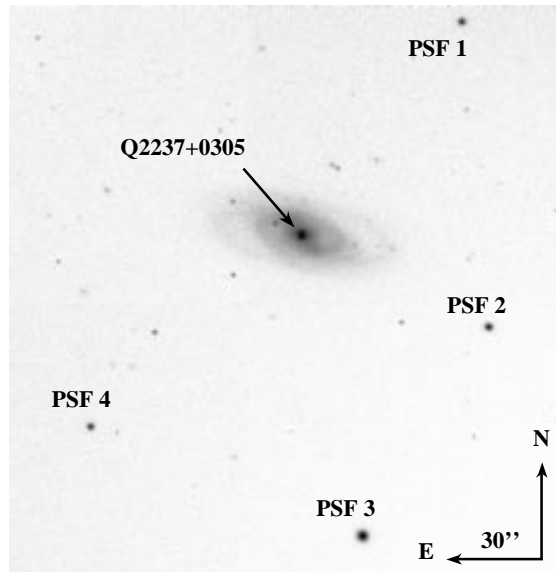


**Fig. 1.** VLT/FORS1 field of view showing the lensed quasar QSO 2237+0305, along with the four PSF stars used to spatially deconvolve the spectra. These stars are also used to cross-calibrate the observations in flux from one epoch to another and to minimize the effect of sky transparency.

aligned along two of the quasar images and four slits were centered on foreground PSF stars. We placed the remaining slits on empty sky regions and used them to carry out sky subtraction of the quasar data.

Two masks were designed to observe the two pairs of quasar images. The PSF stars in both masks were the same. Figure 2 shows the slit positioning with respect to our target. The first mask was aligned on quasar images A and D, while the second was aligned on images B and C. The masks were rotated to position angles that avoid clipping of any quasar image. This is mandatory to carry out spatial deconvolution of the spectra.

Our observing sequences consisted of a short acquisition image, an “image-through-slit” check, followed by a consecutive deep spectroscopic exposure. All individual exposures were 1620 s long. We list the journal of our observations in Table 1. The mean seeing during the three observing seasons was 0.8''. We chose a slit width of 0.7'', approximately matching the seeing and much smaller than the mean separation of 1.4'' between the quasar images. This is mandatory to avoid contamination of an image by the others.

We used the G300V grism in combination with the GG375 order sorting filter. For our slit width, the spectral resolution was  $\Delta\lambda = 15 \text{ \AA}$ , as measured from the FWHM of night-sky emission lines, and the resolving power was  $R = \lambda/\Delta\lambda \approx 400$  at the central wavelength  $\lambda = 5900 \text{ \AA}$ . The useful wavelength range was  $3900 < \lambda < 8200 \text{ \AA}$  with a scale of 2.69  $\text{\AA}$  per pixel in the spectral direction. This configuration favors spectral coverage rather than spectral resolution, allowing us to follow the continuum over a broad spectral range, starting with the very blue portion of the optical spectrum. Even so and in spite of  $R = 400$ , a detailed profile of the BEL is still accessible.

We also observed spectrophotometric standard stars (GD 108, HD 49798, LTT 377, LTT 1020, LTT 1788, and LTT 7987) to remove the response of the telescope, CCD, and

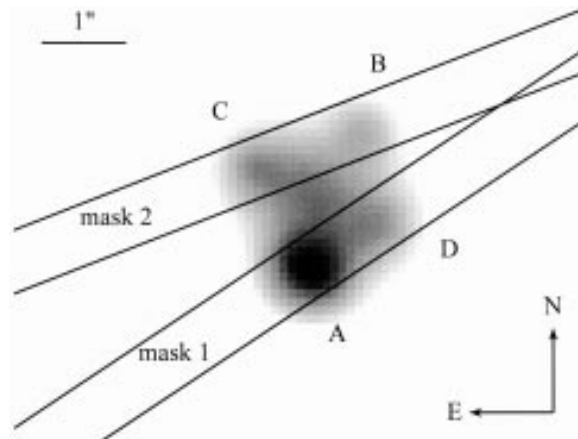


**Fig. 2.** FORS1 *R*-band acquisition image of QSO 2237+0305 taken on epoch # 12 (12–09–2005). The slits used in the two masks are shown. Their width is  $0.7''$ . The Position Angle (PA) of mask 1 is  $PA = -56.5^\circ$  and that of mask 2 is  $PA = -68.5^\circ$ .

grism. We did the relative calibration between the epochs using the PSF stars (see for more details Eigenbrod et al. 2006a).

Finally, it is worth emphasizing that all our VLT data used in the present paper were obtained in service mode, without which this project would have been impossible.

### 3. Data analysis

#### 3.1. Reduction

The data reduction followed the same procedure described in detail in Eigenbrod et al. (2006b). We carried out the standard bias subtraction and flat field correction of the spectra using IRAF<sup>1</sup>. We obtained the wavelength calibration from the spectrum of helium-argon lamps. All spectra, for the object and for the PSF stars were calibrated in two dimensions.

Only one single exposure was taken per mask and per epoch. For this reason, the usual cosmic-ray rejection scheme applied to multiple images could not be applied. Instead, we used the L. A. Cosmic algorithm (van Dokkum 2001), that can handle single images. We visually inspected the cosmic-ray corrected images to check that no data pixel was affected by the process, especially in the emission lines and in the data with the best seeing.

We removed the sky background in a different way in the spectra of the PSF stars and in those of the gravitational lens. For the PSF stars, which are small compared with the slit length ( $19''$ ), we used the IRAF task `background`. This task fits a second order Chebyshev polynomial in the spatial direction to the areas of the spectrum that are not illuminated by the object, and subtracts it from the data. As the lensing galaxy in QSO 2237+0305 is larger than the slit length, this procedure is not applicable. Instead, we used the slits positioned on empty sky regions of the FORS1 field of view, and located next to the gravitational lens. The sky was fitted to these slits and removed from the slit containing the images of QSO 2237+0305.

<sup>1</sup> IRAF is distributed by the National Optical Astronomy Observatories, which are operated by the Association of Universities for Research in Astronomy, Inc., under cooperative agreement with the National Science Foundation.

**Table 1.** Journal of the observations taken on 31 epochs.

ID	Civil date	HJD	Mask	Seeing ["]	Airmass
1	13–10–2004	3292	1	0.86	1.204
1	14–10–2004	3293	2	0.87	1.221
2	14–11–2004	3324	1	0.75	1.184
2	14–11–2004	3324	2	0.68	1.305
3	01–12–2004	3341	1	0.88	1.355
3	01–12–2004	3341	2	0.94	1.609
4	15–12–2004	3355	1	0.99	1.712
4	16–12–2004	3356	2	0.90	1.817
5	11–05–2005	3502	1	0.87	1.568
5	12–05–2005	3503	2	0.51	1.389
6	01–06–2005	3523	1	0.63	1.342
6	01–06–2005	3523	2	0.64	1.224
7	01–07–2005	3553	1	0.57	1.153
8	14–07–2005	3566	1	0.89	1.620
9	06–08–2005	3589	1	0.51	1.135
9	06–08–2005	3589	2	0.61	1.173
10	15–08–2005	3598	1	0.86	1.140
11	25–08–2005	3608	1	0.49	1.261
11	25–08–2005	3608	2	0.54	1.461
12	12–09–2005	3626	1	0.70	1.535
12	12–09–2005	3626	2	0.69	1.341
13	27–09–2005	3641	1	0.92	1.480
13	27–09–2005	3641	2	0.73	1.281
14	01–10–2005	3645	1	0.78	1.281
14	01–10–2005	3645	2	0.87	1.156
15	11–10–2005	3655	1	0.57	1.140
15	11–10–2005	3655	2	0.66	1.134
16	21–10–2005	3665	1	0.70	1.215
16	21–10–2005	3665	2	0.74	1.156
17	11–11–2005	3686	1	0.90	1.137
17	11–11–2005	3686	2	0.90	1.185
18	24–11–2005	3699	1	0.78	1.265
18	24–11–2005	3699	2	0.90	1.443
19	06–12–2005	3711	1	1.10	1.720
19	06–12–2005	3711	2	1.09	1.445
20	24–05–2006	3880	1	0.87	1.709
20	24–05–2006	3880	2	0.90	1.443
21	16–06–2006	3903	1	0.66	1.213
21	16–06–2006	3903	2	0.51	1.155
22	20–06–2006	3907	1	0.64	1.286
22	20–06–2006	3907	2	0.58	1.189
23	27–06–2006	3914	1	0.41	1.145
23	27–06–2006	3914	2	0.50	1.133
24	27–07–2006	3944	1	0.74	1.316
24	27–07–2006	3944	2	0.76	1.204
25	03–08–2006	3951	1	0.73	1.246
25	03–08–2006	3951	2	0.65	1.169
26	13–10–2006	4022	1	0.59	1.176
26	13–10–2006	4022	2	0.52	1.300
27	28–10–2006	4037	1	0.57	1.148
27	28–10–2006	4037	2	0.53	1.138
28	10–11–2006	4050	1	0.89	1.515
28	10–11–2006	4050	2	0.88	1.323
29	27–11–2006	4067	1	0.87	1.255
29	27–11–2006	4067	2	0.92	1.391
30	19–12–2006	4089	2	1.04	2.125
31	22–12–2006	4092	1	0.80	2.018
31	23–12–2006	4093	2	0.76	2.248

#### 3.2. Flux cross-calibration

Once the cosmic rays and sky background were removed, we applied a flux cross-calibration of the spectra as described by Eigenbrod et al. (2006a), using the four PSF stars. The spectra

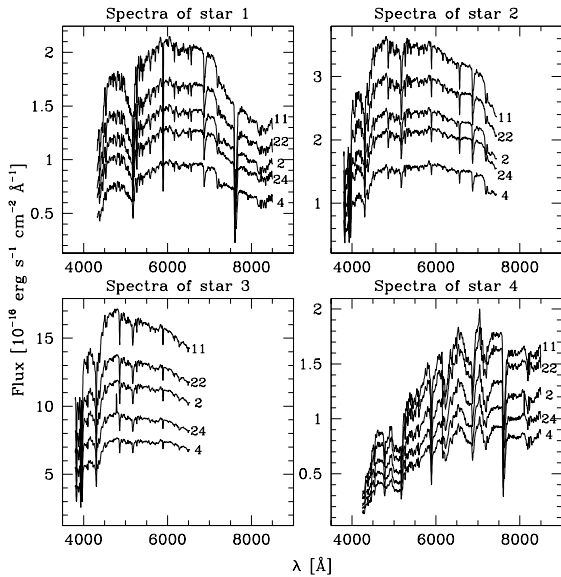


**Fig. 3.** Spectra of the four PSF stars. The spectra in each panel correspond to different observing epochs, chosen to span the full length of the monitoring. The IDs of the observing epochs, as given in Table 1, are indicated. The differences in flux are mainly due to the presence of thin clouds. The purpose of using these stars as flux cross-calibrators is precisely to eliminate these differences, both in intensity and shape.

of these stars are shown in Fig. 3 for five different observing epochs. Our observations show that these stars are non variable.

We created a ratio spectrum for each star, i.e. we divided the spectrum of the star by the spectrum of the same star for a chosen reference exposure. We chose epoch # 2 (14–11–2004) as our reference exposure because of the excellent weather conditions at this particular epoch for both seeing and sky transparency. The computation of these flux ratios was done for all four stars in each exposure and we checked the compatibility of the response curves derived with the four different stars are compatible (see Fig. 4). If not, we rejected one or a maximum of two of the PSF stars. This can happen in some exceptional cases, e.g. when the alignment between the star and the slit is not optimal and generates a color gradient in the spectrum of the misaligned object. Aside from this instrumental effect, the observations show no trace of intrinsic variability of the PSF stars.

After checking that the correction spectra obtained for the four stars were very similar, we computed their mean, which we took as the correction to be applied to the gravitational lens. The high stability of the corrections across the field demonstrates that all residual chromatic slit losses due to the atmospheric refraction are fully corrected. This correction is eased by the fact that: (1) the position angle of the masks is the same for the quasar images and for the PSF stars (i.e. the PSF clipping is the same for the target and the reference stars); (2) we avoid observations at large airmasses (i.e. never larger than 2.5); and (3) the atmospheric refraction corrector on FORS1 is very efficient.

### 3.3. Deconvolution

The lensing galaxy in QSO 2237+0305 is bright. Its central parts have a surface brightness of approximately 18 mag/arcsec<sup>2</sup> in the *R* band, which is comparable to the quasar images. Hence

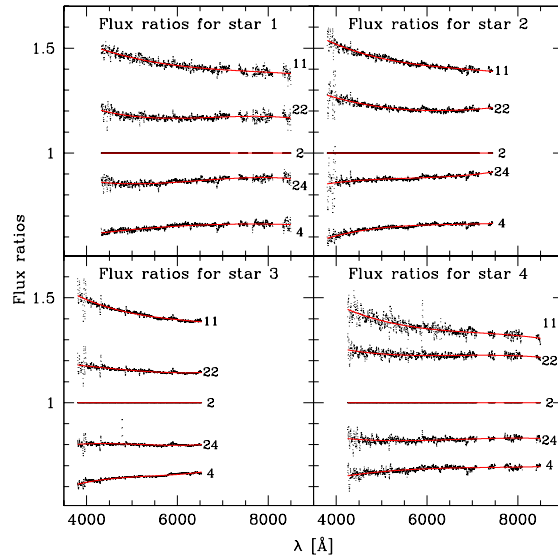


**Fig. 4.** Flux correction for different epochs with respect to the reference epoch # 2 (14–11–2004). Each panel corresponds to one of the 4 PSF stars visible in Fig. 3. In each panel, the dotted line shows the ratio of the spectrum of one PSF star taken at a given epoch and the spectrum of the same star taken at the reference epoch # 2. The curves are polynomials fitting the data. Importantly, the correction derived at a given epoch is about the same for the four stars. The mean of these four curves is used to correct the spectra of the Einstein Cross images. The small parts of the spectra with strong atmospheric absorption are masked. The different spectral ranges are due to different clippings of the spectra by the edges of the CCD.

studying microlensing variations of the quasar images requires very accurate deblending.

In order to carry out this challenging task, we used the spectral version of the MCS deconvolution algorithm (Magain et al. 1998; Courbin et al. 2000), which uses the spatial information contained in the spectra of the PSF stars. The algorithm sharpens the spectra in the spatial direction, and also decomposes them into a “point-source channel” containing the spectra of the two quasar images, and an “extended channel” containing the spectrum of everything in the image that is not a point source, in this case, the spectrum of the lensing galaxy. In Fig. 5, we illustrate the process and the different outputs. In Fig. 7, we show how similar the spectra of the lensing galaxy are, extracted either from two different masks or from data taken at different epochs, hence illustrating the robustness of the deconvolution technique. In Fig. 8, we give an example of decomposition of the data into the quasar and lens spectra after integrating along the spatial direction. The lensing galaxy spectrum shows no trace of the residual quasar BELs. Even when the contrast between the quasar and the galaxy is particularly large, the decomposition is accurate. For example, the CaII H+K doublet in the lens spectrum is well visible, in spite of the presence of the strong quasar C IV emission in the same wavelength range.

### 3.4. Cross-check with the OGLE-III light curves

After reduction and spatial deconvolution, we obtained the extracted spectra of quasar images A and D on 30 different epochs,



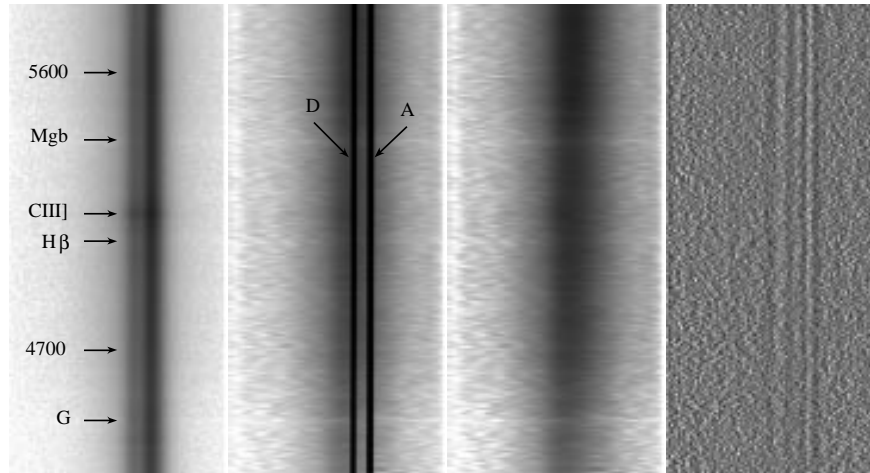


**Fig. 5.** *Left:* portion of the VLT 2D-spectrum of quasar images D and A, taken on epoch # 25 (03-08-2006), on which are indicated the main spectral features of either the quasars or the lens. *Center left:* spatially deconvolved spectrum. The two quasar images are very well separated. *Center right:* spectrum of the lensing galaxy alone. *Right:* residual map of the deconvolution after subtraction of the quasar and lens spectra. Note that the residuals are displayed with much narrower cuts than those used in the other panels. The darkest and brightest pixels correspond to  $-3\sigma$  and  $+3\sigma$  respectively. No significant residuals of the spectral features are visible.

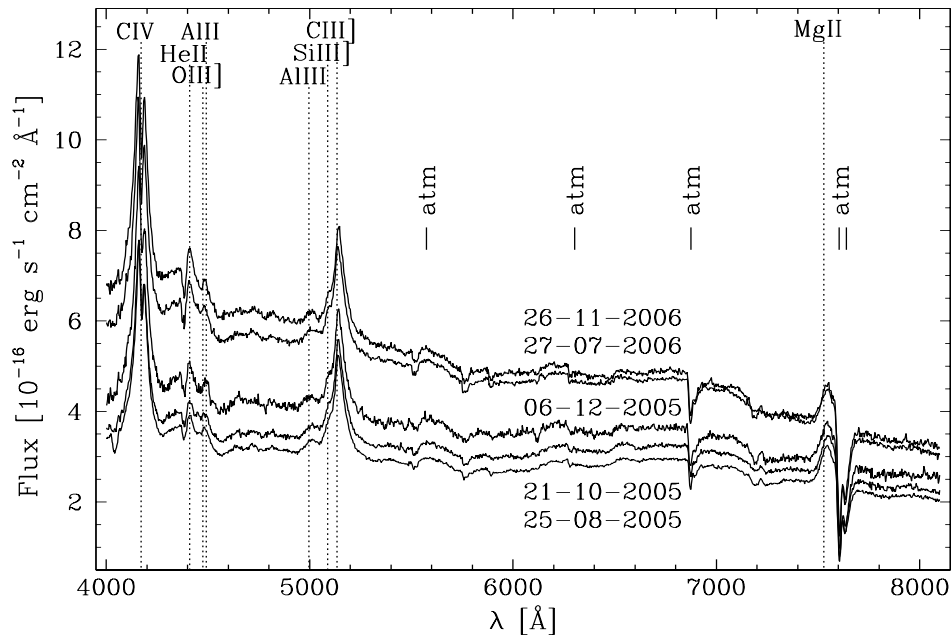


**Fig. 6.** Deconvolved and extracted spectra of quasar image A for five observing epochs. Chromatic variations in the spectra are conspicuous with the blue part of the spectra being more magnified than the red part.

and of B and C on 28 different epochs. Several extracted spectra of image A are shown in Fig. 6. As a sanity check, we compared our results with the OGLE-III photometric monitoring of QSO 2237+0305 (Udalski et al. 2006). We integrated our quasar spectra in the corresponding *V*-band to estimate, from the spectra, the photometric light curves as if they were obtained from imaging. In Fig. 9, we compare our magnitude estimates with the actual OGLE-III measurements. The overall agreement is very good for images A, B, and C. For image D, we have to

shift the OGLE-III light curve by  $-0.5$  mag with respect to the published values. Interestingly, this shift is not needed when we compare our results with the previous OGLE data from the provisional calibration presented in the years 2004–2006. The previous OGLE data also agreed with the photometry of Koptelova et al. (2005). This changed when Udalski et al. (2006) reviewed their calibration and gave image D a larger magnitude of approximately 0.5 mag. They stated that the steep rise of brightness of image D at the end of the 2000 OGLE-II season led to an

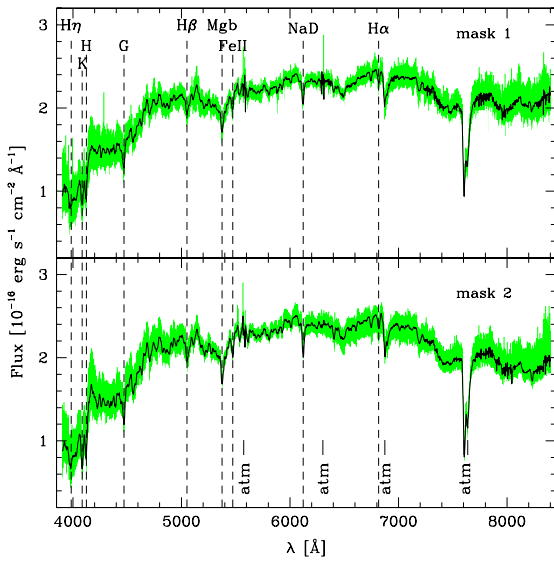


**Fig. 7.** Deconvolved and extracted 1D-spectra of the lensing galaxy. The two panels correspond to the two MOS masks. The shaded areas are the envelopes containing all the spectra of the lens obtained with the corresponding mask. The thick black lines are the means. Note the small scatter between the two spectra.

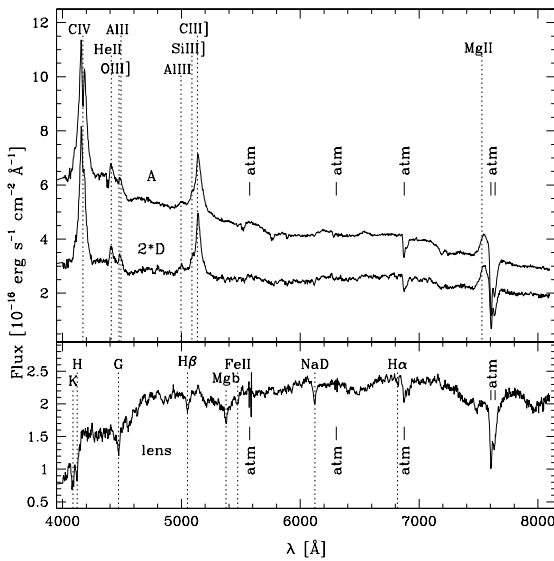


**Fig. 8.** Example of a spectral decomposition. The top panel shows the two extracted spectra for the images A and D for the observations taken on epoch # 25 (03-08-2006) with mask 1. The extracted spectrum of the lensing galaxy, in the bottom panel, shows no trace of contamination by the quasar BELs. For clarity D by a factor of two.

overestimate of the extrapolated magnitude for the beginning of the 2001 OGLE-III season. But this is now discrepant with the photometry of Koptelova et al. (2005). We think that the new extrapolation of the light curve of image D from the end of season 2000 to the beginning of season 2001 might be uncertain,

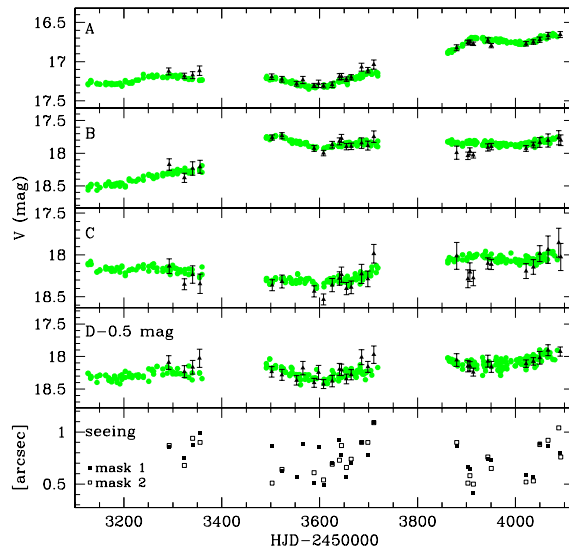


**Fig. 9.** OGLE-III light curves (Udalski et al. 2006) of all four quasar images from April 2004 to December 2006 (dots), compared with the photometry derived by integrating our VLT spectra through the OGLE V-band (dark triangles). The 1-sigma error bars correspond to the photon noise in the spectrum. We shift the OGLE-III light curve of image D by  $-0.5$  mag with respect to the published values. The bottom panel displays the seeing values for each observations.

leading to the observed shift between our data and the OGLE-III light curve of image D. However, aside from this shift, the agreement between the OGLE photometry and our integrated VLT spectra is also very good for image D.

## 4. Multi-component decomposition

Different emission features are known to be produced in regions of different characteristic sizes. As microlensing magnification varies on short spatial scales, sources of different sizes are magnified by differing amounts (e.g. Wambsganss et al. 1990). Emission features from smaller regions of the source are more highly variable due to microlensing than features emitted in more extended regions. In order to study the variation of each spectral feature independently, we need to decompose the spectra into their individual components.

### 4.1. Method

In our analysis of the 1-D spectra of the four quasar images, we follow the multi-component decomposition (MCD) approach (Wills et al. 1985; Dietrich et al. 2003) implemented in Sluse et al. (2007). This method is applied to the rest-frame spectra, assuming they are the superposition of (1) a power law continuum, (2) a pseudo-continuum due to the merging of Fe II and Fe III emission blends, and (3) an emission spectrum due to the other individual BELs. We consider the following emission lines : CIV  $\lambda 1549$ , He II  $\lambda 1640$ , O III  $\lambda 1664$ , Al II  $\lambda 1671$ , Al II  $\lambda 1857$ , Si III  $\lambda 1892$ , C III  $\lambda 1909$ , and Mg II  $\lambda 2798$ . All these features are fitted simultaneously to the data using a standard least-square minimization with a Levenberg-Marquardt based algorithm adapted from the Numerical Recipes (Press et al. 1986).



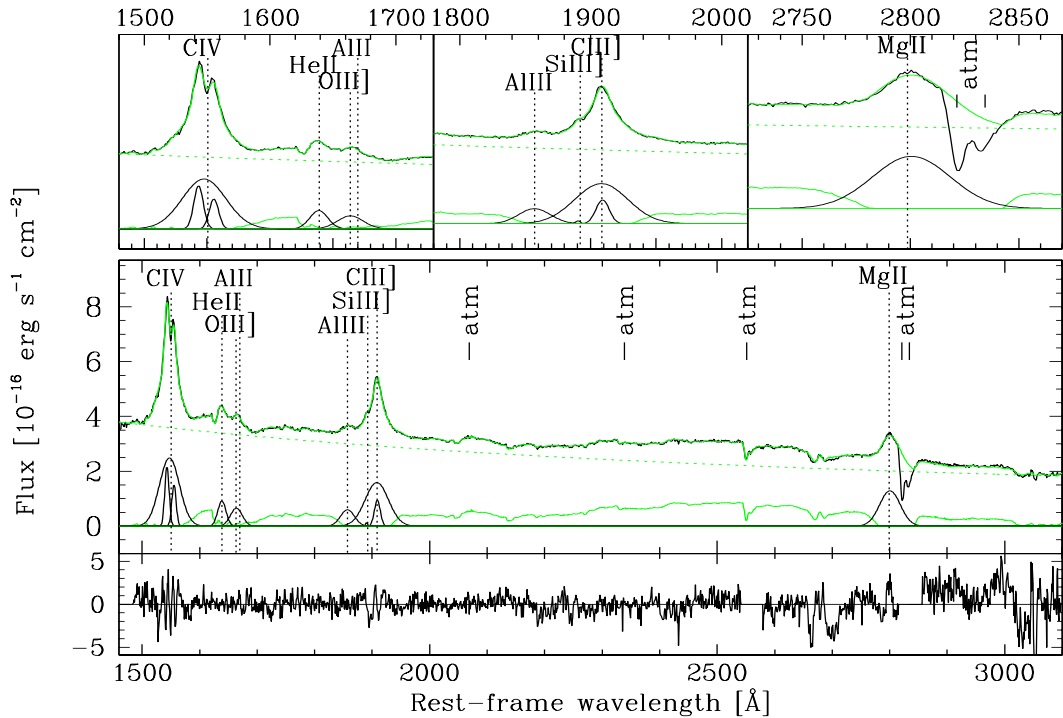


**Fig. 10.** Multi-component decomposition of the spectrum of the brightest quasar image, A, taken on epoch # 2 (14–11–2004). *The upper panels* show the detailed spectral decomposition of the BELs, while *the middle panel* displays the entire spectrum. The continuum is indicated as a dotted curve. The Gaussian lines and iron pseudo-continuum templates are shown below the spectrum. *The bottom panel* is the residual for each pixel normalized by the photon noise per pixel (i.e. the  $y$ -axis is the residual flux in units of  $\sigma$ ).

In the first step, we identify the underlying nonstellar power-law continuum from spectral windows that are free (or almost free) of contributions from the other components, namely the iron pseudo-continuum and the BELs. We use the windows  $1680 \leq \lambda \leq 1710 \text{ \AA}$  and  $3020 \leq \lambda \leq 3080 \text{ \AA}$ . After visual inspection of the iron templates by Vestergaard et al. (2001), we do not expect significant iron emission in these windows.

We characterize the spectral continuum (measured in the restframe) with a power law  $f_\nu \propto \nu^{\alpha_\nu}$ , which translates in wavelength to  $f_\lambda \propto \lambda^{\alpha_\lambda}$  with the relation  $\alpha_\nu = -(2 + \alpha_\lambda)$ , i.e.

$$f_\lambda = f_0 \left( \frac{\lambda}{\lambda_0} \right)^{\alpha_\lambda} = f_0 \left( \frac{\lambda}{\lambda_0} \right)^{-(2+\alpha_\nu)}$$

where  $\lambda_0 = 2000 \text{ \AA}$  and where  $\alpha_\nu$  is the commonly used canonical power index.

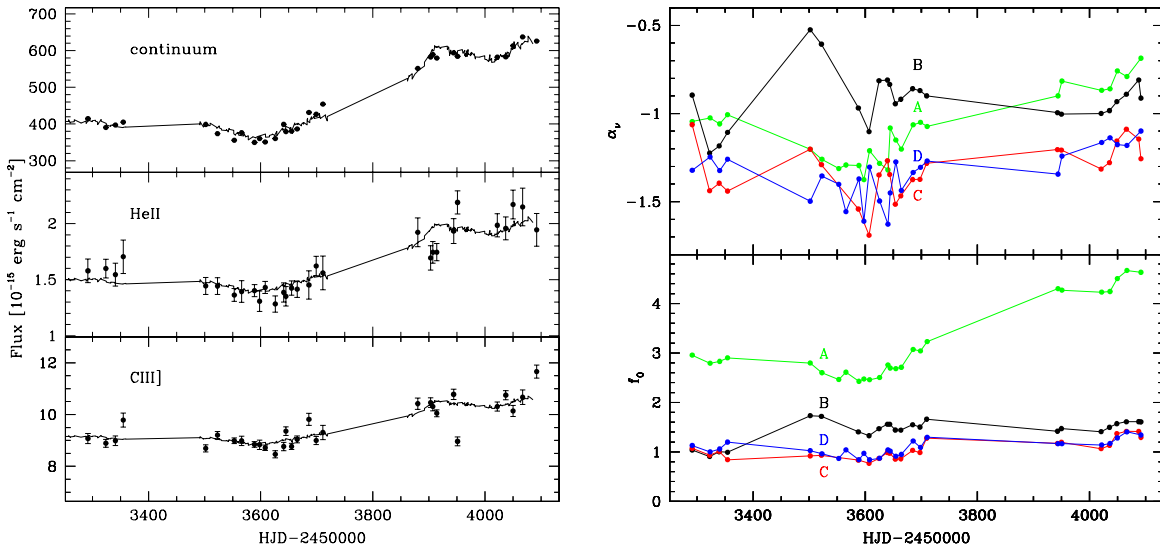
Next, we fit the BELs with Gaussian profiles. We consider a sum of three profiles to fit the absorption feature in the CIV emission line. Two profiles are used for the C III line and one single profile is used to fit simultaneously the O III and Al II lines. All other BELs are fitted with one single profile. We then subtract the BELs and the continuum from the spectra. We consider the residuals as coming from the emission blends of Fe II and Fe III. Hence the averaged and normalized residuals over all epochs define our first iron pseudo-continuum template. We can then proceed iteratively by including this pseudo-continuum iron template in the fitting procedure and rerun it. This gives a better fitting of the emission lines and defines an improved iron pseudo-continuum template. After five of these iterations, typically the fitting does not change significantly anymore.

Figure 10 shows an example of the fitting decomposition described above.

#### 4.2. Results

The light curves for the continuum and for the emission lines can be constructed from the above multi-component decomposition. We show in Fig. 11 an example of variation in the brightest quasar image, A, for the continuum and for two BELs. The error bars give the photon noise, integrated over the corresponding wavelength range. In the right panel of Fig. 11, we show the variability of the continuum in intensity,  $f_0$ , and in slope,  $\alpha_\nu$ , for the 4 quasar images. It is immediately clear that the continuum variations with the largest amplitude are observed in image A, between HJD = 3600 and 3900 days, and in image B between HJD = 3300 and 3500 days. These variations are accompanied by an increase in steepness, i.e. when a quasar image gets brighter, it also gets bluer. This is particularly obvious in Fig. 12, where  $f_0$  and  $\alpha_\nu$  are strongly correlated for images A and B, indicating that significant microlensing events occurred in these two images.

Inaccurate alignment of the quasar images in the slit of the spectrograph is a possible instrumental effect that can mimic microlensing changes in the spectral slope of the quasar images. Indeed, small clipping of one of the quasar images would lead to a stronger flux loss at the bluer wavelengths, hence producing a color gradient in the spectrum and a decrease in the measured value  $\alpha_\nu$ . We have checked all the “through-slit” images taken before each spectrum. Not only do these images show that



**Fig. 11.** *Left:* examples of light curves for the quasar image A. The integrated flux for the continuum, the He II, and C III BELs are given from top to bottom. The continuum is integrated over the entire available wavelength range. In each panel, we fit a scaled version (solid line) of the OGLE-III light curve (Udalski et al. 2006). This nicely illustrates that the BELs vary simultaneously and proportionally to the continuum. *Right:* variability of the best-fit parameters  $\alpha_v$  and  $f_0$  of the continuum (see Sect. 4.1). Note how the changes in slope of the continuum ( $\alpha_v$ ) follow those of the mean intensity ( $f_0$ ).

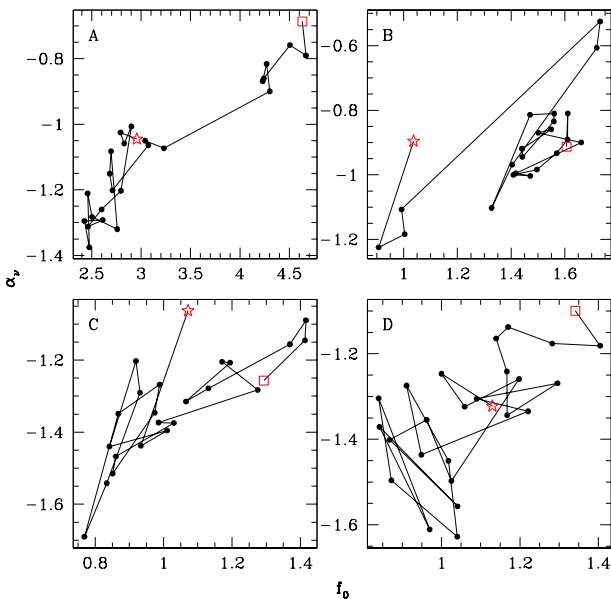


**Fig. 12.** Correlation between the intensity  $f_0$  and slope  $\alpha_v$  of the continuum spectra for all four quasar images. The points are connected chronologically. The first observation epoch is marked by a star and the last one by a square. The correlation is obvious in images A and B spanning a broad range of spectral slopes. In these two images, an increase in intensity is accompanied by an increase in steepness, i.e. when a quasar image gets brighter, it also gets bluer.

the alignment is correct, but it is also very easily reproducible from one epoch to another, even when the FORS1 has been dismounted from and remounted on the telescope.

We have also checked that our fitting procedure does not introduce any spurious correlation between  $\alpha_v$  and  $f_0$ . We check this by using simulated spectra. In order to do that we take a reference spectrum for each quasar image and subtract its continuum. We then take random pairs of  $(\alpha_v, f_0)$  parameters so that the  $\alpha_v$  vs.  $f_0$  plane is well sampled. We chose 400 such pairs and create the corresponding continuum to be added to the reference spectrum. The decomposition procedure is then run on the 400 spectra. We find no correlation at all between the measured  $\alpha_v$  and  $f_0$ . In addition, the parameters used to build the simulated spectra are almost perfectly recovered by the decomposition procedure.

We conclude that genuine chromatic variations are present in the continuum of all images of QSO 2237+0305. The effect is most pronounced in image A during the last observing season, and in image B at the beginning of our monitoring. We show in the following that these observed variations are, in addition, well compatible with the OGLE-III single-band photometric observations.

## 5. Microlensing variability in the OGLE-III photometry

The photometric variations in most gravitationally-lensed quasars are dominated by the intrinsic variations of the quasar, typically of the order of 0.5–1.5 mag, hence making them useful to measure the time delays between the quasar images. Microlensing variations are usually smaller, in the range 0.05–0.1 mag (e.g. the lensed quasars B 1600+434 by Burud et al. 2000; RX J0911+0551 by Hjorth et al. 2002; SBS 1520+530 by Burud et al. 2002b; FBQ 0951+2635 by Jakobsson et al. 2005).

The Einstein Cross is different from this general behavior in two ways: (1) the time delays between each pair of images

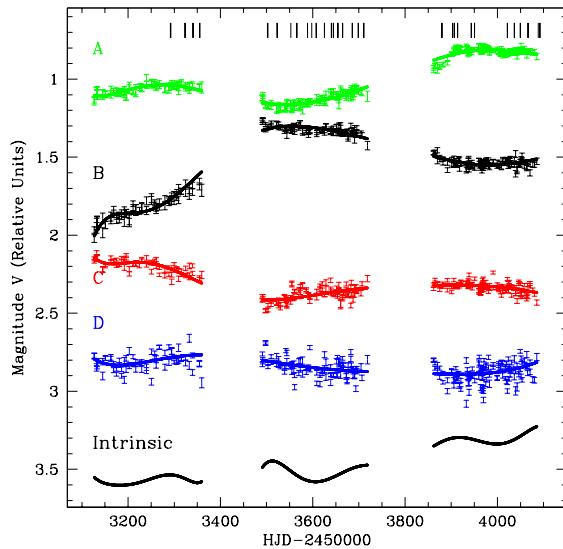


**Fig. 13.** Decomposition of the OGLE-III photometric light curves (Udalski et al. 2006) of the quasar images, into intrinsic quasar variations and microlensing-induced variations (see Sect. 5). The intrinsic variations are shown at the bottom of the figure as a continuous line, while the pure microlensing variations are the data points. The curves are shifted arbitrarily along the  $y$ -axis for clarity. The tickmarks at the top show the epochs of our observations.

are expected to be of the order of one day, hardly measurable; and (2) the microlensing variations dominate the light curves. For these two reasons, microlensing can be fairly well isolated in each quasar image, because it acts differently on the four sightlines.

To separate the intrinsic flux variations of the quasar from the microlensing ones, we perform a polynomial fit to the OGLE-III light curves (Udalski et al. 2006) of Fig. 9. This simple and fully analytical method has been developed by Kochanek et al. (2006), and is also described by Vuissoz et al. (2007). In the present application, the variations of each quasar image are modeled as a sum of two Legendre polynomials: one polynomial is common to all four quasar images and represents the intrinsic variations of the source while a second polynomial, different for each quasar image, represents the additional microlensing variations. In doing so, we rescale the OGLE-III error bars of each image by a factor equal to the flux ratio between each image and image C. This rescaling suppresses the potential problem existing if the fitting procedure considers the variation of image A (with the highest signal-to-noise) as the intrinsic variation of the quasar. The chosen order of the polynomial is 7 for the intrinsic variation, and 10 for the microlensing variation. Higher order polynomials do not significantly improve the fit. The results are displayed in Fig. 13, where the intrinsic variation of the source recovered by the simultaneous fit is shown together with the pure microlensing variations.

We check the efficiency of our method by generating artificial light curves and then using the above polynomial fit to recover the intrinsic and microlensing light curves. These artificial light curves are generated in the same way as described in Eigenbrod et al. (2005), and are composed of an intrinsic light curve to which we add microlensing fluctuations. Both are created in a random walk manner (i.e. not from polynomials). They

are constructed to match the variability properties of the actual light curves, i.e. their timescale and amplitude of variation (for further details see Eigenbrod et al. 2005). We recover the simulated intrinsic light curve of the quasar with a typical error of less than 0.1 mag. The variations of more than 0.4 mag, shown in Fig. 13, both for microlensing and quasar variations, are well above the error estimated from the simulated light curves. In our simulations, we adopt the same photometric error bars as in the light curves of all quasar images, i.e. the re-scaling of the error bars described above in the real data is taken into account. If, on the contrary, we adopt error bars that follow the photon noise, the fitting procedure considers the highest signal-to-noise light curve as the intrinsic quasar light curve.

The light curve most affected by microlensing is that of image B, with a peak-to-peak amplitude of more than 0.7 mag over 3 years. The other quasar images show microlensing-induced variations of up to 0.4 mag, with quasar image A having a sharp event during the last observing season. The intrinsic quasar light curve displays a variation of about 0.4 mag.

The polynomial decomposition of the light curves are compatible with the spectroscopic results. Quasar images A and B, which have the largest microlensing contribution in Fig. 13, respectively at HJD  $\sim 3500$  days and HJD  $\sim 3900$  days, also have a sharp rise in  $\alpha_\nu$  at the same epochs.

## 6. Microlensing variability in the spectra

Chromatic variations of the continuum of images A and B of QSO 2237+0305 are clearly seen in our data. In addition, differential magnification of the continuum with respect to the BELs is also seen in all four quasar images. Such effects have already been observed by Lewis et al. (1998) and Wayth et al. (2005), but only for data over two epochs. Our VLT spectra allow us to follow the variations over two full years, provided the intrinsic variations of the quasar are removed.

### 6.1. Continuum and BELs relative magnifications

Since the time delays in QSO 2237+0305 are negligible, taking the ratio between the above quantities in pairs of quasar images cancels the intrinsic variations. Let  $F(t)$  be the intrinsic source flux, and  $M_i$ ,  $\mu_i$  be the macro and microlensing-magnifications of quasar image  $i$ , respectively. The observed flux ratio between images  $i$  and  $j$  at time  $t$  is then:

$$R_{ij}(t) = \frac{\mu_i(t) M_i F(t)}{\mu_j(t) M_j F(t)} e^{-(\tau_i - \tau_j)} = \frac{\mu_i(t) M_i}{\mu_j(t) M_j} e^{-(\tau_i - \tau_j)}. \quad (1)$$

The extinction  $e^{-\tau_i}$  remains constant in time and is relatively similar in all four quasar images as we show in Sect. 6.3. Hence, it is not expected to strongly affect our results and we will neglect it in the following. The macromagnifications  $M_i$  are best estimated in the mid-IR and radio domain (Falco et al. 1996; Agol et al. 2000). At these wavelengths, the source size is much larger than the typical spatial scale in the microcaustics network, hence leaving it fairly unaffected by microlensing (i.e.  $\mu_i = 1$ ). By multiplying  $R_{ij}$  by  $M_j/M_i$ , using the mid-IR observations, we find the pure-microlensing magnification ratios:

$$r_{ij}(t) = \frac{\mu_i(t)}{\mu_j(t)}. \quad (2)$$

In Fig. 14, we show the variations of  $r_{ij}(t)$  for the integrated flux in the main emission lines and in the continuum. We plot in the

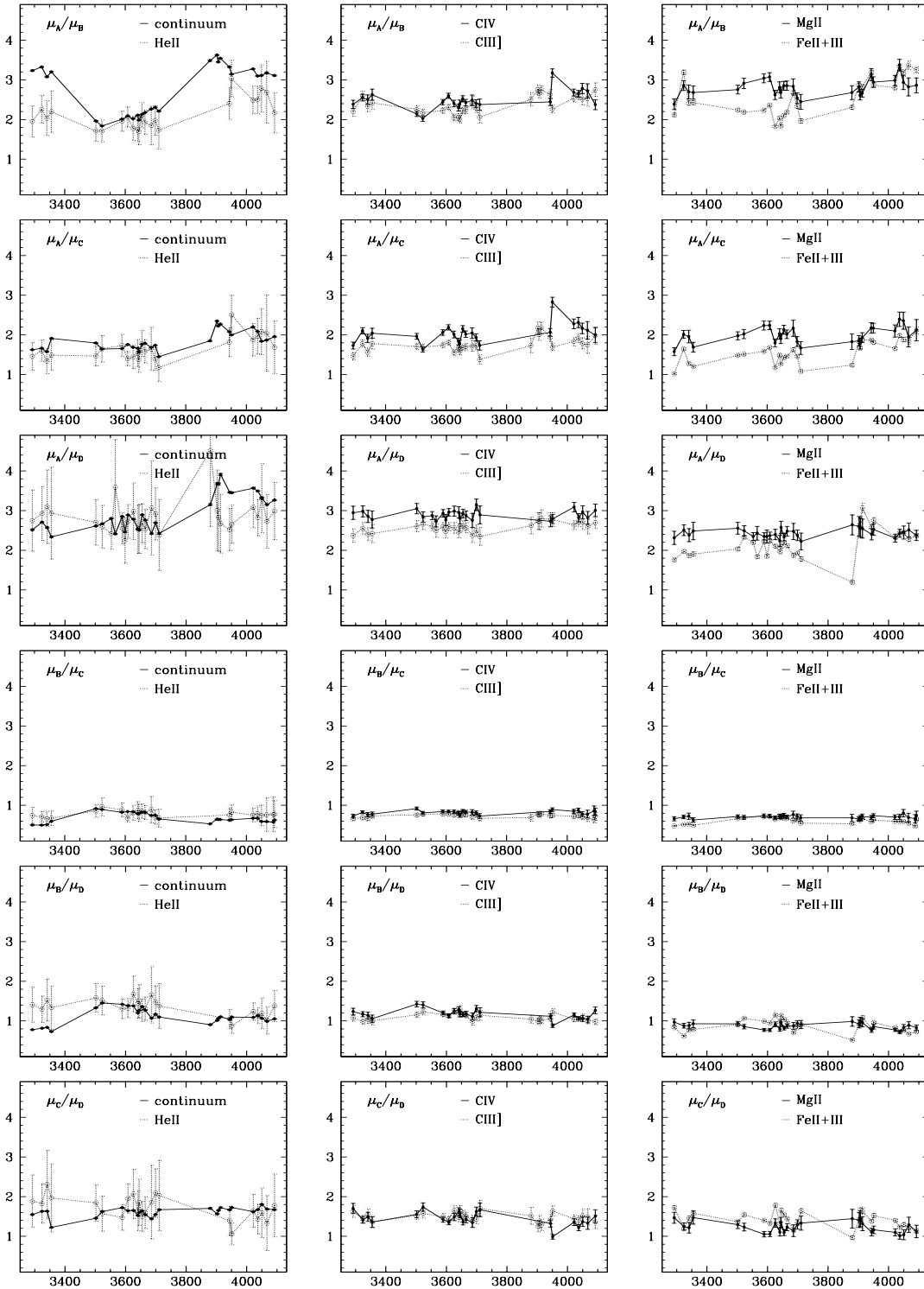


**Fig. 14.** Microlensing-magnification ratios  $r_{ij}$  as a function of time (HJD–2450 000) for all possible combinations of image pairs. These ratios are corrected for the macromagnification by the lensing galaxy following Eq. (2). The ratios are given for the continuum, for the BELs He II, CIV, C III, Mg II and for the iron pseudo-continuum.

figure all possible combinations of image ratios. Several interesting results can be drawn from this figure:

- (a) With the exception of  $r_{BD}$  during the last season (i.e. HJD > 3900 days), none of the ratios  $r_{ij}$  are close to 1, meaning that microlensing is acting at least in three quasar images during the entire monitoring. The evidence for  $r_{BD} \sim 1$  when HJD > 3900 days supports the absence of significant microlensing in images B and D during the last observing season.
- (b) All the BELs have  $r_{ij} \neq 1$  (except  $r_{BD}$ ). The  $r_{ij}$  ratios in the BELs generally closely follow the value measured for the continuum. This demonstrates that the BLR is small enough – probably not larger than a few Einstein radii of a typical microlens in QSO 2237+0305 – so that the BELs can be significantly affected. In addition, the variations observed in the BELs are correlated with those in the continuum.
- (c) The largest changes of magnification ratios involve images A (for HJD  $\sim$  3900 days) and B (for HJD  $\sim$  3500 days). This is seen already in Fig. 13, but the ratios shown here allow us to make sure that the variations are only due to microlensing.
- (d) The ratios  $r_{Aj}$  and  $r_{Cj}$  deviate significantly from 1 during the whole observing period. As an example, we measure in the continuum (resp. C III)  $r_{AD} \sim 2.6$  (resp. 2.8) for HJD < 3900 days and  $r_{CD} \sim 1.6$  (resp. 1.6). Interestingly, these ratios have remained roughly the same since the beginning of the OGLE-III campaign (i.e. HJD  $\sim$  2000 days). Our values of  $r_{AD}$  and  $r_{CD}$  are also similar to the value measured in the H $\beta$  emission line in August 2002 (HJD = 2496 days) by Metcalf et al. (2004). This strongly suggests that images A and C are affected by long-term micro/milli-lensing on periods longer than 5 years.
- (e) The ratio  $r_{CD}$  is the most stable ratio along the monitoring campaign, indicating that no major (short) microlensing event occurred in images C or D.

Because of (b) and (e), we can safely consider that during the time span of our observations, image D is the less affected by microlensing, both on short (i.e. of the order of a few weeks) and long timescales (years). This is consistent with the broadband microlensing light curves of Fig. 13.

We use image D as a reference to study the “short” microlensing events affecting image A at HJD  $\sim$  3900 days and image B at HJD  $\sim$  3500 days. During both events the emission lines are not magnified by the same amount (Fig. 14).

To quantify this, we compute in Table 2 the mean values of  $r_{AD}$  and  $r_{BD}$  during microlensing events and in more “quiescent” phases. For image A (i.e.  $r_{AD}$ ), we clearly see in this table that C IV, C III and He II show very similar magnification ratios, while the Mg II line is less magnified.

All the lines are less magnified than the continuum, consistent with a scheme where the continuum is emitted in the most compact region, and where other emission lines are emitted in larger regions, the largest region being the one with the lowest ionization potential (i.e. Mg II). Indeed the ionization potentials of the different lines are 47.9 eV (C IV), 24.6 eV (He II), 24.4 eV (C III), and 7.6 eV (Mg II). The difference of magnification between C III and Mg II was not observed by Wayth et al. (2005). For image B, the same global trend is observed except that the relative errors on the  $r_{BD}$  ratios are higher due to the lower signal-to-noise ratio of the spectra of image B. The effect is almost absent when  $r_{AD}$  and  $r_{BD}$  are computed in quiescent phases of components A and B.

The behaviour of the Fe II+III emission is more difficult to interpret, as this complex is in fact a blend of many lines. However,

**Table 2.** Mean microlensing ratios for the continuum and for the main BELs. The mean values for  $r_{AD} = \mu_A/\mu_D$  and  $r_{BD} = \mu_B/\mu_D$  are computed for the observations around the epoch in the HJD line, i.e. during microlensing events or during quiescent phases. The values are given along with the dispersion of the points around the mean.

	$\langle r_{AD} \rangle$	$\langle r_{AD} \rangle$	$\langle r_{BD} \rangle$	$\langle r_{BD} \rangle$
HJD	3900 d	3500 d	3500 d	3300 d
State	Micro-A	Quiet-A	Micro-B	Quiet-B
Cont.	$3.46 \pm 0.24$	$2.65 \pm 0.18$	$1.28 \pm 0.12$	$0.79 \pm 0.05$
C IV	$2.89 \pm 0.13$	$2.90 \pm 0.11$	$1.22 \pm 0.11$	$1.15 \pm 0.07$
He II	$3.01 \pm 0.55$	$2.70 \pm 0.33$	$1.50 \pm 0.23$	$1.39 \pm 0.10$
C III	$2.71 \pm 0.07$	$2.54 \pm 0.09$	$1.17 \pm 0.09$	$1.02 \pm 0.04$
Mg II	$2.49 \pm 0.10$	$2.40 \pm 0.10$	$0.88 \pm 0.09$	$0.91 \pm 0.04$
Fe II+III	$2.56 \pm 0.23$	$2.05 \pm 0.17$	$0.99 \pm 0.15$	$0.75 \pm 0.09$

we note that the Fe II+III complex in image A is microlensed at about the same level as the Mg II line. In addition, the difference in magnification of the Fe II+III lines between a microlensing and a quiet phase is larger than for the other lines. This may suggest differential magnification of the emitting regions within the Fe II+III complex, i.e. that the Fe II+III is present both in compact and more extended regions, a conclusion also reached by Sluse et al. (2007).

## 6.2. Line profiles

We have discussed in the previous sections the global intensity changes in the emission lines of QSO 2237+0305. We now investigate the possibility of a change in their profile. Such profile variations may be caused by differential magnification of regions with different velocities in the BLR. This can introduce, e.g., asymmetric changes or even peak displacement of the line (Lewis 1998; Abajas et al. 2002; Lewis & Ibata 2004). Observational evidence for profile variations has been reported, e.g. in HE 2149-27 (Burdud et al. 2002a); SDSS 1004+4112 (Richards et al. 2004; Gómez-Álvarez et al. 2006); SDSS J0924+0219 (Eigenbrod et al. 2006a); and RXJ 1131–1231 (Sluse et al. 2007).

We study the variability of the emission lines in the four quasar images using the continuum-subtracted spectra obtained from the decomposition procedure of Sect. 4.1. We concentrate on the C III emission line, which is easily decomposed into a sum of two components with full-width-half-maximum values about 1100 km s<sup>-1</sup> and 5000 km s<sup>-1</sup>. We will refer to these components in the following as the “narrow” and “broad” components, although the difference made here between narrow and broad is only phenomenological. In particular, the narrow component is not associated, a priori, with the narrow line region (NLR).

We measure the microlensing magnification ratio  $\mu_i(\text{narrow})/\mu_i(\text{broad})$  for the C III emission line in each quasar image. In image A, the magnification of the broad component is  $\sim 1.8$  times larger than the magnification of the narrow component, and this does not change drastically along our whole monitoring campaign. In the other quasar images, the microlensing-magnification of the narrow and broad components are comparable. This implies that the C III emission line is microlensed globally in all images, except in A. In the latter image, the broadest part of the line is more microlensed than the core, indicating that the broadest component of the C III emission is emitted in a more compact region than the core of the emission line.



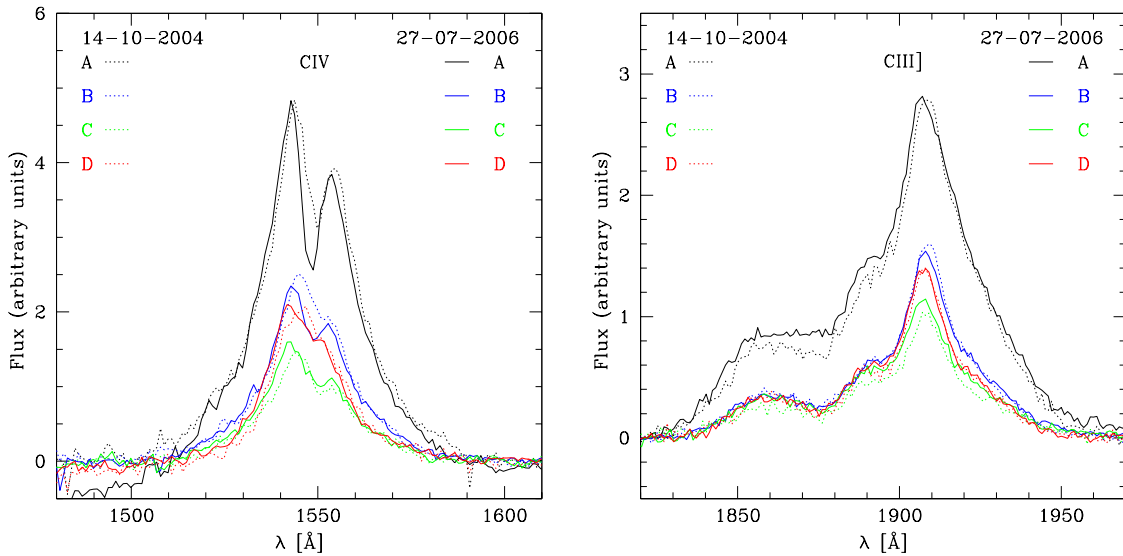


**Fig. 15.** The CIV (*left*) and CIII (*right*) BEL profiles for quasar images A, B, C and D as observed at epoch # 1 (14–10–2004, dotted) and epoch # 24 (27-07-2006, solid). The first epoch is used as a reference while the second epoch falls within the high-magnification episode that occurred at HJD  $\sim$  3900 days in image A (Sect. 6.2). In order to properly show the extra-magnification of the line wings during the strong microlensing episode of image A, we have multiplied the line profile in A observed on 14–10–2004 by a factor 1.05.

The core of the narrow C III emission line is probably associated mainly with photons emitted by the NLR: we observe nearly the same magnification ratio between the narrow and the broad components of the C III emission line than is reported between the narrow O III and the broad H $\beta$  emission lines (Metcalf et al. 2004). This gives a hint that the narrow component of the C III emission line may be partly emitted by the NLR.

However, we do not measure the same microlensing-magnification ratios  $r_{ij}$  in the narrow C III emission as those measured by Metcalf et al. (2004) in the narrow O III emission line. The  $r_{BC}$ ,  $r_{BD}$ ,  $r_{CD}$  ratios measured by these authors are similar for the H $\beta$  BEL and for the narrow O III emission line, but are different from 1, which may be interpreted as a consequence of the microlensing of the NLR. If the NLR is indeed microlensed, the discrepancy between our values and the ones by Metcalf et al. (2004) can simply be explained by the fact that the amplitude of microlensing changes with time. However, there are also two other possible explanations. First, the size of the O III emission region might be comparable with the size of the macrocaustic of the lensing galaxy, such that the O III lensed images are extended and can be resolved by integral field spectroscopy (Metcalf et al. 2004; Yonehara 2006). This may lead to uncertainties in the flux measurements depending on the chosen size of the aperture. Finally, the discrepancy may be explained as well in terms of extinction by the lens (see Sect. 6.3).

The details of the C III profile also show variations. Our spectra show evidence for systematic broadening, by  $\sim$ 10% of the C III emission line in quasar image A during our last observing season (HJD  $>$  3900 days; Fig. 15). In addition, we note evidence for variations in the central parts of the CIV emission lines in all components and at most epochs. An example of these variations is shown in Fig. 15. Their interpretation will be much more complex than for the C III due to the decomposition of

the line into three emission components plus an absorber-like feature.

To look for distortions in the line profiles of images B, C, and D, we normalize the continuum-subtracted spectra of all images so that they share the same C III central intensity. The result is shown for selected epochs in Fig. 16. With this choice of normalization and in the absence of microlensing, the C III lines at a single epoch would match perfectly. It is conspicuous in Fig. 16 that this is not the case. First, we clearly see the effect of differential magnification between the core and the wings of image A at all epochs (the wings of C III in image A are always larger than in the other emission lines). The emission lines in B, C, and D are more similar to one another but there is no epoch where the three line profiles match perfectly, indicative that small microlensing fluctuations affect the C III line. Image C also shows line profile variations, even though the effect is less pronounced than in image A. Finally, we note the absence of any strong line profile variations of image B during the short-term microlensing event occurring in that image at HJD  $\sim$  3500 days.

### 6.3. Differential extinction by the lensing galaxy

Most of the magnification ratios  $r_{ij}$  fluctuate around a mean value. The fluctuations themselves can only be explained by microlensing, but the value of the mean  $\langle r_{ij} \rangle$  is usually different from 1 during our observations. This can, in principle, be explained either by long-term microlensing or by non variable extinction by dust in the lens.

In order to test the latter hypothesis, we use a simple and empirical diagnostic using ratio spectra of pairs of quasar images. In the absence of reddening and microlensing, these ratio spectra should be flat. If dust is present in different amounts on the lines of sight of the images, the ratio spectra will show a

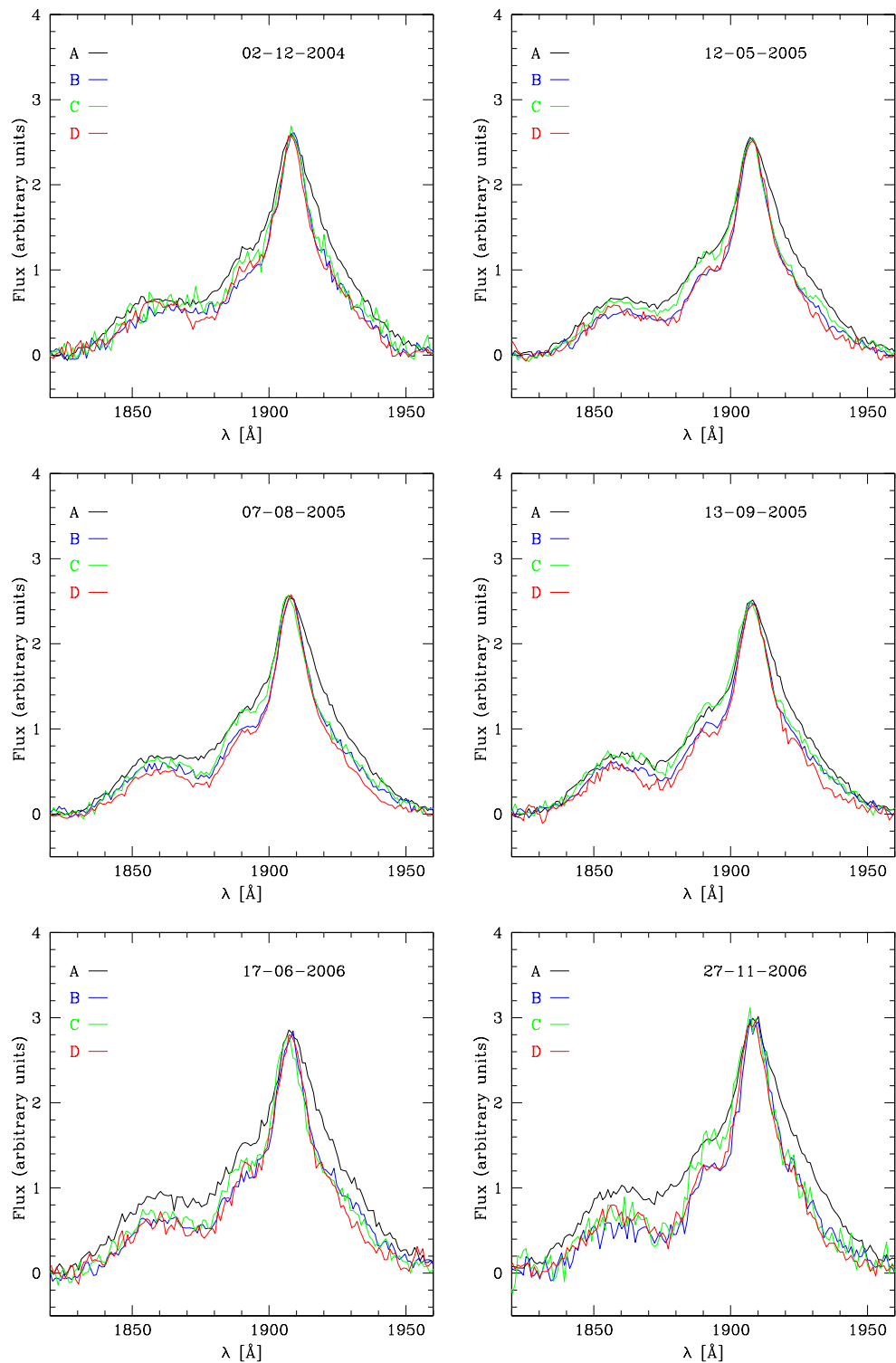


**Fig. 16.** Comparison of the C III BEL profiles of images A, B, C and D of the lensed quasar QSO 2237+0305 on 6 different epochs. The line profiles are normalized so that they have the same peak value. This representation illustrates the difference in the line profiles of the 4 lensed images at several epochs. The most striking effect is the larger wings observed at all epochs in image A. These larger wings are caused by differential microlensing between the wings and the core of the C III line. Small microlensing induced fluctuations of the lines profiles are also observed in images B, C, and D. The epochs are chosen to sample the whole observing period.

non-zero slope, constant with time. Any time-variable change of slope can safely be attributed to microlensing.

We find that the most useful pairs are the ones formed by A&C, B&C, and C&D. Indeed, the C/D ratio spectrum is found to be almost flat all along the years, indicating no significant differential extinction. This is not the case for the two other pairs of ratio spectra which show reddening of image C relative to both A and B, as also reported by Yee (1988). We estimate this differential reddening using the extinction law by Cardelli et al. (1989) and by assuming  $R_V = 3.1$ . We find that the differential extinction  $A_V(C) - A_V(A) \approx A_V(C) - A_V(B)$  is in the range 0.1–0.3 mag. This range of values is sufficient to explain the discrepancy found between the  $r_{ij}$  ratios measured in the C III narrow component and in O III of Sect. 6.2.

Finally, our estimates of the extinction in the lens are too small to explain the highest values of the mean magnification ratios observed in Fig. 14 and Table 2. For instance, the mean of the  $r_{AB}$  or  $r_{AD}$  ratio reaches values larger than 2. Static, long-term microlensing is therefore present in the Einstein Cross, at least in images A and C.

## 7. Conclusions

This paper presents the first long-term (2.2 years) and well-sampled spectrophotometric monitoring of a gravitationally lensed quasar, namely the Einstein Cross QSO 2237+0305. The mean temporal sampling is of one observation every second week. The observations are carried out with the VLT in a novel way, using the spectra of PSF stars, both to deblend the quasar images from the lensing galaxy and to carry out a very accurate flux calibration. This paper, the first of a series, describes the observations and the techniques used to extract the scientific information from the data.

Detailed inverse ray-shooting simulations will be needed to infer quantitative information on the internal structure of the lensed quasar, and will be the topic of the future papers. The main observational facts that these simulations will need to take into account can be summarized as follows.

We find that all images of QSO 2237+0305 are affected by microlensing both on the long and short timescales. Comparison of the image flux ratios with mid-IR measurements reveals that quasar images A and C are both affected by long-term microlensing on a period longer than 5 years. This long-term microlensing affects both the continuum and the BELs.

Furthermore, in quasar image A, the broad component of the C III line is magnified by a factor 1.8 larger than the narrow component. On the contrary, the other quasar images have the same magnification in the narrow and broad components.

On the short timescales, i.e. several months, images A and B are the most affected by microlensing during our monitoring campaign. Image C and especially D are the most quiescent. Image A shows an important brightening episode at HJD  $\sim$  3900 days, and image B at HJD  $\sim$  3500 days. We show that the continuum of these two images becomes bluer as they get brighter, as expected from microlensing magnification of an accretion disk.

We also report microlensing-induced variations of the BELs, both in their integrated line intensities and in their profiles. In image A, we find that the profile of the C III line is broadened during the brightening episode at HJD  $\sim$  3900 days. The C III line profile in image C seems also to be broadened at several epochs. Broadening of the BELs in image B is less obvious.

Variations in the BEL intensities are detected mainly in images A and B. Our measurements suggest that higher ionization

BELs like C IV, C III, are more magnified than lower ionization lines like Mg II. This is compatible with reverberation mapping studies and a stratified structure of the BLR. There is marginal evidence that regions of different sizes are responsible for the Fe II+III emission.

Finally, we estimate the differential extinction between pairs of quasar images due to dust in the lensing galaxy to be in the range 0.1–0.3 mag, with images C and D being the most reddened. This amount of differential extinction is too small to explain the large microlensing-magnification ratios involving images A and C. Long-term microlensing, beyond the duration of our observations, is therefore present in these images.

The timescales of the microlensing variations in QSO 2237+0305 are such that each microlensing event lasts about one observing season (i.e. 8 months), with gaps of several months between events. This means that a relatively loose observing rate of 1 spectrum every 15 days is sufficient to sample the events well enough. In addition, the Einstein Cross is the lensed quasar with the fastest and sharpest microlensing events. It is therefore unique in the sense that only a few years of monitoring can truly constrain the quasar structure on parsec scales (Kochanek 2004). In addition, in the case of the Einstein Cross, the very different behaviours of the BELs and the continuum with respect to microlensing offer considerable hope to reconstruct the two types of regions independently, using ray-shooting simulations.

With two more years of data, we expect to map a total of up to half a dozen microlensing events in the four quasar images, hence providing a unique and useful data set for microlensing and quasar studies.

*Acknowledgements.* We are extremely grateful to all ESO staff for their excellent work. The observations presented in this article have involved a lot of efforts from the ESO staff operating FORS1, to ensure accurate and reproducible mask alignment, to keep the best possible temporal sampling, and to meet the requested seeing value. This project is partially supported by the Swiss National Science Foundation (SNSF).

## References

- Abajas, C., Mediavilla, E., Muñoz, J. A., et al. 2002, *ApJ*, 576, 640
- Agol, E., & Krolik, J. 1999, *ApJ*, 524, 49
- Agol, E., Jones, B., & Blaes, O. 2000, *ApJ*, 545, 657
- Burud, I., Hjorth, J., Jaunsen, A. O., et al. 2000, *ApJ*, 544, 117
- Burud, I., Courbin, F., Magain, P., et al. 2002a, *A&A*, 383, 71
- Burud, I., Hjorth, J., Courbin, F., et al. 2002b, *A&A*, 391, 481
- Cardelli, J. A., Clayton, G. C., & Mathis, J. S. 1989, *ApJ*, 345, 245
- Chartas, G., Eracleous, M., Agol, E., et al. 2004, *ApJ*, 606, 78
- Colley, W. N., & Schild, R. E. 2003, *ApJ*, 594, 97
- Courbin, F., Magain, P., Kirkove, M., & Sohy, S. 2000, *ApJ*, 529, 1136
- Dietrich, M., Hamann, F., Appenzeller, I., et al. 2003, *ApJ*, 596, 817
- Eigenbrod, A., Courbin, F., Vuissoz, C., et al. 2005, *A&A*, 436, 25
- Eigenbrod, A., Courbin, F., Dye, S., et al. 2006a, *A&A*, 451, 747
- Eigenbrod, A., Courbin, F., Meylan, G., et al. 2006b, *A&A*, 451, 759
- Falco, E. E., Lehar, J., Perley, R. A., et al. 1996, *AJ*, 112, 897
- Filippenko, A. V. 1989, *ApJ*, 338, L49
- Gómez-Álvarez, P., Mediavilla, E., Sánchez, S. F., et al. 2004, *AN*, 325, 132
- Gómez-Álvarez, P., Mediavilla, E., Muñoz, J. A., et al. 2006, *ApJ*, 645, 5
- Hjorth, J., Burud, I., Jaunsen, A. O., et al. 2002, *ApJ*, 572, 11
- Huchra, J., Gorenstein, M., Kent, S., et al. 1985, *AJ*, 90, 691
- Irwin, M. J., Webster, R. L., Hewett, P. C., et al. 1989, *AJ*, 98, 1989
- Jakobsson, P., Hjorth, J., Burud, I., et al. 2005, *A&A*, 431, 103
- Kaspi, S., Smith, P. S., Netzer, H., et al. 2000, *ApJ*, 533, 631
- Keeton, C. R., Burles, S., Schechter, P. L., et al. 2006, *ApJ*, 639, 1
- Kent, S. M., & Falco, E. E. 1988, *AJ*, 96, 1570
- Kochanek, C. S. 2004, *ApJ*, 605, 58
- Kochanek, C. S., Morgan, N. D., Falco, E. E., et al. 2006, *ApJ*, 640, 47
- Koptelova, E., Shimanovskaya, E., Artamonov, B., et al. 2005, *MNRAS*, 356, 323
- Lewis, G. F. 1998, *MNRAS*, 297, 69



- Lewis, G. F., & Ibata, R. A. 2004, *MNRAS*, 348, 24
- Lewis, G. F., Irwin, M. J., Hewett, P. C., et al. 1998, *MNRAS*, 295, 573
- Magain, P., Courbin, F., & Sohy, S. 1998, *ApJ*, 494, 452
- Metcalf, R. B., Moustakas, L. A., Bunker, A. J., et al. 2004, *ApJ*, 607, 43
- Mineshige, S., & Yonehara, A. 1999, *PASJ*, 51, 497
- Murray, N., Chiang, J., Grossman, S. A., & Voit, G. M. 1995, *ApJ*, 451, 498
- Nemiroff, R. J. 1988, *ApJ*, 335, 593
- Press, W. H., Flannery, B. P., Teutolsky, S. A., & Vetterling, W. T. 1986, in *Numerical Recipes* (Cambridge University Press)
- Richards, G. T., Keeton, C. R., Pindor, B., et al. 2004, *ApJ*, 610, 679
- Rix, H.-W., Schneider, D. P., & Bahcall, J. N. 1992, *ApJ*, 104, 959
- Schechter, P. L., Udalski, A., Szymański, M., et al. 2003, *ApJ*, 584, 657
- Schneider, D. P., Turner, E. L., Gunn, J. E., et al. 1988, *AJ*, 95, 1619
- Schneider, P., & Wambsganss, J. 1990, *AAP*, 237, 42
- Sluse, D., Claeskens, J.-F., Hutsemékers, D., et al. 2007, *A&A*, 468, 885
- Udalski, A., Szymański, M., Kubiak, M., et al. 2006, *AcA*, 56, 293
- van Dokkum, P. G. 2001, *PASP*, 113, 1420
- Vestergaard, M., & Wilkes, B. J. 2001, *ApJS*, 134, 1
- Vuissoz, C., Courbin, F., Sluse, D., et al. 2007, *A&A*, 464, 845
- Wambsganss, J., & Paczyński, B. 1994, *AJ*, 108, 1156
- Wambsganss, J., Paczyński, B., & Schneider, P. 1990, *ApJ*, 358, 33
- Wandel, A., Peterson, B. M., & Malkan, M. A. 1999, *ApJ*, 526, 579
- Wayth, R. B., O'Dowd, M., Webster, R. L. 2005, *MNRAS*, 359, 561
- Wills, B. J., Netzer, H., & Wills, D. 1985, *ApJ*, 288, 94
- Wisotzki, L., Becker, T., Christensen, L., et al. 2003, *A&A*, 408, 455
- Wisotzki, L., Schechter, P. L., Chen, H.-W., et al. 2004, *A&A*, 419, 31
- Witt, H. J., Mao, S., & Schechter, P. L. 1995, *ApJ*, 443, 18
- Woźniak, P. R., Alard, C., Udalski, A., et al. 2000a, *ApJ*, 529, 88
- Woźniak, P. R., Udalski, A., Szymański, M., et al. 2000b, *ApJ*, 540, L65
- Yee, H. K. C. 1988, *AJ*, 95, 1331
- Yonehara, A. 2006, *ApJ*, 646, 16



---

**7.6 Paper presenting the determination of the energy profile of the accretion disk in QSO 2237+0305**

*Microlensing variability in the gravitationally lensed quasar QSO 2237+0305  $\equiv$  the Einstein Cross*

*II. Energy profile of the accretion disk*

A. Eigenbrod, F. Courbin, G. Meylan, E. Agol, T. Anguita, R. W. Schmidt, & J. Wambsganss

*Astronomy & Astrophysics, 2008, 490, 933*



# Microlensing variability in the gravitationally lensed quasar QSO 2237+0305 ≡ the Einstein Cross

## II. Energy profile of the accretion disk<sup>\*,\*\*</sup>

A. Eigenbrod<sup>1</sup>, F. Courbin<sup>1</sup>, G. Meylan<sup>1</sup>, E. Agol<sup>2</sup>, T. Anguita<sup>3</sup>, R. W. Schmidt<sup>3</sup>, and J. Wambsganss<sup>3</sup>

<sup>1</sup> Laboratoire d’Astrophysique, École Polytechnique Fédérale de Lausanne (EPFL), Observatoire de Sauverny, 1290 Versoix, Switzerland

e-mail: alexander.eigenbrod@epfl.ch

<sup>2</sup> Astronomy Department, University of Washington, Box 351580, Seattle, WA 98195, USA

<sup>3</sup> Astronomisches Rechen-Institut, Zentrum für Astronomie der Universität Heidelberg, Mönchhofstrasse 12-14, 69120 Heidelberg, Germany

Received 1 August 2008 / Accepted 10 September 2008

### ABSTRACT

We present the continuation of our long-term spectroscopic monitoring of the gravitationally lensed quasar QSO 2237+0305. We investigate the chromatic variations observed in the UV/optical continuum of both quasar images A and B, and compare them with numerical simulations to infer the energy profile of the quasar accretion disk. Our procedure combines the microlensing ray-shooting technique with Bayesian analysis, and derives probability distributions for the source sizes as a function of wavelength. We find that the effective caustic crossing timescale is  $4.0 \pm 1.0$  months. Using a robust prior on the effective transverse velocity, we find that the source responsible for the UV/optical continuum has an energy profile well reproduced by a power-law  $R \propto \lambda^\zeta$  with  $\zeta = 1.2 \pm 0.3$ , where  $R$  is the source size responsible for the emission at wavelength  $\lambda$ . This is the first accurate, model-independent determination of the energy profile of a quasar accretion disk on such small scales.

**Key words.** gravitational lensing – quasars: individual: QSO 2237+0305 – accretion, accretion disks

### 1. Introduction

Soon after quasars were discovered, it was suggested that they are powered by the accretion of gas on to supermassive black holes at the centers of galaxies. Since the infalling matter has non-zero angular momentum, it forms a disk spinning around the central black hole (Lynden-Bell 1969). Viscosity within the disk is thought to result in an outward transfer of angular momentum, thereby allowing the material to spiral gradually inward, heating the disk and causing it to emit intensely over a wide range of wavelengths (Shields 1978).

Despite the numerous studies addressing the subject, there are still very few direct observational constraints on the spatial structure of quasar accretion disks. Quasars are located at cosmological distances, and it is particularly difficult to observe the inner regions of these objects. Direct imaging of the inner milli-parsec of a quasar would require angular resolutions on the order of micro- or even nano-arcseconds. There is currently no instrument capable of such performance. Fortunately, nature has provided us with a cosmic magnifying glass in the form of gravitational lensing, which helps to resolve the source, and to reveal the spatial structure of its most inner parts.

Our target is QSO 2237+0305. It was discovered by Huchra et al. (1985) during the Center for Astrophysics Redshift Survey, and is also known as “Huchra’s lens” or the “Einstein Cross”. It is probably the most studied gravitationally lensed quasar. It consists of a  $z_s = 1.695$  source gravitationally lensed into four images arranged in a cross-like pattern around the nucleus of a  $z_l = 0.039$  barred Sab galaxy. The average projected distance of the images from the lens center is  $0.9''$ .

Gravitational lensing is achromatic, in the sense that photons are deflected the same way regardless of their wavelength. However, lensing is sensitive to the source size, and quasar accretion disks are known to vary chromatically from the center to the edge. As a consequence, microlensing of the disk by stars located in the lensing galaxy will affect the quasar images independently, inducing chromatic differences in the spectra of the images (Wambsganss & Paczyński 1991). These differences are directly linked to the energy profile of the disk, i.e. the scaling between the wavelength and the corresponding size of the source emitting at that wavelength. As a consequence, microlensing-induced flux variations can be used to constrain the energy profile of the quasar accretion disk.

Rauch & Blandford (1991) were the first to use this technique, and for the Einstein Cross, they found that the near-ultraviolet emission regions were smaller than expected for thermal emission from an accretion disk. However, more modern work in this system and other gravitational lenses have generally reached the opposite conclusion. For instance,

\* Based on observations made with ESO Telescopes at the Paranal Observatory under program ID 073.B-0243, 074.B-0270, 075.B-0350, 076.B-0197, 177.B-0615.

\*\* Table 6 is only available in electronic form at <http://www.aanda.org>

Pooley et al. (2007) finds that the near-ultraviolet emission regions of ten lensed quasars are a factor of 3–30 larger than the size predicted by simple accretion disk models to produce the observed optical flux. In a more quantitative analysis, Morgan et al. (2007) use the microlensing variability observed for nine gravitationally lensed quasars to show that the accretion disk size is consistent with the expectation from thin disk theory (Shakura & Sunyaev 1973). However, these sizes are larger, by a factor of  $\sim 3$ , than the size needed to produce the observed infrared flux by thermal radiation from a thin disk.

The Einstein Cross is particularly well suited for microlensing studies, because of the symmetric configuration of the lensed images, which results in very short time delays, and because of the low redshift of the lensing galaxy, which places the lensed images in the bulge of the lensing galaxy, where the probability of microlensing by stars is high. Because of this, the Einstein Cross has been intensely monitored by different projects (e.g., Corrigan et al. 1991; Ostensen et al. 1996; Alcalde et al. 2002; Schmidt et al. 2002). The project having the longest duration and the best sampling rate is the Optical Gravitational Lensing Experiment (OGLE) (Woźniak et al. 2000a,b; Udalski et al. 2006). OGLE has monitored QSO 2237+0305 since 1997, and delivers the most complete lightcurves for this system.

Unfortunately, these monitoring campaigns are usually conducted in one photometric band, and hence they can be used to constrain the source size, but not the energy profile, which requires at least two bands. Multi-band monitoring is one approach, but even more effective is long-term spectrophotometric monitoring, as described in our first paper (Eigenbrod et al. 2008, Paper I in the following). In this previous contribution, we describe our observations and data analysis, and report significant flux variations in the continuum and broad emission lines of the spectra of the four lensed images, indicating that both the continuum emitting region and the broad line region are microlensed.

Quasars are known to vary intrinsically, and in order to extract the microlensing-induced flux variations, we need to remove the intrinsic fluctuations from the lightcurves. In practice we do this by considering the difference between the light curves of two images. In the present study we focus on the lightcurves of images A and B, because they are the two images undergoing the strongest flux variations within the time span of our observations. In the case of QSO 2237+0305, we can neglect the time delays between the images, because they are expected to be on the order of one day or less (Schneider et al. 1988; Rix et al. 1992; Wambsganss & Paczyński 1994). We also know that the observed flux  $F$  of a lensed quasar image is the product of the unlensed flux  $F_0$  of the source, the extinction  $e^{-\tau}$ , and the macro and micro-magnification  $\mu_{\text{macro}}$  and  $\mu_{\text{micro}}$

$$F = \mu_{\text{micro}} \mu_{\text{macro}} e^{-\tau} F_0.$$

As observed in Paper I, image A is affected by long-term (more than 5 years) microlensing. Hence the micro-magnification  $\mu_{\text{micro}}$  has two components over the time span of our observation: one constant long-term magnification  $\tilde{\mu}_{\text{micro}}$ , and one variable short-term  $\mu'_{\text{micro}}(t)$

$$\mu_{\text{micro}}(t) = \mu'_{\text{micro}}(t) \tilde{\mu}_{\text{micro}}.$$

We shall mention that this separation in long and short-term microlensing is purely empirical, and only reflects the impossibility of retrieving the intrinsic source flux. The difference in magnitude  $\Delta m$  between image A and B is given by  $\Delta m = -2.5 \log(F_A/F_B)$ .

As observed in Paper I, the extinction remains constant in time in all four images of the Einstein Cross. The macro-magnification given in Table 3 results in a constant magnitude difference on the order of  $-0.1$  mag between images A and B. As a consequence, the time variability that we observe in  $\Delta m$  is only due to short-term microlensing

$$\Delta m = -2.5 \log \left( \frac{\mu'_{\text{micro,A}}}{\mu'_{\text{micro,B}}} \right) + m_0$$

where  $m_0$  is a constant. Microlensing depends on the source size. Smaller sources are more strongly affected by microlensing than larger sources. We also know that bluer photons are emitted closer to the center of a quasar than redder ones. Hence we expect stronger variations of  $\Delta m$  at bluer wavelengths (Wambsganss & Paczyński 1991).

In this paper, we use this chromatic behavior of microlensing to compare the observed variability of  $\Delta m$  at different wavelengths with numerical simulations. Using Bayesian analysis similar to Kochanek (2004) and Anguita et al. (2008), we derive the probability distributions for the size of the source emitting at a given wavelength. This eventually defines the energy profile of the quasar accretion disk.

In the following, we consider a flat cosmology with  $(\Omega_m, \Omega_\Lambda) = (0.3, 0.7)$  and  $H_0 = 70 \text{ km s}^{-1} \text{ Mpc}^{-1}$ .

## 2. Observations

We use two different data sets for this study. The first one is the well sampled  $V$ -band lightcurves of the OGLE<sup>1</sup> project (Udalski et al. 2006), from which we select the data between Julian days 2453 126 (April 30, 2004) and 2454 439 (December 4, 2007), and which comprises 352 data points. We bin the data points separate by less than one day, and are left with 181 points for which we recompute the errors as described in Sect. 4.

The second data set is our deep spectrophotometric monitoring obtained with the FORS1 spectrograph mounted on the Very Large Telescope (VLT) of the European Southern Observatory (ESO). In Paper I, we presented the spectra of all four quasar images on 31 different epochs between October 2004 and December 2006. We have now completed one more year of monitoring, and a total of 43 different epochs spanning more than three years until December 2007 are now available. The journal of the new observations is given in Table 1. We remind that we use two masks for the spectroscopic observations. The mask 1 has a slit centered on quasar images A and D, while the mask 2 has a slit centered on B and C. In the present study, we are interested in the difference magnitude  $\Delta m$  between images A and B. Thus, we will only consider the epochs where both masks 1 and 2 (see Paper I), and hence both quasar images have been observed on the same night. We therefore drop the epochs with ID 7, 8, 10, and 30, which reduces the number of usable epochs to 39. The reduction and further processing of the new data are done following the same procedure as described in Paper I; we spatially deconvolve our spectra to remove the lensing galaxy, and we decompose the spectra into a sum of broad emission lines, continuum and iron pseudo-continuum. We fit the continuum with a power-law

$$f_\nu \propto \nu^{\alpha_\nu} \quad \Rightarrow \quad f_\lambda = f_0 (\lambda/\lambda_0)^{-(2+\alpha_\nu)}$$

where  $\lambda_0 = 2000 \text{ \AA}$  in the source frame, and where  $\alpha_\nu$  is the commonly used canonical power index.

<sup>1</sup> <http://www.astrow.edu.pl/~ogle/ogle3/huchra.html>

**Table 1.** Journal of the second part of our spectroscopic monitoring of QSO 2237+0305. The Julian dates are given in HJD-2 450 000.

ID	Civil date	HJD	Mask	Seeing ["]	Airmass
32	10-07-2007	4292	1	0.63	1.153
			2	0.55	1.132
33	15-07-2007	4297	1	0.57	1.158
			2	0.54	1.220
34	25-07-2007	4307	1	0.79	1.231
			2	0.83	1.161
35	03-08-2007	4316	1	0.68	1.412
			2	0.68	1.278
36	27-08-2007	4340	1	0.88	1.133
			2	0.89	1.143
37	06-09-2007	4350	1	0.67	1.396
			2	0.72	1.252
38	20-09-2007	4364	1	0.73	1.230
			2	0.83	1.167
39	23-09-2007	4367	1	1.23	1.530
			2	1.10	1.344
40	05-10-2007	4379	1	0.59	1.153
			2	0.55	1.132
41	10-10-2007	4384	1	0.76	1.283
			2	0.64	1.195
42	15-11-2007	4420	1	1.07	1.189
			2	0.80	1.148
43	01-12-2007	4436	1	1.00	1.502
			2	0.82	1.318

**Table 2.** Wavelength intervals and central wavelength  $\lambda_c$  (in Å measured in the source frame) of the six photometric bands.

Band	$[\lambda_{\min}, \lambda_{\max}]$	$\lambda_c$
1	[1500, 1750]	1625
2	[1750, 2000]	1875
3	[2000, 2250]	2125
4	[2250, 2500]	2375
5	[2500, 2750]	2625
6	[2750, 3000]	2875

Based on this method, we could identify strong variations in the exponent  $\alpha_\nu$ , and intensity  $f_0$  in the spectra of quasar images A and B. This indicates that the amplitude of the variations are significantly higher in the blue than in the red part of the spectra. In order to study in more detail these chromatic fluctuations of the continuum, we define six wavelength ranges, that we will use as photometric bands. The bands all have the same width and cover the whole wavelength range between 1500 and 3000 Å measured in the source frame, see Table 2. For each of these bands we compute the  $\Delta m$  lightcurve by integrating the continuum power-law in the corresponding wavelength range. We give the corresponding AB magnitudes of the four quasar images in Table 6. By subtracting the magnitude of image B from that of image A, we obtain six 39-epoch lightcurves, as displayed in Fig. 1. We immediately see that the lightcurves for the redder bands (e.g. band #6) vary less than the bluer ones (e.g. band #1).

### 3. Microlensing simulations

In order to simulate the microlensing effects, we have to choose a macro-model for the lensing galaxy. Many models have been proposed for the Einstein Cross (see for instance the summary in Table 2 of Wyithe et al. 2002). We choose the macro-model

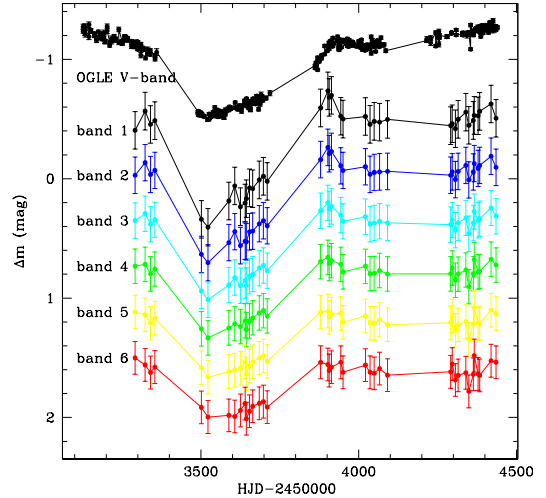
**Fig. 1.** The difference lightcurve  $\Delta m$  between quasar images A and B measured in different wavelength bands. For clarity we shift the curves along the vertical direction. The binned OGLE observations with 181 data points measured in the V-band (Udalski et al. 2006). From our 39-epoch spectrophotometric monitoring, we compute the difference lightcurves of the continuum integrated in the six bands defined in Table 2.**Table 3.** Macro-lensing parameters for images A and B from Kochanek (2004).

Image	$\kappa$	$\gamma$	$\mu_{\text{macro}}$
A	0.394	0.395	4.735
B	0.375	0.390	4.192

proposed by Kochanek (2004). The surface density  $\kappa$ , the shear  $\gamma$ , and the corresponding macro-magnifications  $\mu_{\text{macro}}$  are given in Table 3. The convergence  $\kappa$  is usually separated into a compact matter distribution  $\kappa_*$  and a smooth matter distribution  $\kappa_c$  composed of gas and dark matter. However, as the quasar images are located within the bulge of the lensing galaxy, we do not expect a strong contribution from the smooth matter (Kochanek et al. 2007), so we neglect  $\kappa_c$ , which amounts to assuming the entire surface mass density is in stars (i.e.  $\kappa = \kappa_*$ ).

The next step is to define the mass distribution of the microlenses. Earlier investigations of microlensing have led to the conclusion that the magnification probability distribution is not very sensitive to the mass function of the microlenses (e.g. Wambsganss 1992; Lewis & Irwin 1995; Wyithe & Turner 2001; Congdon et al. 2007), but that it depends on the mean microlens mass  $\langle M \rangle$ , which sets the parameter scales, such as the Einstein radius. The determination of  $\langle M \rangle$  is not trivial because of the degeneracies existing between  $\langle M \rangle$ , the effective transverse velocity, and the source size. Several studies succeeded in getting an estimate of  $\langle M \rangle$ , and currently favor  $\langle M \rangle \simeq 0.1 M_\odot$  (e.g. Wambsganss et al. 1990b; Lewis & Irwin 1996). We will assume this value for all the microlenses distributed in the lens plane. This value is also consistent with the mean mass found by the MACHO collaboration who studied microlensing from objects located towards the bulge of the Milky Way (Alcock et al. 1997). See also Wyithe et al. (2000b), who give a summary of the determinations of microlens masses in other galaxies.



The masses of the microlenses sets the Einstein radius  $r_E$ . For QSO 2237+0305, the Einstein radius projects in the source plane as

$$r_E = D_s \sqrt{\frac{4 G \langle M \rangle}{c^2} \frac{D_{ls}}{D_s D_l}} = 5.77 \times 10^{16} \langle M / 0.1 M_\odot \rangle^{1/2} \text{ cm.}$$

Having defined  $\kappa$ ,  $\gamma$  and the mass of the microlenses, we can go one step further in our simulations, and start generating large magnification patterns for the two quasar images A and B. We do this using the inverse ray-shooting method (Wambsganss 1990; Wambsganss et al. 1990a). For each image, we shoot approximately  $10^{11}$  rays from the observer through the lens plane back to the source plane, where the rays are collected in a 10 000 by 10 000 pixels array, corresponding to 100 by 100 Einstein radii.

In order to study a sample of different source sizes, the magnification patterns are convolved with a set of source profiles. Microlensing-induced flux variations are relatively insensitive to the source profile, but they depend on its characteristic size. Mortonson et al. (2005) showed that the half-light radius is the most important quantity for controlling the shape of microlensing light curves, whereas the source profile is less important. For simplicity we choose a Gaussian profile for the surface brightness, and we define the size of the source as the Full Width at Half Maximum (FWHM), which is twice as large as the half-light radius, and 2.35 greater than the Gaussian width  $\sigma$ .

The relative size of source with respect to the Einstein radius controls the smoothing of the magnification pattern. Very large source sizes (i.e. larger than  $4 r_E$ ) produce magnification patterns that are so strongly smoothed, that they are unable to account for the amplitude (i.e. higher than 1 mag) of the flux variations seen in the OGLE lightcurves. Hence, as was shown in previous studies (e.g. Wyithe et al. 2000a; Yonehara 2001), we can safely rule out continuum source sizes larger than  $4 r_E$ . On the other hand, very small source sizes (i.e. smaller than  $0.01 r_E$ ) give very moderately smoothed magnification patterns, which lead to sharp magnification events that are not observed in the OGLE lightcurves. The lower bound found in that way for the source size is  $0.01 r_E$  (e.g. Kochanek 2004; Anguita et al. 2008).

In the present study, we vary the FWHM of the Gaussian profile from 1 to 400 pixels, which corresponds to  $0.01 r_E$  and  $4.00 r_E$ , respectively. We consider 45 different source sizes between these two extreme values. They are 1, 2, 4, 6, 8, 10, 12, 14, 16, 18, 20, 22, 24, 26, 28, 30, 35, 40, 45, 50, 55, 60, 65, 70, 75, 80, 85, 90, 95, 100, 120, 140, 160, 180, 200, 220, 240, 260, 280, 300, 320, 340, 360, 380, and 400 pixels.

#### 4. Microlensing simulations fitting the OGLE data

Our simulations are conducted following the method described in Kochanek (2004). This technique is based on a Bayesian analysis, that determines the probability distributions for the physical parameters of interest by comparing trial lightcurves with the observed data. Because we want to infer probability distributions, we need to simulate a large number of these trial lightcurves in order to obtain a statistically significant sample. Thus, for each of our 45 source sizes, we simulate 10 000 light curves for both quasar images A and B by tracing source trajectories across the corresponding magnification patterns. We extract the pixel counts along the positions of the trajectory using bi-linear interpolation and we convert them into magnitudes. We subtract the simulated lightcurve of image B from that of image A, and obtain a total of  $4.5 \times 10^5$  difference lightcurves (10 000 for 45 different source sizes). Eventually, we want to compare this large

library of simulated difference lightcurves to the  $\Delta m$  observed in the OGLE data, but before we do that, we specify some characteristics of the simulated source trajectories.

The simulated lightcurves are obtained from source trajectories across the magnification patterns, and these trajectories are characterized by parameters of two kinds: physical and trajectory parameters. The physical parameters are the local magnification tensor  $\kappa$  and  $\gamma$ , the mass  $\langle M \rangle$  of the microlenses, the size  $R_s$  of the source, the effective transverse velocity  $V$  of the source, and the magnitude offset  $m_0$  between the two images due to a combination of the macro-magnification, long-term microlensing, and differential extinction between the images. Because the scales of the magnification patterns are defined in terms of Einstein radii, our computational variables for the source size and velocity are in fact the scaled source size  $\hat{R}_s = R_s / \langle M / 0.1 M_\odot \rangle^{1/2}$  and the scaled transverse velocity  $\hat{V} = V / \langle M / 0.1 M_\odot \rangle^{1/2}$ . Following these definitions,  $\hat{R}_s$  is the relative size of the source with respect to the Einstein radius, and  $\hat{V}$  is the velocity with which the source is moving across the magnification pattern.

Each source trajectory is also defined by the trajectory parameters  $(\theta, \mathbf{x}_{0,A}, \mathbf{x}_{0,B})$ , where  $\theta$  is the direction angle,  $\mathbf{x}_{0,A}$  are the coordinates of the starting point in the magnification pattern of image A, and  $\mathbf{x}_{0,B}$  in the pattern of image B. The trajectory is constrained to have identical directions  $\theta$  and velocities  $V$  across the patterns of images A and B. The direction is set to be the same in both patterns because the shear direction between images A and B is approximately the same (Witt & Mao 1994), and because we assume the motion of the source to be primarily due to the bulk motion of the lensing galaxy rather than to the individual motions of the stars. Kundic & Wambsganss (1993) and Wambsganss & Kundic (1995) show that the velocity dispersion of the stars can statistically be interpreted as a bulk velocity artificially increased by an efficiency factor  $a \simeq 1.3$ .

For each particular choice of the parameters, that we write  $p = (\kappa, \gamma, \langle M \rangle, \hat{R}_s, \hat{V}, m_0, \theta, \mathbf{x}_{0,A}, \mathbf{x}_{0,B})$ , we get one simulated difference lightcurve  $\Delta m'_k(p)$ , that can be compared to the observed data  $D = \Delta m_k$  by measuring the goodness of fit with a  $\chi^2$  statistic

$$\chi_{\text{OGLE}}^2(p) = \sum_{k=1}^{n_{\text{obs}}} \left( \frac{\Delta m_k - \Delta m'_k(p)}{\sigma_k} \right)^2$$

where  $\sigma_k$  are the uncertainties of the OGLE data, and  $n_{\text{obs}} = 181$  is the number of the binned OGLE data points. We determine the  $\sigma_k$  from the photometric errors  $\sigma_{\text{OGLE}}$  given by the OGLE project, from the standard deviation between the binned points  $\sigma_{\text{bin}}$ , and from the systematic error of the OGLE data  $\sigma_{\text{sys}}$ , with  $\sigma_k^2 = \sigma_{\text{OGLE}}^2 + \sigma_{\text{bin}}^2 + \sigma_{\text{sys}}^2$ . We estimate the systematic error  $\sigma_{\text{sys}}$  by carrying out a polynomial fit of the OGLE difference lightcurve  $\Delta m_k$ , using a polynomial of high enough order that the residuals are uncorrelated, i.e. such that the auto-correlation function of the residuals reduces to less than 0.5 within a separation of a few data points. We find that a polynomial on order 7 is sufficient, and  $\sigma_{\text{sys}} = 0.03$  mag.

By varying the parameters we construct our library of  $4.5 \times 10^5$  lightcurves. This produces an ensemble of models, which given the data and using Bayesian analysis (see Sect. 5) can infer the probability distributions for the parameters. The size of the magnification patterns is approximately one hundred times greater than the time scale of the observations multiplied by the effective velocity. Hence the available parameter space is huge, and it is relatively easy to find good fits to the data.

In our simulations we fix the values of  $\kappa$ ,  $\gamma$ , and  $\langle M \rangle$ , and are left with the following set of variable parameters



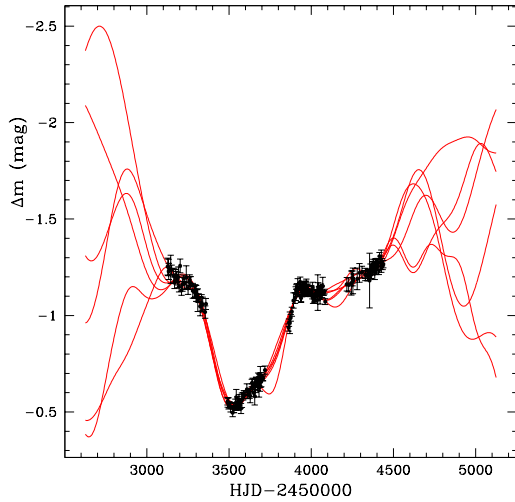


**Fig. 2.** Examples of six simulated lightcurves fitting the observed OGLE difference lightcurve  $\Delta m$  between quasar images A and B.

$p = (\hat{R}_s, \hat{V}, m_0, \theta, \mathbf{x}_{0,A}, \mathbf{x}_{0,B})$ . The physical parameters that we want to investigate are the source size and the effective transverse velocity. The other parameters, i.e.  $(m_0, \theta, \mathbf{x}_{0,A}, \mathbf{x}_{0,B})$ , have no direct physical implications, and can be chosen arbitrarily. They are therefore called nuisance parameters. The influence of these parameters on the inferred probability distributions of  $\hat{R}_s$  and  $\hat{V}$  vanishes when using Bayesian analysis and a sufficiently large library of simulated lightcurves, as described in Sect. 5.

A first guess for the nuisance parameters  $(m_0, \theta, \mathbf{x}_{0,A}, \mathbf{x}_{0,B})$  is chosen randomly following a uniform distribution. In the Bayesian analysis, lightcurves with low  $\chi^2_{\text{OGLE}}$  values have relatively higher weights, and contribute more to the final probability distributions. An effective and fast method consists in searching for trajectories with low  $\chi^2_{\text{OGLE}}$  values. To do this and hence minimize the necessary computing time, we follow the procedure described in Anguita et al. (2008), and optimize the seven parameters  $(\hat{V}, m_0, \theta, \mathbf{x}_{0,A}, \mathbf{x}_{0,B})$  with a  $\chi^2$ -based minimization algorithm using a Levenberg-Marquardt least squares routine in IDL<sup>2</sup>. We verify that this minimization technique still samples uniformly the whole magnification pattern. Finally we obtain a trajectory library containing  $4.5 \times 10^5$  trajectories (10 000 trajectories for 45 different source sizes) fitting the OGLE data. All the source trajectories have a reduced  $\chi^2_{\text{OGLE}}/n_{\text{d.o.f.}} < 10$ , where  $n_{\text{d.o.f.}} = 345$  is the number of degrees of freedom, i.e. the number of observations minus the number of fitted parameters (here 7). Six examples of the simulated lightcurves are given in Fig. 2.

## 5. Bayesian analysis

In the previous section, we have described how we build our large library of trial lightcurves. We will now use these lightcurves to determine the probability distributions for the parameters  $\hat{R}_s$  and  $\hat{V}$  based on Bayesian analysis as described by Kochanek (2004). Following Bayes' theorem the probability of the parameters  $p = (\kappa, \gamma, \langle M \rangle, \hat{R}_s, \hat{V}, m_0, \theta, \mathbf{x}_{0,A}, \mathbf{x}_{0,B})$ , given the data  $D = \Delta m_k$ , is

$$P(p|D) = \frac{P(D|p)P(p)}{P(D)} = \frac{L(D|p)}{N} P(p)$$

<sup>2</sup> <http://cow.physics.wisc.edu/~craigm/idl/>

where  $P(p)$  is the prior,  $L(D|p)$  is the likelihood and  $N$  is a normalization constant.

We do not have any prior information either on the trajectory parameters  $\theta, \mathbf{x}_{0,A}, \mathbf{x}_{0,B}$  or on the magnitude offset  $m_0$ . Therefore we choose these parameters from a random and uniform distribution. This means that the corresponding priors  $P(m_0)$ ,  $P(\theta)$ ,  $P(\mathbf{x}_{0,A})$ , and  $P(\mathbf{x}_{0,B})$  are constant. We also assume that the parameters are independent, i.e. that

$$P(p) = P(\kappa) P(\gamma) P(\langle M \rangle) P(\hat{R}_s) P(\hat{V}) P(m_0) P(\theta) P(\mathbf{x}_{0,A}) P(\mathbf{x}_{0,B}).$$

We define the relative likelihoods of the parameters  $p$  based on the  $\chi^2$  statistics. Usually, this is done following the standard approach for ensemble analysis (e.g., Sambridge 1999), which uses the maximum likelihood estimator

$$L(D|p) = \exp\left(-\frac{1}{2} \chi^2(p)\right).$$

However, as noted by Kochanek (2004), using this standard estimator for the OGLE data works poorly because we are comparing the probabilities of completely different light curves rather than models related to each other by continuous changes of parameters. To circumvent this, we use the likelihood estimator proposed by Kochanek (2004)

$$L(D|p) = \Gamma\left[\frac{n_{\text{d.o.f.}} - 2}{2}, \frac{\chi^2(p)}{2}\right]$$

where  $\Gamma$  is an incomplete Gamma function. Finally, all Bayesian parameter estimates have to be normalized by the requirement that the total probability is unity, i.e.  $\int P(p|D) dp = 1$  and hence

$$N = \int L(D|p) P(p) dp.$$

In practice we sum the probabilities for our random sampling of trajectories, which is equivalent to using Monte Carlo integration methods to compute the integral over the ensemble of all possible trajectories. The sum over the random trajectories will converge to the true integral provided we consider a sufficiently large number of trajectories. The probability of a trajectory  $j$  (defined by the set of parameters  $p_j$ ) given the data  $D$  is

$$P(p_j|D) = \frac{L(D|p_j) P(\hat{R}_{s,j}) P(\hat{V}_j)}{\sum_{j=1}^n L(D|p_j) P(\hat{R}_{s,j}) P(\hat{V}_j)} \quad (1)$$

where  $n$  is the total number of trajectories in the library, and  $P(\hat{R}_{s,j})$  and  $P(\hat{V}_j)$  are the priors on the source size and velocity, respectively. The priors on the other parameters are the same for all trajectories, and cancel out in the fraction above. The final probability distribution of the parameters are obtained by summing the probabilities  $P(p_j|D)$  of all the trajectories  $j$  of the library.

The prior  $P(\hat{R}_{s,j})$  is required because we have not uniformly sampled the parameter space of the source size. We have to correct for this. The prior  $P(\hat{R}_{s,j})$  is related to the density of trajectories as a function of  $\hat{R}_{s,j}$  given our sampling of the source size in 45 different bins. Each bin contains 10 000 trajectories. Therefore, small bins have higher densities, and the corresponding  $P(\hat{R}_{s,j})$  should be proportionally lower to compensate this effect, i.e. if the size of bin  $b$  is  $l_b$ , and if  $\hat{R}_{s,j}$  falls in this bin, then  $P(\hat{R}_{s,j}) \propto l_b$ . Thus each bin has the same density of trajectories.

As already mentioned, there is a strong, essentially linear, correlation between  $\hat{R}_s$  and  $\hat{V}$ , i.e.  $\hat{R}_s \propto \hat{V}^x$  where  $x \simeq 1$

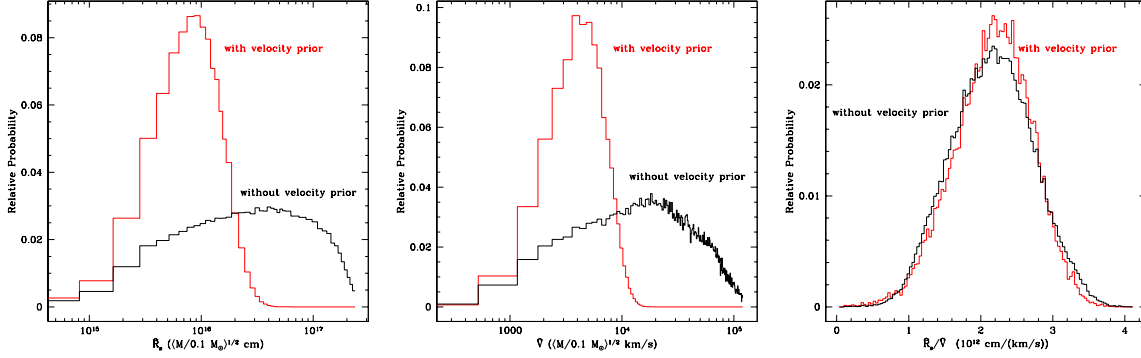


**Fig. 3.** *Left:* the probability distributions for the FWHM  $\hat{R}_s$  of the source, based on the OGLE data. We consider two cases, one with and another without the prior on the velocity. *Center:* same as *left panel*, but for the effective transverse velocity  $\hat{V}$ . *Right:* the probability distributions for the ratio  $\hat{R}_s/\hat{V}$ .

(Kochanek 2004). Furthermore,  $\hat{R}_s$  and  $\hat{V}$  are both defined as functions of  $\langle M \rangle$ , which imply degeneracies between  $\langle M \rangle$ ,  $\hat{V}$ , and  $\hat{R}_s$ . However, since  $R_s = \hat{R}_s \langle M/0.1 M_\odot \rangle^{1/2}$  and  $\langle M \rangle \propto (V/\hat{V})^2$ , the physical size of the source  $R_s \propto V \hat{V}^{-1} \simeq V$  depends essentially on our estimate of the physical velocity  $V$ , and avoids the degeneracies between  $\langle M \rangle$ ,  $\hat{V}$ , and  $\hat{R}_s$ .

Estimates of  $V$  can be obtained from the observations of the motion of other galaxies or galaxy clusters (e.g. Benson et al. 2003), which show that peculiar velocities are typically not higher than  $1500 \text{ km s}^{-1}$ . In order to give a lower weight to trajectories having much higher velocities, we have to introduce a prior on the velocity. Previous studies have considered various priors (e.g. Kochanek 2004; Gil-Merino et al. 2005). Some are more restrictive than others, but most of them have in common that they favor transverse velocities of  $\sim 600 \text{ km s}^{-1}$  in the lens plane, which correspond to projected transverse velocities of  $\sim 6000 \text{ km s}^{-1}$  in the source plane of QSO 2237+0305 (Kayser et al. 1986).

The effective transverse velocity is the result of the relative motion between the source, the lens and the observer (Kayser et al. 1986), and is enhanced by a contribution from the velocity dispersion of the stars in the lensing galaxy (Kundic & Wambsgans 1993; Wambsgans & Kundic 1995). The problem is that we do not know the peculiar velocity of either the source, or the lens. The best we can do is to consider probability distributions for these unknown velocities, based on what we know from the peculiar motion of other galaxies (e.g. Mould et al. 1993; Benson et al. 2003). Kochanek (2004) shows that a good approximation for the probability distribution of the effective transverse velocity in the source-plane is

$$P(V) = \frac{V}{\bar{V}} I_0 \left[ \frac{V\bar{V}}{\sigma^2} \right] \exp \left( -\frac{V^2 + \bar{V}^2}{2\sigma^2} \right) \quad (2)$$

where  $I_0$  is a modified Bessel function,  $\bar{V} \simeq 2500 \text{ km s}^{-1}$  is the mean velocity, and  $\sigma \simeq 3500 \text{ km s}^{-1}$  is the total root mean square velocity obtained by considering all the different velocities contributing to the transverse effective velocity. In our analysis we assume  $\langle M \rangle = 0.1 M_\odot$ , and we define the prior on the scaled velocity  $\hat{V}$  as  $P(\hat{V}) = P(V)$ .

Using Bayesian analysis, and considering both cases with and without velocity prior, we obtain the probability distributions of the source size  $\hat{R}_s$ , the effective transverse velocity  $\hat{V}$ , and the ratio  $\hat{R}_s/\hat{V}$  plotted in Fig. 3. The results are given in Table 4.

**Table 4.** Results from the microlensing simulations and Bayesian analysis applied to the OGLE data.

With velocity prior	
$\hat{R}_s = (9.2^{+6.9}_{-5.8}) \times 10^{15} \langle M/0.1 M_\odot \rangle^{1/2} \text{ cm} = (0.16^{+0.12}_{-0.10}) r_E$	
$\hat{V} = (3.9^{+3.0}_{-1.8}) \times 10^3 \langle M/0.1 M_\odot \rangle^{1/2} \text{ km s}^{-1}$	
$\hat{R}_s/\hat{V} = (2.1 \pm 0.5) \times 10^{12} \text{ cm}/(\text{km s}^{-1})$	
without velocity prior	
$\hat{R}_s = (4.0^{+7.5}_{-3.5}) \times 10^{16} \langle M/0.1 M_\odot \rangle^{1/2} \text{ cm} = (0.69^{+1.30}_{-0.60}) r_E$	
$\hat{V} = (1.8^{+2.8}_{-1.6}) \times 10^4 \langle M/0.1 M_\odot \rangle^{1/2} \text{ km s}^{-1}$	
$\hat{R}_s/\hat{V} = (2.1 \pm 0.6) \times 10^{12} \text{ cm}/(\text{km s}^{-1})$	

## 6. Energy profile of the quasar accretion disk

Accretion disk models for quasars generally make the assumption that the disk is optically thick and geometrically thin; both assumptions are required to cause efficient conversion of the gravitational potential energy of accreting matter into radiation (Pringle & Rees 1972; Shakura & Sunyaev 1973; Novikov & Thorne 1973). Alternative models in which mass is lost in a wind (Kuncic & Bicknell 2007), the disk accretes at greater than the Eddington limit and thus becomes geometrically thick, in which case advection or convection can dominate the radial heat transport (e.g. Abramowicz et al. 1988), or magnetic connections between the black hole and disk modify the rate of energy dissipation (Agol & Krolik 2000).

The peak of the continuum emission in a typical quasar spectral energy distribution is in the ‘‘Big Blue Bump’’, and can be fitted well with a spectrum which scales as  $F_\nu \propto \nu^{1/3} e^{h\nu/kT}$ , with a characteristic temperature  $T = 7 \times 10^4 \text{ K}$  (Krolik 1998b). This is predicted by the standard thick accretion disk model in which  $T \propto R^{-3/4} (1 - (R_{\text{in}}/R)^{1/2})^{1/4}$ , the functional form predicted by non-relativistic thin accretion disks with an inner edge  $R_{\text{in}}$  at which the viscous stress disappears (relativity modifies this somewhat – Krolik 1998a). At large radius  $T \propto R^{-3/4}$ , and the model predicts that the radiative flux  $F$  ( $\text{erg cm}^{-2} \text{ s}^{-1}$ ) at the surface of the disk at a radius  $R$  is proportional to the energy production rate at that radius, resulting in  $F \propto R^{-3}$ . Since we are assuming a blackbody spectrum,  $F \propto T^4$ , and because the wavelength  $\lambda$  of the peak of the black body spectrum is proportional to  $T^{-1}$ , most of the radiation at a given radius  $R$  comes from near a radius

$$R \propto T^{-4/3} \propto \lambda^{4/3}.$$

This defines the energy profile of the quasar, away from the inner edge of the disk, which is identical to the form obtained by Kochanek et al. (2007) from the standard thin accretion disk model of Shakura & Sunyaev (1973).

However, given that we are trying to test the accretion disk model, we allow the temperature to scale as a power-law with radius with arbitrary slope  $T \propto R^{-\zeta}$  (Rauch & Blandford 1991); this functional form is general enough to cover a variety of different alternatives to the standard accretion disk model.

There exist numerous models for quasar accretion disks in the literature. We can not consider all of them here, and we select only a few presenting an interesting variety. One particular model is motivated by the fact that the theoretical optical/UV continuum of a standard thin disk is  $F_\nu \propto \nu^{1/3}$ , which is inconsistent with  $F_\nu \propto \nu^{-1}$  observed in many quasars. Hence, Gaskell (2008) suggests that the observed quasar spectra can be reproduced by accretion disks with a temperature gradient of  $T \propto R^{-0.57}$  instead of  $T \propto R^{-3/4}$ . This implies

$$R \propto \lambda^{1.75}.$$

Another model is proposed by Agol & Krolik (2000), and describes a disk which is powered by the spin of the central black hole. This changes the temperature profile to  $T \propto r^{-7/8}$ , and predicts

$$R \propto \lambda^{8/7}.$$

The three models mentioned above all predict a power-law relation between the wavelength and the corresponding source size

$$R \propto \lambda^\zeta$$

with different values for the index  $\zeta$ . For two different radii  $R$  and  $R_{\text{ref}}$  emitting at the wavelengths  $\lambda$  and  $\lambda_{\text{ref}}$  respectively, we have

$$\frac{R}{R_{\text{ref}}} = \left( \frac{\lambda}{\lambda_{\text{ref}}} \right)^\zeta \quad \Rightarrow \quad \log \left( \frac{R}{R_{\text{ref}}} \right) = \zeta \log \left( \frac{\lambda}{\lambda_{\text{ref}}} \right).$$

To distinguish between these different accretion disk models, we determine in the next section, which power-law is best compatible with our spectroscopic observations, and which of these models can be ruled out for QSO 2237+0305.

## 7. Interpretation of the spectroscopic data

### 7.1. Method

We will now compare the theoretical energy profile with our observations. In the procedure described in the previous sections, we have built a library of simulated lightcurves by tracing a large number of source trajectories through the magnification patterns for various source sizes  $\hat{R}_s$  in order to reproduce the OGLE V-band photometry  $\Delta m$  of QSO 2237+0305. We use this ensemble of models as an input to extend our analysis to our spectroscopic observations. We consider the integrated lightcurves in the six color bands defined in Table 2 as shown in Fig. 1. For each band  $i$ , we have a lightcurve  $\Delta m(\lambda_i, t)$  with 39 epochs. The wavelength  $\lambda_i$  is the central wavelength of band  $i$  as defined in Table 2. We then determine which scaled source size  $\hat{R}_i$  best reproduces the observed lightcurve in band  $i$ .

Each source trajectory  $j$  in the library is defined by a set of the parameters  $p_j = (\kappa_j, \gamma_j, \langle M \rangle_j, \hat{R}_{s,j}, \hat{V}_j, m_{0,j}, \theta_j, \mathbf{x}_{0,A,j}, \mathbf{x}_{0,B,j})$ . For every trajectory  $j$ , we keep all these parameters fixed, except the source size  $\hat{R}_{s,j}$ , that we modify, i.e. we trace the same

source trajectory in all the convolved magnification patterns. By doing this, we get the simulated difference lightcurve  $\Delta m'_j(t)$  corresponding to the 45 different source sizes defined in Sect. 3. We then interpolate the magnitude values of these extracted light curves to obtain continuous values for the source size. For every trajectory  $j$ , this defines a surface  $\Delta m'_j(\hat{R}_s, t)$  in the three-dimensional space defined by  $\hat{R}_s$ ,  $t$  and  $\Delta m$ .

We use these  $\Delta m'_j(\hat{R}_s, t)$  to interpret our spectroscopic data by determining which scaled source size  $\hat{R}_i$  best reproduces the observed lightcurve  $\Delta m(\lambda_i, t)$  in band  $i$ . The size  $\hat{R}_i$  is the value that minimizes the  $\chi^2_{ij}$  between the spectrophotometric observations  $\Delta m(\lambda_i, t)$  and the simulated difference lightcurve  $\Delta m'_j(\hat{R}_i, t)$ . After this second fitting procedure, we update the relative likelihoods of the lightcurves

$$L(D|p_j, i) = \Gamma \left[ \frac{n_{\text{d.o.f.}} - 2}{2}, \frac{\chi^2_{\text{OGLE}}(p_j)}{2} \right] \times \exp \left( -\frac{\chi^2_{ij}}{2} \right)$$

where  $i$  refers to the considered band. In the fitting of the spectroscopic observations  $\Delta m(\lambda_i, t)$ , we are comparing similar light curves, where only  $\hat{R}_i$  is changing. This is a very different situation than when we were fitting the OGLE difference lightcurve and comparing simulations with very different parameters. Hence, we can use here the standard maximum likelihood estimator  $\exp(-\chi^2_{ij}/2)$  to compute the likelihoods  $L(D|p_j, i)$ . We run this procedure for all the simulated source trajectories  $j$  in the library, and use these updated likelihoods to compute the final probability distribution for the parameters of interest, as described in Sect. 5.

### 7.2. Results

For each band  $i$ , we compute the probability distribution of the source-size ratio  $\hat{R}_i/\hat{R}_{\text{ref}}$  following the Bayesian analysis described in Sect. 5 using Eq. (1). The reference radius  $\hat{R}_{\text{ref}}$  at the reference wavelength  $\lambda_{\text{ref}}$  can be chosen arbitrarily, and we simply define the middle band #3 as our reference. The scaling between  $R_s$  and  $\hat{R}_s$  is independent of the considered wavelength and  $R_i/R_{\text{ref}} = \hat{R}_i/\hat{R}_{\text{ref}}$ . Thus, the ratio  $R_i/R_{\text{ref}}$  is not expected to depend on the assumed microlens mass  $\langle M \rangle$ . We plot the ratio  $R_i/R_{\text{ref}}$  against the corresponding wavelength ratio  $\lambda_i/\lambda_{\text{ref}}$ , and determine the slope of the energy profile by fitting a power law

$$R \propto \lambda^\zeta.$$

We do this for the entire library of source trajectories, but also individually for every subsample of the library with the same initial source size  $\hat{R}_s$  used to fit the OGLE data. The resulting index  $\zeta$  is plotted as a function of  $\hat{R}_s$  in Fig. 6. We give two examples of energy profiles in Fig. 4 derived from subsamples of trajectories: one having  $\hat{R}_s = 0.1 r_E = 10$  pixels and another with  $\hat{R}_s = 1 r_E = 100$  pixels. The final energy profile obtained from the whole sample of source trajectories is shown in Fig. 5, given in Table 5, and yields  $\zeta = 1.2 \pm 0.3$  when adding the velocity prior. Without this prior we get a flatter energy profile with  $\zeta = 1.1 \pm 0.3$ .

## 8. Discussion

From the results of our microlensing simulations, we can extract several interesting facts. First, the source FWHM  $\hat{R}_s = (0.16^{+0.12}_{-0.10}) r_E$  we derive from the fitting of the OGLE data

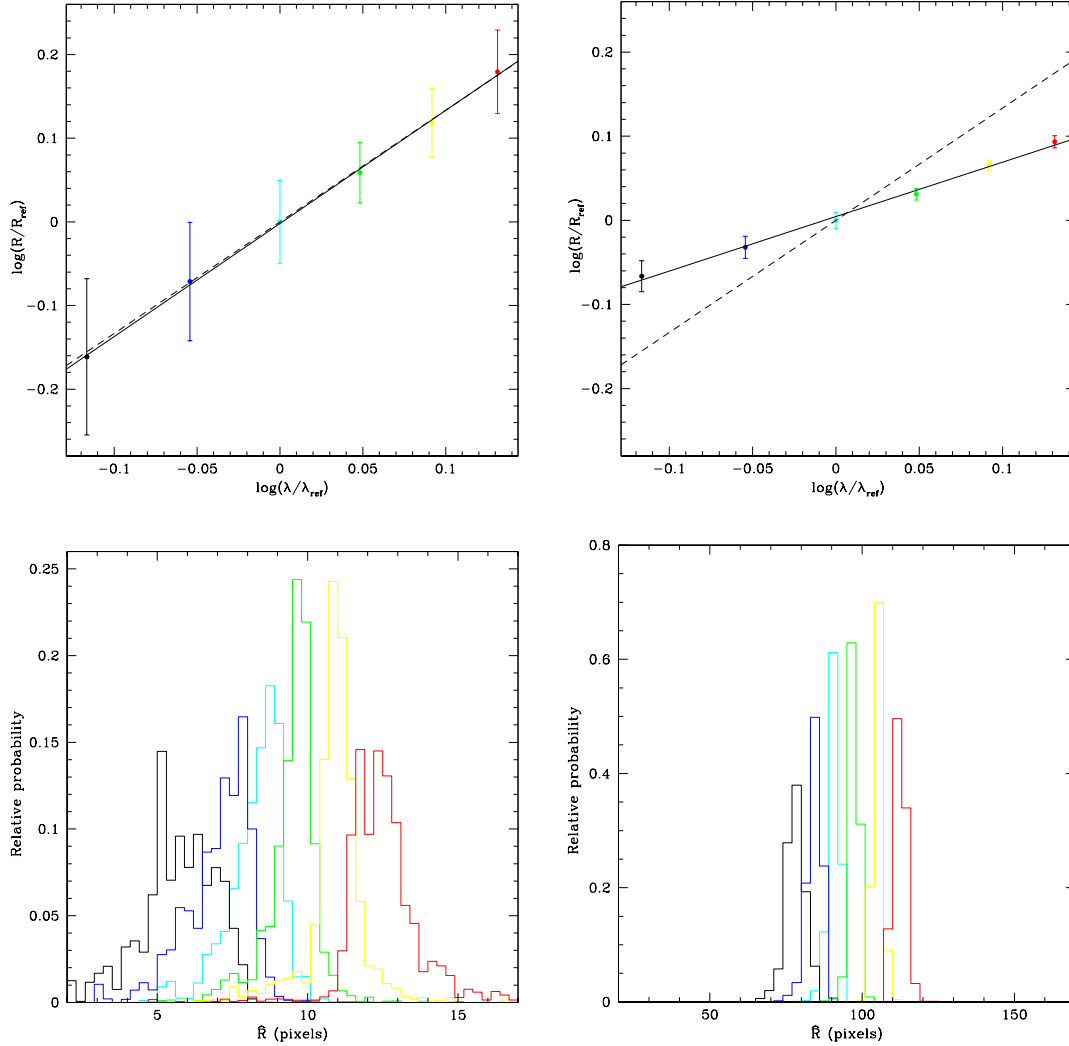


**Fig. 4.** *Top:* the source FWHM ratio  $R_i/R_{\text{ref}} = \hat{R}_i/\hat{R}_{\text{ref}}$  as a function of the wavelength ratio  $\lambda_i/\lambda_{\text{ref}}$  obtained from the trajectories in the library having  $\hat{R}_s = 0.1 r_E = 10$  pixels (*left*) and  $\hat{R}_s = 1 r_E = 100$  pixels (*right*). The reference wavelength is  $\lambda_{\text{ref}} = 2125 \text{ \AA}$  measured in the source frame. The error bars give the  $1\sigma$  uncertainties. The solid line indicates the linear regression across the points. The dashed line shows the relation expected for the standard  $R \propto \lambda^{4/3}$  scaling. *Bottom:* the corresponding probability distributions of the scaled source sizes  $\hat{R}_i$  obtained in the six bands  $i = 1, 2, \dots, 6$ , and using the same color code as in Fig. 1.

(including the prior on the velocity) is well compatible with the upper limit of  $0.98 r_E$  given by Yonehara (2001). Our result is also in good agreement with the FWHM derived by Anguita et al. (2008),  $\hat{R}_s = (0.06 \pm 0.01) r_E$ , and by Kochanek (2004),  $\hat{R}_s = (0.20^{+0.19}_{-0.12}) r_E$ . The differences between these estimates of  $\hat{R}_s$  can have two origins. First, as mentioned by Kochanek (2004), the probability distributions obtained for the parameters depend on the choice of the period of observations. If the considered period is very active in terms of microlensing, the simulations will favor high transverse velocities and/or small source sizes. Second, the choice of the velocity prior has a strong effect on the derived source size. As we observe in Fig. 3, there is a strong correlation between the scaled source size  $\hat{R}_s$  and the scaled effective transverse velocity  $\hat{V}$ . Independently of the velocity prior considered, we find that the source size is directly

proportional to the transverse velocity, with the relation  $\hat{R}_s/\hat{V} = (2.1 \pm 0.6) \times 10^{12} \text{ cm}/(\text{km s}^{-1})$ . This is in excellent agreement with Kochanek (2004), who also finds  $\hat{R}_s/\hat{V} = 2.1 \times 10^{12} \text{ cm}/(\text{km s}^{-1})$ , where  $R_s$  is expressed as the FWHM. This defines the time scale of the observed microlensing-induced fluctuations, which is given by the half-light radius divided by the effective transverse velocity, i.e.  $0.5 \hat{R}_s/\hat{V} = 4.0 \pm 1.0$  months, and which is independent of microlens masses or velocity priors.

The strong correlation between  $\hat{R}_s$  and  $\hat{V}$  (Kochanek 2004) implies that the choice of the velocity prior and the selection of the observation period can both bias our estimate of the source size. The microlensing activity during our observations was not as important as during the periods studied by Kochanek (2004) and Anguita et al. (2008). Furthermore, Anguita et al. (2008) considered a shorter observation period, and used the velocity

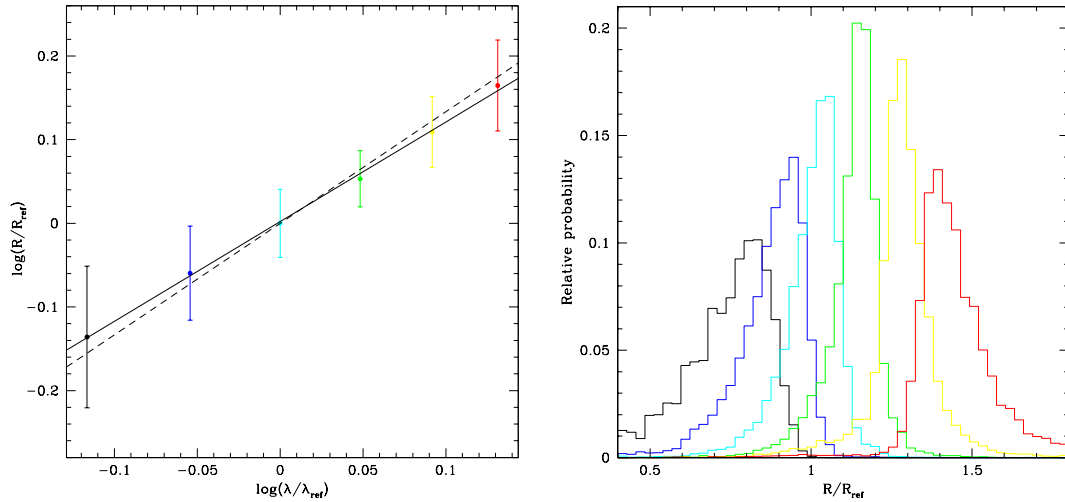


**Fig. 5.** *Left:* the final energy profile obtained from the whole ensemble of source trajectories, including the prior on the velocity. The reference wavelength is  $\lambda_{\text{ref}} = 2125 \text{ \AA}$  measured in the source frame. The error bars give the  $1\sigma$  uncertainties. The solid line indicates the linear regression across the points. The dashed line shows the relation expected for the standard  $R \propto \lambda^{4/3}$  scaling. *Right:* the corresponding probability distributions of the  $R_i$  values obtained in the six bands  $i = 1, 2, \dots, 6$ , and using the same color code as in Fig. 1.

**Table 5.** The relative size  $R_i/R_{\text{ref}}$  obtained for the six photometric bands, including the velocity prior.

Band	$\lambda_c [\text{\AA}]$	$R_i/R_{\text{ref}}$
1	1625	$0.73 \pm 0.14$
2	1875	$0.87 \pm 0.11$
3	2125	$1.00 \pm 0.09$
4	2375	$1.13 \pm 0.09$
5	2625	$1.29 \pm 0.13$
6	2875	$1.46 \pm 0.18$

prior of Gil-Merino et al. (2005), which is more constraining towards high velocities (hence favoring smaller source sizes) than the one we considered in the present study. This explains, why our derived  $\hat{R}_s$  is slightly larger. One possible solution to minimize the bias induced by the selection of the observation period is to consider the longest possible lightcurves, but this has the evident drawback of dramatically increasing the computing effort, making the problem rapidly intractable. However, as discussed in the following, the estimate of the source size has only a limited effect on our determination of the energy profile.

From our library of simulated source trajectories fitting the OGLE data, we extend our analysis to our spectroscopic data, and determine the energy profile  $R \propto \lambda^\zeta$  of the quasar accretion disk. When we consider the whole library and include the prior on the velocity, we get  $\zeta = 1.2 \pm 0.3$ , which is in good agreement with the model of Agol & Krolik (2000) and with the  $\zeta = 4/3$  index expected from the standard accretion disk model. It is less compatible (at  $1\sigma$ ) with the accretion disk model of Gaskell (2008). Our findings are also in good agreement with Anguita et al. (2008), who obtain  $(6400 \text{ \AA}/4700 \text{ \AA})^\zeta = 1.45^{+0.90}_{-0.25}$ , which yields a power-law index  $\zeta = 1.2^{+2.0}_{-0.6}$ . Without the velocity prior, we get a lower value  $\zeta = 1.1 \pm 0.3$ , which is still compatible with  $\zeta = 8/7$  and  $4/3$ , but less with the model of Gaskell (2008). This is expected because, without the prior, large sources gain relatively more importance in the Bayesian analysis, and favor flatter energy profile, as shown in Fig. 6. However, as discussed

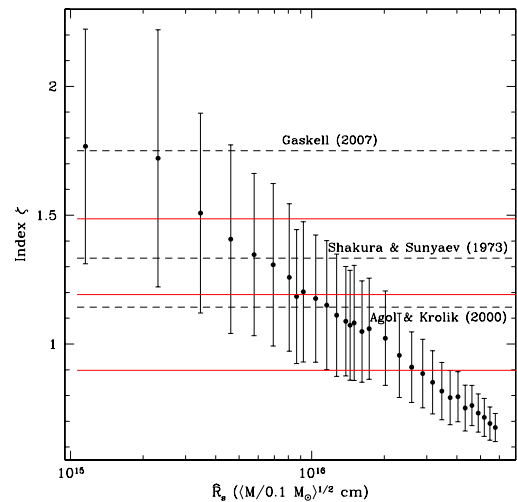


**Fig. 6.** The power-law index  $\zeta$  of the energy profile  $R \propto \lambda^\zeta$  as a function of the scaled FWHM  $\hat{R}_s$  of the source. The points are obtained from the subsamples of trajectories with given  $\hat{R}_s$  fitting the OGLE data and including the prior on the velocity. The horizontal solid red lines indicate the index  $\zeta$  and its  $1\sigma$  deviation obtained by considering the whole library of trajectories and including the velocity prior. The dashed lines show the expected indices for the three indicated accretion-disk models.

earlier, large source sizes imply unlikely high transverse velocities, and hence a much more reliable result is obtained when including the velocity prior.

We observe that our result for the  $R \propto \lambda^\zeta$  scaling is not very sensitive on the velocity prior with respect to other parameters. For instance, we know that the source size  $\hat{R}_s$  is extremely sensitive to such a prior, and can vary over orders of magnitudes if the considered transverse velocity does. On the contrary, the index  $\zeta$  varies only by a few percent, even if the considered velocities are modified by orders of magnitude. Hence, and independently of the determination of  $\hat{V}$  and  $\hat{R}_s$ , the chromatic variations



between two images of a lensed quasar are extremely efficient in constraining the relative sizes of different regions of the accretion disk. This is further confirmed by the fact that Anguita et al. (2008) obtain a value for  $\zeta$  which is in good agreement with ours, even though they derive a slightly smaller source size.

The influence of the initial value of the parameter  $\hat{R}_s$  (chosen to fit the OGLE data) on the resulting energy profile of the accretion disk is obvious in Fig. 6. Sources having sizes in the range  $0.06 \leq \hat{R}_s \leq 0.2 r_E$  are in good agreement with the  $\zeta = 8/7$  and  $4/3$  scalings, while larger sources give flatter energy profiles, and smaller sources steeper profiles. The same behavior is observed, when we omit the velocity prior.

## 9. Conclusion

We present the continuation of our spectrophotometric monitoring of QSO 2237+0305 conducted at the Very Large Telescope of the European Southern Observatory, which extends over more than three years from October 2004 to December 2007. Our program provides the spectra of the four lensed images at 43 epochs. Analysis of these data show that the continuum and the broad line region of the background quasar are microlensed, and that images A and B are particularly affected. In this paper, we focus on the observed variations in the continuum of the spectra of these two images, and use them to constrain the energy profile of the quasar.

We build microlensing magnification patterns with the inverse ray-shooting method (Wambsganss 1990; Wambsganss et al. 1990a), and convolve them with different source sizes. We trace source trajectories through these convolved patterns and fit the observed OGLE difference lightcurve between image A and image B. Combining these simulations with Bayesian analysis following the method proposed by Kochanek (2004), we infer probability distributions for the effective transverse velocity  $V$ , and the source size  $R_s$  of the quasar. Our results are compatible with previous studies.

Besides the OGLE broad-band photometry, we analyze the data of our spectroscopic monitoring and derived the corresponding difference lightcurves in six different photometric bands. Each band is 250 Å wide and together the bands cover the wavelength range between 1500 and 3000 Å (measured in the rest frame of the source). We compute the difference lightcurves between images A and B in these six bands, and observe that, as expected from the microlensing of an accretion disk, bands at bluer wavelengths exhibit stronger flux variations than bands at redder wavelengths.

Based on these chromatic variations and using the ensemble of the microlensing simulations that are fitting the OGLE data, we determine the relative sizes of the regions of the accretion disk emitting in the six photometric bands, i.e. we derive the energy profile of the accretion disk. We find that this profile follows a power-law  $R \propto \lambda^\zeta$  with  $\zeta = 1.2 \pm 0.3$ , which is in good agreement with the standard thin accretion disk model of Shakura & Sunyaev (1973) ( $\zeta = 4/3$ ) and with the model of Agol & Krolik (2000) ( $\zeta = 8/7$ ), where the disk is powered by the spin of the central black hole. Our result is less compatible with the model of Gaskell (2008), which predicts a steeper energy profile ( $\zeta = 1.75$ ). Our result compares well with that obtained by Poindexter et al. (2008) from multi-band photometry of the lensed quasar HE 1104–1805. They analyzed microlensing lightcurves in eleven bands from the optical to the mid-infrared, and found that both the size and energy profile  $\zeta = 1.64^{+0.46}_{-0.56}$  (i.e. their  $\beta^{-1}$ ) of the quasar accretion disk are

consistent with the standard disk model of Shakura & Sunyaev (1973).

We observe that the determination of the power law-index is almost independent of the velocity prior used, whereas the determination of the scaled source size  $\hat{R}_s$  is directly proportional to the scaled effective transverse velocity  $\hat{V}$ . This is easily explained by the fact that the scaling between  $R_s$  and  $\hat{R}_s$  is independent of the considered wavelength, and hence  $R_i/R_{\text{ref}} = \hat{R}_i/\hat{R}_{\text{ref}}$ . As a consequence, the determination of relative source sizes, and hence of the energy profile, is not expected to depend on the assumed microlens mass ( $M$ ).

Quasar microlensing is hence able to resolve structures of accretion disks on scales reaching 0.1 micro-arcsecond, which is more than 10 000 times better than the resolution reached by today's best telescopes. Finally, we should mention several recent studies that compare microlensing in the X-ray and optical domain, and that further demonstrate the efficiency of microlensing in probing the inner parts of quasars. For instance, Morgan et al. (2008) analyze the lightcurves of the lensed quasar PG 1115+080, and find that the effective radius of the X-ray emission is  $1.3^{+1.1}_{-0.5}$  dex smaller than that of the optical emission, with the X-ray emission generated near the inner edge of the accretion disk while the optical emission comes from scales slightly larger than those expected for a standard thin disk. Pooley et al. (2008) observe extreme microlensing-induced (de-) magnification of the lensed images of PG 1115+080, and conclude that about 90% of the matter in the lensing galaxy is in smoothly distributed (dark) material and only about 10% is in compact (stellar) objects. Another example is given by Chartas et al. (2008), who combine X-ray and optical data of HE 1104–1805, and reveal that the X-ray emitting region is compact with a half-light radius smaller than six gravitational radius, i.e. smaller than  $2 \times 10^{15}$  cm, thus placing significant constraints on active galactic nuclei models.

*Acknowledgements.* This project is partially supported by the Swiss National Science Foundation (SNSF).

## References

- Abramowicz, M. A., Czerny, B., Lasota, J. P., & Szuszkiewicz, E. 1988, *ApJ*, 332, 646
- Agol, E., & Krolik, J. H. 2000, *ApJ*, 528, 161
- Alcalde, D., Mediavilla, E., Moreau, O., et al. 2002, *ApJ*, 572, 729
- Alcock, C., Allsman, R. A., Alves, D., et al. 1997, *ApJ*, 479, 119
- Anguita, T., Schmidt, R. W., Turner, E. L., et al. 2008, *A&A*, 480, 327
- Benson, B. A., Church, S. E., Ade, P. A. R., et al. 2003, *ApJ*, 592, 674
- Chartas, G., Kochanek, C. S., Dai, X., Poindexter, S., & Garmire, G. 2008 [arXiv:0805.4492]
- Congdon, A. B., Keeton, C. R., & Osmer, S. J. 2007, *MNRAS*, 376, 263
- Corrigan, R. T., Irwin, M. J., Arnaud, J., et al. 1991, *AJ*, 102, 34
- Eigenbrod, A., Courbin, F., Sluse, D., Meylan, G., & Agol, E. 2008, *A&A*, 480, 647
- Gaskell, C. M. 2008, in *Rev. Mex. Astron. Astrofis. Conf. Ser.*, 32, 1
- Gil-Merino, R., Wambsganss, J., Goicoechea, L. J., & Lewis, G. F. 2005, *A&A*, 432, 83
- Huchra, J., Gorenstein, M., Kent, S., et al. 1985, *AJ*, 90, 691
- Kayser, R., Refsdal, S., & Stabell, R. 1986, *A&A*, 166, 36
- Kochanek, C. S. 2004, *ApJ*, 605, 58
- Kochanek, C. S., Dai, X., Morgan, C., Morgan, N., & Poindexter, S. C. G. 2007, in *Statistical Challenges in Modern Astronomy IV*, ed. G. J. Babu, & E. D. Feigelson, *ASP Conf. Ser.*, 371, 43
- Krolik, J. H. 1998a, *Active Galactic Nuclei: From the Central Black Hole to the Galactic Environment* (Princeton University Press)
- Krolik, J. H. 1998b, in *Non-linear Phenomena in Accretion Disks around Black Holes*, 134
- Kuncic, Z., & Bicknell, G. V. 2007, *Ap&SS*, 311, 127

- Kundic, T., & Wambsganss, J. 1993, *ApJ*, 404, 455
- Lewis, G. F., & Irwin, M. J. 1995, *MNRAS*, 276, 103
- Lewis, G. F., & Irwin, M. J. 1996, *MNRAS*, 283, 225
- Lynden-Bell, D. 1969, *Nature*, 223, 690
- Morgan, C. W., Kochanek, C. S., Morgan, N. D., & Falco, E. E. 2007  
[arXiv:0707.0305]
- Morgan, C. W., Kochanek, C. S., Dai, X., Morgan, N. D., & Falco, E. E. 2008  
[arXiv:0802.1210]
- Mortonson, M. J., Schechter, P. L., & Wambsganss, J. 2005, *ApJ*, 628, 594
- Mould, J. R., Akeson, R. L., Bothun, G. D., et al. 1993, *ApJ*, 409, 14
- Novikov, I. D., & Thorne, K. S. 1973, in *Black Holes (Les Astres Occlus)*, 343
- Ostensen, R., Refsdal, S., Stabell, R., et al. 1996, *A&A*, 309, 59
- Poindexter, S., Morgan, N., & Kochanek, C. S. 2008, *ApJ*, 673, 34
- Pooley, D., Blackburne, J. A., Rappaport, S., & Schechter, P. L. 2007, *ApJ*, 661, 19
- Pooley, D., Rappaport, S., Blackburne, J., et al. 2008,  
[arXiv:0808.3299]
- Pringle, J. E., & Rees, M. J. 1972, *A&A*, 21, 1
- Rauch, K. P., & Blandford, R. D. 1991, *ApJ*, 381, L39
- Rix, H.-W., Schneider, D. P., & Bahcall, J. N. 1992, *AJ*, 104, 959
- Sambridge, M. 1999, *Geophys. J. Int.*, 138, 727
- Schmidt, R. W., Kundić, T., Pen, U.-L., et al. 2002, *A&A*, 392, 773
- Schneider, D. P., Turner, E. L., Gunn, J. E., et al. 1988, *AJ*, 95, 1619
- Shakura, N. I., & Sunyaev, R. A. 1973, *A&A*, 24, 337
- Shields, G. A. 1978, *Nature*, 272, 706
- Udalski, A., Szymanski, M. K., Kubiak, M., et al. 2006, *Acta Astron.*, 56, 293
- Wambsganss, J. 1990, Ph.D. Thesis, Thesis Ludwig-Maximilians-Univ., Munich, Germany, F. R., Fakultät für Physik
- Wambsganss, J. 1992, *ApJ*, 386, 19
- Wambsganss, J., & Kundic, T. 1995, *ApJ*, 450, 19
- Wambsganss, J., & Paczyński, B. 1991, *AJ*, 102, 864
- Wambsganss, J., & Paczyński, B. 1994, *AJ*, 108, 1156
- Wambsganss, J., Paczyński, B., & Katz, N. 1990a, *ApJ*, 352, 407
- Wambsganss, J., Paczyński, B., & Schneider, P. 1990b, *ApJ*, 358, L33
- Witt, H. J., & Mao, S. 1994, *ApJ*, 429, 66
- Woźniak, P. R., Alard, C., Udalski, A., et al. 2000a, *ApJ*, 529, 88
- Woźniak, P. R., Udalski, A., Szymański, M., et al. 2000b, *ApJ*, 540, L65
- Wyithe, J. S. B., & Turner, E. L. 2001, *MNRAS*, 320, 21
- Wyithe, J. S. B., Webster, R. L., & Turner, E. L. 2000a, *MNRAS*, 318, 762
- Wyithe, J. S. B., Webster, R. L., & Turner, E. L. 2000b, *MNRAS*, 315, 51
- Wyithe, J. S. B., Agol, E., & Fluke, C. J. 2002, *MNRAS*, 331, 1041
- Yonehara, A. 2001, *ApJ*, 548, L127

A. Eigenbrod et al.: Microlensing variability in the Einstein Cross. II., *Online Material p 1***Table 6.** Continuum integrated AB magnitudes in the six photometric bands defined in Table 2.

ID	HJD	band 1 (mag)	band 2 (mag)	band 3 (mag)	band 4 (mag)	band 5 (mag)	band 6 (mag)
Image A							
1	3292	17.97 ± 0.05	17.81 ± 0.05	17.67 ± 0.05	17.54 ± 0.06	17.43 ± 0.06	17.33 ± 0.05
2	3324	18.02 ± 0.05	17.87 ± 0.04	17.73 ± 0.04	17.61 ± 0.05	17.50 ± 0.05	17.40 ± 0.04
3	3341	18.02 ± 0.06	17.85 ± 0.05	17.71 ± 0.05	17.59 ± 0.06	17.47 ± 0.06	17.37 ± 0.05
4	3355	17.98 ± 0.08	17.83 ± 0.08	17.69 ± 0.07	17.57 ± 0.08	17.47 ± 0.08	17.37 ± 0.08
5	3502	18.07 ± 0.04	17.88 ± 0.04	17.72 ± 0.04	17.57 ± 0.04	17.44 ± 0.04	17.33 ± 0.04
6	3523	18.16 ± 0.05	17.97 ± 0.05	17.80 ± 0.04	17.64 ± 0.05	17.51 ± 0.05	17.39 ± 0.04
7	3553	18.23 ± 0.04	18.03 ± 0.04	17.85 ± 0.03	17.69 ± 0.04	17.55 ± 0.04	17.42 ± 0.03
8	3566	18.16 ± 0.06	17.96 ± 0.06	17.79 ± 0.05	17.63 ± 0.06	17.49 ± 0.06	17.37 ± 0.05
9	3589	18.24 ± 0.04	18.04 ± 0.04	17.87 ± 0.03	17.71 ± 0.04	17.57 ± 0.04	17.45 ± 0.03
10	3598	18.24 ± 0.06	18.03 ± 0.06	17.84 ± 0.06	17.68 ± 0.06	17.53 ± 0.06	17.39 ± 0.06
11	3608	18.21 ± 0.03	18.02 ± 0.03	17.86 ± 0.03	17.71 ± 0.04	17.58 ± 0.04	17.47 ± 0.03
12	3626	18.21 ± 0.05	18.01 ± 0.05	17.83 ± 0.04	17.68 ± 0.05	17.54 ± 0.05	17.42 ± 0.04
13	3641	18.11 ± 0.05	17.90 ± 0.05	17.73 ± 0.05	17.57 ± 0.05	17.43 ± 0.05	17.30 ± 0.05
14	3645	18.08 ± 0.05	17.91 ± 0.05	17.77 ± 0.05	17.64 ± 0.05	17.52 ± 0.05	17.42 ± 0.05
15	3655	18.10 ± 0.04	17.92 ± 0.04	17.77 ± 0.03	17.63 ± 0.04	17.51 ± 0.04	17.39 ± 0.03
16	3665	18.10 ± 0.04	17.92 ± 0.04	17.75 ± 0.04	17.61 ± 0.04	17.48 ± 0.04	17.36 ± 0.04
17	3686	17.93 ± 0.06	17.77 ± 0.06	17.63 ± 0.06	17.50 ± 0.07	17.39 ± 0.07	17.28 ± 0.06
18	3699	17.94 ± 0.04	17.78 ± 0.04	17.64 ± 0.04	17.51 ± 0.04	17.40 ± 0.04	17.30 ± 0.04
19	3711	17.88 ± 0.07	17.71 ± 0.07	17.57 ± 0.07	17.44 ± 0.07	17.33 ± 0.07	17.22 ± 0.07
20	3880	17.58 ± 0.04	17.47 ± 0.05	17.36 ± 0.04	17.26 ± 0.05	17.17 ± 0.05	17.08 ± 0.04
21	3903	17.50 ± 0.03	17.40 ± 0.04	17.30 ± 0.04	17.20 ± 0.04	17.12 ± 0.04	17.04 ± 0.04
22	3907	17.50 ± 0.03	17.39 ± 0.03	17.28 ± 0.03	17.19 ± 0.04	17.10 ± 0.04	17.02 ± 0.03
23	3914	17.51 ± 0.02	17.41 ± 0.03	17.30 ± 0.03	17.21 ± 0.03	17.12 ± 0.03	17.04 ± 0.03
24	3944	17.53 ± 0.04	17.39 ± 0.04	17.27 ± 0.04	17.16 ± 0.04	17.07 ± 0.04	16.98 ± 0.04
25	3951	17.51 ± 0.03	17.39 ± 0.03	17.28 ± 0.03	17.18 ± 0.03	17.10 ± 0.04	17.02 ± 0.03
26	4022	17.54 ± 0.03	17.41 ± 0.04	17.29 ± 0.03	17.19 ± 0.04	17.09 ± 0.04	17.01 ± 0.03
27	4037	17.53 ± 0.03	17.40 ± 0.03	17.29 ± 0.03	17.19 ± 0.04	17.09 ± 0.04	17.01 ± 0.03
28	4050	17.44 ± 0.04	17.33 ± 0.04	17.23 ± 0.04	17.14 ± 0.04	17.06 ± 0.04	16.99 ± 0.04
29	4067	17.41 ± 0.05	17.29 ± 0.05	17.19 ± 0.05	17.09 ± 0.05	17.01 ± 0.05	16.93 ± 0.05
31	4092	17.40 ± 0.04	17.30 ± 0.05	17.20 ± 0.04	17.12 ± 0.05	17.05 ± 0.05	16.99 ± 0.04
32	4292	17.51 ± 0.03	17.36 ± 0.03	17.22 ± 0.03	17.10 ± 0.03	16.99 ± 0.03	16.89 ± 0.03
33	4297	17.49 ± 0.03	17.33 ± 0.03	17.19 ± 0.03	17.06 ± 0.03	16.95 ± 0.03	16.85 ± 0.03
34	4307	17.42 ± 0.03	17.31 ± 0.03	17.21 ± 0.03	17.12 ± 0.04	17.04 ± 0.04	16.97 ± 0.03
35	4316	17.46 ± 0.03	17.34 ± 0.03	17.23 ± 0.03	17.13 ± 0.03	17.04 ± 0.03	16.97 ± 0.03
36	4340	17.43 ± 0.04	17.29 ± 0.04	17.17 ± 0.04	17.06 ± 0.04	16.97 ± 0.04	16.88 ± 0.04
37	4350	17.44 ± 0.03	17.36 ± 0.03	17.29 ± 0.03	17.23 ± 0.03	17.18 ± 0.03	17.13 ± 0.03
38	4364	17.40 ± 0.03	17.28 ± 0.03	17.18 ± 0.03	17.09 ± 0.03	17.00 ± 0.03	16.93 ± 0.03
39	4367	17.35 ± 0.06	17.23 ± 0.06	17.11 ± 0.06	17.02 ± 0.07	16.93 ± 0.07	16.85 ± 0.06
40	4379	17.39 ± 0.02	17.26 ± 0.02	17.15 ± 0.02	17.05 ± 0.03	16.96 ± 0.03	16.87 ± 0.02
41	4384	17.41 ± 0.03	17.29 ± 0.03	17.20 ± 0.03	17.11 ± 0.04	17.03 ± 0.04	16.96 ± 0.03
42	4420	17.39 ± 0.05	17.25 ± 0.05	17.13 ± 0.05	17.02 ± 0.05	16.93 ± 0.05	16.84 ± 0.05
43	4436	17.39 ± 0.03	17.23 ± 0.04	17.09 ± 0.03	16.96 ± 0.04	16.85 ± 0.04	16.75 ± 0.03
Image B							
1	3293	19.08 ± 0.12	18.94 ± 0.12	18.82 ± 0.11	18.71 ± 0.13	18.62 ± 0.13	18.53 ± 0.11
2	3324	19.29 ± 0.10	19.11 ± 0.09	18.94 ± 0.08	18.79 ± 0.09	18.66 ± 0.09	18.54 ± 0.09
3	3341	19.18 ± 0.14	18.99 ± 0.14	18.83 ± 0.12	18.69 ± 0.14	18.57 ± 0.14	18.45 ± 0.13
4	3356	19.17 ± 0.14	19.00 ± 0.14	18.85 ± 0.13	18.72 ± 0.14	18.60 ± 0.14	18.49 ± 0.13
5	3503	18.43 ± 0.05	18.35 ± 0.05	18.28 ± 0.04	18.22 ± 0.05	18.17 ± 0.05	18.12 ± 0.05
6	3523	18.46 ± 0.06	18.36 ± 0.06	18.28 ± 0.06	18.21 ± 0.06	18.15 ± 0.06	18.09 ± 0.06
9	3589	18.76 ± 0.05	18.61 ± 0.06	18.48 ± 0.05	18.37 ± 0.06	18.26 ± 0.06	18.17 ± 0.05
11	3608	18.85 ± 0.05	18.68 ± 0.05	18.53 ± 0.05	18.40 ± 0.05	18.28 ± 0.05	18.18 ± 0.05
12	3626	18.67 ± 0.06	18.55 ± 0.06	18.44 ± 0.06	18.35 ± 0.07	18.26 ± 0.07	18.18 ± 0.06
13	3641	18.61 ± 0.06	18.48 ± 0.07	18.38 ± 0.06	18.28 ± 0.07	18.20 ± 0.07	18.12 ± 0.06
14	3645	18.62 ± 0.07	18.49 ± 0.08	18.38 ± 0.07	18.28 ± 0.08	18.19 ± 0.08	18.11 ± 0.07
15	3655	18.73 ± 0.06	18.58 ± 0.06	18.45 ± 0.06	18.34 ± 0.06	18.24 ± 0.06	18.15 ± 0.06
16	3665	18.72 ± 0.06	18.58 ± 0.06	18.46 ± 0.06	18.35 ± 0.07	18.25 ± 0.07	18.16 ± 0.06
17	3686	18.63 ± 0.10	18.50 ± 0.10	18.38 ± 0.09	18.28 ± 0.10	18.19 ± 0.10	18.10 ± 0.09
18	3699	18.66 ± 0.08	18.53 ± 0.08	18.41 ± 0.08	18.31 ± 0.09	18.22 ± 0.09	18.13 ± 0.08
19	3711	18.56 ± 0.11	18.42 ± 0.11	18.30 ± 0.10	18.20 ± 0.11	18.10 ± 0.11	18.01 ± 0.10
20	3880	18.83 ± 0.12	18.74 ± 0.13	18.59 ± 0.12	18.47 ± 0.14	18.35 ± 0.14	18.25 ± 0.12
21	3903	18.89 ± 0.07	18.77 ± 0.07	18.60 ± 0.07	18.45 ± 0.08	18.31 ± 0.08	18.19 ± 0.07
22	3907	18.83 ± 0.06	18.71 ± 0.07	18.53 ± 0.07	18.38 ± 0.07	18.25 ± 0.07	18.12 ± 0.07
23	3914	18.86 ± 0.05	18.74 ± 0.06	18.57 ± 0.05	18.42 ± 0.06	18.29 ± 0.06	18.17 ± 0.05
24	3944	18.76 ± 0.07	18.60 ± 0.07	18.47 ± 0.06	18.35 ± 0.07	18.24 ± 0.07	18.15 ± 0.06
25	3951	18.72 ± 0.06	18.56 ± 0.06	18.43 ± 0.06	18.31 ± 0.06	18.20 ± 0.06	18.10 ± 0.06



Table 6. continued.

ID	HJD	band 1 (mag)	band 2 (mag)	band 3 (mag)	band 4 (mag)	band 5 (mag)	band 6 (mag)
26	4022	18.76 ± 0.06	18.61 ± 0.06	18.48 ± 0.05	18.36 ± 0.06	18.25 ± 0.06	18.15 ± 0.05
27	4037	18.69 ± 0.05	18.54 ± 0.05	18.41 ± 0.05	18.29 ± 0.05	18.19 ± 0.05	18.09 ± 0.05
28	4050	18.63 ± 0.09	18.49 ± 0.09	18.36 ± 0.08	18.25 ± 0.09	18.15 ± 0.09	18.06 ± 0.08
29	4067	18.59 ± 0.12	18.46 ± 0.12	18.34 ± 0.12	18.23 ± 0.12	18.13 ± 0.12	18.05 ± 0.12
30	4089	18.57 ± 0.14	18.45 ± 0.14	18.34 ± 0.13	18.25 ± 0.14	18.16 ± 0.14	18.08 ± 0.13
31	4093	18.60 ± 0.10	18.46 ± 0.10	18.34 ± 0.09	18.23 ± 0.10	18.13 ± 0.10	18.05 ± 0.09
32	4292	18.66 ± 0.06	18.49 ± 0.07	18.34 ± 0.06	18.21 ± 0.07	18.09 ± 0.06	17.98 ± 0.06
33	4297	18.66 ± 0.07	18.49 ± 0.07	18.35 ± 0.06	18.22 ± 0.07	18.11 ± 0.07	18.00 ± 0.06
34	4307	18.54 ± 0.09	18.40 ± 0.09	18.28 ± 0.08	18.17 ± 0.09	18.08 ± 0.09	17.99 ± 0.08
35	4316	18.66 ± 0.08	18.50 ± 0.09	18.36 ± 0.08	18.24 ± 0.09	18.12 ± 0.09	18.02 ± 0.08
36	4340	18.69 ± 0.13	18.51 ± 0.13	18.35 ± 0.12	18.20 ± 0.13	18.07 ± 0.13	17.96 ± 0.12
37	4350	18.59 ± 0.08	18.46 ± 0.08	18.34 ± 0.08	18.23 ± 0.08	18.14 ± 0.08	18.05 ± 0.08
38	4364	18.60 ± 0.09	18.44 ± 0.09	18.31 ± 0.09	18.20 ± 0.10	18.09 ± 0.09	18.00 ± 0.09
39	4367	18.59 ± 0.16	18.46 ± 0.17	18.34 ± 0.15	18.24 ± 0.17	18.15 ± 0.17	18.07 ± 0.16
40	4379	18.62 ± 0.05	18.45 ± 0.06	18.30 ± 0.05	18.17 ± 0.06	18.05 ± 0.06	17.94 ± 0.05
41	4384	18.68 ± 0.06	18.51 ± 0.07	18.36 ± 0.06	18.24 ± 0.07	18.12 ± 0.07	18.01 ± 0.06
42	4421	18.72 ± 0.09	18.54 ± 0.09	18.39 ± 0.08	18.25 ± 0.09	18.13 ± 0.09	18.02 ± 0.08
43	4436	18.60 ± 0.07	18.43 ± 0.07	18.28 ± 0.06	18.14 ± 0.07	18.02 ± 0.07	17.91 ± 0.06
Image C							
1	3293	19.08 ± 0.11	18.92 ± 0.12	18.78 ± 0.11	18.65 ± 0.13	18.54 ± 0.13	18.44 ± 0.11
2	3324	19.32 ± 0.09	19.09 ± 0.08	18.90 ± 0.08	18.73 ± 0.09	18.57 ± 0.09	18.43 ± 0.08
3	3341	19.22 ± 0.14	19.01 ± 0.14	18.82 ± 0.13	18.65 ± 0.14	18.50 ± 0.14	18.37 ± 0.12
4	3356	19.44 ± 0.16	19.22 ± 0.16	19.02 ± 0.16	18.85 ± 0.18	18.69 ± 0.18	18.55 ± 0.15
5	3503	19.28 ± 0.08	19.09 ± 0.08	18.93 ± 0.08	18.79 ± 0.09	18.66 ± 0.08	18.54 ± 0.08
6	3523	19.29 ± 0.10	19.09 ± 0.10	18.91 ± 0.10	18.76 ± 0.11	18.62 ± 0.10	18.50 ± 0.09
9	3589	19.46 ± 0.09	19.23 ± 0.09	19.02 ± 0.08	18.83 ± 0.09	18.67 ± 0.09	18.52 ± 0.08
11	3608	19.59 ± 0.09	19.32 ± 0.09	19.10 ± 0.08	18.89 ± 0.09	18.71 ± 0.08	18.54 ± 0.08
12	3626	19.38 ± 0.10	19.17 ± 0.11	18.99 ± 0.10	18.83 ± 0.11	18.68 ± 0.11	18.55 ± 0.10
13	3641	19.21 ± 0.10	19.02 ± 0.10	18.85 ± 0.10	18.70 ± 0.11	18.56 ± 0.10	18.44 ± 0.09
14	3645	19.25 ± 0.12	19.04 ± 0.12	18.86 ± 0.12	18.70 ± 0.13	18.56 ± 0.13	18.43 ± 0.11
15	3655	19.44 ± 0.09	19.20 ± 0.10	19.00 ± 0.09	18.82 ± 0.10	18.65 ± 0.10	18.50 ± 0.09
16	3665	19.41 ± 0.10	19.19 ± 0.10	18.99 ± 0.09	18.81 ± 0.10	18.66 ± 0.10	18.51 ± 0.09
17	3686	19.19 ± 0.15	18.98 ± 0.15	18.80 ± 0.14	18.63 ± 0.15	18.48 ± 0.15	18.35 ± 0.13
18	3699	19.24 ± 0.12	19.03 ± 0.12	18.84 ± 0.11	18.68 ± 0.12	18.53 ± 0.12	18.40 ± 0.11
19	3711	18.94 ± 0.14	18.74 ± 0.14	18.57 ± 0.14	18.42 ± 0.15	18.28 ± 0.15	18.16 ± 0.13
20	3880	18.86 ± 0.18	18.76 ± 0.20	18.61 ± 0.20	18.47 ± 0.22	18.35 ± 0.21	18.24 ± 0.19
21	3903	19.19 ± 0.12	19.05 ± 0.14	18.84 ± 0.13	18.67 ± 0.14	18.51 ± 0.14	18.36 ± 0.13
22	3907	19.12 ± 0.13	18.98 ± 0.14	18.77 ± 0.14	18.59 ± 0.15	18.43 ± 0.15	18.29 ± 0.13
23	3914	19.15 ± 0.10	19.01 ± 0.12	18.81 ± 0.11	18.63 ± 0.12	18.47 ± 0.12	18.32 ± 0.11
24	3944	19.01 ± 0.08	18.83 ± 0.09	18.67 ± 0.08	18.52 ± 0.09	18.39 ± 0.09	18.28 ± 0.08
25	3951	18.99 ± 0.07	18.80 ± 0.08	18.64 ± 0.07	18.50 ± 0.08	18.37 ± 0.07	18.25 ± 0.07
26	4022	19.14 ± 0.11	18.94 ± 0.12	18.76 ± 0.11	18.61 ± 0.12	18.46 ± 0.12	18.34 ± 0.10
27	4037	19.07 ± 0.11	18.87 ± 0.11	18.70 ± 0.10	18.55 ± 0.11	18.41 ± 0.11	18.29 ± 0.10
28	4050	18.83 ± 0.11	18.65 ± 0.11	18.50 ± 0.11	18.36 ± 0.12	18.24 ± 0.11	18.12 ± 0.11
29	4067	18.78 ± 0.19	18.61 ± 0.20	18.47 ± 0.19	18.34 ± 0.20	18.22 ± 0.20	18.11 ± 0.19
30	4089	18.80 ± 0.21	18.62 ± 0.23	18.47 ± 0.22	18.33 ± 0.23	18.21 ± 0.23	18.10 ± 0.20
31	4093	18.92 ± 0.20	18.72 ± 0.20	18.55 ± 0.19	18.40 ± 0.21	18.27 ± 0.20	18.15 ± 0.18
32	4292	18.75 ± 0.06	18.57 ± 0.06	18.42 ± 0.06	18.28 ± 0.06	18.16 ± 0.06	18.05 ± 0.06
33	4297	18.73 ± 0.06	18.57 ± 0.07	18.42 ± 0.06	18.29 ± 0.07	18.18 ± 0.07	18.07 ± 0.06
34	4307	18.57 ± 0.08	18.43 ± 0.09	18.31 ± 0.08	18.20 ± 0.09	18.11 ± 0.09	18.02 ± 0.08
35	4316	18.71 ± 0.08	18.55 ± 0.09	18.42 ± 0.08	18.29 ± 0.09	18.18 ± 0.09	18.08 ± 0.08
36	4340	18.79 ± 0.12	18.59 ± 0.13	18.42 ± 0.12	18.26 ± 0.13	18.12 ± 0.13	17.99 ± 0.12
37	4350	18.79 ± 0.09	18.63 ± 0.09	18.50 ± 0.08	18.38 ± 0.09	18.27 ± 0.09	18.18 ± 0.08
38	4364	18.80 ± 0.09	18.62 ± 0.10	18.46 ± 0.09	18.32 ± 0.10	18.19 ± 0.10	18.08 ± 0.09
39	4367	18.50 ± 0.14	18.37 ± 0.15	18.26 ± 0.14	18.17 ± 0.16	18.08 ± 0.16	18.00 ± 0.14
40	4379	18.98 ± 0.07	18.77 ± 0.08	18.58 ± 0.07	18.41 ± 0.08	18.26 ± 0.07	18.12 ± 0.07
41	4384	19.03 ± 0.09	18.82 ± 0.10	18.64 ± 0.09	18.48 ± 0.10	18.34 ± 0.10	18.21 ± 0.09
42	4421	19.18 ± 0.13	18.94 ± 0.13	18.74 ± 0.12	18.55 ± 0.14	18.39 ± 0.13	18.24 ± 0.12
43	4436	19.06 ± 0.09	18.83 ± 0.10	18.63 ± 0.10	18.45 ± 0.10	18.29 ± 0.10	18.14 ± 0.09

A. Eigenbrod et al.: Microlensing variability in the Einstein Cross. II., *Online Material p 3*

Table 6. continued.

ID	HJD	band 1 (mag)	band 2 (mag)	band 3 (mag)	band 4 (mag)	band 5 (mag)	band 6 (mag)
Image D							
1	3292	19.11 ± 0.14	18.91 ± 0.14	18.73 ± 0.14	18.57 ± 0.15	18.42 ± 0.15	18.29 ± 0.13
2	3324	19.23 ± 0.12	19.03 ± 0.12	18.86 ± 0.12	18.71 ± 0.13	18.58 ± 0.13	18.45 ± 0.12
3	3341	19.18 ± 0.14	18.98 ± 0.14	18.79 ± 0.14	18.63 ± 0.15	18.49 ± 0.15	18.36 ± 0.13
4	3355	19.04 ± 0.18	18.84 ± 0.19	18.67 ± 0.18	18.51 ± 0.21	18.38 ± 0.20	18.25 ± 0.18
5	3502	19.25 ± 0.11	19.02 ± 0.11	18.81 ± 0.10	18.63 ± 0.11	18.47 ± 0.11	18.32 ± 0.10
6	3523	19.29 ± 0.11	19.08 ± 0.11	18.89 ± 0.11	18.73 ± 0.12	18.58 ± 0.12	18.45 ± 0.11
7	3553	19.42 ± 0.10	19.20 ± 0.10	19.01 ± 0.09	18.84 ± 0.11	18.68 ± 0.10	18.55 ± 0.09
8	3566	19.26 ± 0.14	19.01 ± 0.14	18.80 ± 0.13	18.61 ± 0.15	18.44 ± 0.14	18.28 ± 0.13
9	3589	19.44 ± 0.09	19.23 ± 0.09	19.04 ± 0.09	18.87 ± 0.10	18.73 ± 0.10	18.59 ± 0.09
10	3598	19.35 ± 0.15	19.10 ± 0.15	18.87 ± 0.14	18.68 ± 0.15	18.50 ± 0.15	18.34 ± 0.13
11	3608	19.43 ± 0.09	19.22 ± 0.09	19.05 ± 0.08	18.89 ± 0.10	18.75 ± 0.10	18.62 ± 0.09
12	3626	19.43 ± 0.12	19.20 ± 0.12	18.99 ± 0.11	18.81 ± 0.12	18.65 ± 0.12	18.50 ± 0.11
13	3641	19.27 ± 0.12	19.02 ± 0.12	18.79 ± 0.11	18.60 ± 0.13	18.42 ± 0.13	18.26 ± 0.11
14	3645	19.26 ± 0.12	19.03 ± 0.12	18.83 ± 0.11	18.65 ± 0.13	18.50 ± 0.13	18.35 ± 0.11
15	3655	19.33 ± 0.10	19.13 ± 0.10	18.96 ± 0.09	18.81 ± 0.11	18.67 ± 0.11	18.54 ± 0.10
16	3665	19.33 ± 0.11	19.10 ± 0.11	18.91 ± 0.10	18.73 ± 0.12	18.58 ± 0.11	18.43 ± 0.10
17	3686	19.03 ± 0.15	18.82 ± 0.15	18.64 ± 0.15	18.48 ± 0.16	18.33 ± 0.16	18.20 ± 0.14
18	3699	19.14 ± 0.11	18.94 ± 0.11	18.76 ± 0.11	18.60 ± 0.12	18.46 ± 0.12	18.33 ± 0.10
19	3711	18.95 ± 0.17	18.75 ± 0.18	18.58 ± 0.17	18.42 ± 0.19	18.28 ± 0.18	18.16 ± 0.16
20	3880	19.00 ± 0.11	18.83 ± 0.13	18.66 ± 0.12	18.51 ± 0.14	18.37 ± 0.13	18.25 ± 0.12
21	3903	19.08 ± 0.10	18.93 ± 0.12	18.77 ± 0.11	18.63 ± 0.13	18.50 ± 0.13	18.39 ± 0.11
22	3907	19.07 ± 0.08	18.92 ± 0.09	18.75 ± 0.09	18.61 ± 0.10	18.48 ± 0.10	18.36 ± 0.09
23	3914	19.13 ± 0.07	18.98 ± 0.08	18.83 ± 0.07	18.70 ± 0.08	18.58 ± 0.08	18.47 ± 0.08
24	3944	19.08 ± 0.12	18.87 ± 0.12	18.69 ± 0.12	18.52 ± 0.13	18.38 ± 0.13	18.24 ± 0.11
25	3951	19.04 ± 0.11	18.85 ± 0.10	18.68 ± 0.10	18.53 ± 0.11	18.40 ± 0.11	18.28 ± 0.10
26	4022	19.06 ± 0.07	18.88 ± 0.08	18.72 ± 0.07	18.58 ± 0.08	18.46 ± 0.08	18.34 ± 0.07
27	4037	19.03 ± 0.07	18.85 ± 0.07	18.70 ± 0.07	18.56 ± 0.08	18.44 ± 0.08	18.32 ± 0.07
28	4050	18.93 ± 0.12	18.75 ± 0.12	18.59 ± 0.12	18.45 ± 0.13	18.32 ± 0.13	18.20 ± 0.12
29	4067	18.84 ± 0.11	18.65 ± 0.11	18.49 ± 0.10	18.35 ± 0.12	18.22 ± 0.12	18.11 ± 0.10
31	4092	18.87 ± 0.09	18.70 ± 0.09	18.55 ± 0.09	18.42 ± 0.10	18.30 ± 0.10	18.19 ± 0.09
32	4292	19.00 ± 0.09	18.78 ± 0.09	18.58 ± 0.09	18.41 ± 0.10	18.25 ± 0.09	18.11 ± 0.08
33	4297	18.95 ± 0.08	18.73 ± 0.08	18.53 ± 0.08	18.36 ± 0.09	18.21 ± 0.08	18.07 ± 0.08
34	4307	18.81 ± 0.11	18.63 ± 0.12	18.48 ± 0.12	18.34 ± 0.13	18.22 ± 0.13	18.11 ± 0.11
35	4316	18.85 ± 0.11	18.69 ± 0.12	18.54 ± 0.11	18.41 ± 0.12	18.30 ± 0.12	18.20 ± 0.11
36	4340	18.73 ± 0.13	18.55 ± 0.13	18.39 ± 0.13	18.24 ± 0.14	18.12 ± 0.14	18.00 ± 0.12
37	4350	18.86 ± 0.11	18.75 ± 0.12	18.65 ± 0.12	18.57 ± 0.14	18.50 ± 0.14	18.43 ± 0.12
38	4364	18.76 ± 0.10	18.59 ± 0.11	18.44 ± 0.10	18.31 ± 0.11	18.19 ± 0.11	18.09 ± 0.10
39	4367	18.59 ± 0.18	18.41 ± 0.19	18.26 ± 0.18	18.12 ± 0.20	17.99 ± 0.20	17.88 ± 0.18
40	4379	18.70 ± 0.07	18.52 ± 0.08	18.36 ± 0.08	18.22 ± 0.08	18.09 ± 0.08	17.97 ± 0.07
41	4384	18.74 ± 0.09	18.57 ± 0.10	18.42 ± 0.10	18.29 ± 0.11	18.18 ± 0.11	18.07 ± 0.09
42	4420	18.61 ± 0.12	18.43 ± 0.13	18.27 ± 0.13	18.13 ± 0.14	18.01 ± 0.14	17.89 ± 0.13
43	4436	18.59 ± 0.09	18.39 ± 0.10	18.21 ± 0.09	18.05 ± 0.10	17.91 ± 0.10	17.78 ± 0.09

*“Never confuse movement with action.”  
Ernest Hemingway (1899 - 1961)*

## Chapter 8

# Dynamics versus gravitational lensing

## 8.1 Introduction

In spite of the many successes of the  $\Lambda$ CDM cosmology on large scales, there are some fundamental difficulties on small, galactic scales. One such difficulty is the so-called cusp/core problem related to the distribution and quantity of dark matter in galaxies. A central assumption of the current  $\Lambda$ CDM cosmological model is that galaxies form and evolve inside extended dark matter halos (e.g., White & Rees, 1978; Davis et al., 1985). These halos are possibly universal in their density profile with steep inner density profiles forming a central cusp (e.g., Navarro et al., 1997; Merritt et al., 2005).

Extended dark matter halos have been detected observationally using various techniques, predominantly through dynamical tracers in spiral galaxies (e.g., van Albada et al., 1985), early-type galaxies (e.g., Loewenstein & White, 1999; Gerhard et al., 2001), and clusters of galaxies (e.g., Zwicky, 1937b), but also through other techniques such as combined weak and strong gravitational lensing (e.g., Kneib et al., 2003). All these studies lead to the conclusion that dark matter halos are extended and have steep and divergent (i.e. cuspy) inner density profiles (with  $\rho \propto r^{-1}$  or steeper). Large dark matter cores and very low dark matter central densities, seem to be excluded.

However, there are several studies that reach the opposite conclusion. For instance, rotation curves of dark matter dominated low surface brightness (LSB) galaxies (e.g., Moore, 1994; van den Bosch et al., 2000) and several results from strong lensing indicate that galactic dark matter halos have a density profile with a flat central core rather than a cusp. In particular, studies of lensed quasars (e.g., Impey et al., 1998; Kochanek, 2002, 2003b) have shown that the determination of the Hubble constant  $H_0$  from the time-delay method (Refsdal, 1964a) is strongly dependent on the mass profile of the lens. Isothermal mass profiles typically predict low values of  $H_0 \simeq 50 \text{ km s}^{-1} \text{ Mpc}^{-1}$ , whereas models with constant mass-to-light ratios, e.g., de Vaucouleurs profiles, predict values  $H_0 \simeq 70 \text{ km s}^{-1} \text{ Mpc}^{-1}$  comparable with the result of the HST Key Project. This leads to the conclusion that, if the  $H_0$  value of the Key Project is correct, then lensing galaxies have preferentially mass profiles with constant mass-to-light ratios, without central cusps.

Given these contradictory results, further studies are necessary. One approach is to compare the mass distribution inferred from gravitational lensing with that inferred from stellar dynamics. The combination of these two independent techniques can better constrain the dark matter distribution in galaxies, and will show how well the commonly used parametric lens models can reconstruct the gravitational potential of a lensing galaxy.

Treu & Koopmans (2004) and Koopmans et al. (2006) applied this approach to a sample of early-type lensing galaxies. From the study of these lenses, they concluded that a significant amount of dark matter is present in the inner parts of these galaxies, with a slope of the total density profile close to that of an isothermal mass distribution. However, their results are limited by the use of simple spherical dynamical models. Indeed, most galaxies are significantly flattened and are not accurately described by spherical models. Non-spherical models provide a more realistic description of galaxies, but require significantly more spatially resolved kinematic measurements. Unfortunately, not every lens is close or bright enough to obtain such kinematic data. Barnabè & Koopmans (2007) developed more complex models assuming axisymmetric potentials. Czoske et al. (2008) successfully applied these models to the two-dimensional kinematic data of the early-type lensing galaxy in SDSS J2321–097 and found that this galaxy has a total density profile well described by a power law very close to an isothermal density distribution. They also found that the lens has a dark matter contribution of  $\sim 30\%$  inside the effective radius.

The studies cited above focused on elliptical galaxies, which is not surprising as most strong lenses are elliptical galaxies (e.g., Turner et al., 1984; Fukugita & Turner, 1991). Dynamical studies of spiral lensing galaxies are less common. Maller et al. (2000) were the first to consider dynamical models for a spiral lensing galaxy. They showed how gravitational lensing can be used to break the disk/halo degeneracy in spiral galaxies, and applied their method to the spiral lens in B 1600+434. A similar study was done by Trott & Webster (2002) for the spiral galaxy in QSO 2237+0305. They found that the dark matter halo, modeled as a softened isothermal sphere, has a large core radius ( $13.4 \pm 0.4$  kpc), but their solution is not unique and their model requires further information on the kinematics of the lens. Recently, van de Ven et al. (2008) acquired integral-field spectroscopy of the inner 2 kpc of the lens in QSO 2237+0305. They found that the luminous and total mass distribution are nearly identical around the Einstein angle  $\theta_E \simeq 0.89''$  with a slope that is close to isothermal. They also state that it is likely that dark matter does not play a significant role in the inner region of this early-type spiral galaxy. However, one limitation of their work is that they derive the density of the lensing galaxy from the observed surface brightness assuming a constant mass-to-light ratio. Hence, they do not consider the potential mass contributions of an extended dark matter halo. Furthermore, their kinematic data only extends to the inner  $\sim 2$  kpc. Their dynamical models are therefore principally sensitive to the mass located in the bulge, whereas gravitational lensing is sensitive to all the “projected” mass located within the quasar images including the contribution from the halo.

In this chapter, we present additional spectroscopic data of the lensing galaxy of the Einstein Cross. Our observations were acquired with the Very Large Telescope (VLT) of the European Southern Observatory (ESO) using three different instruments: SINFONI to study the inner kiloparsec of the lensing galaxy, FLAMES for the regions up to 4 kpc, and FORS2 for the most extended parts of the disk reaching 30 kpc, corresponding to about  $40''$  at  $z_l = 0.039$  (see Fig. 8.1). Our project was conducted under the programs 076.B-0607 and 381.A-0120 for a total observing time of 20 hours.

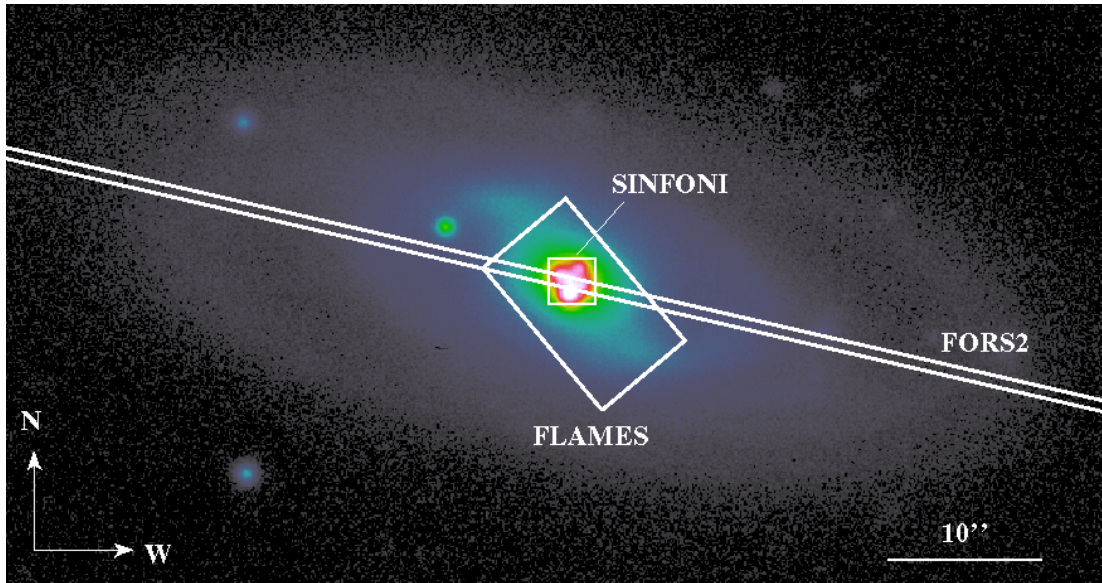


Figure 8.1: The fields of view of the three different instruments used to measure the kinematics of QSO 2237+0305. The underlying R-band image is a combination of ten individual exposures acquired with FORS1 of the ESO-VLT during the pre-imaging of our spectroscopic monitoring program. The total exposition time is 440 s.

## 8.2 Integral-field spectroscopy with FLAMES

### 8.2.1 Observations and data reduction

We started our observations in October 2005 and acquired integral-field spectroscopy of the lensing galaxy of QSO 2237+0305 with the spectrograph FLAMES/GIRAFFE (Pasquini et al., 2002) of the ESO-VLT. The journal of the observations is given in Table 8.1. The observations were acquired in the ARGUS mode. The ARGUS integral field unit consists of a rectangular array of  $14 \times 22$  microlenses, which provides a sampling of  $0.52''/\text{microlens}$  and a total aperture of  $7'' \times 12''$  with the low resolution grating. The field unit was rotated to a position angle of 40 deg (counted counterclockwise from North to East) in order to be well aligned with the bar of the lensing galaxy. We use the low-resolution setup LR4, which covers the wavelength range  $5020 - 5830 \text{ \AA}$  and gives a spectral resolution of  $R = \lambda/\Delta\lambda \simeq 9600$  at the central wavelength of  $5400 \text{ \AA}$ .

The data are reduced using the GIRAFFE Base-Line Data Reduction Software<sup>1</sup>. This software goes through all the standard reduction steps. The raw data are bias subtracted, flat fielded, and bad pixels are removed. The spectral lines of the five simultaneous thorium-argon lamp calibration fibers are used to adjust the localizations of the spectra, which are previously guessed from the flat fields. Additional thorium-argon lamp exposures provide the wavelength calibration. The spectra are free from strong OH emission lines and there is no significant atmospheric absorption in the region of interest, i.e. at the wavelengths of the Mg I and Fe II absorption lines in the lens frame. The spectra of each microlens are extracted and assembled to generate a data cube containing all the spectral

<sup>1</sup><http://girbldrs.sourceforge.net>

Table 8.1: Journal of the FLAMES observations. Each exposures is 2280 s long.

ID	Date	Seeing ["]	Airmass
1	07/10/2005	0.45	1.347
2	07/10/2005	0.39	1.226
3	07/10/2005	0.50	1.159
4	07/10/2005	0.67	1.372
5	08/10/2005	0.68	1.243
6	09/10/2005	0.86	1.299
7	09/10/2005	1.03	1.201

and two-dimensional spatial information. In total, seven exposures are obtained, hence providing seven data cubes. To combine the cubes, we compute the light centroid in each spatial plane contained in a cube (i.e. at each wavelength) and align them spatially. The combination of all aligned cubes leads to a total integration time of 15960 s = 4.4 hours.

In addition to these data, integral-field spectroscopy of the K0-III star HD 19640 has been acquired using the same instrumental setup. The spectrum of this giant star reproduces well the spectrum of an early-type galaxy, and can hence be used as a template for the cross-correlation of the spectra of the lensing galaxy.

## 8.2.2 Data analysis and results

We use the spectra of the K0-III star HD 19640 as a template to determine the radial velocity and line-of-sight velocity dispersion fields in the lensing galaxy of QSO 2237+0305. Our procedure follows the method described by Falco et al. (1997) and is based on the Fourier cross-correlation method (Tonry & Davis, 1979), as implemented in the IRAF<sup>2</sup> command `fxcor`. In the following, we describe how we apply this procedure to the galaxy spectrum obtained from one microlens of the spectrograph. We repeat this procedure with the spectra obtained from the other microlenses and hence, determine the velocity and velocity dispersion fields over the field of view of the spectrograph.

Our procedure starts by subtracting a continuum from both the object and template spectrum by fitting a cubic spline of order 12 with ten iterations to reject points with residuals higher than  $2\sigma$  and lower than  $-2\sigma$  from the fit, where  $\sigma$  is the rms dispersion of each fit. We restrict the region of the spectra to be used for the cross-correlation to the main absorption lines in order to avoid contributions from the QSO spectrum and sky emission. In the FLAMES spectra the main absorption features are the Mg I absorption triplet at 5175 Å in the rest frame and the Fe I absorption at 5270 Å. The selected wavelength range is indicated in Fig. 8.2.

Both the stellar template and galaxy spectra have been acquired with the same instrumental setup. This guarantees that both spectra have the same spectral resolution and that no rebinning is necessary at this stage. It is also important that the velocity resolutions of the galaxy and the template match. Fortunately, the lensing galaxy has a low redshift, and both resolutions are compatible. Otherwise, we would have convolved the

<sup>2</sup>IRAF is distributed by the National Optical Astronomy Observatories, which are operated by the Association of Universities for Research in Astronomy, Inc., under cooperative agreement with the National Science Foundation.

template spectrum with a Gaussian-broadening function to match the velocity resolution of the galaxy.

Given the spectrum  $f(x)$  of the lensing galaxy and  $t(x)$  of the template, `fxcor` computes the cross-correlation function  $g(x)$ , which translates to a simple multiplication in Fourier space

$$g(x) = (f \star t)(x) \doteq \int_{-\infty}^{\infty} f^*(\xi) t(x + \xi) d\xi \quad \Rightarrow \quad \mathcal{G}(k) = \mathcal{F}^*(k) \mathcal{T}(k)$$

where  $*$  denotes complex conjugation,  $k$  is the wavenumber, and  $\mathcal{G}$ ,  $\mathcal{F}$ , and  $\mathcal{T}$  are the Fourier transforms of  $g$ ,  $f$ , and  $t$ , respectively. The command `fxcor` locates the cross-correlation peak and fits a Gaussian function to it after background subtraction. The velocity shift between the galaxy and the template is inferred from the location of the peak of the Gaussian fit. Prior to the Fourier transformation, we apodize the spectra by 5% at each end with a cosine bell to minimize spectral aliasing effects. In addition, the lowest wave number portion of the Fourier-transformed spectra ( $\leq 160 \text{ \AA}^{-1}$ ) are filtered out with a Hanning filter in order to remove any remaining low-frequency background.

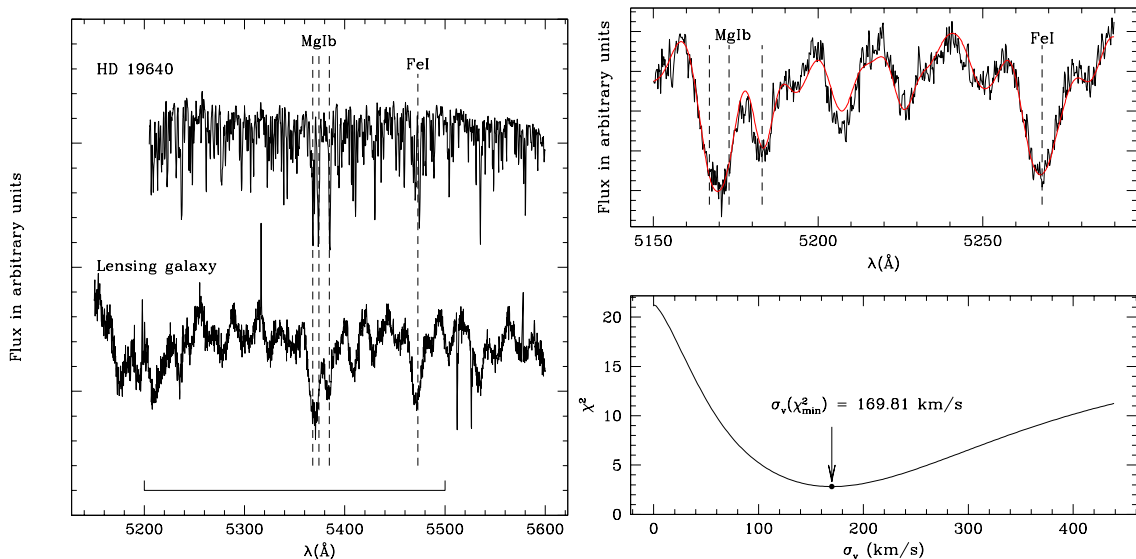


Figure 8.2: *Left*: Normalized and continuum subtracted spectra of the lensing galaxy of QSO 2237+0305 and of the star HD 19400 obtained from one FLAMES microlens. The spectrum of the star has been shifted to the redshift of the lensing galaxy. The major absorption lines are indicated. The interval marked at the bottom of the plot shows the wavelength range used for the cross-correlation. *Top right*: Fit of a convolved version of the spectrum of HD 19400 (red curve) to the spectrum of the lensing galaxy (black curve). *Bottom right*: Determination of the velocity dispersion that best matches the spectrum of the lensing galaxy.

Once the velocity shift between the stellar template and the galaxy spectrum is determined, we can determine the velocity dispersion of the galaxy. To do so, we first resample the normalized and continuum subtracted galaxy and stellar template spectra using the IRAF task `dispcor` to obtain a linear sampling of the spectra in velocity space, which

corresponds to a logarithmic sampling in wavelength. Indeed, a shift  $dv$  in velocity corresponds to a shift  $d\lambda$  in wavelength with  $dv/c = d\lambda/\lambda = d\ln(\lambda)$ . Based on the measured radial velocity, we shift the resampled galaxy spectrum to the rest-frame.

We convolve the resampled template spectrum with a series of Gaussians with increasing width  $\sigma_v$  from 0 to 400 km/s. We fit these broadened spectra to the rest-frame galaxy spectrum. For each value of  $\sigma_v$  we compute the  $\chi^2(\sigma_v)$  value between the galaxy spectrum and the broadened template spectrum. The velocity dispersion of the galaxy spectrum is then determined from the minimum of the  $\chi^2(\sigma_v)$ , see Fig. 8.2.

We apply this procedure to every galaxy spectrum obtained with the microlenses of FLAMES and obtain the velocity and velocity dispersion fields shown in Fig. 8.3. The velocity field clearly shows the rotation of the lensing galaxy, which reaches 180 km/s at about 4 kpc. The rotation is well aligned with the major axis of the galaxy at PA = 77 deg. The determination of the velocity dispersions are more difficult, especially in the regions far away from the lens center, where the spectra have lower signal-to-noise ratios. Reliable values are only obtained for the central microlenses. We obtain a relatively flat velocity dispersion field with values of  $175 \pm 30$  km/s.

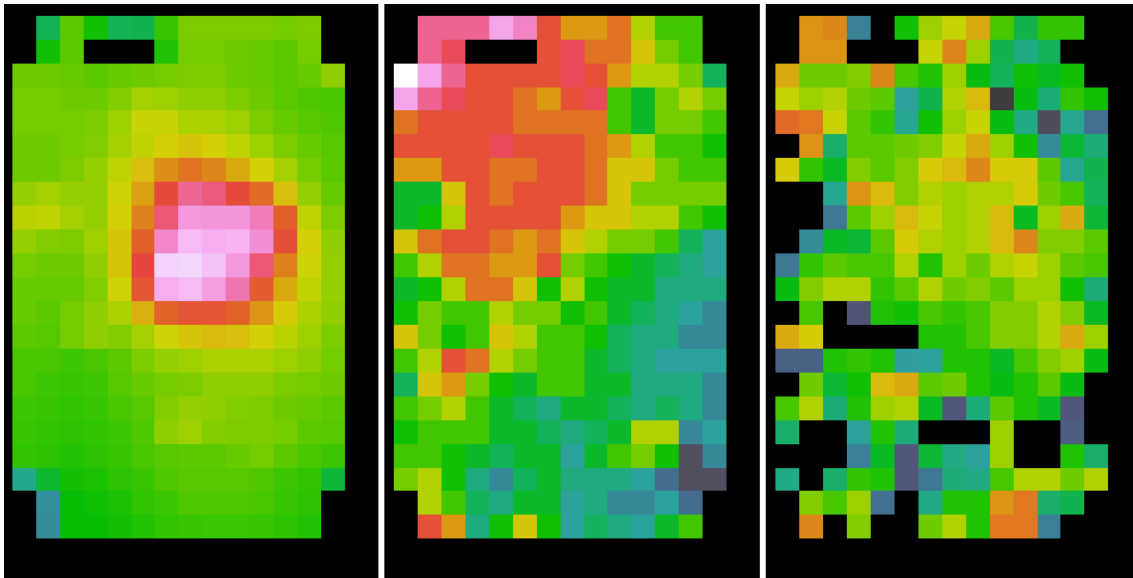


Figure 8.3: *Left:* Integrated spectra. The central illumination is due to the images of QSO 2237+0305 and to the bright center of the lensing galaxy. The field of view is  $7'' \times 12''$  and the position angle is 40 deg counted counterclockwise from North to East. *Middle:* Radial velocity field. The disk rotation is clearly visible and reaches  $\pm 180$  km/s. *Right:* Line-of-sight velocity dispersion field. Given the signal-to-noise of the spectra, reliable velocity dispersions could only be obtained for the central microlenses of the spectrograph.



## 8.3 Integral-field spectroscopy with SINFONI

### 8.3.1 Observations and data reduction

We observed the nucleus of the lensing galaxy in QSO 2237+0305 with SINFONI of the ESO-VLT. SINFONI consists of a near-infrared integral-field spectrometer coupled to a visible adaptive optics system (Eisenhauer et al., 2003; Bonnet et al., 2004). The guiding of the adaptive optics system is done directly on the bright quasar image A.

The SINFONI field of view is sliced into 32 slitlets. Pre-optics allow to choose the angular size of the slitlets on the sky. We chose the angular size of 100 mas, which provides a field of view of  $3'' \times 3''$  and a rectangular size of  $100 \times 50$  mas per spaxel (i.e. spatial pixel). The spaxel is projected on two CCD pixels by the SINFONI collimator and camera optics. We observed our target in the H-band with a useful spectral range of  $1.45 - 1.85 \mu\text{m}$  and, given the angular size of the slitlets, we reach a spectral resolution of  $R \simeq 2700$ .

The integration cycle is composed of a sequence of object and sky exposures in order to remove the sky emission lines which are abundant in the infrared. The sequence consists of one object exposure, followed by two sky exposures and one second object exposure. Each individual exposure is 600 s long and the total object integration time for one cycle is 1200 s. In total, we obtain eleven of these cycles, which leads to a total object integration time of  $13200 \text{ s} = 3.7 \text{ hours}$ , see Table 8.2.

Table 8.2: Journal of the SINFONI observations. The integration time per integration cycle is 1200 s.

ID	Date	Seeing ["]	Airmass
1	14/10/2005	0.32	1.161
2	23/10/2005	0.36	1.136
3	23/10/2005	0.39	1.158
4	25/10/2005	0.25	1.136
5	25/10/2005	0.33	1.168
6	29/10/2005	0.39	1.156
7	29/10/2005	0.28	1.135
8	30/10/2005	0.39	1.152
9	30/10/2005	0.30	1.135
10	30/10/2005	0.29	1.209
11	30/10/2005	0.29	1.322

### 8.3.2 Data analysis and results

The data were reduced using the SINFONI data reduction pipeline (Abuter et al., 2006). The pipeline performs all the usual steps needed to reduce near-infrared spectra, but with additional routines for reconstructing the data cubes. Following subtraction of the sky frames from the on-source frames, the data were flat fielded and corrected for bad pixels and image distortions. The data were then interpolated to linear wavelength and spatial scales, after which the slitlets were aligned and stacked up to create a data cube. From our eleven integration cycles, the pipeline constructs eleven data cubes and, eventually,

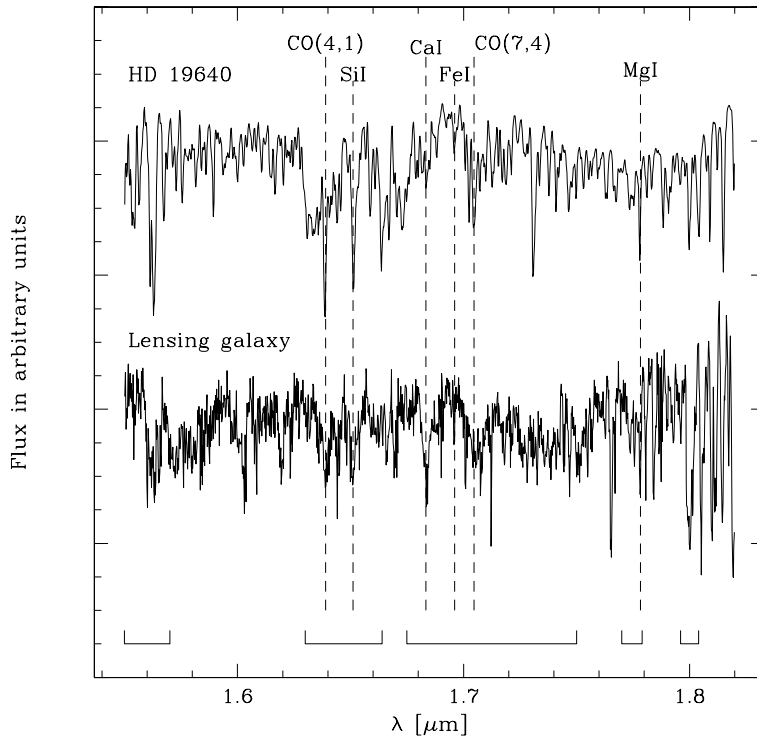


Figure 8.4: Normalized and continuum subtracted spectra of the lensing galaxy of QSO 2237+0305 and of the star HD 19400 obtained from one SINFONI pixel. There are numerous absorption lines in the near-infrared and only the most prominent ones are indicated. The interval marked at the bottom of the plot shows the wavelength range used for the cross-correlation.

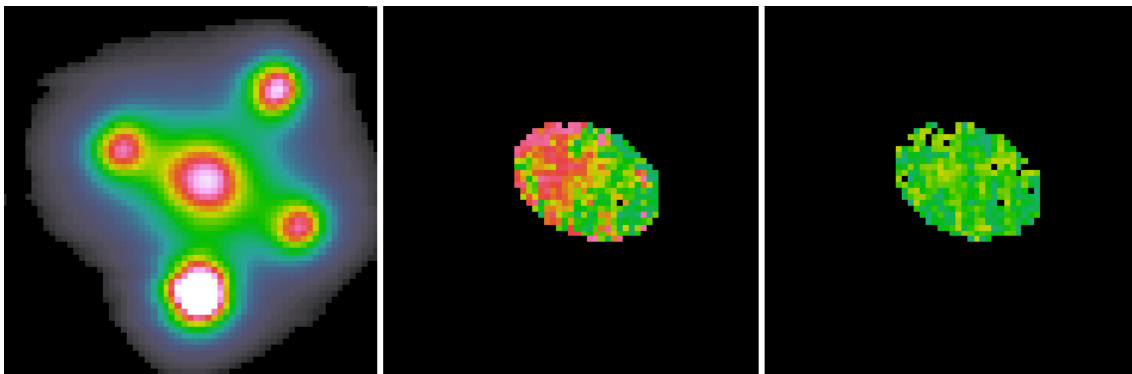


Figure 8.5: *Left*: Integrated spectra. The field of view is  $3'' \times 3''$ . North is up and East to the left. *Middle*: Radial velocity field. A small rotation reaching  $\pm 60$  km/s is visible. *Right*: Line-of-sight velocity dispersion field. Only the most central parts of the galaxy are bright enough to measure reliable radial velocities and dispersions. The velocity dispersion field is relatively flat with a mean value of  $160 \pm 20$  km/s.

combines them to create one final cube. As the eleven cubes are dithered spatially, we

reach a final scale of  $50 \times 50$  mas/pixel. As for the FLAMES data, we have observed the star HD 19640, which provides a stellar template spectrum for the future cross-correlation of the spectra.

We follow the same procedure as for the FLAMES data to determine both the velocity and velocity dispersion fields shown in Fig. 8.5. A small rotation reaching 60 km/s is seen in the nucleus of the lensing galaxy. The velocity dispersion field is flat with values in the range  $160 \pm 20$  km/s.

## 8.4 Long-slit spectroscopy with FORS2

### 8.4.1 Observations and data reduction

In addition to the integral field spectroscopy obtained with FLAMES and SINFONI, we also acquired long-slit spectroscopy with the FOcal Reducer and low dispersion Spectrograph (FORS2) of the ESO-VLT. These additional data extend our analysis to the outer parts of the disk of the lensing galaxy reaching distances up to 30 kpc from the center. For the data acquisition we used the standard-resolution collimator and the  $2 \times 2$  pixel binning, which provide a field of view of  $6.8' \times 6.8'$  with a pixel scale of  $0.252''$ . We used the holographic G1400V grism without filter, which gives a useful wavelength range  $4560 < \lambda < 5860$  Å and a scale of  $0.62$  Å per pixel in the spectral direction. Our long slit has a width of  $0.7''$  and is oriented along the major axis of the lensing galaxy, i.e. to a position angle of  $77$  deg counted counterclockwise from North to East. This setup reaches a medium spectral resolution  $R \simeq 2100$  at the central wavelength  $\lambda = 5200$  Å. Our observing sequence consisted of a short acquisition image, an “image-through-slit” check, followed by one consecutive deep spectroscopic exposure. We acquired four exposures leading to a total integration time of  $9200$  s = 2.6 hours.

Table 8.3: Journal of the FORS2 observations. Each exposures is 2300 s long.

ID	Date	Seeing ["]	Airmass
1	31/05/2008	1.66	1.290
2	29/06/2008	1.91	1.159
3	08/07/2008	1.59	1.558
4	08/07/2008	1.70	1.323

### 8.4.2 Data analysis and results

We carry out the standard bias subtraction and flat-field correction of the spectra using IRAF. The flat fields are created from the combination of five dome exposures and are normalized to have a unity average. The wavelength calibrations are obtained from the spectrum of helium-argon lamps. The wavelength solution is fitted in both spatial and spectral dimensions with the IRAF task `fitcoords` using a fifth order Chebyshev polynomial along the spectral direction and a fourth order Chebyshev polynomial fit along the spatial direction. The object spectra are then rectified with the task `transform` applying a cubic interpolation. This procedure ensures that the sky lines are well aligned with the columns of the CCD after the wavelength calibration. Cosmic rays are removed using

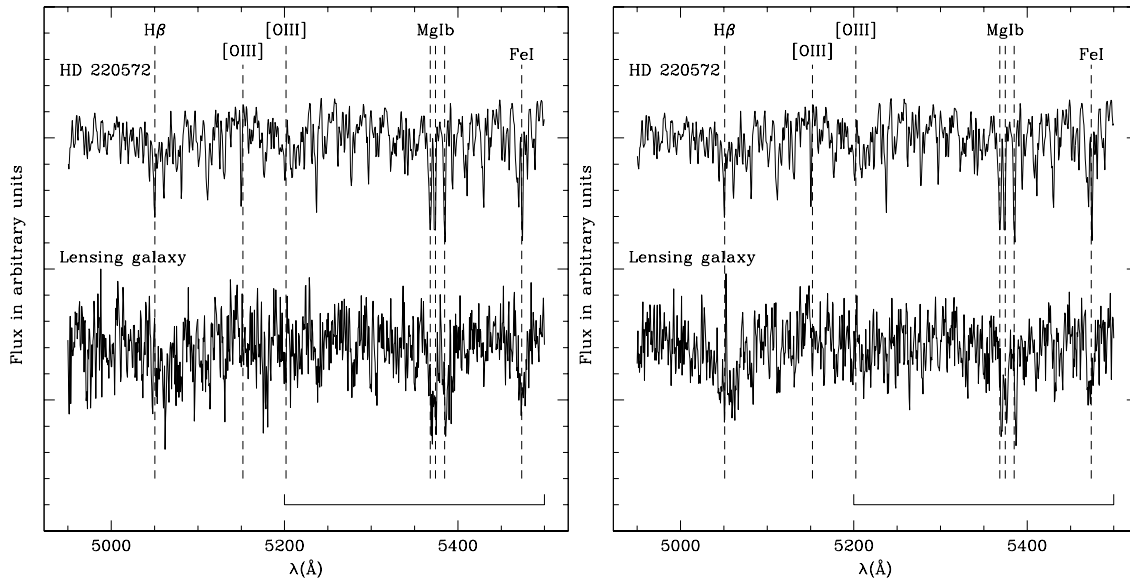


Figure 8.6: Normalized and continuum subtracted spectra of the lensing galaxy of QSO 2237+0305 and of the star HD 220572 obtained with FORS2. The spectrum of the star has been shifted to the redshift of the lensing galaxy. The major absorption and emission lines are indicated. The interval marked at the bottom of the plot shows the wavelength range used for the cross-correlation. *Left:* Spectrum of the central region of the galaxy. *Right:* Spectrum of the galaxy at 9 kpc from the center showing  $H\beta$  and  $[O\text{III}]$  emission.

the L. A. Cosmic algorithm (van Dokkum, 2001). The sky background is removed with the IRAF task `background` by fitting a first order Chebyshev polynomial in the spatial direction to the areas of the spectrum that are not illuminated by the object.

We shift the four individual object spectra with `fitcoords` in order to align them spatially. We create a combined spectrum from all aligned exposures removing the lower and higher pixels and applying an appropriate flux scaling. The final combined spectrum can then be used to infer the velocity and velocity dispersion along the slit. As for the FLAMES and SINFONI observations, we also acquired a spectrum of a giant K0-III star. This time it is HD 220572.

We combine the CCD lines along the spatial direction in order to obtain individual spectra with a signal-to-noise ratio superior to 5. We use these spectra to infer the velocity and velocity dispersion fields following the same method as described for the FLAMES data. The results are shown in Fig. 8.7. We estimate the systematic error on the velocities by carrying out a polynomial fit of the rotation curve using a polynomial of high enough order so that the residuals are uncorrelated, i.e. such that the auto-correlation function of the residuals reduces to less than 0.5 within a separation of a few data points. We find that a polynomial of order 7 is sufficient, and that the systematic error reaches 20 km/s.

The velocity dispersion estimated from the spectrum of the central  $0.89''$  reads  $168 \pm 8$  km/s. It decreases for larger radii and reaches  $50 \pm 30$  km/s at about 8 kpc. The systematic error of the individual velocity dispersion measurements is 30 km/s as estimated from a polynomial fit of order 3.

The spectrum of the lensing galaxy is shown in Fig. 8.6 and displays strong Mg I and Fe I absorption features everywhere in the galaxy from the center out to 30 kpc. For radii larger than 9 kpc, we also find H $\beta$  and [O III] emission. These lines are probably emitted by the gas of the disk. Separate velocity estimates from the absorption and emission lines result in the same rotation curve, which indicates that the gas and stars share the same dynamics in the outer regions of the galaxy.

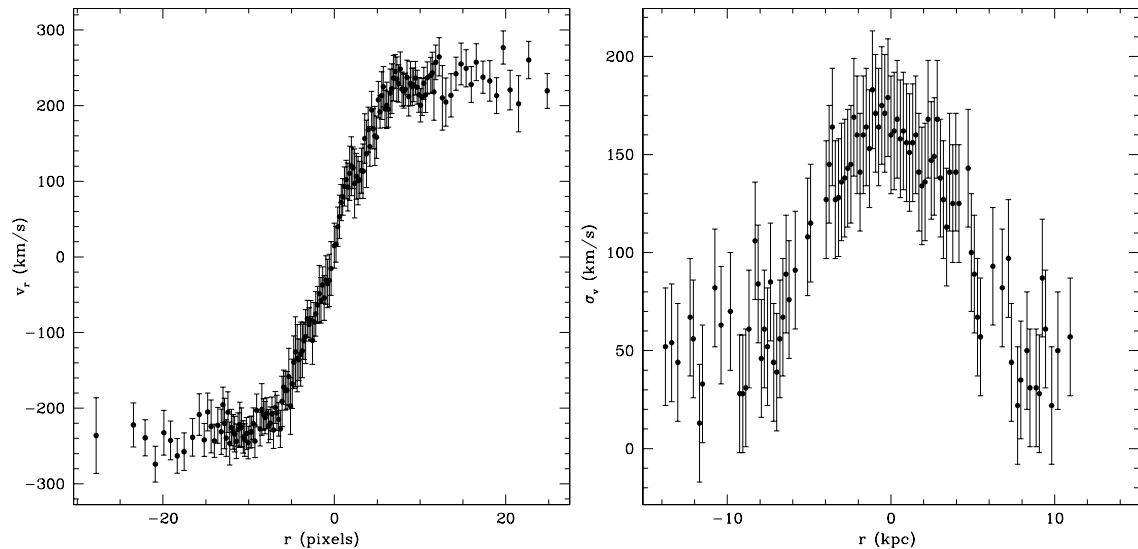


Figure 8.7: Left: Radial velocities obtained from the FORS2 long-slit spectra. *Right:* Line-of-sight velocity dispersion along the FORS2 slit.

## 8.5 Discussion

We have acquired integral-field and long-slit spectroscopy of the lensing galaxy of the Einstein Cross using the three spectrographs SINFONI, FLAMES, and FORS2 of the ESO-VLT. We derive the line-of-sight velocity  $v_r$  and velocity dispersion  $\sigma_v$  maps of the bulge-dominated inner region (i.e.  $< 4$  kpc). From the FORS2 data, we determine for the first time the rotation and velocity dispersion curves of the lensing galaxy up to 30 kpc from its center.

We measure the velocity dispersion within the central  $0.89''$  using the FORS2 spectra and obtain  $168 \pm 8$  km/s. This is consistent with the estimates derived from the SINFONI and FLAMES integral-field spectroscopy. The FORS2 value is also in excellent agreement with the results of van de Ven et al. (2008), who measured a central velocity dispersion of  $166 \pm 2$  km/s. The King and de Vaucouleurs models of Kent & Falco (1988) as well as the more detailed model of Schmidt et al. (1998) predict a similar value of about 166 km/s. Barnes et al. (1999) found a value of  $165 \pm 23$  km/s based on their two H I rotation curve measurements. Finally, we should mention that all these values differ from the first direct measurement of the velocity dispersion by Foltz et al. (1992), who obtained  $215 \pm 30$  km/s. However, it is likely that their long-slit measurement is affected by the bright quasar images.

From the observed geometry of the isophotes, van de Ven et al. (2008) deduce that the

galaxy is inclined at  $i = 68$  deg with respect to the sky plane<sup>3</sup>. Because of this inclination, the radial velocity  $v_r$  differs from the true rotation velocity  $V$

$$v_r = V \sin i$$

The rotation curves of  $V$ , obtained from the three spectrographs along the major axis of the lensing galaxy (i.e. at PA = 77 deg), are mutually consistent, see the left panel of Fig. 8.8. The FORS2 rotation curve reaches 260 km/s at 8 kpc and remains flat out to 30 kpc. The derived velocities are slightly smaller but compatible with the H I measurements of Barnes et al. (1999), who obtained  $v_r / \sin i = 310 \pm 15$  and  $295 \pm 15$  km/s at  $29 \pm 1''$  and  $38 \pm 1''$ , respectively. The FLAMES velocity maps show regular rotation up to  $\sim 140$  km/s around the minor axis of the bulge, consistent with an axisymmetric rotation.

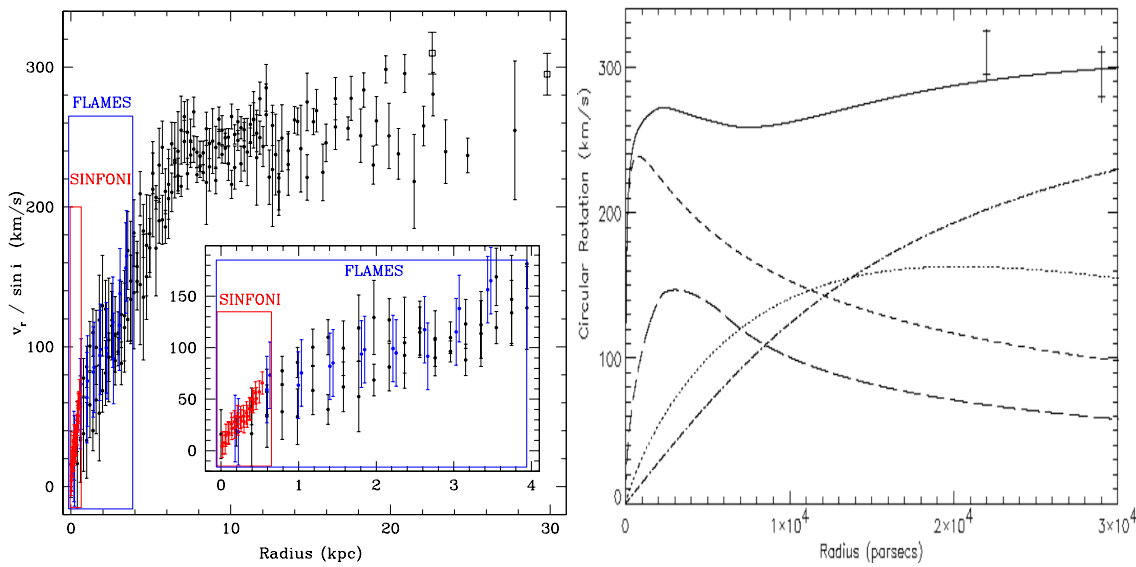


Figure 8.8: *Left*: Rotation curve corrected for the inclination ( $i = 68$  deg). The red, blue, and black dots are the SINFONI, FLAMES, and FORS2 measurements, respectively. The open squares are the two velocities from the H I measurements of Barnes et al. (1999). The inset shows the rotation curve of the central region in more detail. *Right*: Circular velocity from the lens model of Trott & Webster (2002). The curves are total (solid), halo (dash-dot), disk (dotted), bulge (short dashed) and bar (long dashed). The two vertical lines denote the velocities from Barnes et al. (1999).

For a rotating system at equilibrium, the centrifugal force seen by a test particle of mass  $m$  at radius  $r$  is compensated by the gravitational force  $F$ . The particle follows a circular orbit with a circular velocity  $v_{\text{circ}}$  given by

$$m \frac{v_{\text{circ}}^2}{r} = F \quad \Rightarrow \quad v_{\text{circ}}^2 = \frac{r}{m} F$$

Trott & Webster (2002) constructed a simple model for the mass distribution of the lensing galaxy of QSO 2237+0305. They considered analytical mass distributions for the bulge,

<sup>3</sup>We remind that a face-on galaxy has an inclination  $i = 0$  deg and an edge-on  $i = 90$  deg.

bar, disk, and halo. They constrained their model from both the lensing data and the two HI measurements of Barnes et al. (1999). They derived the circular velocity curve shown in the right panel of Fig. 8.8. This curve is essentially flat from 2 to 30 kpc with a steep slope in the central 2 kpc. A similar circular velocity curve is obtained from the axisymmetric models of van de Ven et al. (2008).

For radii larger than 8 kpc, the circular velocities  $v_{\text{circ}}$  of Trott & Webster (2002) and van de Ven et al. (2008) are compatible with (but slightly higher than) the velocities  $V$  obtained from our spectroscopic data. This suggests that the visible matter located at  $r > 8$  kpc typically follows circular orbits, e.g., in a disk-like structure. However, at smaller radii  $V$  is significantly smaller than  $v_{\text{circ}}$ , which indicates that the region inside  $\sim 8$  kpc is not rotationally supported and that the velocity dispersion becomes important. This is clearly visible in the right panel of Fig. 8.7 where the velocity dispersion increases from  $\sim 8$  kpc inwards. These facts are further confirmed by the detection of  $\text{H}\beta$  and  $[\text{O III}]$  emission at  $r > 9$  kpc, which indicates the presence of gas, which is typically found in the disks but not in the bulges of spiral galaxies.

From all these observations, we conclude that there are two dynamical regimes in the lensing galaxy: a central bulge-dominated region and a more extended circularly rotating region. The bulge-dominated region is slowly rotating and is dominated by random motions, i.e. by the velocity dispersion. At a distance of about 8 kpc from the center, the dynamics change and the visible matter essentially follows circular orbits located in the disk plane. This value of 8 kpc is a bit lower than expected from the model of Trott & Webster (2002), where the mass of the bulge dominates the dynamics out to 10 kpc. This small discrepancy may indicate that the mass of the bulge has potentially been overestimated in their model.

The models of van de Ven et al. (2008) are based on the assumption of a constant mass-to-light ratio, which they use to derive the mass distribution of the lensing galaxy from the observed surface brightness. Hence, they do not consider the potential mass contributions of an extended dark matter halo. Furthermore, given the small spatial extent (i.e.  $< 2$  kpc) of their kinematic data, their dynamical models are not constrained in the outer parts of the galaxy, where the mass contribution from the halo may be important.

Given this situation, it is imperative to build new dynamical models based on both the gravitational lensing data and our extended spectroscopic data. Indeed, the flatness of the observed rotation curve strongly suggests the presence of an extended dark matter halo (van Albada et al., 1985), and we have now sufficient data to precisely determine the amount and distribution of dark matter in the lensing galaxy of QSO 2237+0305.





*“The journey is the reward.”  
Confucius (551- 479 BC)*

## Chapter 9

# General conclusions and outlook

In this thesis, we consider several applications related to gravitationally lensed quasars. We make extensive use of the spectrographs of the Very Large Telescope with a total of 185 hours of observation.

The first part of our study is related to the COSMOGRAIL project, which aims at determining the Hubble constant  $H_0$  from the time-delay method. In order to optimize the observing strategy of the COSMOGRAIL targets, we have undertaken a set of simple but realistic numerical simulations. The results of these simulations help to determine the optimal combination of predicted time delay, object visibility and temporal sampling. They also help to estimate which gravitational lenses are best suited for a  $H_0$  determination. These simulations have been used to define the observing strategies of the COSMOGRAIL targets and have led to the determination of several time delays (Vuissoz et al., 2007, 2008). These time delays have an uncertainty below 4%, which is twice better than the accuracy usually reached by previous monitorings of lensed quasars. Furthermore, as the monitoring continues, these values will further improve, together with several other COSMOGRAIL time delays that will be published in the foreseeable future.

From spectroscopic observations obtained with the Very Large Telescope, we determine the redshift of the lensing galaxies in sixteen gravitationally lensed quasars. This represents about 25% of all currently known redshifts of galaxies lensing background quasars. The comparison of our results with previous studies suggests that photometric redshift estimates are in general not very accurate indicators of the true redshift. Absorption lines present in the spectra of the lensed quasar images are much better indicators but caution should be used in their identification. Our new lens redshifts have a direct impact on several studies, especially the lens redshift of HE 2149–2745, which is one of lens systems that has been used to argue possible low  $H_0$  values (e.g., Kochanek, 2002, 2003b). The new redshift significantly increases the derived  $H_0$ , and weakens the possible low  $H_0$  problem (e.g., Oguri, 2007).

In analyzing data of the VLT archives, we show that multi-object spectroscopy is better suited for the determination of lens redshifts than long-slit spectroscopy. The additional spatial information obtained from the simultaneous observation of foreground

stars is essential for the spatial deconvolution of the data. There are still other data in the archives that can potentially be deconvolved and hence, provide the lens redshift for other lensed quasars.

In addition, the quality (i.e. good signal-to-noise ratios and flux calibration) of our spectra is sufficient for a stellar-population analysis. From such an analysis, one can infer the stellar mass of the lensing galaxies. The comparison with the total mass inferred from gravitational lensing can then determine the quantity of dark matter in the lensing galaxies (e.g., Ferreras et al., 2008).

Additional results of our analysis are the spectra of the lensed quasar images. As shown for SDSS J0924+0219, these observations can be used to study the quasar variability and potentially also chromatic flux variations induced by microlensing. These flux variations provide interesting constraints on the geometry and dimension of the broad line and continuum emitting regions (e.g., Richards et al., 2004; Popović, 2006).

Increasing the number of known lens redshifts is important for several reasons. First, lens redshifts are essential for the determination of  $H_0$ . Increasing the number of time-delay lenses with known lens redshifts will improve the precision of the subsequent  $H_0$  estimation (e.g., Oguri, 2007; Coles, 2008). Second, lens redshifts can be used to compute statistics of gravitational lenses that provide constraints on the density of dark energy  $\Omega_{\Lambda 0}$  (e.g., Fukugita et al., 1990; Turner, 1990). Increasing the number of known lens redshifts will improve the statistics and, therefore, yield better estimates of  $\Omega_{\Lambda 0}$  (e.g., Oguri et al., 2008).

In the main part of this thesis, we perform a detailed analysis of the gravitationally lensed quasar QSO 2237+0305 also known as the Einstein Cross. We present our three-year long spectrophotometric monitoring conducted at the Very Large Telescope. We find that all images of the Einstein Cross are affected by microlensing in both the continuum and the broad emission lines. Images A and B are the most affected by microlensing during our monitoring campaign, and the spectral continuum becomes bluer as the images get brighter, as expected from microlensing of an accretion disk. We also report microlensing-induced flux variations of the broad emission lines, both in their profile and integrated intensity. Our measurements suggest that higher ionization lines are more magnified than lower ionization lines, which is consistent with the results of reverberation mapping studies and a stratified structure of the broad line region (e.g., Peterson, 1993; Kaspi et al., 2000).

In a subsequent analysis, we study in more detail the variations observed in the continuum of the spectra of the quasar images A and B. We combine the inverse ray-shooting technique with Bayesian analysis to infer probability distributions for the effective transverse velocity and the size of the source responsible for the optical and ultraviolet continuum. Our results are well compatible with previous studies. We derive the currently best estimate of the energy profile of a quasar accretion disk. We find that the energy profile of QSO 2237+0305 follows a power-law  $R \propto \lambda^\zeta$  with  $\zeta = 1.2 \pm 0.3$ , which is in good agreement with the predictions of the standard thin accretion disk model, and with the results obtained from microlensing studies of other lensed quasars (e.g., Poindexter et al., 2008).

We find that the determination of the power-law index  $\zeta$  is almost independent of the mean microlens mass and velocity prior considered. As a consequence, microlensing studies are extremely efficient in constraining the relative sizes of the different emitting regions in the source, i.e. we can accurately infer the energy profile of the accretion disk and probe the lensed quasar of the scale of several milli-parsecs. This corresponds to a

---

spatial resolution of about one micro-arcsecond, which is more than ten thousand times better than the resolution reached by today's best telescopes. Furthermore, the intensity and profile variations observed in the broad emission lines offer considerable hope to infer quantitative information on the geometry and size of the broad line region, as well.

Finally, we take advantage of the proximity of the spiral lensing galaxy in the Einstein Cross to conduct a detailed study of its stellar kinematics using long-slit and integral-field spectroscopy. We obtain for the first time the rotation curve of this galaxy, and the flatness of the curve at large radii suggests the presence of an extended dark matter halo. We conclude from our observations that there are two dynamical regimes in the lensing galaxy: a central bulge-dominated region and a more extended circularly rotating region. The comparison of the observed kinematics with the predictions of dynamical models possibly indicate that the mass of the bulge has been overestimated in the models. It is thus imperative to build new dynamical models based on both the gravitational lensing data and our extended spectroscopic data. The combination of these two independent data sets is promising for the determination of the distribution of dark matter in the lensing galaxy, and especially in its extended halo.

In this thesis, we have seen how quasar lensing can be used to address several astrophysical and cosmological questions. Gravitational lensing has, indeed, become an increasingly important tool in these domains, and many more fascinating results are expected in the future as new data are acquired, e.g., from weak-lensing surveys. Hopefully, in the coming years, gravitational lensing will help to better understand the nature of dark matter and dark energy, which remain two of the most challenging mysteries of modern cosmology.



# Bibliography

- Abajas, C., Mediavilla, E., Muñoz, J. A., Popović, L. Č., & Oscoz, A. 2002, *ApJ*, 576, 640
- Abuter, R., Schreiber, J., Eisenhauer, F., et al. 2006, *New Astronomy Review*, 50, 398
- Agol, E., Jones, B., & Blaes, O. 2000, *ApJ*, 545, 657
- Agol, E. & Krolik, J. 1999, *ApJ*, 524, 49
- Agol, E., Wyithe, S., Jones, B., & Fluke, C. 2001, *Publications of the Astronomical Society of Australia*, 18, 166
- Alcalde, D., Mediavilla, E., Moreau, O., et al. 2002, *ApJ*, 572, 729
- Alcock, C., Akerloff, C. W., Allsman, R. A., et al. 1993, *Nature*, 365, 621
- Alcock, C., Allsman, R. A., Alves, D., et al. 1997a, *ApJ*, 486, 697
- Alcock, C., Allsman, R. A., Alves, D., et al. 1997b, *ApJ*, 479, 119
- Anguita, T., Schmidt, R. W., Turner, E. L., et al. 2008, *A&A*, 480, 327
- Antonucci, R. R. J. 1983, *Nature*, 303, 158
- Antonucci, R. R. J. & Miller, J. S. 1985, *ApJ*, 297, 621
- Astier, P., Guy, J., Regnault, N., et al. 2006, *A&A*, 447, 31
- Aubourg, E., Bareyre, P., Brehin, S., et al. 1993, *Nature*, 365, 623
- Avila, G., Rupprecht, G., & Beckers, J. M. 1997, in *Presented at the Society of Photo-Optical Instrumentation Engineers (SPIE) Conference, Vol. 2871, Proc. SPIE Vol. 2871*, p. 1135-1143, *Optical Telescopes of Today and Tomorrow*, Arne L. Ardeberg; Ed., ed. A. L. Ardeberg, 1135–1143
- Barnabè, M. & Koopmans, L. V. E. 2007, *ApJ*, 666, 726
- Barnes, D. G., Webster, R. L., Schmidt, R. W., & Hughes, A. 1999, *MNRAS*, 309, 641
- Barnes, J. & Hut, P. 1986, *Nature*, 324, 446
- Beaulieu, J.-P., Bennett, D. P., Fouqué, P., et al. 2006, *Nature*, 439, 437

- Bennett, C. L., Halpern, M., Hinshaw, G., et al. 2003, *ApJS*, 148, 1
- Benson, B. A., Church, S. E., Ade, P. A. R., et al. 2003, *ApJ*, 592, 674
- Bernstein, G. & Fischer, P. 1999, *AJ*, 118, 14
- Beskin, G. M. & Oknyanskij, V. L. 1995, *A&A*, 304, 341
- Blandford, R. & Narayan, R. 1986, *ApJ*, 310, 568
- Blandford, R. D. & Begelman, M. C. 2004, *MNRAS*, 349, 68
- Bonamente, M., Joy, M. K., LaRoque, S. J., et al. 2006, *ApJ*, 647, 25
- Bonnet, H., Abuter, R., Baker, A., et al. 2004, *The Messenger*, 117, 17
- Bourassa, R. R. & Kantowski, R. 1975, *ApJ*, 195, 13
- Burud, I., Magain, P., Sohy, S., & Hjorth, J. 2001, *A&A*, 380, 805
- Chae, K.-H., Turnshek, D. A., & Khersonsky, V. K. 1998, *ApJ*, 495, 609
- Chang, K. & Refsdal, S. 1979, *Nature*, 282, 561
- Chartas, G., Kochanek, C. S., Dai, X., Poindexter, S., & Garmire, G. 2008, *astro-ph/0805.4492*
- Chiba, M. & Futamase, T. 1999, *Progress of Theoretical Physics Supplement*, 133, 115
- Clowe, D., Bradač, M., Gonzalez, A. H., et al. 2006, *ApJ*, 648, L109
- Coles, J. 2008, *ApJ*, 679, 17
- Colless, M., Dalton, G., Maddox, S., et al. 2001, *MNRAS*, 328, 1039
- Colley, W. N., Schild, R. E., Abajas, C., et al. 2003, *ApJ*, 587, 71
- Congdon, A. B., Keeton, C. R., & Osmer, S. J. 2007, *MNRAS*, 376, 263
- Cooke, J. H. & Kantowski, R. 1975, *ApJ*, 195, L11
- Corrigan, R. T., Irwin, M. J., Arnaud, J., et al. 1991, *AJ*, 102, 34
- Courbin, F., Eigenbrod, A., Vuissoz, C., Meylan, G., & Magain, P. 2005, in *IAU Symposium*, Vol. 225, *Gravitational Lensing Impact on Cosmology*, ed. Y. Mellier & G. Meylan, 297–303
- Courbin, F., Magain, P., Kirkove, M., & Sohy, S. 2000, *ApJ*, 529, 1136
- Crenshaw, D. M., Kraemer, S. B., & George, I. M., eds. 2002, *Astronomical Society of the Pacific Conference Series*, Vol. 255, *Mass Outflow in Active Galactic Nuclei: New Perspectives*, ed. D. M. Crenshaw, S. B. Kraemer, & I. M. George
- Czoske, O., Barnabè, M., Koopmans, L. V. E., Treu, T., & Bolton, A. S. 2008, *MNRAS*, 384, 987
- Davis, M., Efstathiou, G., Frenk, C. S., & White, S. D. M. 1985, *ApJ*, 292, 371

- Davis, S. W., Woo, J.-H., & Blaes, O. M. 2007, *ApJ*, 668, 682
- de Vaucouleurs, G. 1953, *MNRAS*, 113, 134
- Dietrich, M., Hamann, F., Appenzeller, I., & Vestergaard, M. 2003, *ApJ*, 596, 817
- Djorgovski, S. & Davis, M. 1987, *ApJ*, 313, 59
- Eigenbrod, A., Courbin, F., Dye, S., et al. 2006a, *A&A*, 451, 747
- Eigenbrod, A., Courbin, F., & Meylan, G. 2007, *A&A*, 465, 51
- Eigenbrod, A., Courbin, F., Meylan, G., et al. 2008a, *A&A*, 490, 933
- Eigenbrod, A., Courbin, F., Meylan, G., Vuissoz, C., & Magain, P. 2006b, *A&A*, 451, 759
- Eigenbrod, A., Courbin, F., Sluse, D., Meylan, G., & Agol, E. 2008b, *A&A*, 480, 647
- Eigenbrod, A., Courbin, F., Vuissoz, C., et al. 2005, *A&A*, 436, 25
- Einstein, A. 1936, *Science*, 84, 506
- Eisenhauer, F., Abuter, R., Bickert, K., et al. 2003, in Presented at the Society of Photo-Optical Instrumentation Engineers (SPIE) Conference, Vol. 4841, Instrument Design and Performance for Optical/Infrared Ground-based Telescopes. Edited by Iye, Masanori; Moorwood, Alan F. M. Proceedings of the SPIE, Volume 4841, pp. 1548-1561 (2003)., ed. M. Iye & A. F. M. Moorwood, 1548–1561
- Eisenstein, D. J., Zehavi, I., Hogg, D. W., et al. 2005, *ApJ*, 633, 560
- Faber, S. M. & Jackson, R. E. 1976, *ApJ*, 204, 668
- Falco, E. E., Gorenstein, M. V., & Shapiro, I. I. 1985, *ApJ*, 289, L1
- Falco, E. E., Kochanek, C. S., & Munoz, J. A. 1998, *ApJ*, 494, 47
- Falco, E. E., Lehar, J., Perley, R. A., Wambsganss, J., & Gorenstein, M. V. 1996, *AJ*, 112, 897
- Falco, E. E., Shapiro, I. I., Moustakas, L. A., & Davis, M. 1997, *ApJ*, 484, 70
- Fanaroff, B. L. & Riley, J. M. 1974, *MNRAS*, 167, 31P
- Ferreras, I., Saha, P., & Burles, S. 2008, *MNRAS*, 383, 857
- Foltz, C. B., Hewett, P. C., Webster, R. L., & Lewis, G. F. 1992, *ApJ*, 386, L43
- Frank, J., King, A., & Raine, D. J. 2002, *Accretion Power in Astrophysics: Third Edition* (Accretion Power in Astrophysics, by Juhan Frank and Andrew King and Derek Raine, pp. 398. ISBN 0521620538. Cambridge, UK: Cambridge University Press, February 2002.)
- Freedman, W. L., Madore, B. F., Gibson, B. K., et al. 2001, *ApJ*, 553, 47
- Friedmann, A. 1922, *Zeitschrift fur Physik*, 10, 377

- Fukugita, M., Futamase, T., & Kasai, M. 1990, *MNRAS*, 246, 24P
- Fukugita, M. & Turner, E. L. 1991, *MNRAS*, 253, 99
- Gavazzi, R., Treu, T., Koopmans, L. V. E., et al. 2008, *ApJ*, 677, 1046
- Gerhard, O., Kronawitter, A., Saglia, R. P., & Bender, R. 2001, *AJ*, 121, 1936
- Gil-Merino, R., Wambsganss, J., Goicoechea, L. J., & Lewis, G. F. 2005, *A&A*, 432, 83
- Grieger, B. 1990, *Ap&SS*, 171, 115
- Hawley, J. F. & Krolik, J. H. 2001, *ApJ*, 548, 348
- Hinshaw, G., Weiland, J. L., Hill, R. S., et al. 2008, *astro-ph/0803.0732*
- Hook, I. M., McMahon, R. G., Boyle, B. J., & Irwin, M. J. 1994, *MNRAS*, 268, 305
- Hubble, E. 1929, *Proceedings of the National Academy of Science*, 15, 168
- Hubeny, I., Agol, E., Blaes, O., & Krolik, J. H. 2000, *ApJ*, 533, 710
- Huchra, J., Gorenstein, M., Kent, S., et al. 1985, *AJ*, 90, 691
- Impey, C. D., Falco, E. E., Kochanek, C. S., et al. 1998, *ApJ*, 509, 551
- Inada, N., Becker, R. H., Burles, S., et al. 2003, *AJ*, 126, 666
- Inada, N., Burles, S., Gregg, M. D., et al. 2005, *AJ*, 130, 1967
- Inada, N., Oguri, M., Becker, R. H., et al. 2006, *AJ*, 131, 1934
- Inada, N., Oguri, M., Shin, M.-S., et al. 2008, *astro-ph/0809.0912*
- Irwin, M. J., Webster, R. L., Hewett, P. C., Corrigan, R. T., & Jedrzejewski, R. I. 1989, *AJ*, 98, 1989
- Jaffe, W., Ford, H., Ferrarese, L., van den Bosch, F., & O'Connell, R. W. 1996, *ApJ*, 460, 214
- Jones, M. E., Edge, A. C., Grainge, K., et al. 2005, *MNRAS*, 357, 518
- Kaspi, S., Maoz, D., Netzer, H., et al. 2005, *ApJ*, 629, 61
- Kaspi, S., Smith, P. S., Netzer, H., et al. 2000, *ApJ*, 533, 631
- Kayser, R., Refsdal, S., & Stabell, R. 1986, *A&A*, 166, 36
- Keeton, C. R. 2001a, *astro-ph/0102341*
- Keeton, C. R. 2001b, *astro-ph/0102340*
- Keeton, C. R., Burles, S., Schechter, P. L., & Wambsganss, J. 2006, *ApJ*, 639, 1
- Keeton, C. R., Kochanek, C. S., & Seljak, U. 1997, *ApJ*, 482, 604
- Kent, S. M. & Falco, E. E. 1988, *AJ*, 96, 1570



- Kinney, A. L., Calzetti, D., Bohlin, R. C., et al. 1996, *ApJ*, 467, 38
- Kishimoto, M., Antonucci, R., Blaes, O., et al. 2008, *Nature*, 454, 492
- Kneib, J.-P., Ellis, R. S., Santos, M. R., & Richard, J. 2004, *ApJ*, 607, 697
- Kneib, J.-P., Ellis, R. S., Smail, I., Couch, W. J., & Sharples, R. M. 1996, *ApJ*, 471, 643
- Kneib, J.-P., Hudelot, P., Ellis, R. S., et al. 2003, *ApJ*, 598, 804
- Kochanek, C. 2003a, in *HST Proposal*, 9744
- Kochanek, C. S. 1996, *ApJ*, 473, 595
- Kochanek, C. S. 2002, *ApJ*, 578, 25
- Kochanek, C. S. 2003b, *ApJ*, 583, 49
- Kochanek, C. S. 2004, *ApJ*, 605, 58
- Kochanek, C. S., Dai, X., Morgan, C., Morgan, N., & Poindexter, S. C. G. 2007, in *Astronomical Society of the Pacific Conference Series*, Vol. 371, *Statistical Challenges in Modern Astronomy IV*, ed. G. J. Babu & E. D. Feigelson, 43
- Kochanek, C. S. & Dalal, N. 2004, *ApJ*, 610, 69
- Kochanek, C. S., Falco, E. E., Impey, C. D., et al. 2000, *ApJ*, 543, 131
- Kochanek, C. S. & Schechter, P. L. 2004, in *Measuring and Modeling the Universe*, ed. W. L. Freedman, 117
- Komatsu, E., Dunkley, J., Nolta, M. R., et al. 2008, *ArXiv e-prints*
- Koopmans, L. V. E., Treu, T., Bolton, A. S., Burles, S., & Moustakas, L. A. 2006, *ApJ*, 649, 599
- Koptelova, E., Shimanovskaya, E., Artamonov, B., et al. 2005, *MNRAS*, 356, 323
- Koratkar, A. & Blaes, O. 1999, *PASP*, 111, 1
- Kormann, R., Schneider, P., & Bartelmann, M. 1994, *A&A*, 284, 285
- Kroupa, P. 2002, *Science*, 295, 82
- Kundić, T., Turner, E. L., Colley, W. N., et al. 1997, *ApJ*, 482, 75
- Kundić, T. & Wambsganss, J. 1993, *ApJ*, 404, 455
- Lemaître, G. 1927, *Annales de la Société Scientifique de Bruxelles*, 47, 49
- Lewis, G. F. & Gil-Merino, R. 2006, *ApJ*, 645, 835
- Lewis, G. F. & Irwin, M. J. 1995, *MNRAS*, 276, 103
- Lewis, G. F. & Irwin, M. J. 1996, *MNRAS*, 283, 225

- Lewis, G. F., Miralda-Escude, J., Richardson, D. C., & Wambsganss, J. 1993, *MNRAS*, 261, 647
- Loewenstein, M. & White, III, R. E. 1999, *ApJ*, 518, 50
- Lynden-Bell, D. 1969, *Nature*, 223, 690
- Magain, P., Courbin, F., & Sohy, S. 1998, *ApJ*, 494, 472
- Maller, A. H., Simard, L., Guhathakurta, P., et al. 2000, *ApJ*, 533, 194
- Mao, S. & Paczyński, B. 1991, *ApJ*, 374, L37
- Maoz, D. 2005, in *IAU Symposium*, Vol. 225, *Gravitational Lensing Impact on Cosmology*, ed. Y. Mellier & G. Meylan, 413–418
- Maza, J., Ortiz, P. F., Wischnjewsky, M., Antezana, R., & González, L. E. 1995, *Revista Mexicana de Astronomía y Astrofísica*, 31, 159
- Merritt, D., Navarro, J. F., Ludlow, A., & Jenkins, A. 2005, *ApJ*, 624, L85
- Mineshige, S. & Yonehara, A. 1999, *PASJ*, 51, 497
- Momcheva, I., Williams, K., Keeton, C., & Zabludoff, A. 2006, *ApJ*, 641, 169
- Moore, B. 1994, *Nature*, 370, 629
- Morgan, C. W., Kochanek, C. S., Dai, X., Morgan, N. D., & Falco, E. E. 2008, *astro-ph/0802.1210*
- Morgan, N. D., Caldwell, J. A. R., Schechter, P. L., et al. 2004, *AJ*, 127, 2617
- Morgan, N. D., Dressler, A., Maza, J., Schechter, P. L., & Winn, J. N. 1999, *AJ*, 118, 1444
- Morgan, N. D., Gregg, M. D., Wisotzki, L., et al. 2003, *AJ*, 126, 696
- Mortonson, M. J., Schechter, P. L., & Wambsganss, J. 2005, *ApJ*, 628, 594
- Mould, J. R., Akeson, R. L., Bothun, G. D., et al. 1993, *ApJ*, 409, 14
- Munshi, D., Valageas, P., van Waerbeke, L., & Heavens, A. 2008, *Phys. Rep.*, 462, 67
- Navarro, J. F., Frenk, C. S., & White, S. D. M. 1996, *ApJ*, 462, 563
- Navarro, J. F., Frenk, C. S., & White, S. D. M. 1997, *ApJ*, 490, 493
- Nemiroff, R. J. 1988, *ApJ*, 335, 593
- Novikov, I. D. & Thorne, K. S. 1973, in *Black Holes (Les Astres Occlus)*, 343–450
- Ofek, E. O., Maoz, D., Rix, H.-W., Kochanek, C. S., & Falco, E. E. 2006, *ApJ*, 641, 70
- Oguri, M. 2007, *ApJ*, 660, 1
- Oguri, M., Inada, N., Castander, F. J., et al. 2004, *PASJ*, 56, 399
- Oguri, M., Inada, N., Strauss, M. A., et al. 2008, *AJ*, 135, 512

- Ostensen, R., Refsdal, S., Stabell, R., et al. 1996, *A&A*, 309, 59
- Paczynski, B. 1986a, *ApJ*, 301, 503
- Paczynski, B. 1986b, *ApJ*, 304, 1
- Pasquini, L., Avila, G., Blecha, A., et al. 2002, *The Messenger*, 110, 1
- Pelt, J., Hoff, W., Kayser, R., Refsdal, S., & Schramm, T. 1994, *A&A*, 286, 775
- Pelt, J., Kayser, R., Refsdal, S., & Schramm, T. 1996, *A&A*, 305, 97
- Penzias, A. A. & Wilson, R. W. 1965, *ApJ*, 142, 419
- Percival, W. J., Cole, S., Eisenstein, D. J., et al. 2007, *MNRAS*, 381, 1053
- Perlmutter, S., Aldering, G., Goldhaber, G., et al. 1999, *ApJ*, 517, 565
- Peterson, B. M. 1993, *PASP*, 105, 247
- Poindexter, S., Morgan, N., & Kochanek, C. S. 2008, *ApJ*, 673, 34
- Pooley, D., Blackburne, J. A., Rappaport, S., & Schechter, P. L. 2007, *ApJ*, 661, 19
- Popović, L. C. 2006, *Serbian Astronomical Journal*, 173, 1
- Press, W. H., Rybicki, G. B., & Hewitt, J. N. 1992, *ApJ*, 385, 404
- Pringle, J. E. & Rees, M. J. 1972, *A&A*, 21, 1
- Rauch, K. P. & Blandford, R. D. 1991, *ApJ*, 381, L39
- Rees, M. J. 1984, *ARA&A*, 22, 471
- Refsdal, S. 1964a, *MNRAS*, 128, 307
- Refsdal, S. 1964b, *MNRAS*, 128, 295
- Refsdal, S. & Stabell, R. 1993, *A&A*, 278, L5
- Richards, G. T., Keeton, C. R., Pindor, B., et al. 2004, *ApJ*, 610, 679
- Riess, A. G., Strolger, L.-G., Casertano, S., et al. 2007, *ApJ*, 659, 98
- Rix, H.-W., Schneider, D. P., & Bahcall, J. N. 1992, *AJ*, 104, 959
- Robertson, H. P. 1935, *ApJ*, 82, 284
- Saha, P., Courbin, F., Sluse, D., Dye, S., & Meylan, G. 2006, *A&A*, 450, 461
- Saha, P. & Williams, L. L. R. 1997, *MNRAS*, 292, 148
- Saha, P. & Williams, L. L. R. 2004, *AJ*, 127, 2604
- Sambridge, M. 1999, *Geophysical Journal International*, 138, 727
- Schechter, P. L. 2005, in *IAU Symposium*, Vol. 225, *Gravitational Lensing Impact on Cosmology*, ed. Y. Mellier & G. Meylan, 281–296

- Schechter, P. L., Udalski, A., Szymański, M., et al. 2003, *ApJ*, 584, 657
- Schechter, P. L. & Wambsganss, J. 2002, *ApJ*, 580, 685
- Schechter, P. L., Wambsganss, J., & Lewis, G. F. 2004, *ApJ*, 613, 77
- Schmidt, R. & Wambsganss, J. 1998, *A&A*, 335, 379
- Schmidt, R., Webster, R. L., & Lewis, G. F. 1998, *MNRAS*, 295, 488
- Schmidt, R. W., Kundić, T., Pen, U.-L., et al. 2002, *A&A*, 392, 773
- Schneider, D. P., Turner, E. L., Gunn, J. E., et al. 1988, *AJ*, 95, 1619
- Schneider, P., Ehlers, J., & Falco, E. E. 1992, *Gravitational Lenses* (Springer-Verlag Berlin Heidelberg New York. Astronomy and Astrophysics Library)
- Schneider, P., Kochanek, C. S., & Wambsganss, J. 2006, in *Saas-Fee Advanced Course 33: Gravitational Lensing: Strong, Weak and Micro*, ed. G. Meylan, P. Jetzer, & P. North
- Schneider, P. & Weiss, A. 1987, *A&A*, 171, 49
- Schramm, T. 1990, *A&A*, 231, 19
- Schramm, T., Kayser, R., Chang, K., Nieser, L., & Refsdal, S. 1993, *A&A*, 268, 350
- Schwarzschild, K. 1916, *Sitzungsberichte der Königlich Preussischen Akademie der Wissenschaften*, 1, 189
- Seitz, C. & Schneider, P. 1994, *A&A*, 288, 1
- Seyfert, C. K. 1941, *PASP*, 53, 231
- Shakura, N. I. & Sunyaev, R. A. 1973, *A&A*, 24, 337
- Shalyapin, V. N., Goicoechea, L. J., Alcalde, D., et al. 2002, *ApJ*, 579, 127
- Shapiro, I. I., Ash, M. E., Ingalls, R. P., et al. 1971, *Physical Review Letters*, 26, 1132
- Shields, G. A. 1978, *Nature*, 272, 706
- Smith, J. E., Robinson, A., Alexander, D. M., et al. 2004, *MNRAS*, 350, 140
- Spergel, D. N., Bean, R., Doré, O., et al. 2007, *ApJS*, 170, 377
- Springel, V., White, S. D. M., Jenkins, A., et al. 2005, *Nature*, 435, 629
- Stone, J. M., Pringle, J. E., & Begelman, M. C. 1999, *MNRAS*, 310, 1002
- Stoughton, C., Lupton, R. H., Bernardi, M., et al. 2002, *AJ*, 123, 485
- Sunyaev, R. A. & Zeldovich, Y. B. 1970, *Ap&SS*, 7, 3
- Surdej, J., Magain, P., Swings, J.-P., et al. 1988, *A&A*, 198, 49
- Tonry, J. & Davis, M. 1979, *AJ*, 84, 1511

- Tonry, J. & Schneider, D. P. 1988, *AJ*, 96, 807
- Treu, T. & Koopmans, L. V. E. 2004, *ApJ*, 611, 739
- Trott, C. M. & Webster, R. L. 2002, *MNRAS*, 334, 621
- Tully, R. B. & Fisher, J. R. 1977, *A&A*, 54, 661
- Turner, E. L. 1990, *ApJ*, 365, L43
- Turner, E. L., Ostriker, J. P., & Gott, III, J. R. 1984, *ApJ*, 284, 1
- Tytler, D., O'Meara, J. M., Suzuki, N., & Lubin, D. 2000, *Phys. Rep.*, 333, 409
- Udalski, A., Szymanski, M., Kaluzny, J., et al. 1993, *Acta Astronomica*, 43, 289
- Udalski, A., Szymanski, M. K., Kubiak, M., et al. 2006, *Acta Astronomica*, 56, 293
- Udomprasert, P. S., Mason, B. S., Readhead, A. C. S., & Pearson, T. J. 2004, *ApJ*, 615, 63
- Vakulik, V. G., Dudinov, V. N., Zheleznyak, A. P., et al. 1997, *Astronomische Nachrichten*, 318, 73
- van Albada, T. S., Bahcall, J. N., Begeman, K., & Sancisi, R. 1985, *ApJ*, 295, 305
- van de Ven, G., Falcon-Barroso, J., McDermid, R. M., et al. 2008, *astro-ph/0807.4175*
- van den Bosch, F. C., Robertson, B. E., Dalcanton, J. J., & de Blok, W. J. G. 2000, *AJ*, 119, 1579
- van Dokkum, P. G. 2001, *PASP*, 113, 1420
- Van Waerbeke, L., Mellier, Y., Erben, T., et al. 2000, *A&A*, 358, 30
- Vanden Berk, D. E., Richards, G. T., Bauer, A., et al. 2001, *AJ*, 122, 549
- Vuissoz, C., Courbin, F., Sluse, D., et al. 2008, *astro-ph/0803.4015*
- Vuissoz, C., Courbin, F., Sluse, D., et al. 2007, *A&A*, 464, 845
- Walker, A. G. 1935, *MNRAS*, 95, 263
- Walsh, D., Carswell, R. F., & Weymann, R. J. 1979, *Nature*, 279, 381
- Wambsganss, J. 1990, PhD thesis, Thesis Ludwig-Maximilians-Univ., Munich (Germany, F. R.). Fakultät für Physik., (1990)
- Wambsganss, J. 1992, *ApJ*, 386, 19
- Wambsganss, J. 1999, *Journal of Computational and Applied Mathematics*, 109, 353
- Wambsganss, J. & Kundić, T. 1995, *ApJ*, 450, 19
- Wambsganss, J. & Paczyński, B. 1991, *AJ*, 102, 864
- Wambsganss, J. & Paczyński, B. 1994, *AJ*, 108, 1156

- Wambsganss, J., Paczyński, B., & Katz, N. 1990a, *ApJ*, 352, 407
- Wambsganss, J., Paczyński, B., & Schneider, P. 1990b, *ApJ*, 358, L33
- Wambsganss, J., Schmidt, R. W., Colley, W., Kundić, T., & Turner, E. L. 2000, *A&A*, 362, L37
- White, S. D. M. & Rees, M. J. 1978, *MNRAS*, 183, 341
- Williams, K. A., Momcheva, I., Keeton, C. R., Zabludoff, A. I., & Lehár, J. 2006, *ApJ*, 646, 85
- Williams, L. L. R. & Saha, P. 2000, *AJ*, 119, 439
- Wills, B. J., Netzer, H., & Wills, D. 1985, *ApJ*, 288, 94
- Wisotzki, L., Christlieb, N., Liu, M. C., et al. 1999, *A&A*, 348, L41
- Wisotzki, L., Schechter, P. L., Bradt, H. V., Heinmüller, J., & Reimers, D. 2002, *A&A*, 395, 17
- Wisotzki, L., Schechter, P. L., Chen, H.-W., et al. 2004, *A&A*, 419, L31
- Witt, H. J. 1993, *ApJ*, 403, 530
- Witt, H. J. & Mao, S. 1994, *ApJ*, 429, 66
- Witt, H. J. & Mao, S. 1997, *MNRAS*, 291, 211
- Witt, H. J., Mao, S., & Schechter, P. L. 1995, *ApJ*, 443, 18
- Wood-Vasey, W. M., Miknaitis, G., Stubbs, C. W., et al. 2007, *ApJ*, 666, 694
- Woźniak, P. R., Alard, C., Udalski, A., et al. 2000a, *ApJ*, 529, 88
- Woźniak, P. R., Udalski, A., Szymański, M., et al. 2000b, *ApJ*, 540, L65
- Wyithe, J. S. B., Agol, E., & Fluke, C. J. 2002, *MNRAS*, 331, 1041
- Wyithe, J. S. B. & Turner, E. L. 2001, *MNRAS*, 320, 21
- Wyithe, J. S. B. & Webster, R. L. 1999, *MNRAS*, 306, 223
- Wyithe, J. S. B., Webster, R. L., & Turner, E. L. 1999, *MNRAS*, 309, 261
- Wyithe, J. S. B., Webster, R. L., & Turner, E. L. 2000a, *MNRAS*, 315, 51
- Wyithe, J. S. B., Webster, R. L., Turner, E. L., & Mortlock, D. J. 2000b, *MNRAS*, 315, 62
- Yonehara, A. 2001, *ApJ*, 548, L127
- Young, P. 1981, *ApJ*, 244, 756
- Zheng, W., Kriss, G. A., Telfer, R. C., Grimes, J. P., & Davidsen, A. 1997, *ApJ*, 475, 469
- Zwicky, F. 1937a, *Physical Review*, 51, 290
- Zwicky, F. 1937b, *ApJ*, 86, 217
- Zwicky, F. 1937c, *Physical Review*, 51, 679

# Publications

## Publications related to this thesis

- “Microlensing variability in the gravitationally lensed quasar QSO 2237+0305  $\equiv$  the Einstein Cross. II. Energy profile of the accretion disk”, Eigenbrod, A., Courbin, F., Meylan, G., Agol, E., Anguita, T., Schmidt, R. W., Wambsganss J., 2008, *Astronomy & Astrophysics*, v. 490, pp. 933-943
- “Microlensing variability in the gravitationally lensed quasar QSO 2237+0305  $\equiv$  the Einstein Cross. I. Spectrophotometric monitoring with the VLT”, Eigenbrod, A., Courbin, F., Sluse, D., Meylan, G., Agol, E., 2008, *Astronomy & Astrophysics*, v. 480, pp. 647-661
- “COSMOGRAIL: the COSmological MONitoring of GRAvItational Lenses. VI. Redshift of the lensing galaxy in seven gravitationally lensed quasars”, Eigenbrod, A., Courbin, F., Meylan, G., 2007, *Astronomy & Astrophysics*, v. 465, pp. 51-56
- “COSMOGRAIL: the COSmological MONitoring of GRAvItational Lenses. V. The time delay in SDSS J1650+4251”, Vuissoz, C., Courbin, F., Sluse, D., Meylan, G., Ibrahimov, M., Asfandiyarov, I., Stoops, E., Eigenbrod, A., Le Guillou, L., van Winckel, H., Magain, P., 2007, *Astronomy & Astrophysics*, v. 464, pp. 845-851
- “COSMOGRAIL: the COSmological MONitoring of GRAvItational Lenses III. Redshift of the lensing galaxy in eight gravitationally lensed quasars”, Eigenbrod, A., Courbin, F., Meylan, G., Vuissoz, C., Magain, P., 2006, *Astronomy & Astrophysics*, v. 451, pp. 759-766
- “COSMOGRAIL: the COSmological MONitoring of GRAvItational Lenses II. SDSS J0924+0219: the redshift of the lensing galaxy, the quasar spectral variability and the Einstein rings”, Eigenbrod, A., Courbin, F., Dye, S., Meylan, G., Sluse, D., Saha, P., Vuissoz, C., Magain, P., 2006, *Astronomy & Astrophysics*, v. 451, pp. 747-757
- “COSMOGRAIL: the COSmological MONitoring of GRAvItational Lenses I. How to sample the light curves of gravitationally lensed quasars to measure accurate time delays.”, Eigenbrod, A., Courbin, F., Vuissoz, C., Meylan, G., Saha, P., Dye, S., 2005, *Astronomy & Astrophysics*, v. 436, pp. 25-35

## Publications in conference proceedings

- “Microlensing variability in the gravitationally lensed quasar Q 2237+0305 = the Einstein Cross”,  
Eigenbrod, A., Courbin, F., Sluse, D., Meylan, G., Agol, E., 2008, Proceedings of the Manchester Microlensing Conference: The 12th International Conference and ANGLES Microlensing Workshop
- “COSMOGRAIL: the COSmological MONitoring of GRAvitational Lenses”,  
Courbin, F., Eigenbrod, A., Vuissoz, C., Meylan, G., Magain, P., 2005, in Impact of Gravitational Lensing on Cosmology, IAU Symposium, vol. 225. edited by Y. Mellier & G. Meylan, Cambridge, UK, Cambridge University Press, pp. 297-303 (ISBN 0521851963)

## Publications unrelated to this thesis

- “Limitations in lens modeling for doubly imaged quasars and impact on  $H_0$ : the study case of QJ 0158–4325”,  
Faure, C., Anguita, T., Eigenbrod, A., Kneib, J.-P., Chantry, V., Alloin, D., Morgan, N., Covone, G., 2008, submitted to Astronomy & Astrophysics
- “A sharp look at the gravitationally lensed quasar SDSS J0806+2006 with Laser Guide Star Adaptive Optics at the VLT”,  
Sluse, D., Courbin, F., Eigenbrod, A., Meylan G., 2008, accepted for publication in Astronomy & Astrophysics
- “An Exploratory Search for  $z \sim 6$  Quasars in the UKIDSS Early Data Release”,  
Glikman, E., Eigenbrod, A., Djorgovski, S. G., Meylan, G., Thompson, D., Mahabal, A., Courbin, F., 2008, The Astronomical Journal, v. 136, pp. 954-962
- “Deep optical spectroscopy of extended Lyman alpha emission around three radio-quiet  $z=4.5$  quasars”,  
Courbin, F., North, P., Eigenbrod, A., Chelouche, D., 2008, Astronomy & Astrophysics, v. 488, pp. 91-97
- “GRB 050509b: the elusive optical/nIR/mm afterglow of a short-duration GRB”,  
Castro-Tirado, A. J., de Ugarte Postigo, A., Gorosabel, J., Fathkullin, T., Sokolov, V., Bremer, M., Marquez, I., Marin, A. J., Guziy, S., Jelinek, M., Kubanek, P., Hudec, R., Vitek, S., Mateo Sanguino, T. J., Eigenbrod, A., Perez-Ramirez, M. D., Sota, A., Masegosa, J., Prada, F., Moles, M., 2005, Astronomy & Astrophysics, v. 439, pp. L15-L18
- “Red giants in open clusters. XI. Membership, duplicity, and structure of NGC 2477”,  
Eigenbrod, A., Mermilliod, J.-C., Claria, J. J., Andersen, J., Mayor, M., 2004, Astronomy & Astrophysics, v. 423, pp. 189-197



## Alexander EIGENBROD

Address :           Route de la Chenalette 30  
                  1163 Etoy  
                  Switzerland  
Date of birth :     April 17th 1980  
Place of birth :   Wedel Holstein, Germany  
Nationality :      German  
Civil status :     Single



### Education

2004–2008 **PhD thesis in Physics**  
Laboratoire d’Astrophysique, Ecole Polytechnique Fédérale de Lausanne  
”Astrophysical Applications of Gravitationally Lensed Quasars:  
From Dark Matter Halos to the Structure of Quasar Accretion Disks”  
1998–2003 **Master in Physics**  
Institut d’Astronomie, Université de Lausanne  
”Structure et cinématique des amas ouverts d’âge intermédiaire”  
1995–1998 **Federal Maturity in Science**  
Gymnase du Bugnon, Lausanne

### Professional Experiences

2004–2008 **Research and teaching assistant**  
Laboratoire d’Astrophysique, Ecole Polytechnique Fédérale de Lausanne  
Research about gravitational lensing. Supervision of exercises in general  
physics, astrophysics, and observational cosmology.  
2003–2004 **Research and teaching assistant**  
Institut d’Astronomie, Université de Lausanne  
Research about open clusters. Supervision of astrophysics labs and  
exercises for master students.  
2001–2003 **Teaching assistant**  
Institut de Physique de la matière condensée, Université de Lausanne  
Supervision of physics labs for undergraduate students.

### Prizes and awards

1. Nominated for the EPFL doctorate awards (final selection in 2010)
2. Prize of German of the “Département de la formation et de la jeunesse” (1998)
3. Prize Robert Delacrausaz in Physics (1995)

### Referee activity

1. Astrophysical Journal
2. Astronomy & Astrophysics
3. Revista Mexicana de Astronomía y Astrofísica

### Invited talks

1. *Imaging of a Gravitational Lensed Quasar at Micro-arcsecond Scales*, General Assembly of the Swiss Society of Astronomy and Astrophysics, Universität Bern, Switzerland, October 26, 2007.
2. *Integral Field Spectroscopy of the Lensing Galaxy in the Einstein Cross*, Applications of Gravitational Lensing: Unique Insights into Galaxy Formation and Evolution, Kalvi Institute for Theoretical Physics, University of California, Santa Barbara, United States, October 03 - 06, 2006.
3. *Microlensing in the Einstein Cross with the VLT*, 8ème Journée des Lacs Alpains de Cosmologie, Geneva Observatory, Switzerland, January 26, 2005.

### Posters

1. *Microlensing Variability in the Gravitationally Lensed Quasar QSO 2237+0305  $\equiv$  the Einstein Cross. I. Spectrophotometric Monitoring with the VLT*, Manchester Microlensing Conference, University of Manchester, United Kingdom, January 21 - 25, 2008.
2. *The Dark Matter in the Lensing Galaxy of the Einstein Cross*, La Journée de la Recherche, Ecole Polytechnique Fédérale de Lausanne, Switzerland, November 16, 2006.
3. *Integral Field Spectroscopy of the Lensing Galaxy in the Einstein Cross*, Applications of Gravitational Lensing: Unique Insights into Galaxy Formation and Evolution, Kalvi Institute for Theoretical Physics, University of California, Santa Barbara, United States, October 03 - 06, 2006.
4. *Detailed Observations and Modeling of Gravitational Lenses*, La Journée de la Recherche, Ecole Polytechnique Fédérale de Lausanne, Switzerland, November 11, 2005.

### Languages

1. German : mother tongue
2. French : fluent (scolarity followed in French)
3. English : fluent

### Computer Sciences

- Operating systems : Windows, UNIX, Linux and Mac OS
- Programming and markup languages : fortran, python, IDL, html
- Software : LaTeX, MS office

### Other achievements and interests

- International press release about the microlensing study of the Einstein Cross (8th December, 2008)
- Selected for the first round of psychological tests of the ESA astronaut selection 2008
- Member of the Swiss Society of Astrophysics and Astronomy
- Member of the scuba-diving center Maui-Diving, Diving Licence CMAS P2+
- Member of the aviation school AéroFormation, Restricted Private Pilot Licence
- Other sports: fitness, tennis, snowboard, football
- Participation in the organization of ATHLETISSIMA, the international athletics meeting in Lausanne (editions 2003 - 2007)